NDT Applications for the Assessment of Asphalt Pavements, Plate Thickness, and Steel-Grout Coupling

by

Yen Chieh Wu

A thesis

presented to the University of Waterloo

in fulfillment of the

thesis requirement for the degree of

Master of Applied Science

in

Civil Engineering

Waterloo, Ontario, Canada, 2012

I hereby declare that I am the sole author of this thesis. This is a true copy of the thesis, including any required final revisions, as accepted by my examiners.

I understand that my thesis may be made electronically available to the public.

ABSTRACT

Nondestructive testing (NDT) uses different wave propagation modes to evaluate the internal structure of materials, revealing internal damage such as corrosion and fracturing that cannot be detected by traditional methods. Civil infrastructures are considered high priority assets in Ontario and Canada because of their value, high consequence of failure, and the continual influence of aging effects. Unexpected failure of infrastructure not only costs more than planned replacements but also results in increased safety risks. The in-situ condition assessment of civil infrastructure is critical for the successful implementation of maintenance and safety programs. Therefore, reliable nondestructive methods of inspection are required for the implementation of economical and efficient maintenance and asset management programs.

Continuing technological developments in data collection, acquisition equipment, and data processing techniques have provided useful applications of nondestructive methods in many engineering fields. Among the many applications, this research study examines three applications of nondestructive testing in civil engineering: (1) condition assessment of construction joints in asphalt pavements, (2) average thickness evaluation of steel pipes, and (3) void and debonding detection in grouted steel tanks.

The study on asphalt focuses on the improvement of the coupling system between the transducers and the asphalt surface, and the development of a new data processing technique to reduce user input and increase the reliability of the condition assessment of longitudinal joints. The current wavelet transmission coefficient (WTC) method requires user input, making the automatic data processing difficult. In the WTC method, the coupling between the transducers and the asphalt surface requires the use of epoxy and aluminum plates. This procedure is not practical for testing in-service roads. A new coupling mechanism using polyurethane foam to provide a spring action on the transducers and calibrated weights to generate a compression force was developed and showed good results, reducing the testing time by up to 50%. A new and robust data analysis methodology, called instantaneous transmission coefficient (ITC), is proposed based on measured instantaneous frequencies and damping ratios. The main advantage of the ITC procedure is that it can be performed

automatically, reducing user input. A laboratory scale asphalt slab is used to evaluate the new methodology. Results show good agreement between the WTC and ITC measurements for both jointed and joint-free areas.

The second study investigates the feasibility of the multichannel analysis of surface waves (MASW) technique for the evaluation of the average wall thickness of steel pipes. Electromagnetic NDT methods, such as the eddy current and the remote field testing, are common tools for thickness measurement of conductive materials. However, these methods give only localized results where measurements are made, making the process time consuming and inaccurate for assessing the full cross-sectional area of the pipe. Lamb waves have been used previously in the evaluation of steel pipes; however, the existing techniques require prior calibration to a theoretical wave mode, and their accuracy decreases with the length of the pipe evaluated due to wave attenuation effects. Preliminary results show the capability of the MASW test for providing reliable thickness information. The measured dispersion curves include information of fundamental modes and the higher modes, providing an improved characterization of the medium. Thicknesses between 3.2 mm and 12.7 mm are tested with an error of less than 2%.

The third study explores the detection of voids in a steel tank filled with lightweight grout. A joint analysis of surface waves and Lamb waves is used for void detection and the identification of debonding conditions in a laboratory scale model of a steel tank filled with grout. Different configurations of the MASW method are conducted using an instrumented hammer (large wavelengths, 10 cm $< \lambda <$ 25 cm) and a 50 kHz piezoelectric transmitter (small wavelengths, 5 cm $< \lambda <$ 9 cm) as sources. The attenuation coefficient computed from the Fourier spectra of the measured signals indicates that the presence of a void has an effect on the propagation of the wave. The comparison between experimental and theoretical dispersion curves show that mainly Lamb waves are generated during the testing of the steel tank; thus, detecting the debonding conditions between the steel plate and the grout. Lamb modes are used successfully for detecting the presence of a void beneath the steel wall. The laboratory measurements are effective in the detection of the void, showing amplitudes up to 50% higher, likely because the deformation of the wall is attenuated by the grout.

ACKNOWLEDGEMENTS

First and foremost, I express my sincerest gratitude to Dr. Giovanni Cascante for his guidance and expertise. I greatly appreciate his time, inspiration and encouragement through this research work. His perpetual energy and enthusiasm in research have been extremely motivating.

My deepest gratitude goes to Dr. Mahesh D. Pandey for his kind support and the review of my work.

I would like to acknowledge the contribution of the Ministry of Transportation of Ontario (MTO); special thanks to Pamela Marks and Joseph Ponniah for their support and suggestions. My sincere appreciation is also expressed to Sensors & Software for their assistance in the GPR tests.

My gratitude also goes to Dr. Jeff West for his involvement in the grouted steel tank study; his insightful comments and revisions helped improve the quality of the final version of this thesis.

I would like to thank John Boldt and Jorge Cruz from the machine shop for their assistance in preparing the test specimens. I greatly appreciate their enthusiasm and willingness to help.

My gratitude is extended to all the members in our NDT group. Special thanks to Antonin du Tertre for teaching me how to use the laboratory equipment. I would like to thank Soheil Moayerian, Paul Groves, Serhan Kirlangic and Hassan Ali for creating an enjoyable working environment. Research life became smooth and rewarding thanks to my friends and colleagues.

Finally, none of this would have been possible without the encouragement and support of my family.

TABLE OF CONTENTS

LIST OF TABLES

LIST OF FIGURES

CHAPTER 1. INTRODUCTION

1.1 Background

Nondestructive testing (NDT) uses the propagation of different wave modes for the evaluation of the internal structure of materials. Continuing technological developments in data collection, acquisition equipment and data processing techniques have provided useful applications of nondestructive methods in many engineering fields. Among the many applications, wave-based technologies can be used for the evaluation of asphalt pavements, for the thickness investigation of steel pipes, and void detection. The frequency of mechanical waves is changed accordingly to the required depth of the features of interest in the investigation. Seismic waves ($f < 20$ kHz) and ultrasonic waves (20 kHz $< f <$ 1 MHz) are currently used to detect anomalies from millimeter size to tens of meter dimensions. This research examines three separate applications of NDT in civil engineering: the condition assessment of joints in asphalt slabs, the thickness evaluation of steel pipes, and the void detection in grouted steel tanks.

Traditionally, poor-quality longitudinal construction joints often contribute to the poor performance of hot mix asphalt pavements (HMA). Poor contact between adjacent faces of the joints is typically associated with low compaction or improper construction practice; which in turn may lead to poorly constructed joints in asphalt pavements. Currently, density measurements are used to assess the level of contact or bonding between the joints; however, this method involves coring at five different locations across the joint. This approach is not only destructive but also time consuming; therefore, a fast and inexpensive nondestructive method was needed. Laboratory experiments have showed that there is a high correlation ($R^2 > 0.99$) between the attenuation of compression waves and the degree of compaction or number of gyrations. The number of gyrations is a measure of the level of bonding among aggregate-asphalt contacts; therefore, the attenuation of ultrasonic waves is sensitive to the properties of the asphalt-aggregate contacts developed in HMA during compaction. This strong correlation supports the potential use of mechanical waves for the condition

assessment of longitudinal joints in asphalt pavements, as the quality of the joint depends on the contacts between two adjacent HMA mats.

An innovative nondestructive test for condition assessment of the longitudinal joints in asphalt pavements was developed at the University of Waterloo in collaboration with the Ministry of Transportation, Ontario (Jiang, 2007). Novel experimental and signal processing techniques were used to minimize the variability associated with unknown limitations of different factors such as properties of transducers, wave travel paths, and the effects of source/receiver coupling. Nevertheless, this technique requires more user input, as it involves selecting peak values from the wavelet transform, making the automatic data processing difficult. Furthermore, the coupling of the transducers to the asphalt surface was accomplished using epoxy and aluminum plates, which is not practical for testing in-service roads.

The first study presented in this research consists of the improvement of the existing methodology by optimizing the coupling mechanisms and the development of a new data processing technique reducing the user input. An experimental program is designed to investigate new coupling mechanisms and evaluate the possibility of eliminating the use of epoxy and aluminum plates, to reduce the testing time. A new transmission coefficient (ITC) is developed based on the instantaneous frequency and damping measurements; the ITC procedure can be performed automatically, reducing the user input.

Wave-based technologies are also used to measure material thickness in a wide variety of industries, including manufacturing quality control and in-service monitoring (Basravi, 2004). In many cases, nondestructive methods can be used to precisely measure wall thickness in situations where access is available to only one side of a test piece, as in a pipe or tank, where simple mechanical measurements are impossible or impractical. The loss of wall thickness in pipelines affects the reliability and safety of a plant (Hwang et al., 2002). The pipelines are usually covered with a layer of insulation for thermal loss; therefore, the wall thinning must be detected without removing the insulation. A fast and accurate tool to measure wall thickness is especially needed for evaluating pipe assemblies such as heat exchangers and heat generators at power plants and petrochemical facilities, without shutting down the manufacturing process.

Several nondestructive technologies are used for the measurement of wall thickness of steel pipes, such as eddy current testing and ultrasonic techniques. Although ultrasonic thickness measurement is one of the most popular methods for determining steel plate thicknesses (Damgaard, 2009), it allows the detection of pipe wall thickness along the total length by provinding results only where measurements were made. This process is time consuming and inaccurate for assessing the full cross-sectional area of the pipe. The second study presented in this research utilizes the multichannel analysis of surface waves technique for the evaluation of an average thickness of steel plates.

Another common challenge in NDT is the detection of voids or flaws in a material in contact with a steel plate, where only the surface of the plate can be instrumented. Most electromagnetic methods cannot be used on steel because of the metal's high conductivity, which reduces the penetration depth available to evaluate the material underneath. Similarly, while high-frequency ultrasonic methods are suited for detection of the thickness of the steel plate, the generated energy is not enough to penetrate to the material beneath the plate. This work is applied to the decommissioning of a large steel tank in an industrial environment. Dismantling or demolishing the tank was not feasible, so it was proposed to solidify the tank for permanent decommissioning using a lightweight cement-bentonite grout.

The actual conditions in the field constrained the direct observation of the grouting operation; hence it was proposed to investigate nondestructive methods to detect air and water pockets, or voids, in the grout, as well as separation of the grout from the interior surface of the tank due to grout shrinkage after hardening. Recent studies have shown the effectiveness of impact echo (IE) and pulse-echo ultrasonic techniques in applications involving delaminations, voids, thickness variations and corrosion in concrete sections (Aggelis et al., 2010; Beutel et al., 2008; Shah and Ribakov, 2008; Dilek, 2007). These studies show that both IE and ultrasonic methods work well when used for detecting faults or voids within uniform concrete sections, and where surface conditions are favorable for the coupling of ultrasonic transducers. There are limited published results for more uncommon applications, such as the use of ultrasonic wave-based techniques to locate voids in grout enclosed by a steel tank.

The third study presented in this research involves testing with multichannel analysis of surface waves on a steel tank filled with grout, where high-frequency ultrasonic and low-frequency acoustic waves are generated to evaluate the steel plate thickness and detect voids in the grout.

1.2 Research Objectives

The overall goal of this research is to investigate three potential applications of nondestructive testing in the practice of civil engineering. The primary objective of the asphalt study is the improvement of the coupling mechanism between the transducer and the medium, and the development of a new data processing technique to reduce user input for the analysis of NDT measurements. Exploratory ground penetrating radar (GPR) measurements are used in conjunction with the ultrasonic techniques for a comprehensive evaluation of pavement condition across a construction joint.

The main objective of the steel pipe study is to evaluate the application of the multichannel analysis of surface waves (MASW) technique in determining an average thickness in a steel pipe section. The determination of effective thickness is verified with theoretical dispersion curves.

The third study focuses on the applicability of the MASW technique for the detection of voids and debonding in a grouted steel tank by using low-frequency and high-frequency mechanical waves. Furthermore, Lamb waves are also used to detect debonding between the steel tank and the grout.

1.3 Research Methodology

The methodology employed to achieve the research objectives can be subdivided in the three studies:

General

- Review the theory of wave propagation in a medium and relate wave characteristics to material properties.

- Study the different signal processing techniques for data collection and signal processing for wave-based testing methods.
- Review the nondestructive testing methods for material characterization, assess the advantages and limitations related to each method, and develop an improved technique with complementary use of wave characteristics for material characterization tests.

Study 1

- Evaluate the effects of different coupling configuration and the relative receiver transfer functions of the experimental test setup by performing a calibrated test on two standard materials.
- Study the effects of different coupling mechanisms on a density-controlled pavement slab to improve the WTC technique by considering various experimental setups, using: aluminum plate, vacuum grease or glue as couplant, vertical pressure, and cylindrical foam wrap as an isolator.
- Improve the WTC technique with an alternative use of wave characteristics for material characterization tests: Hilbert transform and analytic signals, overcoming the WTC limitations.
- Conduct laboratory experiments on a fabricated pavement slab to investigate the viability and effectiveness of using instantaneous material damping values to assess the condition of asphalt joints. Compare the wave-based test results with ground penetrating radar measurements.

Study 2

- Perform experimental tests on samples of cold rolled steel plates using the multichannel analysis of surface waves technique.
- Compute the average wall thickness from the theoretical dispersion curves and determine the feasibility of the MASW method.

Study 3

- Conduct experimental tests on a grouted steel tank using high-frequency ultrasonic waves and low-frequency acoustic waves to generate Lamb waves and Rayleigh waves, respectively. Evaluate the grout-steel coupling and detect the voids in the grout.
- Perform experimental tests at locations of suspected voids and where voids were not expected. Verify the location of the voids in a destructive evaluation.

1.4 Thesis Organization

The opening chapter provides an introduction, presents objectives and gives the general outline of this research study.

Chapter 2 presents relevant background information, while providing an overview of the theory of wave propagation and its relationship to the elastic properties of materials. Wave equations are provided to determine wave velocities; physical phenomena associated to wave propagation, such as wave reflection, transmission, mode conversion and superposition are discussed. The definitions of material and geometrical attenuation are reviewed.

Chapter 3 reviews different signal processing techniques used to analyze the data from nondestructive tests. The signals can be analyzed in both time and frequency domains. Techniques, such as Fourier transform, short time Fourier transform, wavelet transform and Hilbert-Huang transform, are described, and the main advantages and limitations are discussed.

Chapter 4 presents different NDT methods used in the condition assessment of asphalt slabs, wall thickness evaluation of steel pipes and void detection in grout. Electromagnetic and ultrasonic methods are described, and the main limitations to each method are discussed. Techniques based on wave attenuation are also described.

Chapter 5 presents the measurement of the frequency response curves of the twenty piezoelectric accelerometers used herein. The pulsed velocity method is used on two calibration bars, with two different coupling configurations. The relative characterization is

important for removing the undesirable effects induced by manufacturing differences. Thus, the selection of receivers used in Studies 1, 2 and 3 are based on the results of this calibration procedure.

Chapter 6 presents the results from the evaluation of the asphalt pavement (Study 1), starting with a brief description of the experimental setup and testing methodology. This first study is focused on the improvement of the coupling between the medium and the transducers, and the development of a new data processing technique to reduce user input. The effects of different coupling mechanisms are evaluated to optimize the coupling and improve the signal quality. The second part of this study is focused on the development of a new robust experimental and analytical methodology (instantaneous transmission coefficient), based on the calculation of instantaneous frequencies and damping ratios using the Hilbert transform. Finally, wave-based test results are compared to ground penetrating radar measurements.

Chapter 7 presents the application of the MASW technique for the evaluation of average thickness of steel plates (Study 2). This study involves testing on steel plates with different thicknesses and a pipe sample; the experimental dispersion curves are constructed from the response signals. The comparison with the theoretical dispersion curves provides information about the thickness of the steel wall.

Chapter 8 evaluates the ultrasonic testing for the detection of voids or debonding in a grouted steel tank (Study 3). The methodology consists of four test configurations, performed at different locations of the tank and using different frequency ranges. A series of experiments are conducted at the locations of suspected voids and where voids were not expected.

Finally, the conclusions and recommendations are presented in Chapter 9.

CHAPTER 2. THEORY OF WAVE PROPAGATION

2.1 Background

Nondestructive testing techniques use the analysis of elastic wave properties to provide information on the internal characteristics of a material. When a perturbation is created in an elastic medium, mechanical waves are generated. The wave propagation depends on the type of wave and the elastic properties of the medium though which the wave travels. The most commonly used wave properties are wavelength (λ), frequency (f) and velocity (V) which are related by:

$$V = f\,\lambda \tag{2-1}$$

Thus, the frequency is inversely proportional to the wavelength, and high frequency waves have smaller wavelengths than low frequency waves.

An elastic wave can also be characterized by its time period (T) and wave number (k), as follows

$$T = \frac{1}{f} \tag{2-2}$$

$$k = \frac{2\,\pi}{\lambda} \tag{2-3}$$

2.2 Modes of Propagation

Wave propagation is generally described by oscillatory patterns or wave modes. Wave modes are characterized in terms of the direction of the particle motion in relation to the direction of propagation. Elastic waves propagate mainly as three types of waves: body waves, surface waves and Lamb waves. Body waves propagate in a radial direction outward from the source. Surface waves are confined to propagating at surfaces and interfaces. Lamb

waves are generated in a medium with two free surfaces as surface waves interact with the boundaries.

2.2.1 Body Waves

Body waves travel through the internal volume of an elastic medium, and propagate outwards from a source in a semi-spherical wave front. Body waves are non-dispersive in a homogenous medium; the velocity of propagation remains constant for any frequency component. Body waves consist mainly of two types of wave modes: compression (P-waves) and shear (S-waves), as illustrated in Figure 2-1.

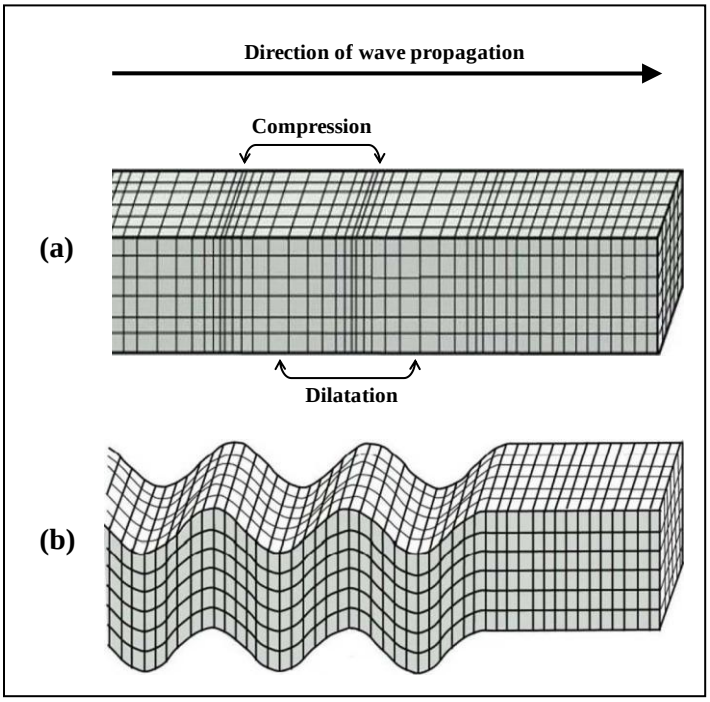

Figure 2-1. Particle motion of body waves: **(a)** P-waves, and **(b)** S-waves. (Bolt 1978)

2.2.1.1. Compression waves

Compression waves, also known as P-waves, primary waves, and longitudinal waves, travel with particle motions (compression and dilatation) parallel to the direction of propagation, as illustrated in Figure 2-1(a). P-waves can travel through any medium that provides resistance

to compression and elongation of the particles; therefore, they exist in solids, liquids and gas. When travelling though solids, compression waves are the fastest among the other modes, and they are the first wave mode to arrive; hence, they are known as primary waves.

2.2.1.2. Shear waves

Shear waves, also known as S-waves, secondary waves, and transverse waves, propagate with oscillatory particle motion perpendicular to the direction of propagation, as illustrated in Figure 2-1(b). S-wave propagation consists of pure shear strain with no change in volumetric strain. These waves cannot propagate through fluids (liquid and gas) due to the lack of shear stiffness. Since shear waves travel at a lower speed than P-waves, they are called also secondary waves.

2.2.1.3. Wave velocity

Wave velocity, also known as group velocity, is the speed of a wave propagating in a medium. Wave velocity provides information about material properties, such as elasticity, stiffness and density. Each material permits a particular velocity of wave propagation; therefore, material characterization can be performed by measuring this velocity.

Wave velocity is proportional to material elasticity and inversely proportional to material mass density. Since P-waves travel by dilatation and compression of the particles, they are controlled by Young's modulus; in contrast, S-waves are controlled by the shear modulus.

Wave propagation in an infinite isotropic elastic solid satisfies Newton's second law of motion, which leads to the following equation in the Cartesian coordinate system $x(x_1, x_2, x_3)$:

$$\rho \frac{\partial^2 u_i}{\partial t^2} = \sum_{j=1}^{n} \frac{\partial \sigma_{ij}}{\partial x_j} \tag{2-4}$$

where $i, j \epsilon [1, 2, 3]$, $n = 3$, ρ is the material mass density, $u(u_1, u_2, u_3)$ are the displacements of a point in $x(x_1, x_2, x_3)$, t is the time, and $\sigma(\sigma_{11}, \sigma_{12}, \ldots \sigma_{33})$ are the stress components of an element within the solid.

According to Hooke's law, the stresses acting on an elementary volume can be expressed as a linear combination of strains. Then the stress components in Equation (2-4) can be rewritten as

$$\sigma_{ij} = \lambda \, \Delta \, \delta_{ij} + 2 \, \mu \, \varepsilon_{ij} \tag{2-5}$$

where λ is Lamé's elastic constant, μ is the shear modulus, $\Delta = \varepsilon_{11} + \varepsilon_{22} + \varepsilon_{33}$ is the volumetric strain, and δ_{ij} is the Kronecker's constant which is equal to 1 if $i = j$ and 0 otherwise.

The strain is given as a function of the displacement:

$$\varepsilon_{ij} = \frac{1}{2}\left(\frac{\partial u_i}{\partial x_j} + \frac{\partial u_j}{\partial x_i}\right) \tag{2-6}$$

By substituting Equations (2-5) and (2-6) into Equation (2-4), the equation of motion can be reduced to

$$\rho \, \frac{\partial^2 u_i}{\partial t^2} = (\lambda + \mu) \, \frac{\partial \Delta}{\partial x_i} + \mu \sum_{j=1}^{n} \frac{\partial^2 u_i}{\partial x_j^2} \tag{2-7}$$

The displacements can be divided into two parts: longitudinal with zero rotation, and transverse with zero dilatation, each of which correspond to P-wave and S-wave modes, respectively. Since the S-wave mode has no volume change associated with it, the shear wave velocity (V_S) can be determined from Equation (2-7) as

$$V_S = \sqrt{\frac{\mu}{\rho}} \tag{2-8}$$

Similarly, the compression wave velocity (V_P) is obtained as

$$V_P = \sqrt{\frac{\lambda + 2\,\mu}{\rho}} = \sqrt{\frac{M}{\rho}} \tag{2-9}$$

where M is the constraint modulus. The shear modulus (μ) and constraint modulus (M) can be expressed in terms of Young's modulus (E) and Poisson's ratio (ν) as

$$\mu = \frac{E}{2\,(1+\nu)} \tag{2-10}$$

$$M = \frac{(1-\nu)E}{(1+\nu)(1-2\,\nu)} \tag{2-11}$$

where ν is Poisson's ratio defined as the ratio of the transverse strain by the longitudinal strain:

$$\nu = -\frac{\varepsilon_{transverse}}{\varepsilon_{longitudinal}} \tag{2-12}$$

Poisson's ratio can also be expressed in terms of the P-wave and S-wave velocities, as follows

$$\nu = \frac{2(V_S/V_P)^2 - 1}{2\,[(V_S/V_P)^2 - 1]} \tag{2-13}$$

The ratio of P-wave and S-wave velocities is given by

$$\frac{V_P}{V_S} = \sqrt{\frac{2(1-\nu)}{(1-2\nu)}} \tag{2-14}$$

For a Poisson's ratio of 0.25 and 0.30, Equation (2-14) gives an average $V_S = 0.56\ V_P$.

2.2.2 Surface Waves

Surface waves are confined to the surface of an elastic medium. They can also propagate along the interface between different media. The most commonly discussed surface waves are Rayleigh and Love waves, as illustrated in Figure 2-2. Rayleigh waves, also known as R-waves, propagate outwards from a source with the particle motion of a retrograde ellipse with the major axis perpendicular to the free surface and the direction of propagation. Love waves (L-waves) are confined to a horizontal plane with the particle motion perpendicular to the direction of propagation.

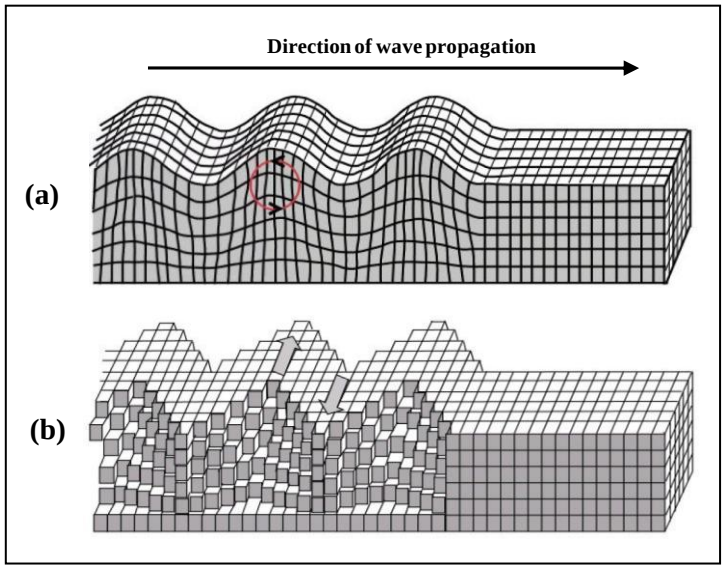

Figure 2-2. Particle motion of surface waves: **(a)** R-waves, and **(b)** L-waves (Bolt 1978).

Usually, L-waves are not generated in ultrasonic testing using high frequencies, because they have a low upper frequency bandwidth.

The effective depth of penetration of an R-wave is approximately one wavelength (Richart et al., 1970); however, most of the energy is concentrated between the surface and a depth of one-third to one-half of the wavelength. A penetration depth of approximately one-third of the wavelength are effectively used for material characterization (Stokoe II and Nazarian, 1983). The horizontal (u_x) and vertical (u_z) displacements for R-waves are given by (Viktorov, 1967)

$$u_x = A\, i \left(k\, e^{-\alpha z} - \frac{\beta^2 + k^2}{2k}\, e^{-\beta z} \right) e^{i(kx-\omega t)}$$
$$u_z = A \left(-\alpha\, e^{-\alpha z} + \frac{\beta^2 + k^2}{2\beta}\, e^{-\beta z} \right) e^{i(kx-\omega t)} \qquad (2\text{-}15)$$

where $\alpha = \sqrt{k^2 - (\omega/V_P)^2}$, $\beta = \sqrt{k^2 - (\omega/V_S)^2}$, A is a constant, i is the imaginary unit, x is the horizontal distance, z is the vertical distance from the source, k is the angular wave

number, and ω is the angular frequency. Positive vertical displacements and negative horizontal displacements near the surface result in a retrograde elliptical particle motion.

R-waves are non-dispersive in homogenous media, where the R-wave velocity (V_R) is constant and is independent of frequency. The velocity in a homogenous medium can be approximated as a function of V_S and Poisson's ratio (Achenbach, 1973):

$$V_R = \frac{0.862 + 1.14\,\nu}{1 + \nu}\,V_S \tag{2-16}$$

As Poisson's ratio varies from 0 to 0.5, Equation (2-16) gives V_R = (0.86 to 0.95) V_S. Approximately 67% of the energy introduced from a source is carried by Rayleigh waves (Richart et al., 1970).

In layered media, R-wave velocity varies with frequency or wavelength. This phenomenon is known as dispersion, where different wavelengths propagate at different velocities. High frequencies generate short wavelengths with limited penetration, and propagate at the velocity of the upper layers. Low frequencies generate large wavelengths with deeper penetration, and the wave velocity is determined by the properties of the deeper layers (Figure 2-3).

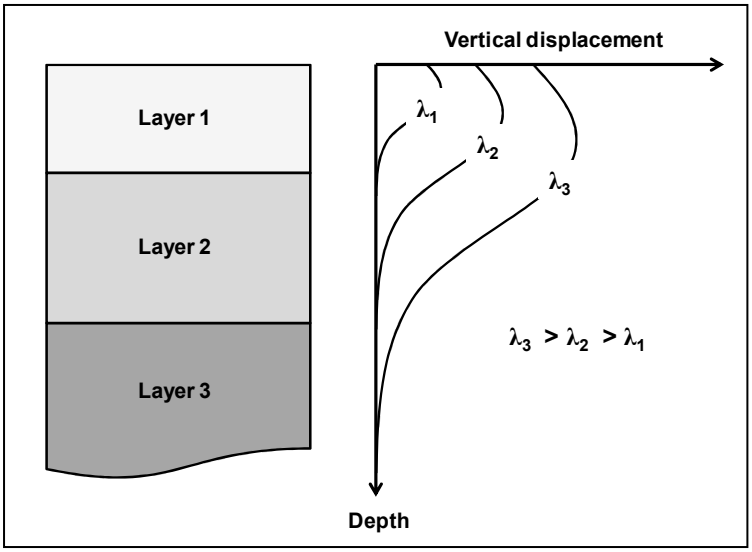

Figure 2-3. Surface waves in layered media.

In a dispersive medium, two different velocities have to be considered: wave velocity (group velocity) and phase velocity. The phase velocities are not constant; they vary with the different frequency components present in the surface wave energy. The group velocity is characterized by the energy propagation and is always constant. The phase velocity is expressed as a function of circular frequency and wave number:

$$V_{ph} = \frac{\omega}{k} \tag{2-17}$$

where $\omega = 2\pi f$ is the angular frequency and k is the wave number.

2.2.3 Lamb Waves

The interaction of the surface waves with the boundaries, in a medium with two free surfaces and with a thickness of approximately one wavelength, can generate Lamb waves (also known as plate waves). Plate waves have symmetrical (longitudinal or extensional) and anti-symmetrical (flexural or bending) mode shapes of propagation. Symmetric Lamb modes generate waves with symmetric thickness variation with respect to a plane at the middle thickness of the medium; conversely, anti-symmetric Lamb modes generate waves with anti-symmetric thickness variation, as can be seen in Figure 2-4.

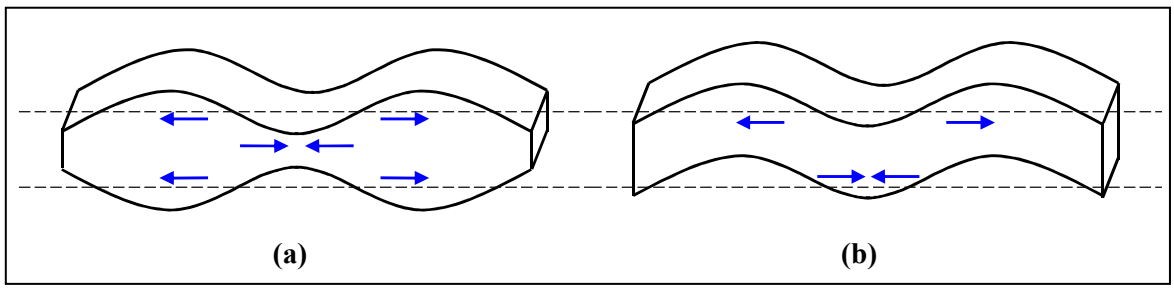

Figure 2-4. Lamb wave mode shapes: **(a)** symmetrical and **(b)** anti-symmetrical.

The displacements for symmetrical ($u^{<s>}$) and anti-symmetrical ($u^{<a>}$) Lamb modes are given by (Viktorov, 1967):

$$
\begin{aligned}
u_x{}^{<s>} &= Ak\left[\frac{\cosh(\alpha z)}{\sinh(\alpha h)} - \frac{2\alpha\beta}{k^2+\beta^2}\frac{\cosh(\beta z)}{\sinh(\beta h)}\right] e^{i\left(kx-\omega t-\frac{\pi}{2}\right)} \\
u_y{}^{<s>} &= -A\alpha\left[\frac{\sinh(\alpha z)}{\sinh(\alpha h)} - \frac{2k^2}{k^2+\beta^2}\frac{\sinh(\beta z)}{\sinh(\beta h)}\right] e^{i(kx-\omega t)} \\
u_x{}^{<a>} &= Bk\left[\frac{\sinh(\alpha z)}{\cosh(\alpha h)} - \frac{2\alpha\beta}{k^2+\beta^2}\frac{\sinh(\beta z)}{\cosh(\beta h)}\right] e^{i\left(kx-\omega t-\frac{\pi}{2}\right)} \\
u_y{}^{<a>} &= -B\alpha\left[\frac{\cosh(\alpha z)}{\cosh(\alpha h)} - \frac{2k^2}{k^2+\beta^2}\frac{\cosh(\beta z)}{\cosh(\beta h)}\right] e^{i(kx-\omega t)}
\end{aligned}
\tag{2-18}
$$

where A and B are constants, h is the half thickness of the plate, and z is the vertical distance from a plane at half the thickness of the plate.

Unlike R-waves, the wave velocity varies with frequency. The wave propagation of Lamb modes is controlled by the Rayleigh-Lamb frequency equation (Graff, 1975):

$$
\frac{tanh(\beta h)}{tanh\,(\alpha h)} + \left[\frac{4\alpha\beta k^2}{(\beta^2-k^2)^2}\right]^{\pm 1} = 0 \tag{2-19}
$$

where the exponent +1 and -1 represent the solutions for the symmetric and anti-symmetric Lamb modes, respectively, h is half the thickness of the plate, and α and β are defined by

$$
\alpha^2 = k^2 - \frac{\omega^2}{{V_P}^2} \qquad\qquad \beta^2 = k^2 - \frac{\omega^2}{{V_S}^2} \tag{2-20}
$$

where k is the wave number, V_P is the P-wave velocity and V_S is the S-wave velocity.

Equation (2-19) has multiple solutions, each of which is a Lamb wave of the plate and has a characteristic mode shape. Unlike body waves and Rayleigh waves, whose velocities are only functions of elastic constants of the material properties, Lamb waves are dispersive in homogenous media where the wave velocity is also a function of frequency .

For a typical 6 mm thick steel plate, with V_P = 5418 m/s, V_S = 3159 m/s, V_R = 2902 m/s and h = 3 mm, the dispersion curves for Lamb modes are illustrated in Figure 2-5. Fundamental symmetric and anti-symmetric modes, S0 and A0, and higher modes (S1, A1, S2, A2, S3 and A3) are notated in Figure 2-5.

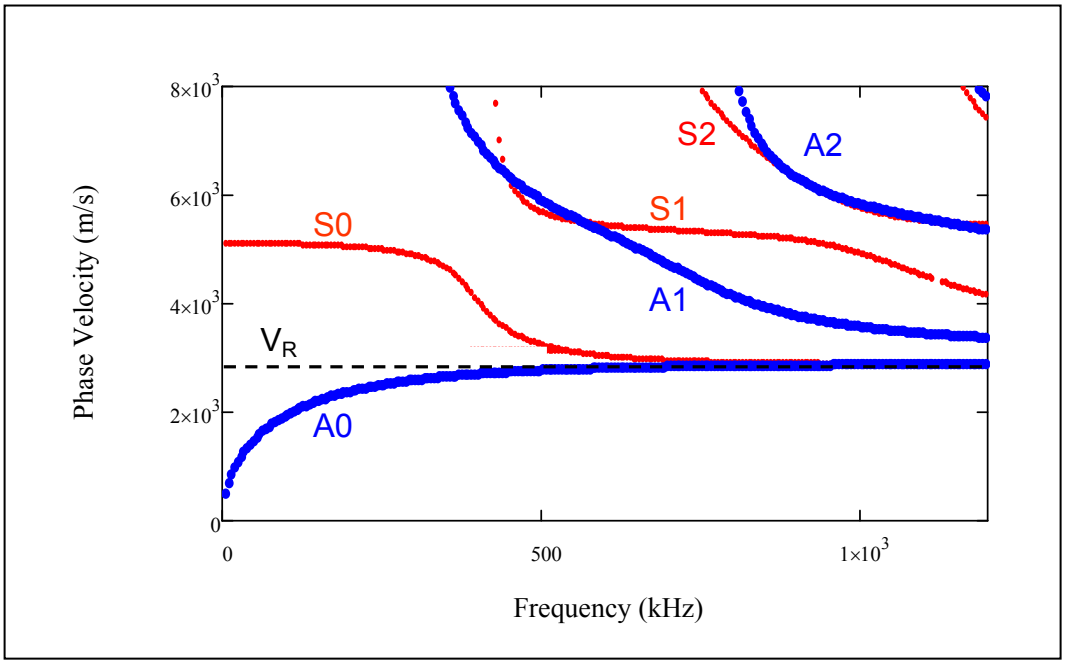

Figure 2-5. Theoretical Lamb wave dispersion curves for a typical steel plate, with V_P = 5418 m/s, V_S = 3159 m/s, V_R = 2902 m/s and h = 3mm.

At high frequencies, where the plate thickness is large relative to the wavelength, the plate behaves like a half-space for R-wave propagation, and Rayleigh waves can propagate independently on the top surface of the plate without any interference from the bottom surface. Lamb wave modes tend toward a constant Rayleigh velocity at high frequencies.

Each Lamb mode defines a characteristic relationship of phase velocity (or wave number) and frequency. High-order Lamb modes appear at frequencies higher than 400 kHz; the S0 is considered nearly non-dispersive at frequencies below 400 kHz. This phenomenon can be seen in Figure 2-5, where both fundamental modes, S0 and A0, converge to V_R at larger frequencies ($f \geq 900$kHz) , with wavelengths approximately half the plate thickness ($\lambda = h =$ 3 mm).

Figure 2-6 shows the comparison of the mode shape for normalized displacements vs. normalized depth between R-wave and fundamental symmetrical Lamb mode (S0) at frequencies of 50 kHz and 100 kHz. The particle displacements at 50 kHz generated by the R-wave and S0 do not match; in contrast, for a higher frequency (100 kHz), these mode displacements are nearly identical.

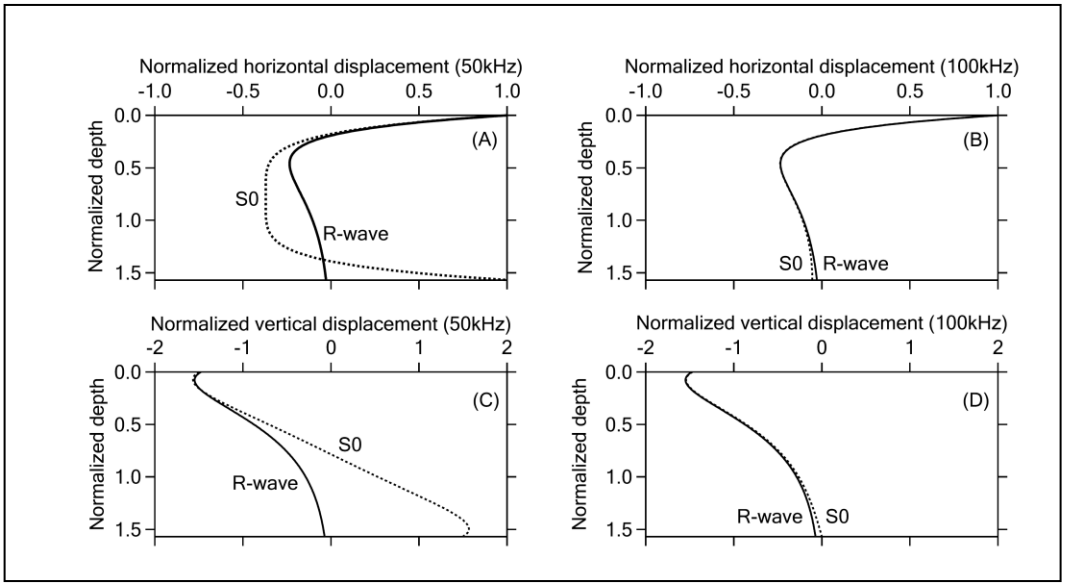

Figure 2-6. Comparison of R-wave and Lamb mode S0 at 50 kHz and 100 kHz.

2.3 Physical Phenomena of Wave Propagation

Wave propagation in a layered or heterogenous medium can be significantly affected by reflection, mode conversion, interference, and other phenomena not included in the theoretical models used to evaluate the material properties. In nondestructive testing, waves interact with discontinuities present in a medium as well as specimen boundaries; thus, the impact of these phenomena on the measured waves must be characterized and minimized.

2.3.1 Acoustic Impedance

The acoustic impedance (Z) of a material is given as the product of its density (ρ) and acoustic velocity (V):

$$Z = \rho V \tag{2-21}$$

The acoustic impedance determines how much of an incident wave is reflected back or refracted through the medium when it hits the interface between two different media. Typical acoustic impedance values for common construction materials are listed in Table 2-1.

Table 2-1. Acoustic impedance of typical construction materials. (Jiang, 2007)

Material	Acoustic impedance (km/m^2s)
Air	4.1×10^{-1}
Water	1.5×10^{6}
Soil	$(1 \text{ to } 3) \times 10^{6}$
Bitumen	1×10^{6}
Asphalt	5×10^{6}
Concrete	$(8 \text{ to } 10) \times 10^{6}$
Granite	$(15 \text{ to } 17) \times 10^{6}$
Steel	4.6×10^{7}

2.3.2 Reflection and Transmission

As an incident wave strikes the interface between two different media of different material properties, part of the wave is reflected and part is transmitted across the interface. The exact behavior of reflection and transmission depend on the material properties on both sides of the interface.

Figure 2-7 shows the reflected and transmitted waves that are generated from an incident wave due to different impedance values of the two materials. Considering two materials with

impedances Z_1 and Z_2, the portion of the reflected and transmitted waves can be determined using the reflection (*Re*) and transmission coefficients (*Tr*):

$$Re = \frac{1 - (Z_1/Z_2)}{1 + (Z_1/Z_2)} \tag{2-22}$$

$$Tr = \frac{2(Z_1/Z_2)}{1 + (Z_1/Z_2)} \tag{2-23}$$

These expressions show that the ratio of the acoustic impedances completely determines the nature of the reflection and the transmission at the interface (Yang, 2009). Both media are uniform when $Z_1/Z_2 = 1$, such that 100% of the waves are transmitted (*Tr* =1) and none are reflected (*Re* = 0).

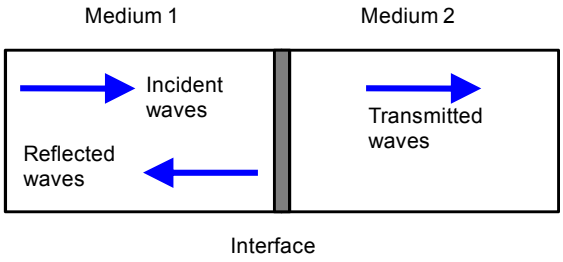

Figure 2-7. Wave reflection and transmission through an interface between two different media.

The direction of the reflected wave follows Snell's law, where the angles of incidence (θ_i) and reflection (θ_r) are identical for the same type of wave, as illustrated in Figure 2-8. According to Snell's law, the angle of transmission (θ_t) depends on the angle of incidence and the wave velocities of the two media, as follows

$$\frac{\sin\theta_i}{V_1} = \frac{\sin\theta_r}{V_1} = \frac{\sin\theta_t}{V_2} \tag{2-24}$$

where V_1 and V_2 are the wave velocities of media *1* and *2*, respectively.

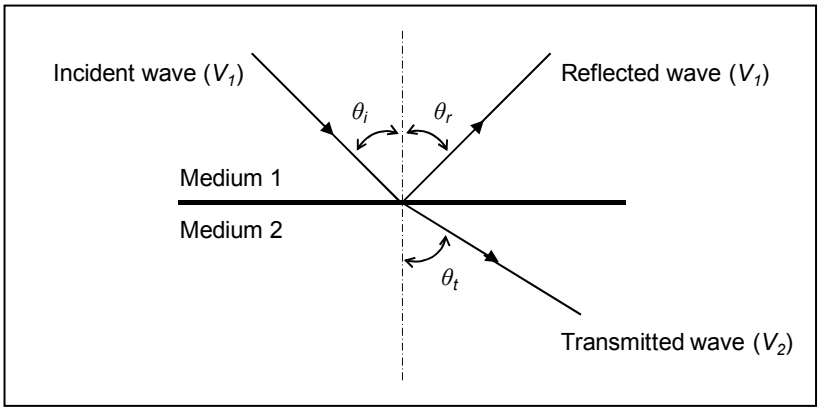

Figure 2-8. Snell's law for wave reflection and transmission.

2.3.3 Mode Conversion

Mode conversion occurs when a wave transforms into another type of wave mode as it propagates through an interface between materials with different acoustic impedances. For instance, if a compression wave (P) strikes an interface, particle vibration can be generated in both longitudinal and transversal directions. As a result, the incident P-wave can be reflected and transmitted as a shear wave (S), as shown in Figure 2-9.

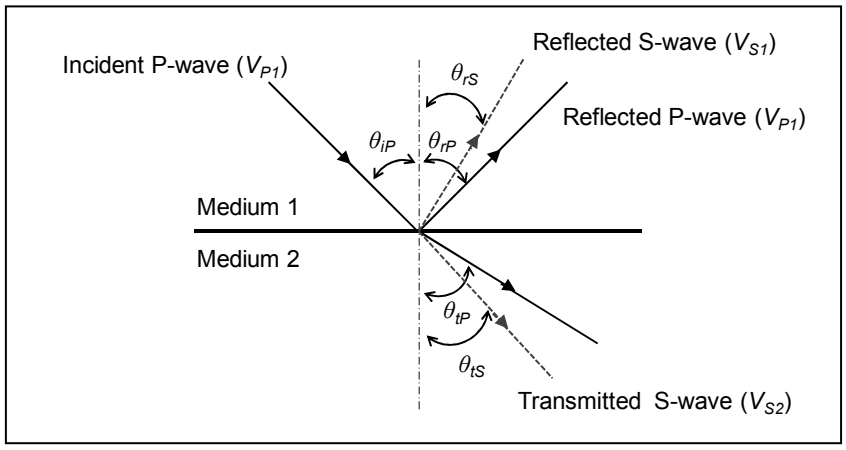

Figure 2-9. Mode conversion phenomena (Blitz and Simpson, 1996).

According to Snell's law, the wave velocities and angles of reflected and transmitted waves are related by the following equation:

$$\frac{\sin\theta_{iP}}{V_{P1}} = \frac{\sin\theta_{rP}}{V_{P1}} = \frac{\sin\theta_{rS}}{V_{S1}} = \frac{\sin\theta_{tP}}{V_{P2}} = \frac{\sin\theta_{tS}}{V_{S2}} \tag{2-25}$$

where V_P and V_S are the P-wave and S-wave velocities, respectively, with the subscripts *1* and *2* denoting media 1 and 2, respectively; the direction of wave is given by θ, where subscript labels *i* indicate incident, *r* reflected, *t* transmitted, *P* P-waves and *S* S-waves, as shown in Figure 2-9.

Mode conversion can also be produced when a shear wave enters an interface; thus, a converted compression wave can be reflected and/or transmitted according to Snell's law. As this phenomenon enables different wave modes to propagate at different velocities and in different directions, it can generate inexact results in signal analysis. The imprecision caused by mode conversion can be avoided by increasing the incident angle (Blitz and Simpson, 1996).

2.3.4 Superposition of waves

This phenomenon, also known as interference, occurs when two or more waves travelling along the same path overlap. The total superimposed particle displacement at any point corresponds to the sum of the amplitude of each individual wave. The sum reaches its maximum when there is no phase difference (known as constructive interference); and is minimum when the phase difference corresponds to π (destructive interference). Two sine waves with the same frequency were generated to illustrate the superposition phenomenon, as shown in Figure 2-10.

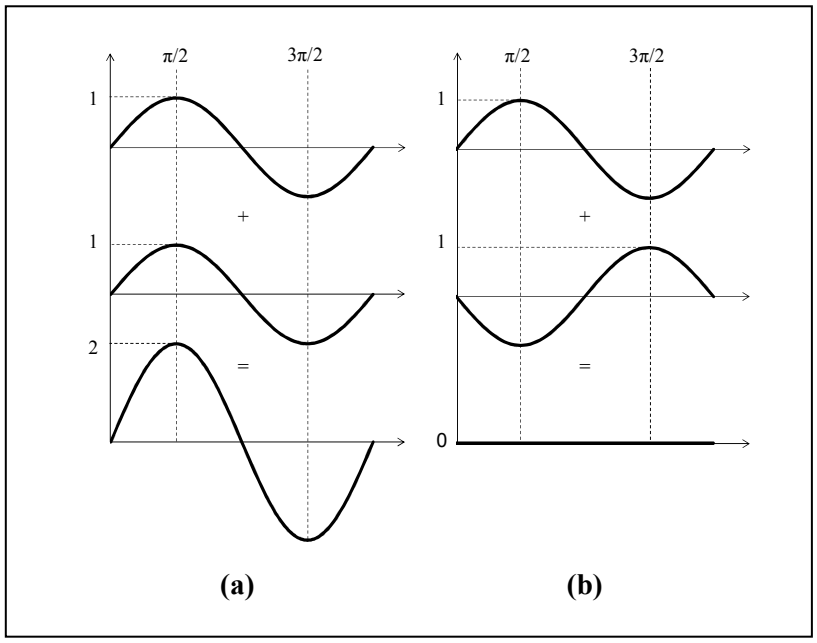

Figure 2-10. Superposition of two sine waves: **(a)** in phase and **(b)** out of phase.

2.4 Wave Attenuation

Attenuation is the decay rate of energy as the wave propagates through a medium. This energy loss is closely related to the material properties of the medium; hence, attenuation can be evaluated for material characterization. Attenuation is primarily caused by three phenomena: (a) energy is deviated from the original wave beam by reflection, transmission and/or mode conversion (scattering); (b) part of the wave energy is converted into heat by absorption; and (c) energy is lost as the wavefront spreads out and the wave propagates away from the source. The combined energy lost by scattering and absorption is known as material attenuation, and the loss by wavefront spread is often referred to as geometric attenuation.

2.4.1 Material Attenuation

Material attenuation is comprised of scattering and absorption. Scattering is the reflection of waves in directions other than its original direction of propagation. Scattering depends on the

acoustic impedance change at the interfaces, and on the grain sizes and orientation in heterogenous media. Since the grain sizes are comparable to the wavelengths, the wave is randomly reflected and refracted at each grain boundary, resulting in a loss of energy.

Absorption results from particle vibrations; the relative motion of these particles causes friction and absorbs part of the energy, converting it directly into heat. In general, low frequencies generate slower particle oscillations compared to high frequencies; therefore, they cause less energy loss and are able to penetrate deeper depths.

Material attenuation causes an exponential decrease of wave amplitude, given as a function of distance (Nasseri-Moghaddam, 2006):

$$\left(\frac{A_2}{A_1}\right) = e^{-\alpha\,(R_2 - R_1)} \tag{2-26}$$

where A_1 and A_2 are the wave amplitudes at distances R_1 and R_2 from the source, respectively, and α corresponds to the attenuation coefficient, in *nepers/length*.

The attenuation coefficient is a measuret of fractional loss of energy per unit length, and depends on material properties and varies with frequency.

2.4.2 Geometric Attenuation

Geometric attenuation follows the principle of energy conservation, where there is no energy loss in the wavefront. As the wave propagates away from the source, the energy is spread out over a larger wavefront area, causing a decrease in amplitude.

In general, the geometric attenuation can be expressed as the ratio of two amplitudes (Nasseri-Moghaddam, 2006):

$$\frac{A_2}{A_1} = \left(\frac{R_2}{R_1}\right)^{-\beta} \tag{2-27}$$

where A_1 and A_2 are the wave amplitudes at distances x_1 and x_2 from the source, respectively, and β corresponds to the geometric attenuation coefficient which depends on the wavefront shape. Body waves propagate in spherical wavefronts, for which β is equal to 1; therefore,

the amplitude decreases in proportion to the distance from the source. Surface waves have a cylindrical wavefront with β equaling to 0.5; therefore, the amplitude decreases in proportion to the square root of the distance from the source.

Both geometric attenuation and material attenuation increase as the wave propagates away from the source. The combined effect can be described as:

$$\frac{A_2}{A_1} = \left(\frac{R_2}{R_1}\right)^{-\beta} e^{-\alpha (R_2 - R_1)} \tag{2-28}$$

Alternatively, attenuation can also be characterized by the damping ratio (ξ), which is calculated as the amplitude reduction per cycle of oscillation:

$$\xi = \frac{1}{\Delta\varphi} \ln \frac{A_i}{A_{i+n}} \tag{2-29}$$

where A_i and A_{i+n} are maximum amplitudes for the cycles of oscillation i and $i+n$, respectively; $\Delta\varphi$ is the phase change between the two cycles.

2.5 Chapter Summary

This chapter describes the different wave modes that propagate in a medium, including body waves (P and S-waves) and surface waves (Rayleigh, Love and Lamb waves). Wave equations have been provided to determine wave velocities for P-waves, S-waves and R-waves. Then, wave velocities have been characterized by material properties. Physical phenomena associated to wave propagation, such as wave reflection, transmission, mode conversion and superposition are discussed. Finally, the mechanics of material and geometrical attenuation are described.

CHAPTER 3. SIGNAL PROCESSING TECHNIQUES

3.1 Background

Signal processing techniques can be applied to the analysis of signals measured in nondestructive tests. Typically, when a signal is measured, it is viewed in the time domain which provides certain information about the tested material for a preliminary evaluation. However, other important information, such as wave energy and phase velocities, can be obtained only in the frequency domain (Achenbach, 1973).

Several signal processing techniques, used to perform the frequency analysis in this study, are described in the following sections.

3.2 Time Domain Analysis

Time domain analysis, a method of representing a waveform by plotting amplitude over time, shows the variation of the signal amplitude with time. The recorded amplitude can be any real values: voltage, displacement, velocity, acceleration, etc.

This method is often used to determine the first arrival of a signal, and allows wave velocities to be calculated. The time history of a recorded signal is shown in Figure 3-1.

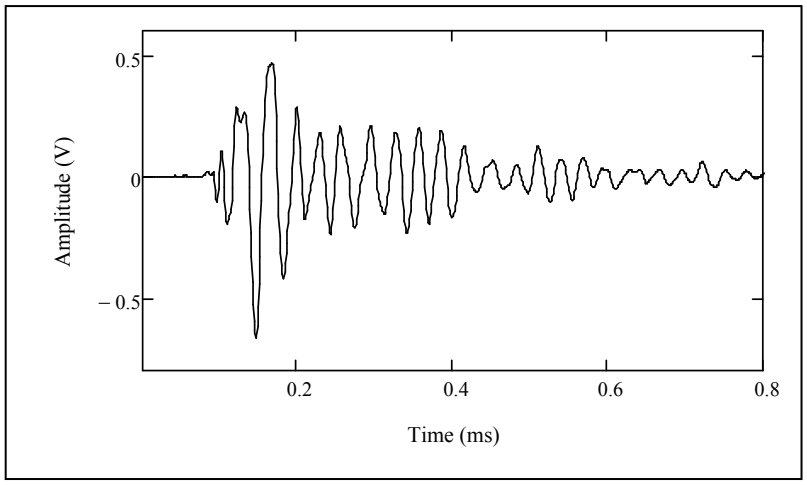

Figure 3-1. Time history of a recorded signal.

Other useful information, such as wave reflections and scatterings, can be drawn from a time history recording, and can allow the estimation of layer thicknesses and elastic profiles of the medium.

3.3 Frequency Domain Analysis

The frequency domain analysis is a method of representing a waveform by plotting amplitude over frequency; it describes the frequency content present in the signal. The frequency domain plot shows how much of the signal's energy is present as a function of frequency.

A given signal can be converted from the time domain to the frequency domain by performing the Fourier Transform. However, this technique does not describe the variation of the frequency content over time. Thus, other methods such as short time Fourier transform, wavelet transform, Hilbert transform and Hilbert-Huang transform are preferred over the more conventional Fourier transform .

3.3.1 Fourier Transform

This method decomposes a signal (represented as a complex waveform) into the sum of sinusoidal functions with different amplitudes, phases and frequencies. As a result, the signal is presented as the superposition of a series of sine and cosine functions.

Fourier transforms can be performed in a discrete or continuous form; the former is generally referred to as Fourier series.

Fourier series

Given a periodic function, $x(t)$, of period 2π and t are real numbers, where $x(t+2\pi) = x(t)$, it can be represented by a Fourier series as

$$x(t) = a_0 + \sum_{n=1}^{\infty} [a_n \cos(\omega_n t) + b_n \sin(\omega_n t)] \quad (3\text{-}1)$$

where, $\omega_n = n \frac{2\pi}{T}$ and n is an integer counter.

The Fourier coefficients of the function $x(t)$ are defined as

$$a_0 = \frac{1}{T} \int_0^T x(t) dt \quad (3\text{-}2)$$

$$a_n = \frac{2}{T} \int_0^T x(t) \cos(\omega_n t)\, dt \quad (3\text{-}3)$$

$$b_n = \frac{2}{T} \int_0^T x(t) \sin(\omega_n t)\, dt \quad (3\text{-}4)$$

where a_0 represents the average value of $x(t)$, and a_n and b_n represent the projection of $x(t)$ on sine and cosine functions of argument $\varphi_n = \omega_n t$, respectively.

The complex exponential form of the Fourier series is expressed as

$$x(t) = \sum_{n=-\infty}^{\infty} c_n e^{i\omega_n t} \quad (3\text{-}5)$$

where i denotes the complex component, and the coefficient, c_n , is expressed as

$$c_n = \frac{a_n - i b_n}{2} \quad (3\text{-}6)$$

or

$$c_n = \frac{1}{T} \int_0^T x(t) e^{-i\omega_n t}\, dt \quad (3\text{-}7)$$

Fourier series are valid only with periodic functions; for non periodic functions, the discrete variables become continuous and the summation is replaced by an integral. The Fourier transform is used to analyze non periodic functions.

Fourier transform

Fourier transforms are the continuous form of the Fourier series; this method decomposes a non periodic function into sine and cosine functions with different amplitudes and frequencies. The Fourier transform of function *x(t)* is defined by replacing Equations (3-5) and (3-7), as follows

$$x(t) = \frac{1}{2\pi}\int_{-\infty}^{\infty} X(\omega)\ e^{i\omega t}\, d\omega \tag{3-8}$$

$$X(\omega) = \int_{-\infty}^{\infty} x(t)\ e^{-i\omega t}\, dt \tag{3-9}$$

The expression (3-8) is known as the inverse Fourier transform.

Equations (3-8) and (3-9), known as the Fourier transform pairs, are continuous. The information recorded with digital signal processing is given in discrete form; therefore, the discrete Fourier transform are defined as follows

$$x(n\,\Delta t) = \frac{\Delta\omega}{2\pi}\sum_{k=0}^{N-1} X(k\,\Delta\omega)\ e^{i\frac{2\pi\,k\,n}{N}} \tag{3-10}$$

$$X(k\,\Delta\omega) = \Delta t\sum_{n=0}^{N-1} x(n\,\Delta t)\ e^{-i\frac{2\pi\,k\,n}{N}} \tag{3-11}$$

where $n = 0, 1 \ldots N\text{-}1$ and $k = 0, 1 \ldots N\text{-}1$ are integer counters, N is the total number of sampled points, $\Delta\omega$ is the angular frequency resolution and Δt is the time sampling interval. The frequency resolution is expressed as a function of the sampling time:

$$\Delta\omega = \frac{2\pi}{N\,\Delta t} \tag{3-12}$$

Fourier transforms provide information about the magnitude and phase of the signal. Figure 3-2 shows a typical time signal with the corresponding Fourier magnitude and phase spectra.

The primary drawback of Fourier transforms is that they have only frequency resolution and no time resolution. This means that although all the frequencies present in a signal can be determined, the exact instant they are present is still unknown.

Even though this technique is very practical for signal processing, it does not describe the variation of the frequency content over time. Thus, other methods are considered.

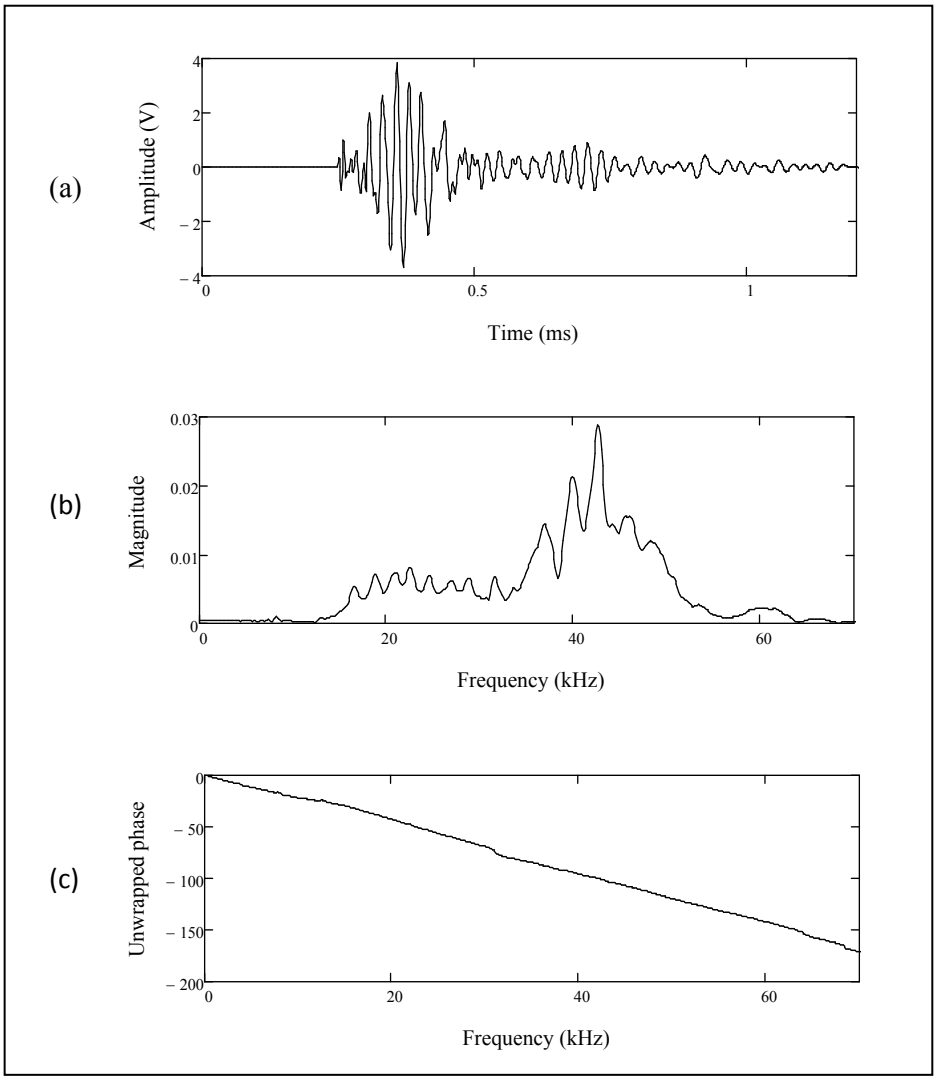

Figure 3-2. (a) Typical time signal, (b) corresponding Fourier magnitude spectrum and (c) corresponding wrapped phase spectrum.

3.3.2 Short Time Fourier Transform

The short time Fourier transform (STFT) allows the evaluation of the time dependent behavior of the different frequencies in a signal, overcoming the main drawback of Fourier transform. The signal to be transformed, $x(t)$, is multiplied by a window function, $w(t)$. Then, the Fourier transform is applied to the windowed signal. As the window is shifted along the time signal, the Fourier spectra are computed, and the signal is mapped into a 2D function of time and frequency. The STFT is defined as

$$\mathrm{X}(\omega, \mathrm{b}) = \int_{-\infty}^{\infty} x(t)\, w(t-b)\, e^{-i\omega t}\, dt \tag{3-13}$$

where b is the shift time used to localize the window function at different locations along the time axis. The STFT, commonly known as windowed Fourier transform, employs a window function that can be Hanning, Hamming, Kaiser or Gaussian. The width of the applied window and the resolutions in time and frequency can be expressed by the following relationship:

$$\Delta \mathrm{f} = \frac{1}{N_w\, \Delta t} \tag{3-14}$$

where N_w is the size of the window.

Equation (3-14) indicates that both the frequency and time resolutions are controlled by the window size; therefore, there is a trade-off in selecting the time and frequency resolution. A narrow window has good resolution in time, but provides poor frequency resolution. Conversely, a wide window has poor time resolution, but provides good resolution in frequency. As a result, low frequencies are not captured with narrow windows and high frequencies are not detected with wide windows.

3.3.3 Wavelet Transform

The wavelet transform (WT) can be considered as a solution to overcome the limitation of the Fourier transform; wavelets are localized in both time and frequency whereas the Fourier

transform is localized only in frequency. Wavelets are mathematical functions that cut up data into different frequency components, and then study each component with a resolution matched to its scale. A window is shifted along the signal and, for every position, a spectrum is calculated. The fundamental idea behind wavelets is to complete the analysis according to scale. The end results consist of a collection of time-frequency representations of the signal, all with different resolutions.

Furthermore, Fourier analysis uses functions of sines and cosines to represent a signal; however, these functions are non-local and extend to infinity. Consequently, they do a very poor job in approximating sharp spikes or discontinuities in the signal. With wavelet analysis, the functions used to approximate a signal are contained in finite domains. Therefore, they are well-suited for analyzing the discontinuities present in a signal, overcoming an additional drawback of Fourier analysis.

A continuous wavelet transform is used to divide a continuous-time function into wavelets. Unlike Fourier transform, the continuous wavelet transform constructs a time-frequency representation of a signal that offers good time and frequency localization. It is given by the following expression:

$$WT(a,b) = \frac{1}{\sqrt{|a|}} \int_{-\infty}^{\infty} x(t) \cdot \psi^* \left(\frac{t-b}{a}\right) dt \tag{3-15}$$

where *x(t)* is the time signal. *ψ(t)* is a continuous function (known as the mother wavelet) in both the time domain and the frequency domain, and the star denotes the complex conjugate. The translation parameter, *b,* is used to shift the window *ψ(t)* in time, and it relates to the location of the wavelet function as it is shifted through the signal. The scale parameter, *a,* is used to scale the function, and it corresponds to frequency information. Large scales (low frequencies) dilate the signal and provide detailed information hidden in the signal, while small scales (high frequencies) compress the signal and provide global information about the signal.

All the wavelet functions used in the transformation are derived from the mother wavelet through translation (shifting) and scaling (dilation or compression). The WT merely performs the convolution operation of the signal and the basis function (mother wavelet).

The discrete form of the WT can be defined as follows

$$W_{k,m} = \frac{1}{\sqrt{k}} \sum_{n=0}^{N-1} x_n \cdot \psi^* \left(\frac{n-m}{k}\right) \Delta t \tag{3-16}$$

where, N is the number of points used to discretize the signal, x_n denotes the discrete-time signal for a time period given by $N \cdot \Delta t$, Δt is the time interval or resolution, the integer counter k gives the frequency scale, and the integer counter m defines the time shift. Figure 3-3 shows an example of a wavelet transform using a Morlet function.

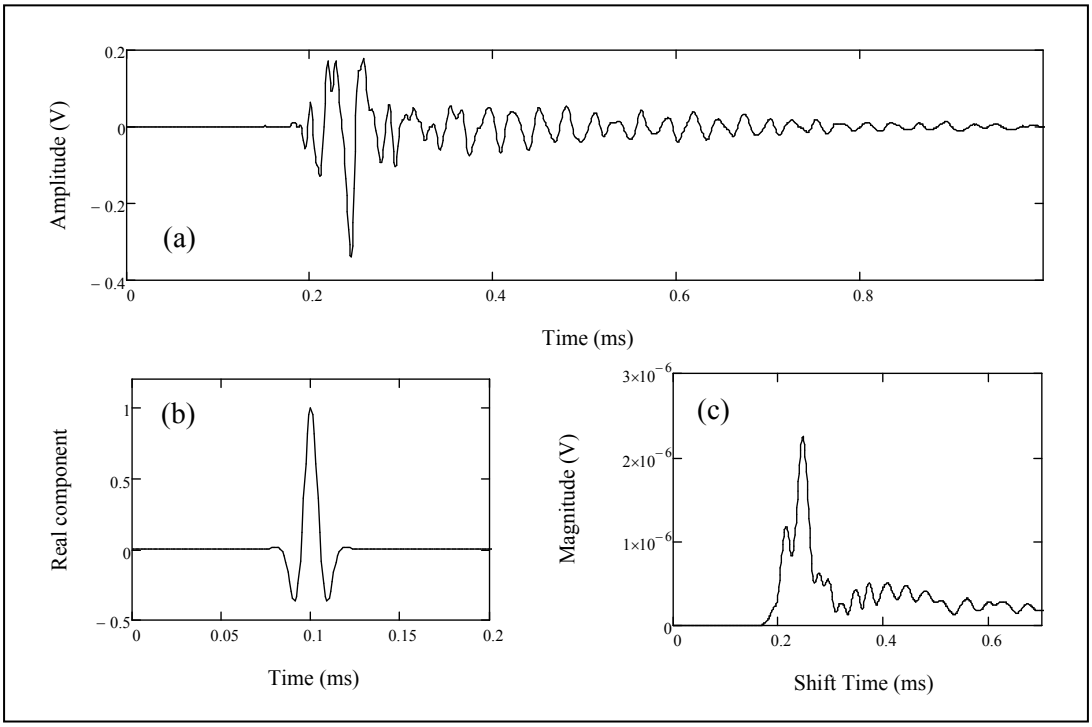

Figure 3-3. (a) Typical time signal, (b) Morlet function as a mother wavelet and (c) the corresponding wavelet transform magnitude, for f_0 = 45 kHz and $\tau = 2.0 \times 10^{-5}$.

3.3.4 Hilbert and Hilbert-Huang Transform

The Hilbert–Huang transform (HHT) provides another method for transforming time domain data to the frequency domain. The HHT has the advantage of providing the time dependence of both the amplitude and frequency that are extracted from the time series data. A

distinguishing feature of this transform is the nature of its basis. Unlike the Fourier or wavelet transforms, the basis states are extracted from the data itself and are unique for each data set. The basis states can display both amplitude and frequency variations during the course of the sampling period and allow for a generalization of a Fourier expansion of the time series. The basis states are extracted from the data by a sifting process called empirical mode decomposition. Each basis state is referred to as an intrinsic mode function and extracts a different frequency range from the time series.

Once the signal is deconstructed, Hilbert spectral analysis is readily performed on each intrinsic mode function. The combination of empirical mode decomposition and Hilbert spectral analysis via the Hilbert transform makes up the Hilbert–Huang transform.

The local information is extracted from a real signal by employing an associated analytic signal, x_a, comprised of the original signal x and its Hilbert transform $\hat{x}$: $x_a = x + i\,\hat{x}$.

By definition, the Hilbert transform of a function, *x(t)*, is denoted as follows:

$$\hat{x}(t) = P\,\frac{1}{\pi}\int_{-\infty}^{\infty}\frac{x(\tau)}{t-\tau}\,d\tau \tag{3-17}$$

where P denotes the Cauchy principal value. Essentially, the Hilbert transform is a convolution of x with the function $1/t$. The effect of this convolution is to emphasize the local properties of *x(t)*, such as the time structure of the signal's amplitude and frequency. To extract this local information from the analytic signal, the polar representation of the complex valued signal is used, as follows

$$x_a = A(t)e^{i\theta(t)} \tag{3-18}$$

which defines the amplitude envelope *A(t)* and the instantaneous phase *θ(t)*. Time dependent changes in frequency can be measured by calculating the instantaneous frequency, which is the derivative of the instantaneous phase. These steps constitute the Hilbert spectral analysis. Figure 3-4 shows a typical time signal with its corresponding Fourier spectrum (in frequency) and magnitude of its analytic signal (in time). Figure 3-4(b) verifies that the spectrum obtained from the original time signal is identical to the spectrum obtained from the

analytic signal. The magnitude of the analytic signal is the complex envelope of the original signal and its Hilbert transform, as shown in Figure 3-4(c).

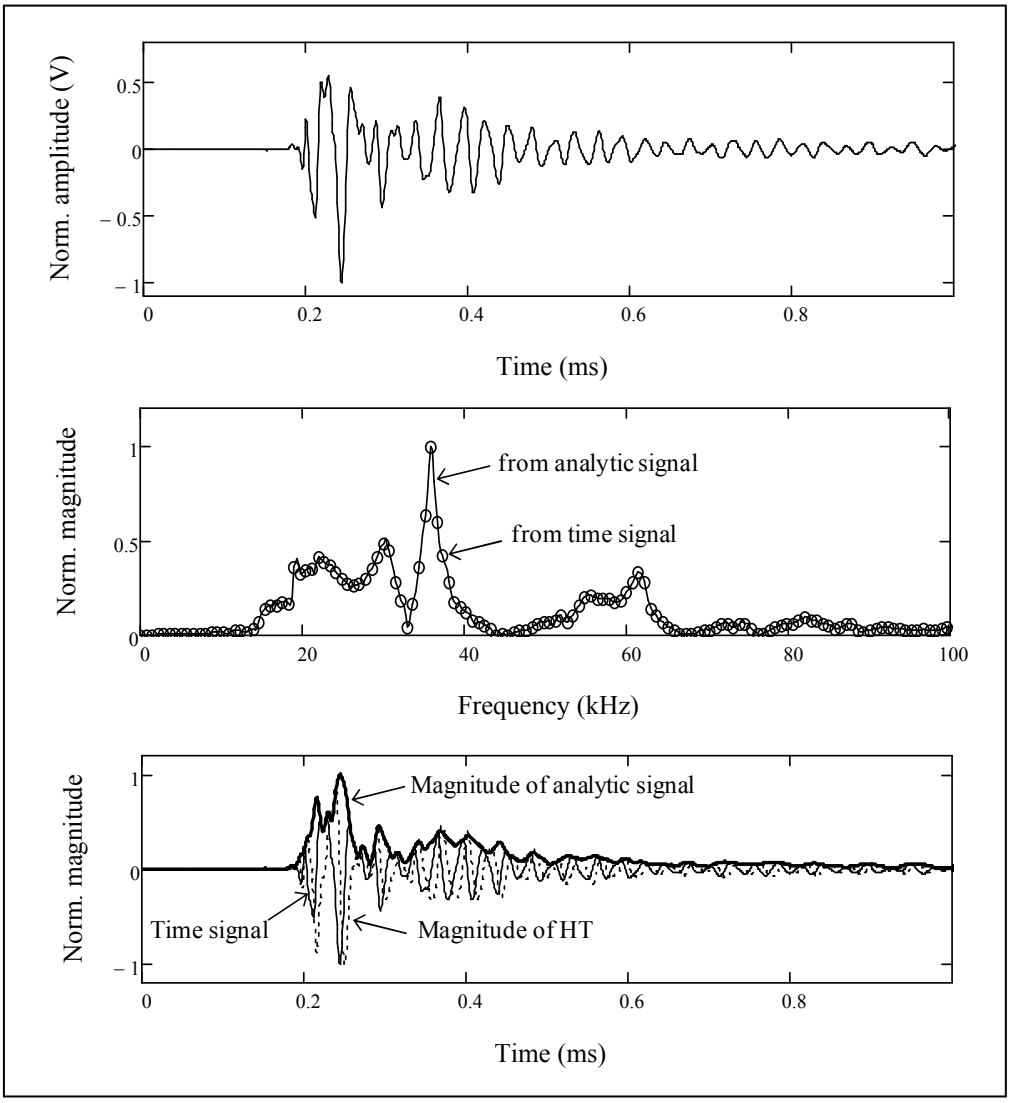

Figure 3-4. (a) Typical time signal, (b) frequency spectra and (c) magnitude of analytic signal.

The HHT is carried out in two stages: (1) the empirical mode decomposition (EMD) process, which deconstructs the signal into a set of intrinsic mode functions (IMF) via a sifting process, and (2) the extraction of frequency vs. time information from each of the IMFs in combination with its Hilbert transform (HT).

In the decomposition process, the first IMF contains the highest frequencies associated with the original signal, and each subsequent IMF contains lower frequency components. Each IMF extracted from the signal by a sifting process meets the following criteria: the number of extrema and the number of zero crossings differ by one at the most, and the mean value of the envelopes defined by the local maxima and local minima is zero.

In the second stage of the HHT process, amplitudes and frequencies are extracted from the IMFs. The instantaneous amplitude and angular frequency associated with each IMF depend on the amplitude and phase of a complex number defined by the IMF and its HT. The real part of the complex number is the IMF, and the imaginary part of the number is the IMF's HT. The instantaneous amplitude is essentially the amplitude of this complex value. The instantaneous angular frequency associated with that IMF is basically the derivative of the unwrapped phase.

The EMD process can be carried out in six steps:

1. Determine the location of all maxima, $x_{max}(t)$, and minima, $x_{min}(t)$, of signal $x(t)$.
2. Fit a cubic spline though the $x_{max}(t)$ and another though the $x_{min}(t)$.
3. Calculate the mean of the spline curves at each point $m(t) = [x_{max}(t) + x_{min}(t)]/2$.
4. Substract the trend, $m(t)$. Let $d(t) = x(t) - m(t)$.
5. If $d(t)$ meets the criteria defining a IMF, let $c_i(t) = d(t)$ and advance i by one. Extract the residual $r(t) = x(t) - d(t)$. If $d(t)$ does not meet the criteria, further sifting is required; repeat steps 1 through 5 substituting $d(t)$ for $x(t)$.
6. Repeat steps 1 through 5 until the residual becomes monotonic and no more IMFs can be extracted.

Although the process is computationally much more demanding than taking the Fourier or wavelet transforms, the HHT not only provides instantaneous frequency and amplitude descriptions, but also results in representations that are more meaningful physically.

3.4 Chapter Summary

This chapter reviews the different signal processing techniques used to analyze signals in both time and frequency domains, such as Fourier transform, short time Fourier transform,

wavelet transform and Hilbert-Huang transform. These techniques are described, and the main advantages and drawbacks of each are discussed.

Fourier transforms convert a signal from the time domain to the frequency domain; however, this technique does not describe the variation of the frequency content over time. To overcome this limitation, the short time Fourier transform can be used to indicate the signal's frequency distribution over time. However, there is a trade-off in selecting the time and frequency resolutions. Unlike Fourier transform, the wavelet transform constructs a time-frequency representation of a signal that offers good time and frequency localization; nevertheless, WT is controlled by a wave function (mother wavelet) with a specific center frequency. The Hilbert transform has the advantage of providing the time dependence of both the amplitude and frequency that are extracted from the data itself and are unique for each data set. Selecting a proper signal processing technique is critical in the field of material characterization using wave-based testing methods.

CHAPTER 4. NONDESTRUCTIVE TESTING METHODS

4.1 Introduction

This chapter presents the most popular technologies in the nondestructive testing area and their application in asphalt slab evaluation and steel thickness estimation. In general, these techniques are preferred over the more traditional destructive methods since they are less expensive. NDT methods are non-invasive, they do not induce damage on the material being tested, and do not require access to both surfaces. Wave-based methods are commonly used to evaluate the internal condition and the elastic properties of materials, because wave propagation is affected by the elastic properties and density of the medium.

The most novel ultrasonic wave testing techniques involve the spectral analysis of surface waves (SASW), multi-channel analysis of surface waves (MASW), and the computation of different transmission coefficients based on Fourier transforms, wavelet transforms and Hilbert transforms.

4.2 Nondestructive Testing Methods for Asphalt Pavements

Over the last few decades, a variety of NDT methods have been developed and applied in engineering with different success rates (Nazarian et al., 1983; Song et al., 2003). Several nondestructive technologies are used particularly for the condition assessment of asphalt slabs, which are based on deflection tests, electromagnetic methods, and ultrasonic testing methods.

4.2.1 Deflection Testing

Nondestructive deflection equipment operates by applying a load to the pavement surface and measuring the resulting surface deflections using velocity transducers or geophones. The type of load applied may be static, steady-state harmonic or transient impulse. Typical testing equipments and their primary drawbacks are discussed in the following sections.

4.2.1.1. Static Devices

Static deflection devices apply either a static or slow-moving load to the pavement surface and measure the resulting deflections. The most commonly used static deflection device is the Benkelman Beam, as shown in Figure 4-1. Developed for the Western Association of State Highway Organizations (WASHO) Road Test, it has been used extensively by highway agencies for pavement research, evaluation, and overlay design around the world.

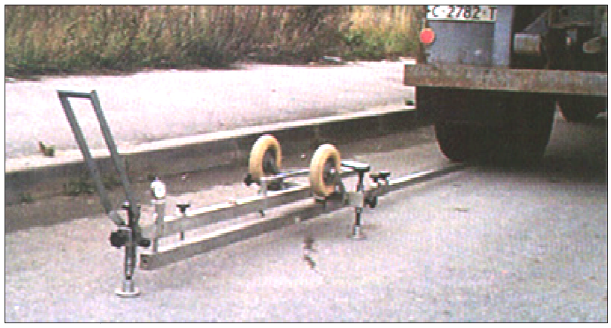

Figure 4-1. Benkelman Beam (www.crbl-bg.net).

The Benkelman Beam consists of a simple lever arm attached to a lightweight aluminum or wood frame. Measurements are made by placing the tip of the beam probe between the dual tires of a loaded (usually an 80 kN axle load) truck at the point where the deflection is to be determined. As the loaded vehicle moves away from the test point, rebound or upward movement of the pavement is measured by the dial gauge. Standard Benkelman Beam tests are described in AASHTO T 256 and ASTM D 4695.

This equipment is simple and inexpensive. However, it is slow, labor intensive, and on stiff pavements, the support legs may be within the deflected area, resulting in inaccurate measurements.

4.2.1.2. Vibratory Devices

The steady-state or dynamic vibratory device uses a relatively large static preload and a sinusoidal vibration to the pavement with a dynamic force generator. These devices consist of a dynamic force generator (that produces the oscillating load), a motion measuring

instrument (to measure the oscillating load), a calibration unit and several deflection measuring devices (transducers, accelerometers, seismometers, etc.). The most commonly used vibratory device is the Dynaflect, as shown in Figure 4-2.

Figure 4-2. Dynaflect (pavementinteractive.org)

The Dynaflect is an electromechanical system. The cyclic force generator utilizes a pair of eccentric masses rotating in opposite directions. A static weight of 2,000 lb is used and produces a 1,000 lb peak-to-peak dynamic force at a fixed frequency of 8 Hz. The load is applied through two rigid steel wheels, and the resulting deflections are recorded by five velocity transducers (geophones). Standard steady state deflection tests are described in AASHTO T 256.

This device is limited by a small maximum peak-to-peak force, which is more suitable on thin pavements, and cannot be used for testing heavy highway or airfield pavements.

4.2.1.3. Impulse Devices

Currently, the impulse deflection device is the most popular and widely used pavement deflection measurement technology. This device is typically referred to as a falling weight deflectometer (FWD). The impulse load is generated by a falling mass; the amount of impact load, duration and loading area is adjusted in such a way that it closely corresponds to the actual loading by a standard truck on in-service roads (Sebaaly et al., 1991). Variations in the applied peak force levels are achieved by varying the magnitude of the dropping mass and the height of the drop.

Impulse load devices can apply loads from 1,360 to over 22,700 kg based on the device used. Deflections are most commonly measured with velocity transducers (geophones) mounted on a bar and automatically lowered to the pavement surface with the loading plate. The most popular equipment is the Dynatest FWD, as illustrated in Figure 4-3. The standard impact load response test method is specified in ASTM D 4694.

Figure 4-3. Falling Weight Deflectometer.

Some of the advantages of FWD include high productivity, realistic pavement loading levels, low static preload, rapid data acquisition, and the ability to measure and record a deflection basin. However, not only can the inverse analysis (backcalculation) be complex, the initial costs for the impulse equipment are higher than the static and vibratory devices.

4.2.1.4. Multi-depth Deflectometer (MDD)

The multi-depth deflectometer (MDD) is used to measure depth deflection profiles of pavement; effective elastic moduli of multilayered pavement structures can be backcalculated from these measurements. The MDD consists of a series of up to six linear voltage differential transducers (LVDTs) installed vertically into the pavement at preselected depths in a relatively small-diameter hole, as shown in Figure 4-4. Resilient depth deflections are measured with the MDD used in association with a moving load.

Figure 4-4. Multi-depth deflectometer.

A major limitation of this method is that it requires a trench immediately adjacent to the pavement section of interest to ensure the effective placement of modules.

4.2.2 Electromagnetic wave propagation

In electromagnetic wave methods, the reflections of the transmitted waves, caused by any changes in the material and/or layer properties, are recorded and analyzed to determine the required information. In the following sections, two of the most common techniques for application on asphalt pavement, Infrared thermography (IRT) and ground penetrating radar (GPR), are discussed.

4.2.2.1. Infrared thermography (IRT)

Infrared thermography (IRT) employs an infrared scanner to capture the thermal image from the top of the pavement, capturing temperature differentials (as shown in Figure 4-5). Typically, scanners can detect differences as small as 0.1°C. The subsurface defects affect the heat flow within the pavement, and this in turn affects the temperature distribution of the concerned area. In most cases, this method can capture the location and extent of sub-surface distresses in the form of cracking, segregation, ageing, and construction non-homogeneity (Gordon et al., 1998; Mahoney et al., 2000).

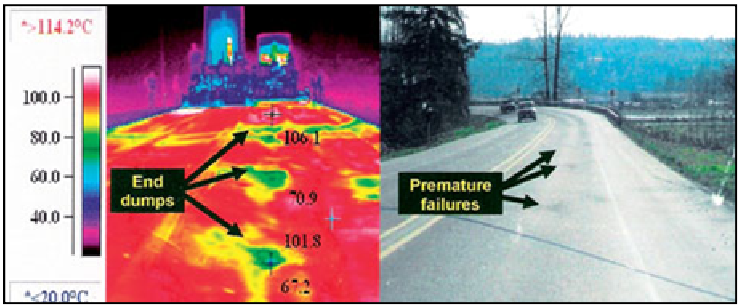

Figure 4-5. Infrared Thermography (instrumentation.co.za).

The delaminated or debonded sections are thinner than the surrounding sound area. With the same input of solar energy, these sections heat and cool faster than the adjacent pavement. The IRT is able to detect this temperature difference, and the flawed sections can be identified.

The various field conditions represent the major drawback of this method. Certain environmental, such as time of testing, cloud cover, wind flow, pavement surface texture, solar radiation, and sub-surface conditions (moisture, frost penetration), conditions can affect the test results.

4.2.2.2. Ground Penetrating Radar (GPR)

Ground penetrating radar (GPR) consists of a radar device that transmits an electromagnetic pulse. Subsurface irregularity such as voids, depth of bedrock, ground water level, pavement moisture content, and frost penetration depth can be estimated by this method (Gordon et al., 1998; Al-Qadi, 1992; Maser, 1999; Maser et al., 2006). GPR devices also provide a continuous data record for the full length of the test section, thereby giving direct information of the test section at each point. A typical GPR device is shown in Figure 4-6.

Figure 4-6. GPR device (www.infrasense.com).

The GPR technique consists, in principal, of a high frequency electromagnetic wave, typically from 1 GHz to 2.5 GHz, emitted from an antenna to the structure under evaluation. The reflected energy caused by changes in the electromagnetic properties of the material is detected by a receiver antenna and recorded for subsequent analysis. The test set-up is mounted on a vehicle which operates on the pavement at a specified speed. The accuracy of this method depends on the resolution of the time scan and the dielectric constant of the tested material. As the equipment moves on the pavement surface, a sequence of wavefronts is generated, and from this, the layer-boundaries can be directly visualized from the graphic output of the collected wavefront data.

GPR is mainly used in the asphalt pavement industry for determining layer thicknesses and detecting cracks and layer delamination. Experimental studies (Surette et al., 2010) showed that the layer thicknesses computed from GPR agreed well with the results from conventional destructive techniques. Other studies demonstrated that the location of surface cracks can be identified with the GPR; however, the crack severity and geometry (depth and width) were not recognized (Ahmad et al., 2011).

GPR is cost effective and fast to perform; however, interpretation of GPR data requires experience and the operator/analyst requires training to obtain reliable results for the evaluation of joint deterioration and pavement structure changes. Moreover, moisture can have a significant impact on the ability of the radar system to penetrate the pavement material.

4.2.3 Ultrasonic Testing (UT)

A stress/elastic wave is a type of mechanical wave that propagates in elastic/viscoelastic materials due to a stress based disturbance. There are two types of stress waves: body waves and surface waves.

Stress waves may be generated through different devices like dropweight, strike hammer, or transducer. The sensing element is also a transducer receiver (e.g. accelerometer). The data is recorded through a data acquisition system and subsequently analyzed to obtain the required estimates.

Different types of ultrasonic testing (UT) methods exist based on the analysis technique and type of waves used. The most popular UT methods include the impact echo (IE), ultrasonic pulse velocity (UPV), spectral analysis of surface waves (SASW) and multi-channel analysis of surface waves (MASW). Methodologies, such as the Fourier transmission coefficient (FTC), the wavelet transmission coefficient (WTC) and the new instantaneous transmission coefficient (ITC), use surface waves and wave attenuation effects for the detection of surface defects.

4.2.3.1. Impact Echo (IE) / Pulse Echo

An impact is generated at the test surface to generate stress waves, and their reflections from any disturbance in layer medium, such as interface, void, and crack, are recorded to extract information on its location. This method generates a short-duration mechanical impact on the free surface, and introduces a stress pulse into the medium propagating radially outward from the source as compression and shear waves. These waves reflect back and forth between the top surface and internal defects or the bottom of the test member, as shown in Figure 4-7. A transducer located near the impact point detects the arrivals of the reflected waves.

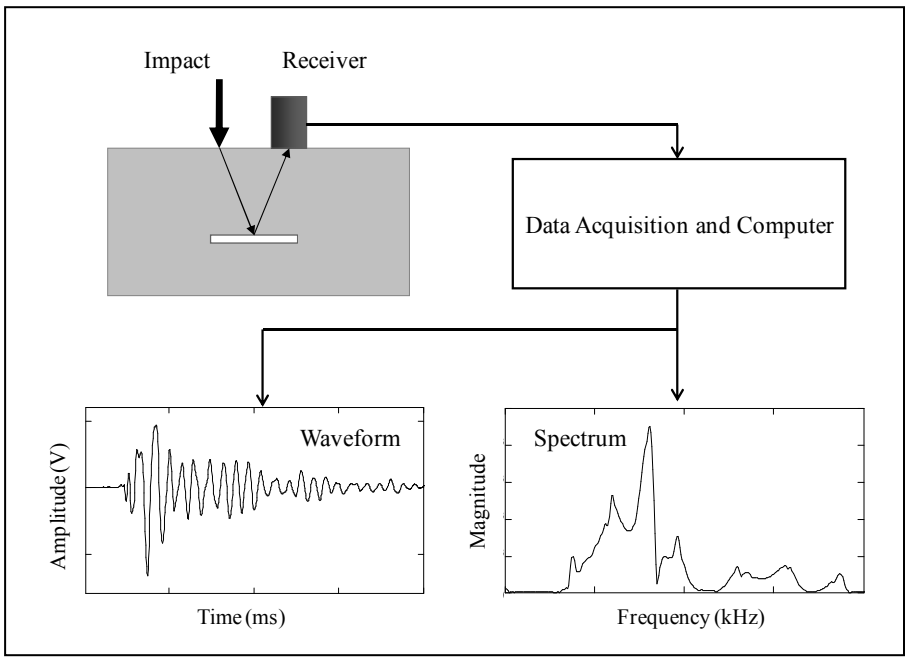

Figure 4-7. Impact echo test setup (Sansalone, 1997).

From the amplitude-time data of reflected body waves, the frequency peaks are identified using frequency domain analysis. Each of these peaks indicates the resonant echo frequencies. The inverse of these frequencies gives the time required for the waves to reflect back from the pavement interface or the crack surface.

The fundamental relationship to interpret the frequency spectrum in the IE method is given by

$$h = \frac{V_p}{2\,f} \tag{4-1}$$

where, h is the distance to a reflecting interface, V_P is the P-wave velocity and f is the frequency of P-wave reflections. Using Equation (4-1), if the P-wave velocity of the medium is known, then the depth h of a defect or boundary can be computed.

The ultrasonic pulse echo method is used for estimating the thickness and depth of surface cracks for asphalt pavements (Underwood and Kim, 2002; Celaya and Nazarian, 2007).

This method has the advantage of requiring access to only one surface; however, the use of low-frequency waves makes it difficult to detect small flaws.

4.2.3.2. Ultrasonic Pulse Velocity (UPV)

In this method, the P-wave velocity in the material medium is determined to calculate its elastic modulus or Poisson's ratio. As elastic moduli indicate compressive strength of the material, wave velocities can be theoretically related to the strength of the material.

Measurements are performed by allowing body waves to interact with a volume of material between two ultrasonic transducers placed at each end of the specimen. One transducer is used as a transmitter and converts a pulse of electric energy into a pulse of acoustic wave energy. When the energy propagates through the specimen and reaches the receiver, it is converted back into an electric pulse, which is displayed in an oscilloscope. A typical UPV test setup is shown in Figure 4-8.

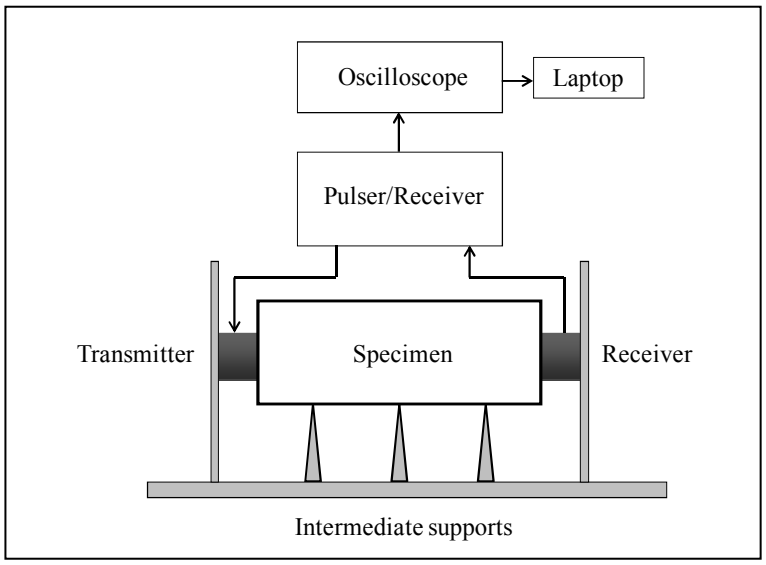

Figure 4-8. Ultrasonic pulse velocity test setup.

P-wave and S-wave velocities in ultrasonic testing are determined by dividing the length of the specimen by the travel time:

$$V_P \, or \, V_S = \frac{\Delta L}{\Delta t} \tag{4-2}$$

where ΔL is the length and Δt is the travel time. Once the velocities are determined, the Young's modulus (E) and Poisson's ratio (v) can be computed using the equations presented in Section 2.2. Furthermore, if the specimen is restricted from lateral deformation, the axial stress-to-strain ratio defines the constrained modulus (M).

Laboratory studies suggest that the UPV method can estimate the dynamic modulus of asphalt with reasonable accuracy (Jiang et al., 2006). For field testing on in-service pavements, an indirect configuration of sensors needs to be used, since only the top surface is accessible. In studies, UPV has been used to monitor top–down cracking (Khazanovich et al., 2005), fatigue damage and crack healing in asphalt pavements (Abo-Qudais and Suleiman, 2005).

In general, this method requires a calibration stage that consists of measuring the arrival times of different-length specimens of the same material. Next, the arrival times are related to the specimen lengths by performing a linear regression. The time delay introduced by the test equipment and coupling conditions is represented by the intercept. Finally, the intercept is subtracted from the arrival time from the UPV measurements of each specimen.

4.2.3.3. Spectral Analysis of Surface Waves (SASW)

The spectral analysis of surface waves (SASW) method is commonly used for the in-situ determination of the shear modulus profile and the layer thickness in a layered medium (Nazarian et al., 1983), based on the dispersive nature of surface waves. Surface waves are dispersive in layered media where wave velocities vary with frequency or wave number.

Three steps are carried out for the SASW examination (Nazarian et al., 1983): (1) in situ data collection, (b) construction of experimental dispersion curve, and (c) inversion of the dispersion curve.

A typical SASW test setup is illustrated in Figure 4-9. Waves with varying frequencies are transmitted to the medium by a mechanical impact on the ground surface. The in-situ data collection takes place as the propagation of the waves is monitored by two receivers attached to the surface, while a waveform analyzer records the time signals.

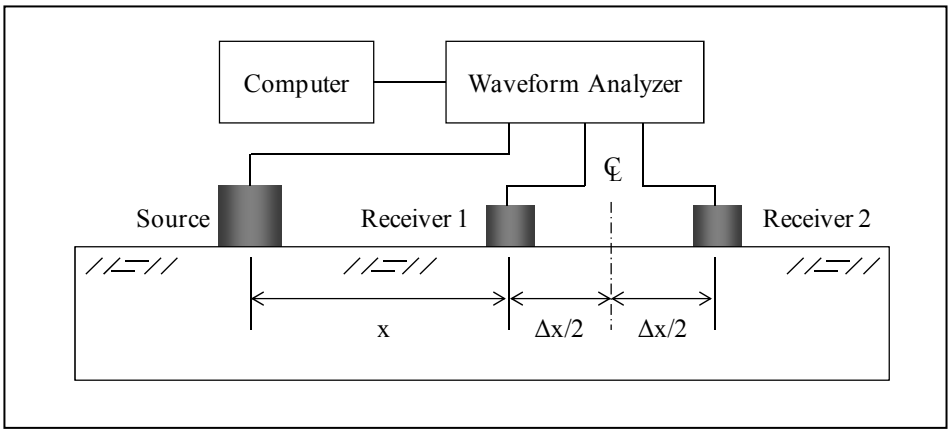

Figure 4-9. Typical SASW test setup.

Source and receiver spacings play an important role as the range of frequencies generated by a single source is limited. Small receiver spacings permit high frequencies and are used for shallow measurements; in contrast, large spacings sample lower frequencies and allow deeper measurements. In addition, surface waves become fully formed beyond a minimum distance from the source; this phenomenon is known as the near-field effect. On the contrary, the signal-to-noise ratio becomes lower as the distance from the source increases, relative to the wavelength (far-field effect). A commonly used criterion for receiver spacing selection is expressed as

$$\frac{\lambda_R}{3} < \Delta x < 2\lambda_R \tag{4-3}$$

where λ_R is the wavelength of R-wave and Δx is the receiver spacing (Heisey et al., 1982).

The phase information is used to generate the experimental dispersion curve. The phase difference between the two receivers is determined at each frequency by

$$\Delta\varphi = Phase(FT_2) - Phase(FT_1) \tag{4-4}$$

where $\Delta\varphi$ is the phase difference, FT_1 and FT_2 are the Fourier transforms of signals recorded by receivers *1* and *2*, respectively; $Phase(FT_1)$ and $Phase(FT_2)$ are the unwrapped phase of respective Fourier transforms.

Then, the phase velocity for each frequency (V_{ph}) can be determined by

$$\mathrm{V_{ph}}(\omega) = \omega \frac{\Delta x}{\Delta \varphi} \tag{4-5}$$

Finally, the inversion of the dispersion curve involves an iterative process in which a theoretical curve is constructed by assuming a shear wave velocity profile. The experimental and theoretical curves are then compared, and the assumed shear wave velocity is modified through an iterative process until the two curves match within a reasonable tolerance.

The surface impact generated by the source creates surface waves and body waves simultaneously. Thus, boundary reflections and body waves can lead to abrupt changes in the phase velocity, adversely affecting the experimental dispersion curve. This issue may be addressed by properly adjusting the source-receiver geometry; however, this compromises the measurable depth of the test.

The SASW is used for many applications in civil engineering, such as determining the pavement system profiles, assessing the condition of structural concrete, and measuring crack depths in concrete bridge decks. A recent study used SASW and IE methods simultaneously to provide accurate information about delaminations, internal cracks, crack depths, thickness profiles and material integrity of concrete decks (Tinkey et al., 2011). A prototype scanner (BDS) was developed for the identification of delaminations between asphalt pavement layers; the results suggested that the SASW results were found to best indicate delaminations when compared to impact echo methods.

4.2.3.4. Multichannel Analysis of Surface Waves (MASW)

In general, higher modes of Rayleigh waves have a significant contribution to the vibration modes of a pavement structure. The SASW method considers only the fundamental mode of

R-waves; therefore, the shear velocity profile is very difficult to determine from the inversion process (Park et al., 1999).

The multichannel analysis of surface waves (MASW) method is able to identify and separate the different modes of R-waves. The dispersion curve obtained with this technique comprises the fundamental mode and the higher modes, providing an improved wave velocity profile.

The MASW overcomes the trade-off between receiver spacing and the test depth of the SASW method, since higher modes are included in the analysis. Therefore, the MASW provides a faster data collection and better noise control.

A typical MASW test setup is shown in Figure 4-10. The propagation of surface waves in the medium is recorded by an array of equally spaced receivers.

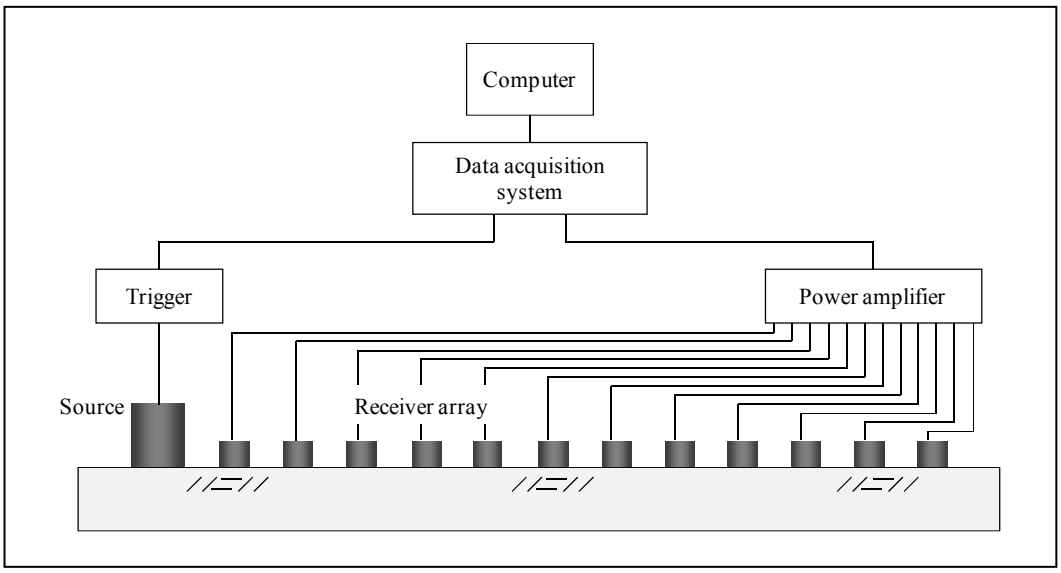

Figure 4-10. MASW test setup.

The MASW algorithm is analogue to SASW. Computer programs (Park et al., 1999; Russo, 2006) are commonly used to construct dispersion curves from the raw data collected by the receivers. First, the DC component and noise are removed from the time signals. Then, the frequency vs. wave number (FK) spectrum is computed for different propagation modes, as shown in Figure 4-11(a). Next, the maxima of the FK spectrum are selected to extract the

experimental dispersion curve, Figure 4-11(b). Finally, the shear velocity profile is determined from the inversion process.

The MASW method can also be used to determine wave attenuation, in both time and frequency domains. In the time domain, the difference of the peak to peak amplitude between the first receiver and subsequent receivers may suggest energy loss. In the frequency domain, the spectra area can be computed as an indicator of attenuation.

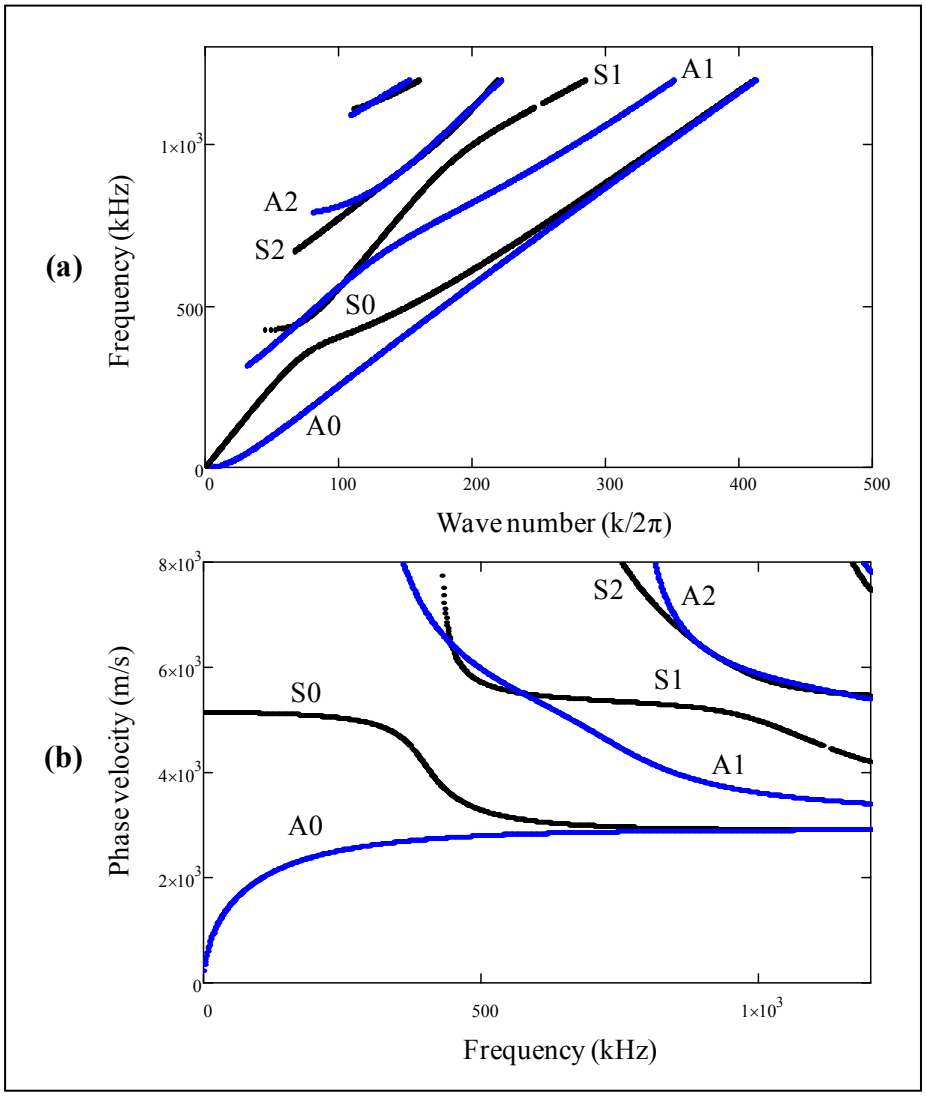

Figure 4-11. **(a)** FK plot and **(b)** the corresponding dispersion curves for a typical 6 mm thick steel plate, with V_P = 5418 m/s, V_S = 3159 m/s and V_R = 2902 m/s.

4.2.3.5. Fourier Transmission Coefficient (FTC)

The Fourier transmission coefficient (FTC) method is an improved surface wave technique for detecting surface defects. This method allows reducing the effects of the unknown characteristics of the transducers and their coupling with the medium (Song et al., 2003). The FTC uses a self-compensating approach that has two main advantages: the wave velocity of the material is not required in advance, and the technique is independent of the type of the coupling conditions. This method is used for the determination of the depth of surface-breaking cracks in concrete (Yang, 2009; Popovics et al., 2000).

The ultrasonic testing of pavement slabs (with construction joints) in the CPATT laboratory at the University of Waterloo confirmed that wave attenuation parameters measured in terms of the FTC are suitable for the condition assessment of longitudinal joints (Jiang, 2007; Yang, 2005).

The FTC coefficients measure the ratio of the wave energy that propagates across the joint with respect to the joint free area. For ideal and perfect joint sections, the FTC should be equal to one.

The FTC method requires two sources and two receivers placed along a line at both sides of a surface defect, as shown in Figure 4-12. The two sources are placed at locations A and E. First, the surface waves generated at location A are recorded simultaneously by the receiver at location B (as the signal f_{AB}) and by the receiver at location D (as f_{AD}). Next, the process is repeated by generating surface waves at location E and recording f_{ED} and f_{EB} at locations D and B, respectively.

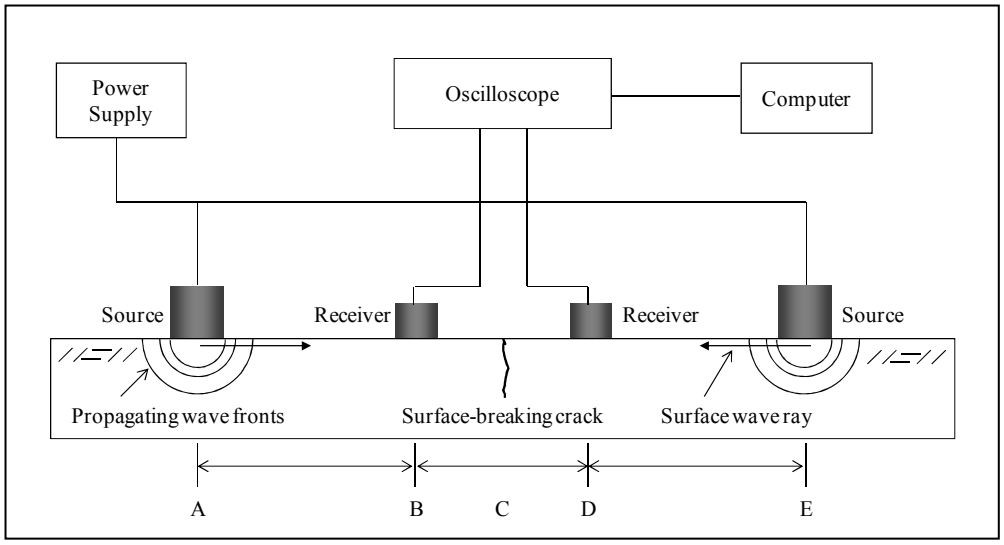

Figure 4-12. Test setup for the measurement of transmission coefficient (TC) (Song et al., 2003).

These received time signals can be expressed in frequency domain as follows:

$$\begin{aligned} F_{AB} &= S_A\, C_A\, M_{AB}\, C_B\, R_B \\ F_{AD} &= S_A\, C_A\, M_{AB}\, M_{BD}\, C_D\, R_D \\ F_{ED} &= S_E\, C_E\, M_{ED}\, C_D\, R_D \\ F_{EB} &= S_E C_E\, M_{ED}\, M_{DB}\, C_B\, R_B \end{aligned} \tag{4-6}$$

where F_{ij} are the Fourier transforms of the time signals f_{jj} ; the first subscript, i, denotes the source location, and the second subscript, j, is the receiver location. S_i represents the source transfer function at locations i. C_i and C_j are the coupling transfer functions at locations i and j. M_{ij} is the transfer functions of the medium between locations i and j, and R_j is the receiver transfer function. The terms M_{ij} and M_{ji} can be considered equal because they indicate the same wave path and geometric attenuation. As a result, the signal transmission between locations B and D can be expressed as follows (Popovics et al., 2000):

$$FTC = \sqrt{\frac{F_{AD} \cdot F_{EB}}{F_{AB} \cdot F_{ED}}} = M_{BD} \tag{4-7}$$

The FTC is an amplitude ratio of measurements near the source and away from the source. The FTC is indicative of wave attenuation for each frequency component transmitted through the fissure. FTC value varies between zero (complete attenuation) and one (complete transmission). In ideal situations where the medium is intact, there is a total transmission of energy and hence the FTC is equal to one.

The coefficient M_{BD} not only gives the attenuation due to a discontinuity or crack (Figure 4-12), but also provides information about the geometrical attenuation between locations B and D. Therefore, measurements should be carried out on both cracked and crack-free surfaces, and the contribution by geometrical attenuation should be removed.

The main limitation of this technique is that the surface waves detected at the near receiver are less affected by geometric attenuation than the signals at the far receiver. In addition, surface waves at the near receiver are less affected by the reflected P-waves from the bottom of the slab. Moreover, reflected waves from the surface crack can also interact with surface waves at both receiver locations, leading to a superposition of the reflected waves that may amplify or reduce signal amplitudes. Therefore, a time window is recommended for isolated analysis of the surface wave portion. Care should be taken when selecting appropriate source-receiver spacing, and the distance between the receiver location and the crack.

4.2.3.6. Wavelet Transmission Coefficient (WTC)

The wavelet transmission coefficient (WTC) method was developed to overcome the main limitations of the FTC method (Yang, 2009). Wavelet transform measures the similarity of a Morlet wavelet to the studied signal as it is shifted over the signal. In the WTC method, the wave attenuation is measured across the joint as well as along the joint-free area using the square configuration shown in Figure 4-13.

Two identical transmitters are placed at locations A and D as the sources, and two receivers are placed at B and C. The generated surface waves by source 1 at D are recorded by receiver 1 at C to measure the first signal across the joint; the second signal is recorded by receiver 2 at B through the joint-free surface. Likewise, the corresponding signals are recorded when the source is at location A.

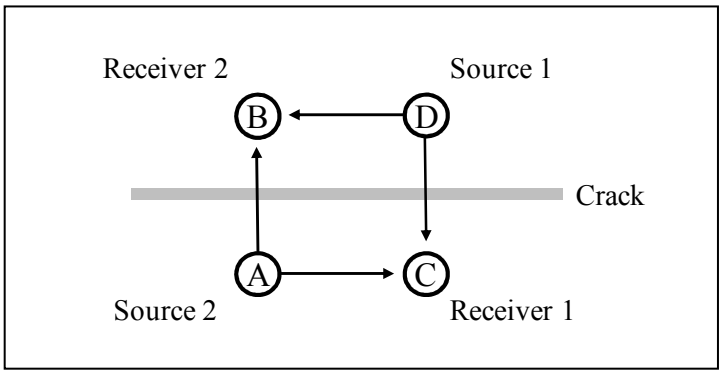

Figure 4-13. Source-receiver locations for WTC measurements.

Similar to the FTC, the WTC can be expressed as follows (for Figure 4-13):

$$WTC = \sqrt{\frac{W_{AB}\, W_{DC}}{W_{AC}\, W_{DB}}} \tag{4-8}$$

where the constants W_{AB}, W_{DC}, W_{AC} and W_{DB}, are obtained as the peak amplitudes of the wavelet transforms of the four time signals f_{AB}, f_{DC}, f_{AC} and f_{DB}, respectively.

Contrary to the FTC method, the WTC uses an equally spaced square configuration that reduces the wave reflection effects in the presence of a crack. Furthermore, WTC overcomes a main limitation of the FTC: since the distances traveled by the four waves are identical, the geometrical attenuation is cancelled.

Wave attenuation measurements using the WTC can be used to identify good quality, medium quality and weak quality joints (Jiang, 2007). The WTC was found to be more suitable as a condition index than the FTC, because it does not require time windowing.

4.2.3.7. Instantaneous Transmission Coefficient (ITC)

The Hilbert transform allows the study of the frequency content of a signal as a function of time. The time and frequency information of the signal is stored in the associated analytic signal. The analytic signal, x_a, combines the original time signal, x, and its Hilbert transform, $\hat{x}$, as

$$x_a = x + i\hat{x} \tag{4-9}$$

Instantaneous parameters, such as amplitude and phase, can be computed from the analytic signal. As an example, a free-decay signal with varying frequency and a constant damping ratio is shown in Figure 4-14 (details in Appendix A). The natural frequency varies linearly from 1 Hz to 2 Hz, and the damping ratio is 1%. The analytic signal associated to the time signal is computed, and time dependent information is extracted.

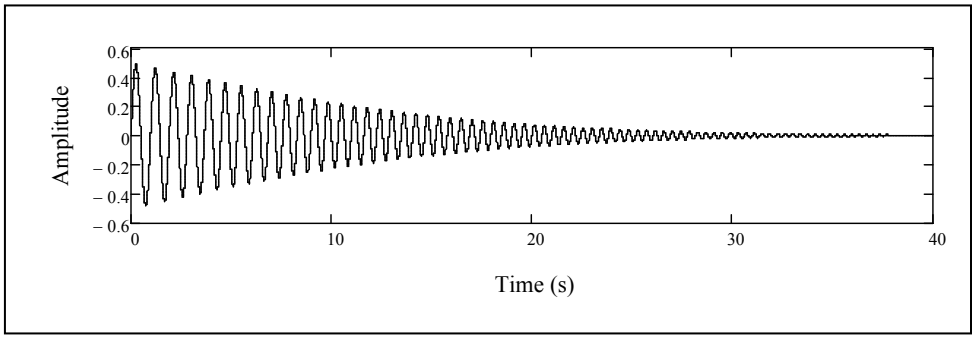

Figure 4-14. Sine wave with frequency of 1 Hz to 2 Hz and damping ratio of 1%.

The imaginary component of the analytic signal can be computed without directly using the Hilbert transform. First, the Fourier transform of the original signal is computed; then, the frequency components above the Nyquist frequency are set to zero. Next, the inverse Fourier transform is computed; and finally, the inverted results are multiplied by a factor of two to compensate for the energy lost induced by using half of the spectrum. The real component of the analytic signal is the signal itself:

$$Re(x_a) = x \tag{4-10}$$

Figure 4-15 presents the real and imaginary components of the analytic signal. As expected, the real components are identical to the original signal values.

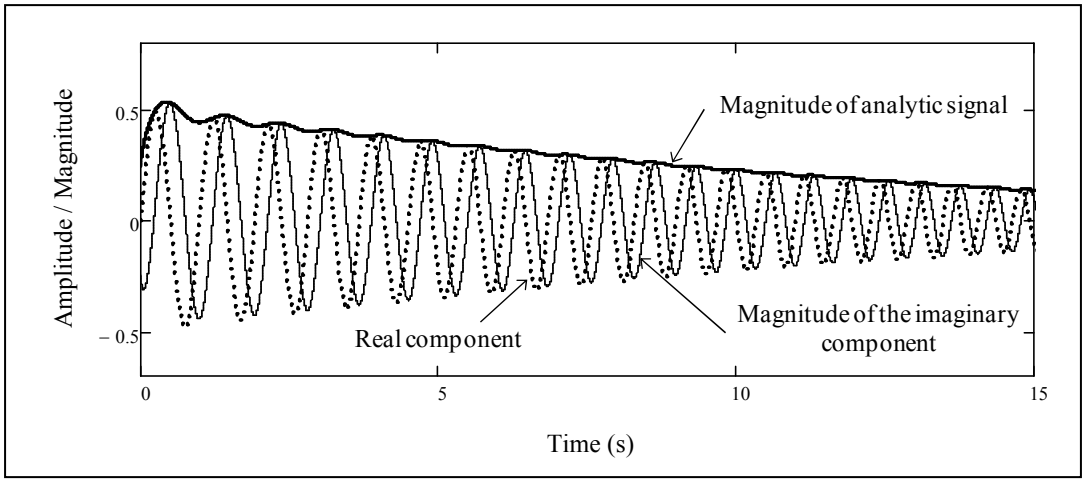

Figure 4-15. Real and imaginary components of the analytic signal corresponding to the free-decay signal shown in Figure 4-14.

Each value of the analytic signal is a complex number, the instantaneous phase, $\theta(t)$, at each entry, j, of the signal can be computed by

$$\theta_j(t) = \tan^{-1}\left[\frac{Im(x_a)_j}{Re(x_a)_j}\right] \tag{4-11}$$

Figure 4-15 shows that the magnitude of the analytic signal represents the envelope of the original signal.

Consequently, the instantaneous amplitude, $A(t)$, can be expressed as

$$A_j(t) = \sqrt{\left[Re(x_a)_j\right]^2 + \left[Im(x_a)_j\right]^2} \tag{4-12}$$

Figure 4-16 shows the unwrapped phase of the analytic signal as a function of time.

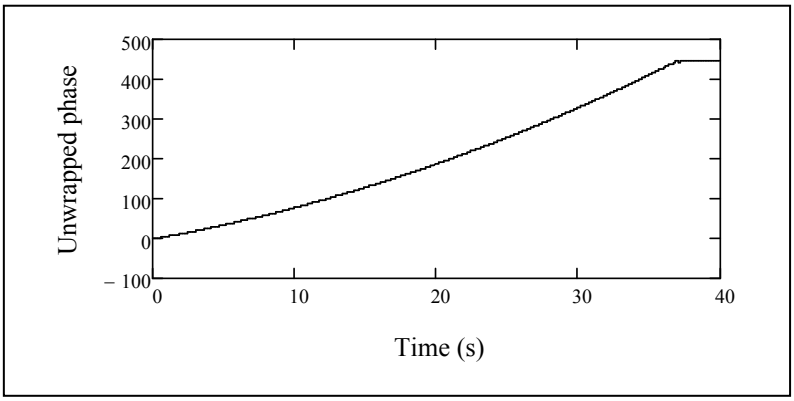

Figure 4-16. Instantaneous unwrapped phase of the analytic signal associated to the sine wave.

The frequency can be defined as the time derivative of the phase; thus, an instantaneous frequency, $\omega(t)$, can be expressed as,

$$\omega_j(t) = \frac{\Delta\theta}{\Delta t} \tag{4-13}$$

The instantaneous amplitude is stable because no derivation is required; however, the instantaneous frequency does require derivation and is sensitive to noise, since the derivation process involves an amplification factor equal to ω (Achenbach, 1973). A low-pass filter can be applied in the frequency domain for noise reduction. Figure 4-17 shows the instantaneous frequency calculated for the time signal after an adaptive smoothing function has been applied.

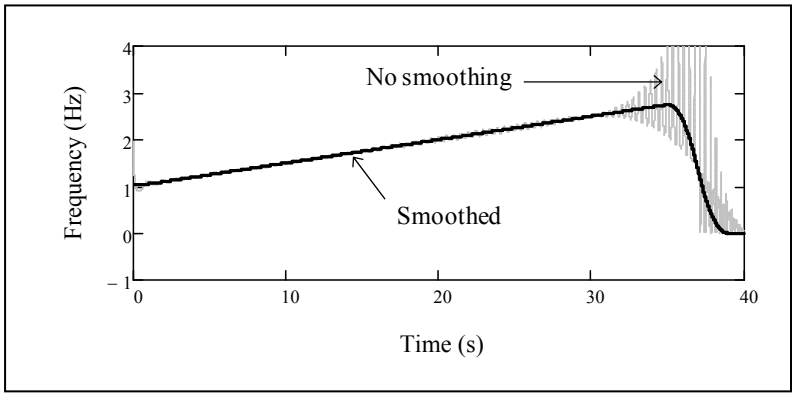

Figure 4-17. Smoothed and unsmoothed instantaneous frequency of the synthetic sine wave.

Material properties such as the damping ratio can be computed directly from the instantaneous properties of the waves propagating in the asphalt. An instantaneous damping ratio can be computed from the analytic signal:

$$\xi_j(t) = \frac{1}{\Delta\theta} \ln \frac{A_j}{A_{j+1}} = \frac{\ln A_j - \ln A_{j+1}}{\theta_j - \theta_{j+1}} \tag{4-14}$$

Equation (4-14) represents the derivative of the natural logarithmic of the instantaneous amplitude with respect to phase angle. The computed damping ratio for the free-decay signal is shown in Figure 4-18.

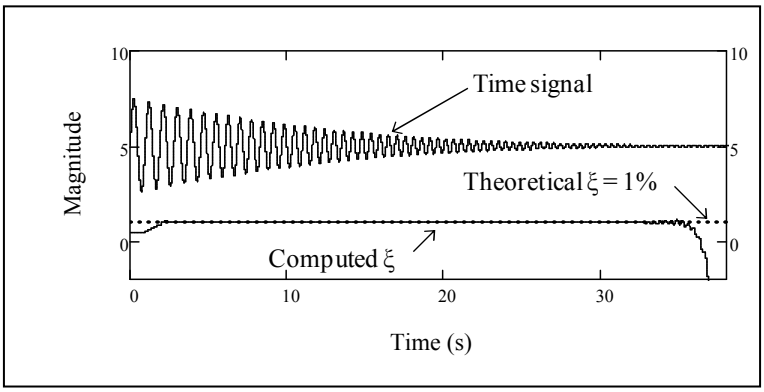

Figure 4-18. Experimental and theoretical damping ratio.

The calculated damping ratio (Figure 4-18) agrees well with the theoretical damping of 1%. Slight differences are noticed at the beginning and end of the time window, as a result of using the derivation function. Nevertheless, for the main part of the signal, where most wave energy is concentrated, the experimental results are consistent with the theoretical values.

Instantaneous parameters can be used for the characterization and detection of damage in an asphalt pavement. In theory, the wave energy is diminished rapidly while travelling through a highly damped medium. The presence of cracks induces larger attenuation effects, because the wave energy is scattered and reflected. Measuring the instantaneous damping values appears to be effective for the condition assessment of pavements.

Following a similar configuration to the WTC method (Figure 4-13), a new transmission coefficient method (instantaneous transmission coefficient - ITC) based on the instantaneous damping is proposed, and is given by

$$ITC = \sqrt{\frac{\xi_{AC}\,\xi_{DB}}{\xi_{AB}\,\xi_{DC}}} \tag{4-15}$$

where the coefficients ξ_{AC}, ξ_{DB}, ξ_{AB} and ξ_{DC}, are the average instantaneous damping ratios of the four measured signals, x_{AC}, x_{DB}, x_{AB} and x_{DC}, in the equal spacing configuration (Figure 4-13).

Unlike FTC and WTC, ITC gives the ratio of the attenuation in terms of the damping in the joint free area with respect to the damping in the jointed area. For a longitudinal joint in perfect condition, the ITC is equal to one because the jointed area provides higher damping effects than the joint free sections.

Similar to the FTC, the ITC provides a self-compensating approach that reduces the unknown effects produced by the different characteristics and coupling of the transducers. This methodology uses time related parameters instead of relying on frequency, which allows the association of temporal and spatial components.

The ITC overcomes the main limitation associated to the WTC technique. The WTC method requires more user input, as it involves selecting peak values from the wavelet transform, making the automatic data processing difficult. The absolute maximum peak can be selected for the computation of the WTC; however, wave reflections may affect these maximum values, resulting in erroneous results. Furthermore, in the WTC method, epoxy and aluminum plates must be used to couple the transducers and the asphalt surface. This is not practical for testing in-service roads. Therefore, the new ITC methodology, with a new coupling system, is tested in the laboratory for assessing the condition of joints, and its results are compared with the results from the FTC and WTC analysis.

4.3 Nondestructive Testing of Steel Pipes for Thickness Estimation

NDT technologies play a very important role in the inspection of industrial components, including manufacturing quality control and in-service monitoring (Basravi, 2004). In many cases, a primary advantage of NDT is the ability to precisely measure material thickness in situations where access to only one side of a test piece is available. This is often the case on

pipes or tanks. The loss of wall thickness in pipelines can affect the reliability and safety of an entire plant (Hwang et al., 2002). Several NDT technologies, such as electromagnetic methods, infrared thermography, and ultrasonic techniques, can be used for the wall thickness measurement of steel pipes.

4.3.1 Electromagnetic methods

Electromagnetic NDT methods are common tools for thickness measurement of conductive materials, as well as for the detection of surface and sub surface flaws (Yin and Peyton, 2007). The conventional eddy current testing (ECT), the pulsed eddy current (PEC) and the remote field testing (RFT) techniques are widely accepted. These techniques are often used in nuclear, aerospace, power, petrochemical and other industries for the detection and sizing of cracks, corrosion and other material discontinuities during manufacturing and in-service. In contrast to volumetric NDT techniques such as radiography and ultrasonic, electromagnetic methods work on the surface to detect internal defects.

4.3.1.1. Eddy Current Testing (ECT)

Eddy current testing (ECT) works on the principle of electromagnetic induction, where a coil (also called probe or sensor) is excited with sinusoidal alternating current with a single frequency between 50 Hz and 5 MHz to induce closed loops of current, known as eddy currents, in the electrically conducting material being tested (Figure 4-19).

Electromagnetic induction is governed by three fundamental laws: Ampere, Faraday, and Lenz laws. Ampere's law provides the magnetic flux density of the changing magnetic field; whereas, Faraday's and Lenz's laws give the magnitude and the direction of the induced electromagnetic field in the coil.

The following sequential events occur in ECT: (1) the coil generates primary magnetic field as per Ampere's law, (2) the primary magnetic field induces eddy currents in the material as per Faraday's law, (3) the eddy currents generate secondary magnetic field in the opposite direction as per Lenz's law, (4) the coil impedance changes in the presence of a defect, and

(5) the impedance change is measured, analyzed and correlated with defect dimensions. The magnitude and phase of the eddy currents affect the loading on the coil, and thus its impedance. A crack on the surface immediately underneath the coil interrupts, or reduces, the eddy current flow by decreasing the loading on the coil and increasing its effective impedance. However, cracks lying parallel to the current path do not cause significant interruption and may not be detected.

ECT is widely used in various industries for flaw detection and measurement. In general, the technique is used to inspect a relatively small area and can be only used to detect surface and near surface defects. Eddy currents, which can be used to measure the thickness of thin materials such as tubing and sheet stock, can also detect corrosion, erosion, and cracking that cause thinning of the material. This technique is well-accepted in the aviation industry for corrosion thinning measurements on aircraft skins. ECT is also a useful tool for inspecting the walls of the tubing used in assemblies such as heat exchangers and heat generators at power plants and petrochemical facilities. The amount of eddy currents generated is related to the volume of the material under investigation; therefore, thick materials are capable of carrying more eddy currents than thin materials. Consequently, the amount of eddy currents generated can be measured and related to material thickness.

A typical ECT configuration is shown in Figure 4-19, where a circular coil is placed close to the conductive material being tested. The alternating current in the coil generates a changing magnetic field that interacts with the test specimen and induces eddy currents. Variations in the phase and magnitude of these eddy currents may be monitored using a second coil, or by measuring changes to the current flowing in the primary coil. Variations in the electrical conductivity or magnetic permeability of the test material, or the presence of any flaws, will cause a change in eddy current flow and a corresponding change in the phase and amplitude of the measured current.

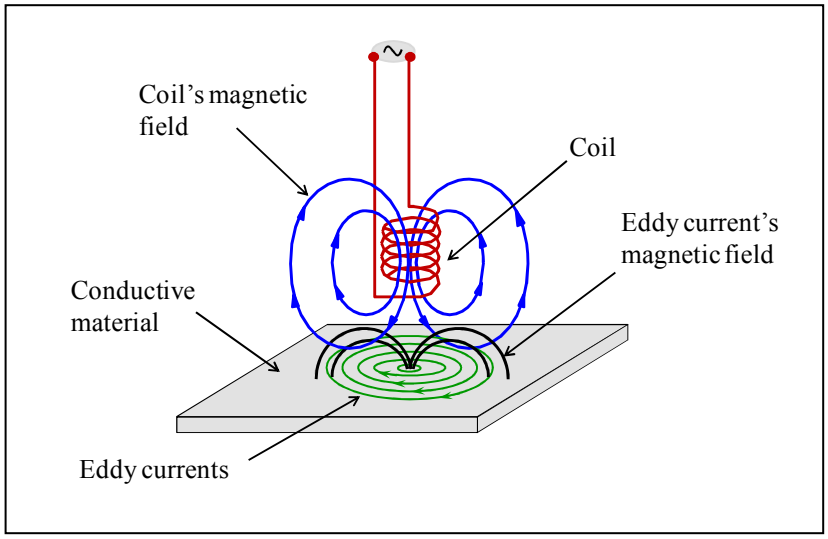

Figure 4-19. Eddy current technique configuration.

Eddy currents concentrate near the surface next to the excitation coil, and their intensity decreases exponentially with depth; this phenomenon is known as the skin effect. The depth that eddy currents penetrate into a material decreases as the frequency of the excitation current increases and as the conductivity and magnetic permeability of the material rises (Figure 4-20). The depth at which eddy current density decreases to 1/e or approximately 37% of the surface density is called the standard depth of penetration (*d*):

$$d \approx \frac{1}{\sqrt{\pi \mu \sigma f}} \tag{4-16}$$

where μ and σ are the magnetic permeability and the electrical conductivity of the material, respectively, and f is the test frequency. It is important to select a test frequency such that the flaw lies within one standard depth of penetration, thus the strength of the eddy currents is sufficient to produce a flaw indication.

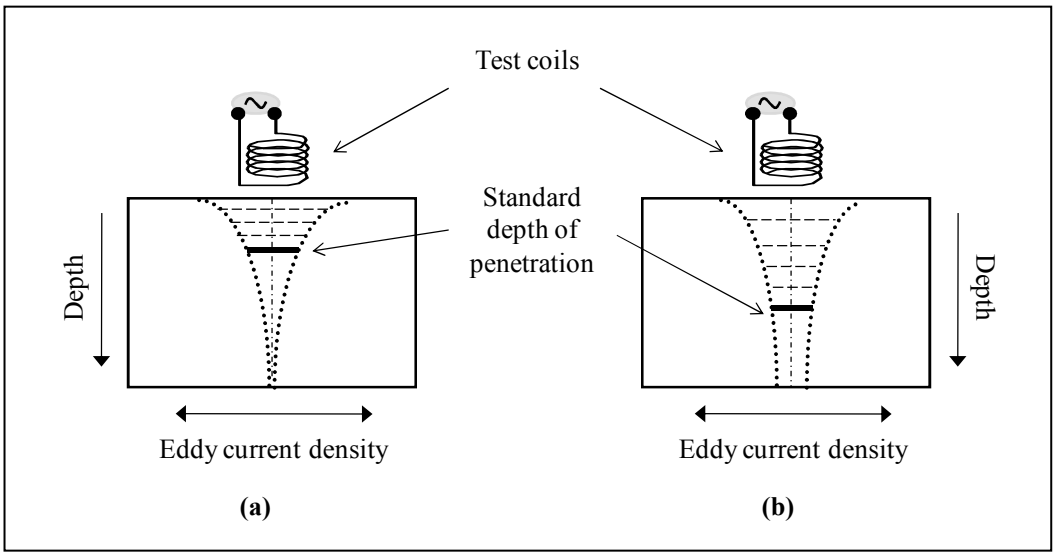

Figure 4-20. Eddy current depth of penetration for: **(a)** high frequency, high conductivity and high permeability; **(b)** low frequency, low conductivity and low permeability.

The phase lag is an important parameter in ECT, as it can be used for estimating the subsurface depth of a discontinuity. Phase lag (θ) can be defined as the shift in phase angle between the eddy current response from a disturbance on the surface and a disturbance at a certain depth:

$$\theta = \frac{x}{d} \tag{4-17}$$

where x is the distance below the surface, and d is the standard depth of penetration. According to Equation (4-17), the eddy currents flowing at one standard depth of penetration (d) below the surface, lag the surface currents by one radian (or 57°). Hence, the phase lag of a signal can be used to estimate the depth of a defect. Although ECT has many applications, it has a low penetration depth, limited by the single frequency sinusoidal excitation. A recent study has suggested a maximum penetration depth of 12 mm (Grimberg et al., 2006).

4.3.1.2. Pulsed Eddy Current (PEC)

In contrast to the conventional ECT, the pulsed eddy current (PEC) technique operates a non sinusoidal excitation (e.g. a pulse or square wave) instead of a single frequency sinusoidal

excitation over a narrow frequency bandwidth. In pulse methods, a wide bandwidth of frequencies is excited; the extent of which varies inversely with the pulse length. Therefore, a range of frequencies are generated simultaneously, providing a depth profile of the material under investigation, and overcoming one of ECT's limitations. The PEC technique has been effectively used for detection of wall thinning and corrosion in aircraft multilayer structures (Robers and Scottini, 2002).

According to recent studies, a differential probe used in PEC systems, which contains an excitation coil with two hall-sensors, has been fabricated to detect wall thinning in an insulated stainless steel pipeline (Angani et al., 2010). A square wave with varying duty cycle and frequency was used to generate a current pulse of 500 mA and 500 μs width to the excitation coil. The calibration sample consists of a stainless steel plate with thickness that varies from 1 mm to 5 mm, overlain by an 8 mm thick plastic insulator. The pulse energy and the power spectrum density of the Fourier transform were measured to describe the PEC response. The results showed a good correlation between the energy of the detected pulse and the sample thickness.

The applied operating principle of pulsed eddy currents can vary from system to system. In order to obtain a quantitative reading for wall thickness, RTD-INCONTEST uses a patented algorithm that relates the diffusive behavior in time with the material properties and the wall thickness.

Although the PEC technique appears effective to detect wall thinning in insulated steel pipelines, this detection is restricted to a localized area of the induced magnetic field. Furthermore, the scanning speed should be relatively slow in order to achieve accurate results, e.g. 50 mm/min (Park et al., 2009).

4.3.1.3. Remote Field Testing (RFT)

Remote field testing (RFT) is mainly applied to locate defects in steel pipes and tubes. In contrast to the conventional eddy current testing, RFT employs widely spaced coils to detect the electromagnetic field. The RFT method is primarily used to inspect ferromagnetic tubing,

as conventional ECT methods have difficulty inspecting the full thickness of the tube wall due to the strong skin effect in ferromagnetic materials.

A typical RFT probe consists of a coil that sends a signal to the detector coils, and records measurements as it is pulled through the pipe. The exciter coil is driven with a low frequency sinusoidal current which generates a magnetic field. This magnetic field propagates outwards from the exciter coil, inducing strong circumferential eddy currents that extend axially and radially in the pipe wall. These eddy currents generate a second magnetic field that opposes the magnetic field from the exciter coil. The detector is placed inside the pipe and detects the magnetic field that has travelled back from the outside of the pipe wall. In areas of wall thinning, the field arrives at the detector with a faster travel time and greater signal strength resulting from the reduced path through the steel.

The signals obtained with RFT are very similar to those obtained with conventional ECT; localized changes in wall thickness result in phase and amplitude changes. These changes can indicate defects such as cracks, corrosion pitting and thinning. Although RFT has been successfully used in nondestructive testing on ferromagnetic pipes, it requires shutting down the manufacturing process, since the measurements are performed by moving the probe along the interior of the pipe.

4.3.2 Infrared Thermography

Infrared thermography (IRT) technologies can detect wall thinning in pipes, and has the advantage of being fast, safe, and nonintrusive (Maldague, 1999). Subsurface defects usually have different thermal properties with respect to the surrounding sound material. A modified IRT tool, pulsed active infrared thermography (PAIRT), produces a transient thermal perturbation of the inspected section to detect the subsurface defects. The different thermal properties are revealed through the evolution of the surface temperature history observed with an infrared camera (Maldague 1993). The pipe wall thickness can be determined by measuring the thermal propagation time following the transient perturbation. The transmission method has the advantage of providing a high thermal contrast on the pipe

surface, and the absence of reflective noise due to temperature perturbation generated inside the pipe (Maldague, 1999).

Under stationary conditions, temperature differences between areas of different wall thicknesses within a pipe are nonexistent. When the corresponding thermal contrasts appear on the front surface, significant thermal contrasts can be obtained under transient conditions. The depth, z, of a material can be related to the time of detection, t, by

$$t = \frac{z^2}{\delta} \tag{4-18}$$

where δ is the thermal diffusivity of the material in m^2/s (Maldague 1993).

According to Equation (4-18), if a portion of a pipe has its wall thickness reduced by a factor of two (due to corrosion), a sudden thermal disturbance reaches the outer surface of this portion after a time period four times smaller than the surrounding portions. In other words, areas with thinner walls will have their temperature affected first. By measuring the time of detection, t, the wall thickness can be quantitatively evaluated providing the thermal diffusivity, δ, of the pipe.

The thermographic inspection, using the transmission method, starts with the generation of a thermal transient inside the pipe by changing the temperature of the circulating fluid. Next, the temperature distribution of the outside surface is detected with the IR camera, and any abnormal temperature patterns are note. Finally, the wall thickness can be determined with Equation (4-18).

Alternatively, if a thermal change in the circulating fluid is not possible, a reflective method can be implemented. In this case, a uniform heat source is applied to the exterior of the pipe to generate a thermal transient. Similar to the transmission method, the temperature distribution of the outside surface is monitored by the IR camera, revealing any abnormal temperature pattern. Finally, the wall thickness is calculated with Equation (4-18).

Given the differences in thermal diffusivities between water and steel, the thermal front reflected at the interface wall-water reaches the exterior surface at different times depending on wall thicknesses, thus allowing wall corrosion to be located.

Although the reflective method has proven to give accurate thickness measurements, the pipe surface temperature must be uniform and the circulating fluid in the pipe must be stopped, shutting down the manufacturing process for a certain period prior to testing. In addition, the IRT techniques give only localized thickness information, similar to the electromagnetic methods.

4.3.3 Ultrasonic Methods

Ultrasonic wave methods are NDT techniques that are commonly used in the investigation of material thicknesses. These techniques consist of emitting ultrasonic waves into the medium under investigation and recording the reflected waves. Since these methods require access to only one free surface, they are highly applicable to the evaluation of pipe wall thickness.

Two devices are presented in the following sections: the ultrasonic thickness gauge and the multiple echo ultrasonic thickness gauge.

4.3.3.1. Ultrasonic Thickness Gauge (UTG)

Ultrasonic thickness gauges (UTG) provide many advantages for measuring the wall thickness of an extruded pipe or tube, to detect out-of-tolerance conditions. The concentricity of an extruded pipe can be monitored on a continuous and automatic basis with no need to cut the pipe or to shut down the manufacturing process. Also, ultrasonic methods allow a fast detection of pipe wall thickness along the total length by giving discrete results at the locations in which measurements were made.

Ultrasonic thickness measurement is currently one of the most popular methods for determining steel plate thicknesses (Damgaard, 2009). This technique typically consists of a transducer emitting ultrasonic waves that travel through the material being tested and reflect off the opposite wall and back to a receiver. The transducer is placed in contact with the surface of the material, and the quality of the measurement can be increased by using a couplant. Similar to the ECT and thermal methods, the measurement can be performed by accessing only one side of the material.

The effectiveness and accuracy of this method when applied to corroded steel plates was determined in a recent study, in which a UTG was used (Damgaard, 2009). In theory, the UTG probe transmits and receives ultrasonic pulses in the form of waves. The transmitted waves return to the probe at different intervals after reflecting from discontinuities in the medium. Given the characteristic wave velocity of the material being tested, the UTG displays the calculated thickness based on the first wave to return. For a steel specimen with a machined semicircular groove, the UTG accurately detects the depth of the groove, but fails to measure the groove width, as the reflection surface at several points was not perpendicular to the direction of wave propagation. UTG measurements appear reliable for determining local thicknesses if the reflection surface is perpendicular to the direction of the wave propagation at the measured point.

According to a manufacturer of UTG, Olympus *Inspection & Measurement Systems*, the most common UTG probes are capable of providing instant digital pipe wall thickness measurements ranging from 0.080 mm to 635 mm, and also permit the use of a very low frequency bandwidth for greater penetration (ranging from 500 kHz to 100 MHz). These probes can collect and display thickness measurements from up to 8 separate transducers around the circumference (multipoint thickness measurements) with a resolution up to 0.001 mm.

A major drawback of this method is that prior to the test, the UTG must be calibrated for the sound velocity and zero offset appropriate for the application at hand. Sound velocity must always be set with respect to the material being measured. Zero offset is usually related to the type of transducer, transducer cable length and mode of measurement being used (Fowler et al., 1997).

4.3.3.2. Multiple Echo Ultrasonic Digital Thickness Gauge

The multiple echo ultrasonic thickness gauge method determines the thickness of a material by measuring the time between the second, third and fourth echoes received, as opposed to the UTG method, which takes into account only the first reflection or echo.

This method (Cygnus Instruments) has the advantage of providing the thickness of the material only and does not include the thickness of the paint or coating; this advantage is especially useful when measuring the thickness of pipes in nuclear industries. The second, third and fourth echoes occur as a result of the waves reflecting backwards and forwards between the front and back walls of the material under investigation, and the time between each echo is measured to determine the thickness (Figure 4-21). Therefore, there is no need to calibrate the instrument prior to the test, overcoming a major limitation of the UTG method. However, only localized information can be derived using this method.

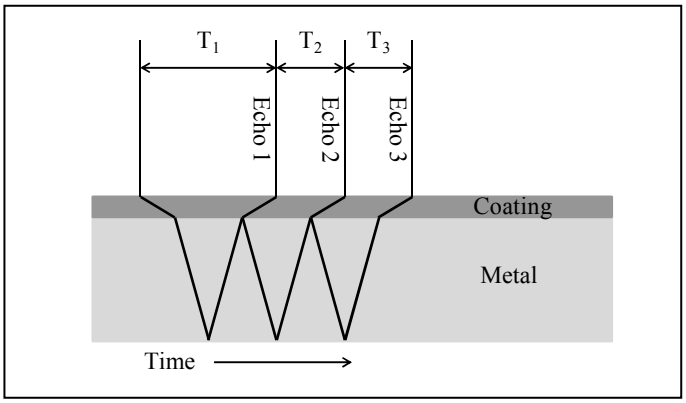

Figure 4-21. Multiple echo ultrasonic digital thickness gauge (Cygnus Instruments).

4.4 Chapter Summary

This chapter reviews the different NDT methods used in the condition assessment of asphalt slabs and wall thickness of steel pipes. The most recently developed NDT techniques consist of electromagnetic and ultrasonic methods. The advantages and drawbacks to each method are summarized in Table 4-1. In general, the selection of an appropriate testing method is critical in material characterization.

Table 4-1. Summary of NDT techniques for various applications.

APPLICATION	TECHNIQUE	MAIN ADVANTAGES	MAIN LIMITATIONS
Deflection testing for asphalt pavements	▪ Static ▪ Vibratory ▪ Impulse ▪ MDD	▪ Inexpensive ▪ Simple	▪ Slow and labor intensive. ▪ Limited maximum peak-to-peak force. ▪ Complex data processing.
Electromagnetic waves for flaw detection	▪ IRT ▪ GPR	▪ Fast ▪ Cost effective	▪ Highly susceptible to environmental conditions. ▪ Interpretation of GPR data requires experience. ▪ Limited to high frequency waves (1 GHz to 2.5 GHz).
Ultrasonic testing for flaw detection (cracks, voids, delamination)	▪ IE	▪ Requires access to only one surface.	▪ Commonly used low frequencies are not sensitive to small flaws.
	▪ UPV	▪ Accurate for estimating dynamic modulus of asphalt.	▪ Requires removal of the time delay due to the equipment and coupling conditions.
	▪ SASW	▪ Accurate for estimating delamination, cracks, thickness profiles and material integrity.	▪ Source-receiver spacing and noise reduction compromises the depth of measurement. ▪ Considers only the fundamental modes of R-waves.
	▪ MASW	▪ Higher modes are considered. ▪ Faster data collection. ▪ Better noise control. ▪ Provides an improved wave velocity profile.	▪ Requires user input during the selection of FK plot maxima.

APPLICATION	TECHNIQUE	MAIN ADVANTAGES	MAIN LIMITATIONS
Transmission coefficient for condition assessment of construction joints	▪ FTC	▪ The wave velocity of the material is not required in advance. ▪ The technique is independent of the type of the coupling conditions.	▪ Time window is needed to isolate the appropriate wave portion for analysis. ▪ The contribution by geometrical attenuation must be removed.
	▪ WTC	▪ The equal spacing configuration helps reducing the wave reflection due to a crack. ▪ The geometrical attenuation is automatically cancelled.	▪ Requires user input, making automatic data processing difficult. ▪ The coupling of the transducer to the asphalt surface is not practical for testing in-service structures.
	▪ ITC	▪ Allows automatic data processing, reducing user input. ▪ The new coupling system reduces the testing time by up to 50%.	▪ The instantaneous is sensitive to noise; thus, a low-pass filter is sometimes necessary for noise reduction.
Electromagnetic methods for estimating steel pipe thickness	▪ ECT	▪ Detects flaws and determines the depth and size of the flaw.	▪ Low penetration, limited by the single sinusoidal excitation (50 Hz to 5 MHz). ▪ Cracks lying parallel to the current path may not be detected. ▪ Gives only localized results only where measurements were made.
	▪ PEC	▪ Uses a non-sinusoidal excitation providing a depth profile of the material being tested.	▪ Gives only localized results only where measurements were made.
	▪ RFT	▪ Useful for inspecting ferromagnetic materials.	▪ Requires shutting down the manufacturing process.
Transmission methods for estimating steel pipe thickness	▪ IRT ▪ PAIRT	▪ High thermal contrast on the pipe surface. ▪ Absence of reflective noise.	▪ The circulating fluid in the pipe must be stopped. ▪ Gives only localized thickness information.

APPLICATION	TECHNIQUE	MAIN ADVANTAGES	MAIN LIMITATIONS
Ultrasonic methods for estimating steel pipe thickness	▪ UTG	▪ No need to cut the pipe or to shut down the manufacturing process.	▪ The equipment must be calibrated for the sound velocity and zero offset, particular for each application.
	▪ Multiple Echo UTG	▪ No need to calibrate the instrument prior to the test.	▪ Gives only localized results only where measurements were made.

CHAPTER 5. CALIBRATION OF ACCELEROMETERS

5.1 Introduction

Wave-based NDT techniques are useful tools for detecting defects in materials. In general, pulse-velocity tests are preferred due to their simplicity; the first arrival of the wave is the single parameter used for determining the elastic modulus of the material. However, as discussed in Section 4.2.3.2, both ends of the specimen have to be accessible, which is not the case for most civil infrastructures. Moreover, the pulse-velocity tests do not provide information about the phase velocity and material damping that are useful parameters for further characterization of the material. Therefore, the full waveform should be analyzed.

The analysis of a complete waveform is complex, as different phenomena affect the wave propagation (Section 2.3). Other factors such as transducer (sources and receivers) coupling and array configurations can also affect the measurements. Hence, transducers should be characterized through a calibration process.

This chapter presents the results of pulsed-velocity tests using two calibration bars and two different coupling configurations in order to determine the relative frequency response of twenty accelerometers. The relative characterization of the accelerometers is important for removing the undesirable effects induced by manufacturer differences between the transducers. The selection of receivers for testing the asphalt slab and steel plate samples is based on the results of this calibration procedure.

5.2 Background

The measured signal, or the response of a medium from propagating waves, is affected by the source, the receiver, the coupling, and the medium itself. In essence, the measured response, *Y(ω)*, in the frequency domain can be expressed as

$$Y(\omega) = X(\omega)H_S(\omega)H_{CS}(\omega)\,H_M(\omega)\,H_{CR}(\omega)\,H_R(\omega) \tag{5-1}$$

where, $X(\omega)$ is the input excitation, H_S and H_R are the transfer functions of the source and receiver, respectively. H_{CS} is the transfer function of the coupling mechanism between the source and the material. H_{CR} is the transfer function of the coupling mechanism between the receiver and the material, and H_M is the transfer function of the medium.

Coupling between the transducers and the specimen is critical to ensure reliable measurement of wave characteristics. Wave energy is significantly attenuated at the transducer-to-air interface; therefore, a proper contact eliminates any air gaps formed by surface irregularities. A couplant is commonly used to fill these gaps. There are several materials that can be used as couplants, such as water, oil, grease, glycerine, petroleum jelly, and kerosene (Hellier et al., 2001). In particular, silicone-high vacuum grease and cyanoacrylate glue have been proven effective for maximizing energy transmission (Jiang, 2007; du Tertre, 2010).

Wave propagation along an infinitely long isotropic bar can be theoretically characterized, and is very similar to wave propagation in plates and thin slabs (Hudson, 1943; Zemanek, 1971). Hence, given the wave velocity and the Poisson's ratio, the corresponding dispersion curve can be computed. Essentially, two main types of modes of propagation occur: symmetrical (or longitudinal), and anti-symmetrical (or flexural) modes.

In a solid circular cylinder, the dispersion curve is given by the frequency equation, which for symmetric waves is

$$[\Omega^2 - 2(\gamma r)^2]^2 J_0(hr)\, J_1(kr) + 4(\gamma r)^2 hr\, kr\, J_0(kr) J_1(hr) - 2\Omega^2 hr\, J_1(hr)\, J_1(kr) = 0$$

$$\textit{where} \qquad (hr)^2 = \alpha^2\Omega^2 - (\gamma r)^2\,, \quad (kr)^2 = \Omega^2 - (\gamma r)^2$$

$$\alpha^2 = \left(\frac{V_S}{V_P}\right)^2 = \frac{(1-2\nu)}{2(1-\nu)} \tag{5-2}$$

where, Ω is the number of shear wavelengths in a circumference = $\omega r/V_S$, γ is the wavenumber, r is the radius of the cylinder, $J_n(x)$ is the Bessel function of the first kind and order n, V_S and V_P are the S-wave and P-wave velocities, respectively, and ν is the Poisson's ratio. The numerical evaluation of the roots of Equation (5-2) provides the dispersion curve for the longitudinal mode. Figure 5-1 shows typical dispersion curves for PVC and aluminum specimens.

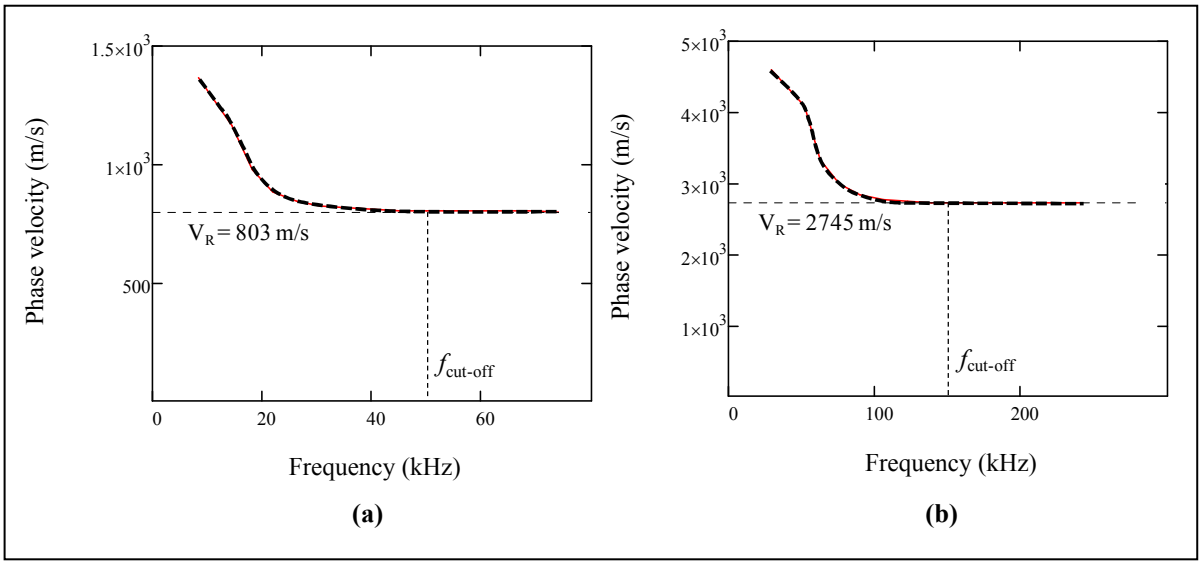

Figure 5-1. Dispersion curves for: **(a)** PVC and **(b)** aluminum specimens.

5.3 Methodology and Experimental Setup

The ultrasonic pulse velocity (UPV) calibration was performed on two specimens: PVC and aluminum cylinders, as shown in Figure 5-2. Two coupling agents: silicone-high vacuum grease and cyanoacrylate glue, were considered. The amount of applied couplant was consistent throughout the tests.

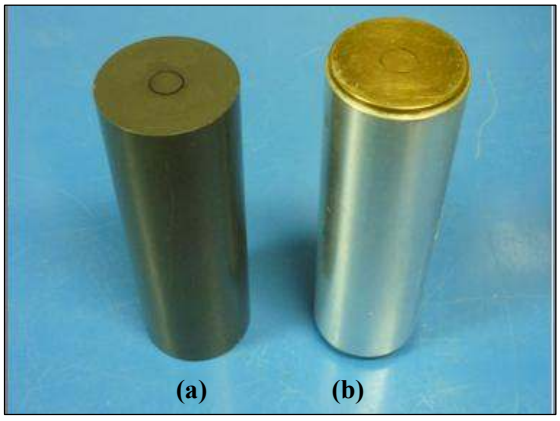

Figure 5-2. Calibration bars: **(a)** PVC and **(b)** aluminum.

The PVC cylinder has a length of 150.6 mm and a diameter of 51.3 mm. The aluminum specimen is 159.5 mm long, and measures 50.2 mm in diameter. PCV and aluminum have densities of 1379 kg/m^3 and 2865 kg/m^3, respectively.

The experimental setup for the test is illustrated in Figure 5-3. The instrumentation consisted of a data acquisition system and a load cell system. The peak-to-peak amplitude of the received signal is indicative of the coupling quality; hence, the contact pressure on the transducers was measured by the load cell throughout the tests. The amplitude of the response signals were scaled accordingly.

The load cell system consisted of a multimeter (HP 34401A), a DC regulated power supply (EXTECH 382213), and a load cell (type 20210-100) attached to a steel frame. The applied pressure was monitored by the multimeter.

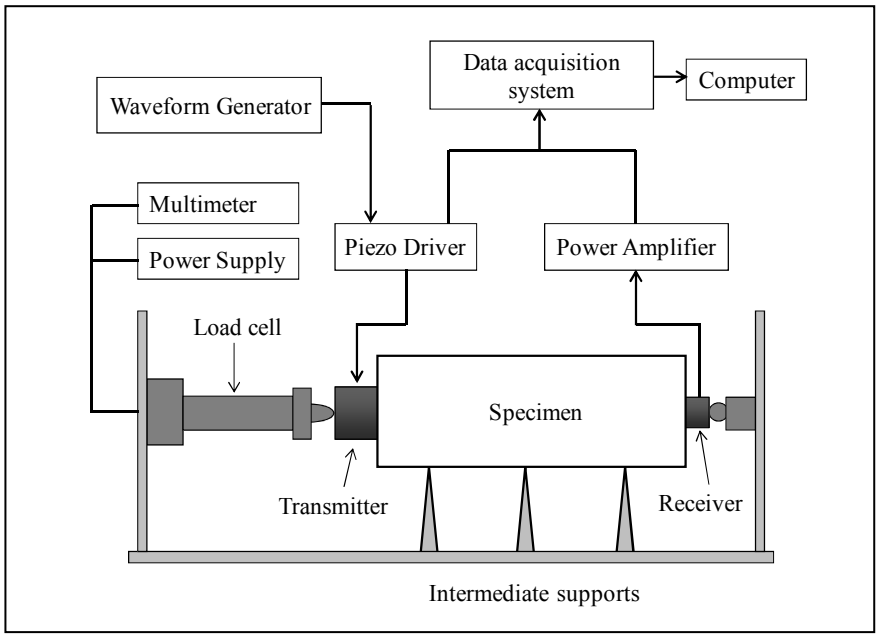

Figure 5-3. Calibration test setup.

A 50 kHz ultrasonic transmitter was used to generate mechanical waves in the specimen. The Fourier spectra of the ultrasonic transmitter excited by a single-cycle sinusoidal pulse suggested three main response frequencies at 25.4 kHz, 36.6 kHz and 49.8 kHz (Tallavo et al., 2009). Twenty Dytran 3055B3 accelerometers with a 35 kHz nominal resonant frequency and a sensitivity of 500±10 mV/g were used. The source pulse was generated by a waveform generator (HP 33120A) and a piezo driver (E1340). The power supply of the accelerometers (Dytran 4123B) has selectable amplification factors of 1, 10 and 100. The time signals were

recorded on a 24-channel data acquisition system with a 1 MHz sampling rate (LDS Nicolet Genesis).

The UPV tests were executed in four sets combining calibration bars and the coupling system:

- Set 1: PVC bar with vacuum grease
- Set 2: PVC bar with glue
- Set 3: aluminum bar with vacuum grease
- Set 4: aluminum bar with glue

Twenty accelerometers were used in each set of tests. Each set of tests consisted of measuring the response signals from the accelerometers, keeping constant the amount of coupling agent and pressure load.

Based on Equation (5-1), the ratio between the output (Y) and the input (X) spectra provides the global transfer function used for the test. A relative transfer function can be computed for each specimen that relates the grease couplant with the glue. The conditions of the source, the receiver, and the medium remain constant; thus, their transfer functions do not change. Consequently, a transfer function ratio can be computed as

$$\frac{[Y(\omega)/X(\omega)]_{grease}}{[Y(\omega)/X(\omega)]_{glue}} = \frac{H_S(\omega)[H_{CS}(\omega)]_{grease}\, H_M(\omega)\, [H_{CR}(\omega)]_{grease}\, H_R(\omega)}{H_S(\omega)[H_{CS}(\omega)]_{glue}\, H_M(\omega)\, [H_{CR}(\omega)]_{glue}\, H_R(\omega)} = \frac{[H_{CS}(\omega)]_{grease}\ [\,H_{CR}(\omega)]_{grease}}{[H_{CS}(\omega)]_{glue}\ [\,H_{CR}(\omega)]_{glue}} \tag{5-3}$$

Also, a relative transfer function for any accelerometer in relation to a reference one (e.g. accelerometer No. 2 in relation to No. 1) for each couplant is given by

$$\frac{[Y(\omega)/X(\omega)]_{acc.2}}{[Y(\omega)/X(\omega)]_{acc.1}} = \frac{H_S(\omega)\, H_{CS}(\omega)\, H_M(\omega)\, H_{CR}(\omega)\, [H_R(\omega)]_{acc.2}}{H_S(\omega) H_{CS}(\omega)\, H_M(\omega)\, H_{CR}(\omega)\, [H_R(\omega)]_{acc.1}} = \frac{[H_R(\omega)]_{acc.2}}{[H_R(\omega)]_{acc.1}} \quad (5\text{-}4)$$

5.4 Results

Each set of tests generated 20 time signal measurements. The responses were processed in time and frequency domain using MathCAD.

The time signals obtained from the accelerometers and the corresponding normalized Fourier spectra are shown in Figure 5-4, Figure 5-5, Figure 5-6, and Figure 5-7, for each set of tests: PVC with grease, PVC with glue, aluminum with grease, and aluminum with glue, respectively. Appendix B shows the arrival time determination and phase information of the signals, as well as the P-wave velocity calculation for all 20 receivers.

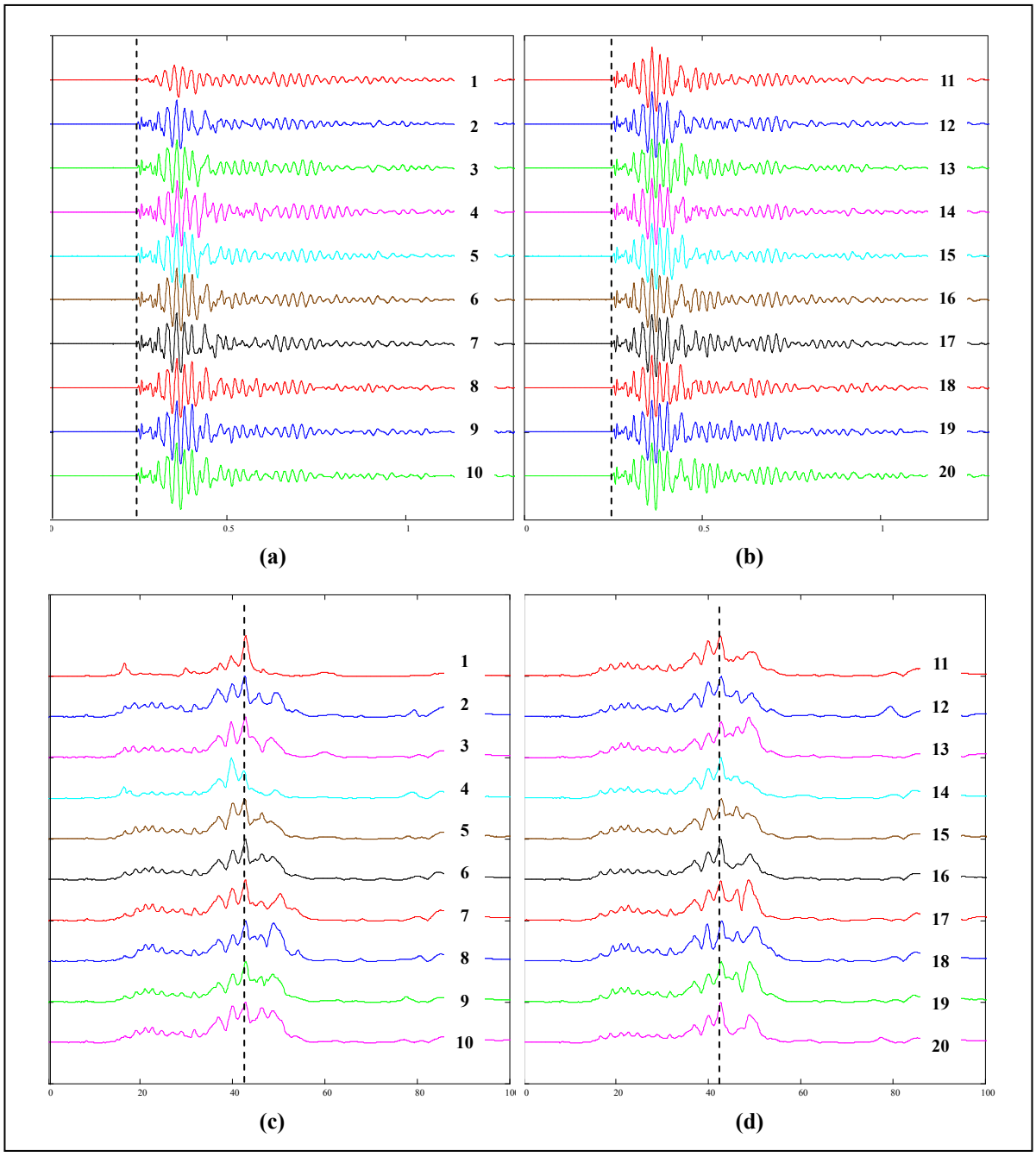

Figure 5-4. PVC bar with glue coupling: time signals for accelerometers **(a)** 1 to 10, and **(b)** 11 to 20; Fourier spectra for accelerometers **(c)** 1 to 10, and **(d)** 11 to 20.

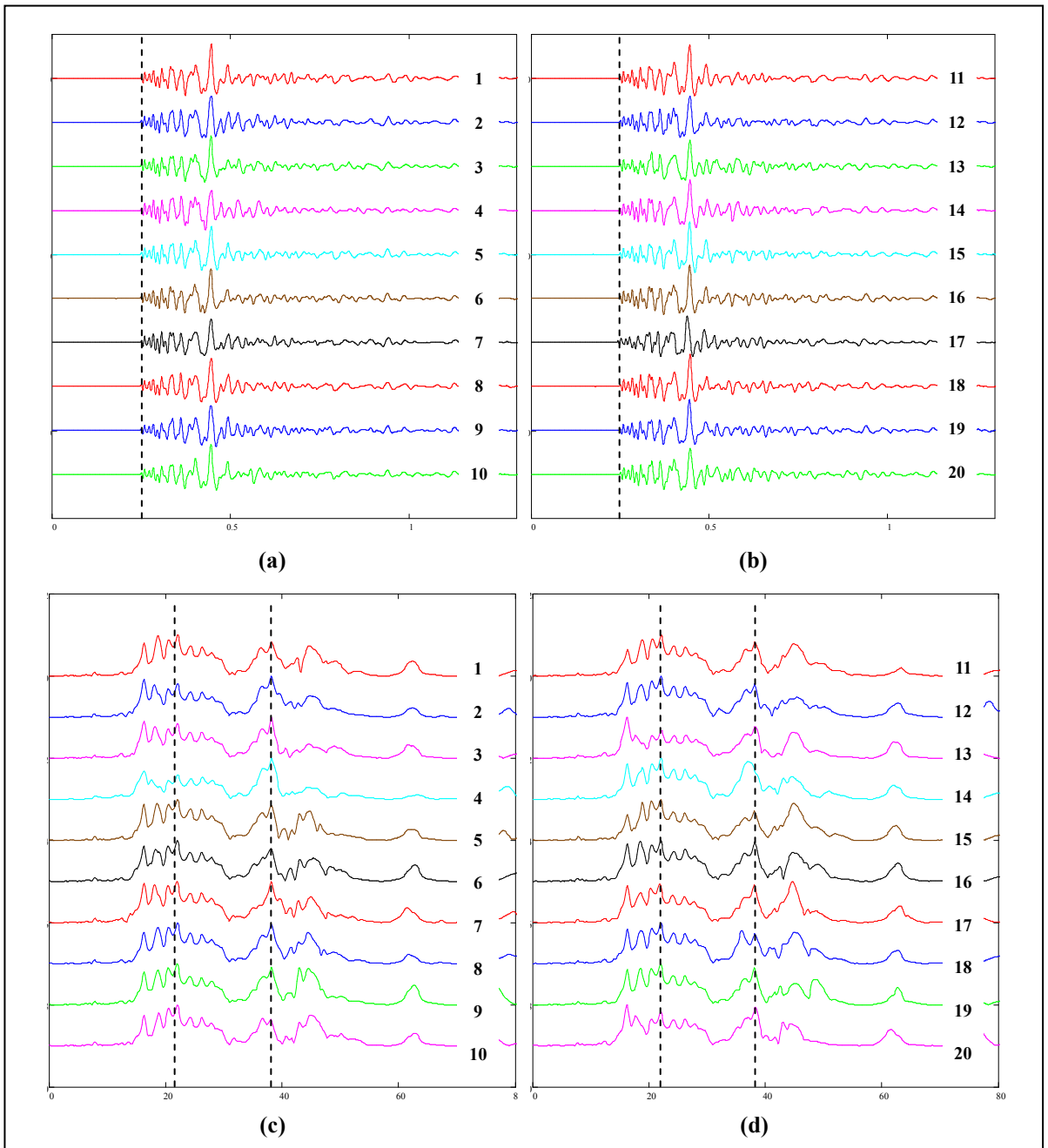

Figure 5-5. PVC bar with glue coupling: time signals for accelerometers **(a)** 1 to 10, and **(b)** 11 to 20; Fourier spectra for accelerometers **(c)** 1 to 10, and **(d)** 11 to 20.

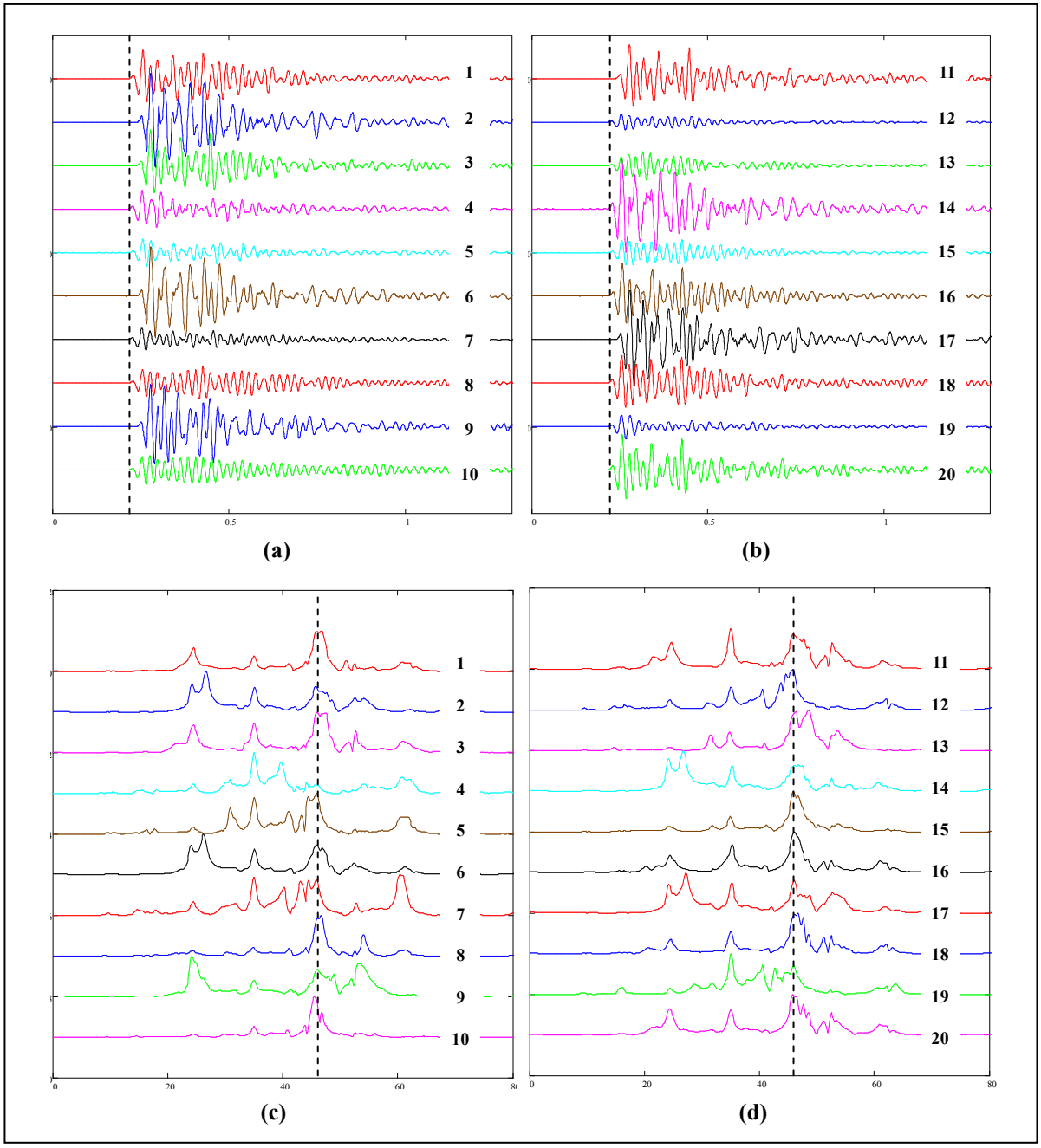

Figure 5-6. Aluminum bar with grease coupling: time signals for accelerometers **(a)** 1 to 10, and **(b)** 11 to 20; Fourier spectra for accelerometers **(c)** 1 to 10, and **(d)** 11 to 20.

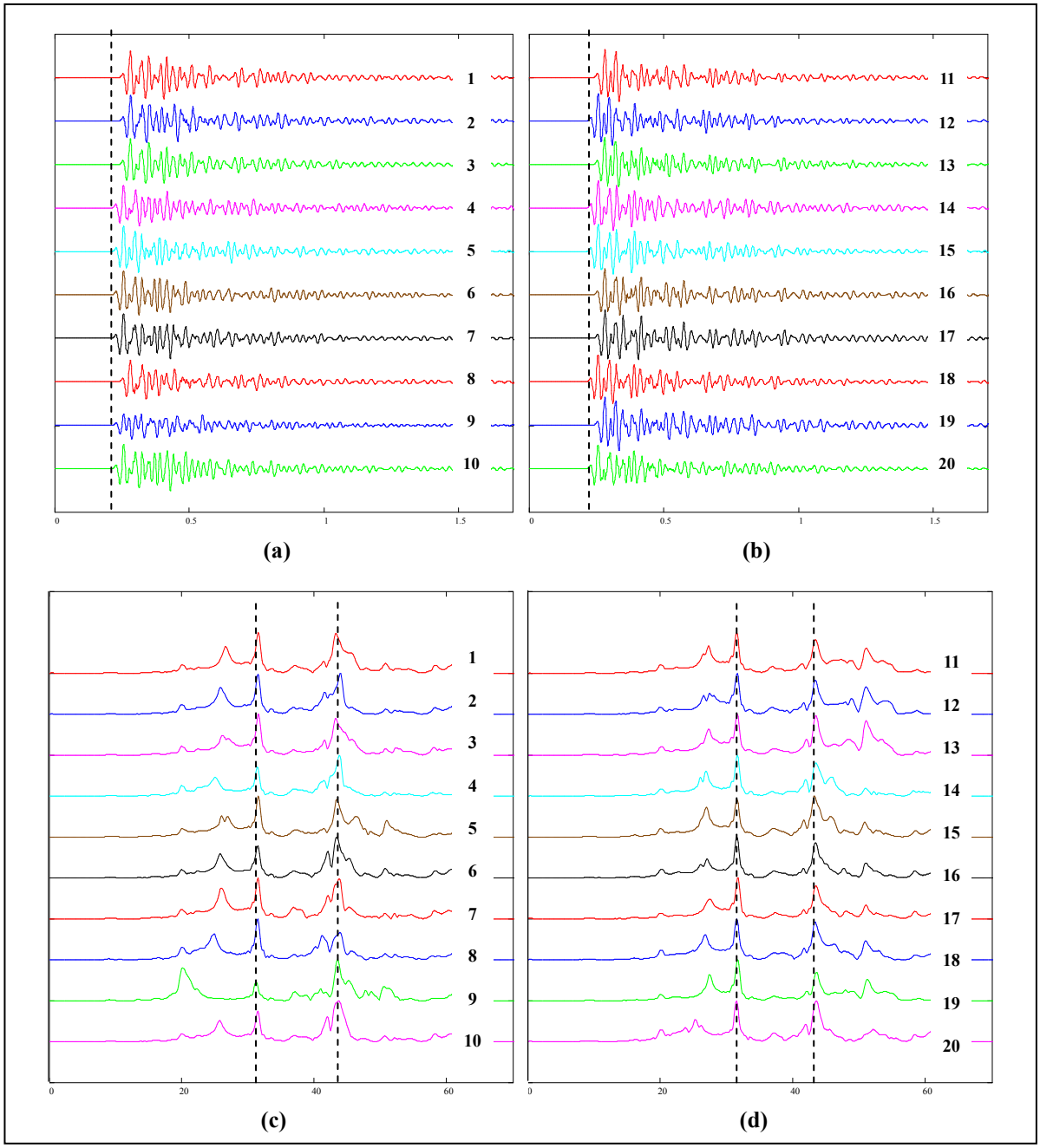

Figure 5-7. Aluminum bar with glue coupling: time signals for accelerometers **(a)** 1 to 10, and **(b)** 11 to 20; Fourier spectra for accelerometers **(c)** 1 to 10, and **(d)** 11 to 20.

The average peak-to-peak amplitude values for each of the four sets of tests are summarized in Table 5-1. The PTP amplitudes obtained from the aluminum specimen, independently of the couplant, are higher than the amplitudes from the PVC specimen, indicating that the aluminum specimen has less damping than the PVC, as expected (Khan et al., 2011).

Table 5-1. Average peak-to-peak amplitude

	PTP Amplitude (V)			
	PVC + grease	**PVC + glue**	**Al + grease**	**Al + glue**
Average	7.1	5.1	17.7	8.0
% Change	28.1%		54.6%	
Std. dev.	0.5	0.2	3.0	0.7
COV	7.1%	4.8%	16.7%	9.0%

The type of couplant also affects the energy transmission. Due to the presence of air gaps and the subsequent decrease in energy, the glue couplant is less effective than the vacuum grease.

The first arrival of each measurement was determined manually using the time signals. Since compression waves propagate faster than any other wave mode, they arrive first; the P-wave velocity is determined by using Equation (4-2). Table 5-2 shows the average P-wave velocity for all four test sets.

Table 5-2. Average P-wave velocity

	V_p (m/s)			
	PVC + grease	**PVC + glue**	**Al + grease**	**Al + glue**
Average	2171.6	2154.9	4902.3	5057.8
% Change	0.8%		3.2%	
Std. dev.	15.4	10.1	224.7	110.6
COV	0.7%	0.5%	4.6%	2.2%

The wave velocity gives information about the material elastic modulus (Section 2). P-wave velocity is proportional to the square root of constraint modulus and inversely proportional to the square root material density, as indicated in Equation (2-8). The PVC specimen has a density of approximately half that of the aluminum specimen; the results indicate that the V_P of the aluminum medium is more than twice that of the PVC. Equation (2-8) predicts that the

constraint modulus of the aluminum is approximately 11 times larger than that of the PVC. As expected, the results indicate that the PVC material has lower stiffness (Young's modulus) than the aluminum. The typical Young's modulus for aluminum is 69 GPa and for PVC is 3.4 GPa. The modulus values given by equations (2-9) and (2-11) (61.8 GPa and 2.8 GPa for aluminum and PVC, respectively) agree well with the literature.

Using the Fourier transform, the time signals are converted into frequency domain. The main frequencies of the Fourier spectra are in the same range as the transducer's main frequencies: 25.4 kHz, 36.6 kHz and 49.8 kHz (Table 5-3). The accelerometers have a nominal resonant frequency of 35 kHz, which is close to one of the transducer's main frequencies.

Table 5-3. Average main frequencies

	Main frequencies (kHz)							
	PVC + grease		**PVC + glue**		**Al + grease**		**Al +glue**	
Average	22.6	42.6	22.0	38.2	34.7	46.7	31.5	43.5
Std. dev.	0.6	0.1	2.5	2.3	4.9	4.8	2.6	0.2
COV	2.7%	0.2%	12.0%	6.0%	16.1%	10.3%	8.2%	0.5%

Figure 5-8 and Figure 5-9 show the average normalized Fourier spectra and the standard deviation for each sample frequency. This calculation involved windowing and zero-padding of the time signals to improve the resolution in frequency. The PVC specimen spectra show two main peak frequencies at 22 kHz and 40 kHz; in contrast, the aluminum specimen contains peak frequencies at 33 kHz and 45 kHz. In all four sets of measurements, a third peak is present at 50 kHz that matches the resonant frequency of the transducer. The nominal resonance frequency of the accelerometers is 35 kHz, and as a result, there is a significant amplification of the response in the vicinity of this frequency.

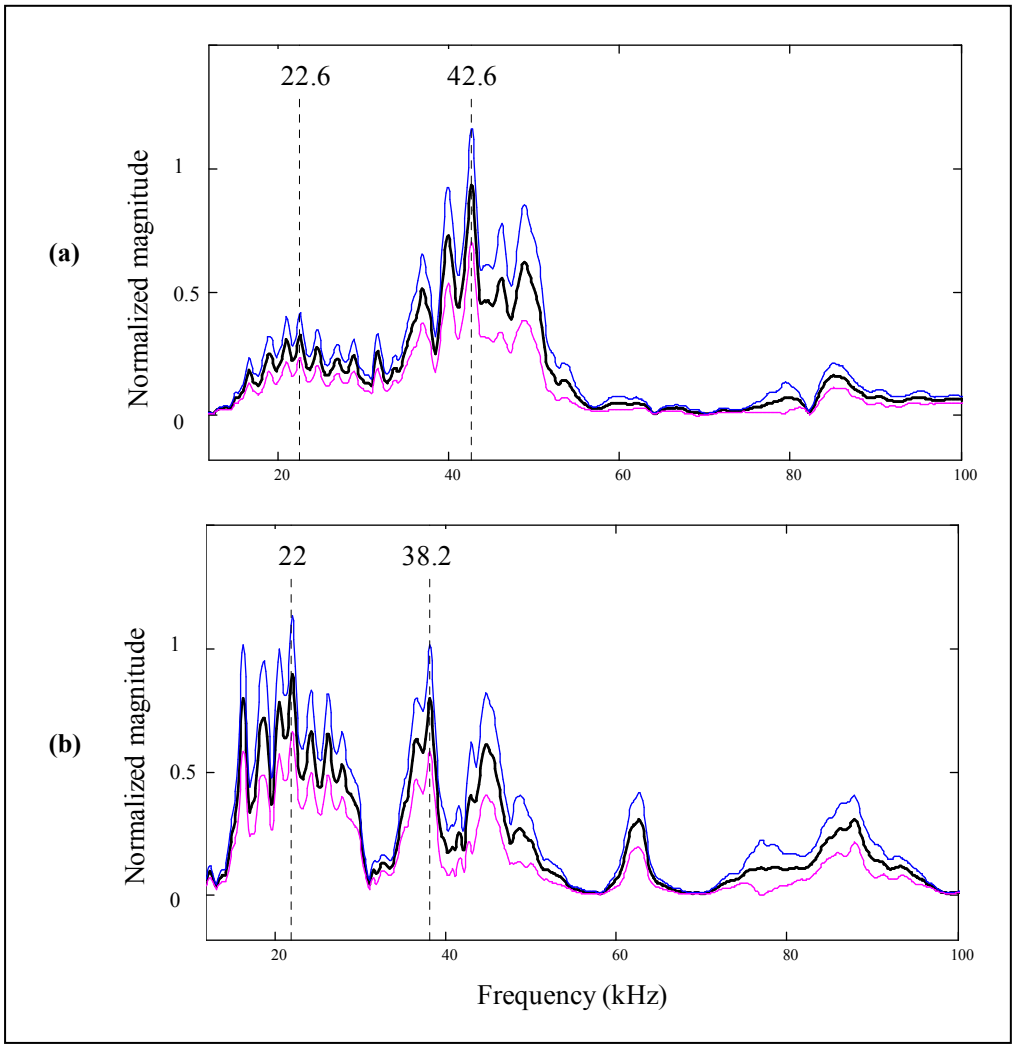

Figure 5-8. Average normalized Fourier spectra ± one standard deviation for: **(a)** PVC + grease, **(b)** PVC + glue.

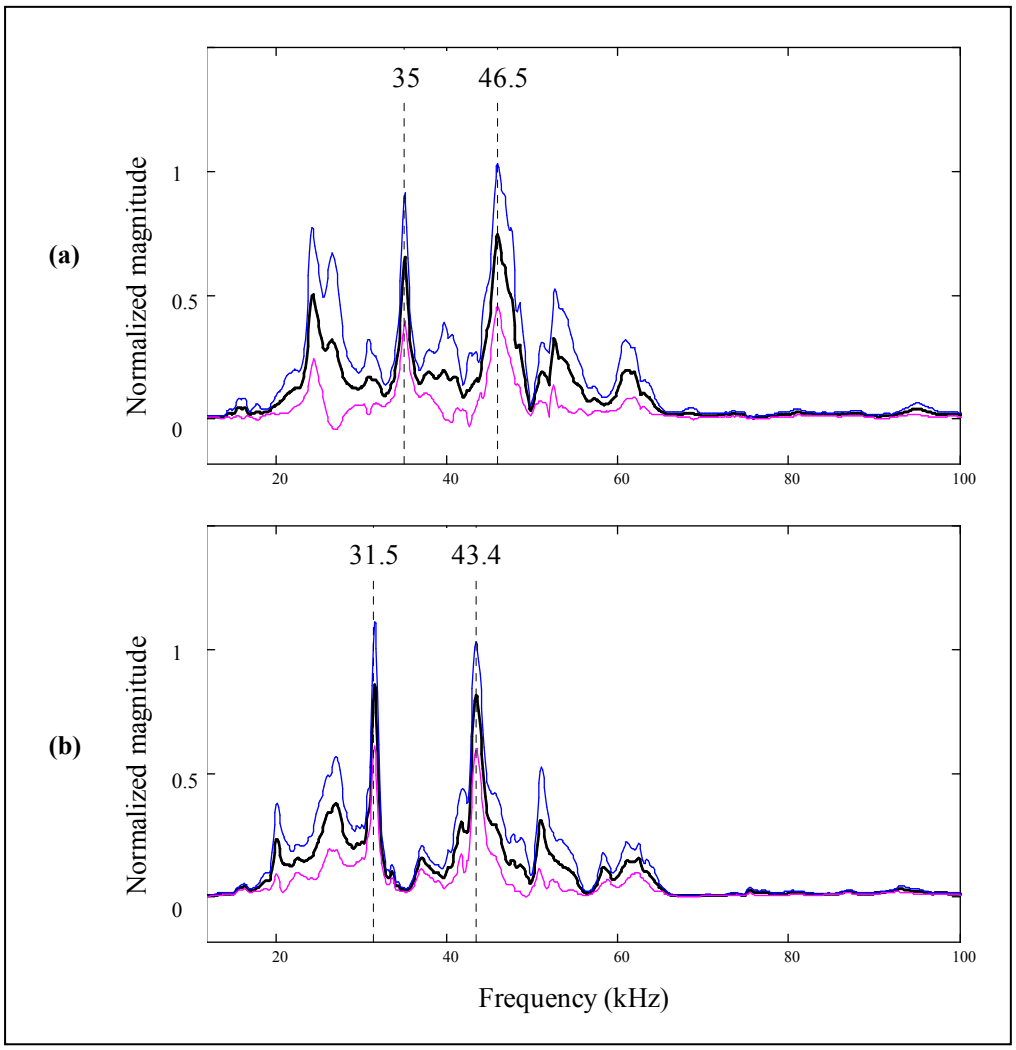

Figure 5-9. Average normalized Fourier spectra ± one standard deviation for: **(a)** Al + grease, **(b)** Al + glue.

The peak-to-peak amplitude (PTP) and the spectral area (SA) can be used as parameters to quantify attenuation in time and frequency domains. The spectral areas were calculated for each accelerometer response. The average values are presented in Table 5-4.

Table 5-4. Average spectral area

	Spectral Area			
	PVC + grease	**PVC + glue**	**Al + grease**	**Al + glue**
Average	3.6	2.7	8.9	4.1
% Change	25.1%		54.2%	
Std. dev.	0.3	0.1	1.6	0.3
COV	7.2%	2.9%	17.5%	7.7%

Table 5-4 shows that the spectral area values using the aluminum specimen are higher than those using the PVC specimen (by 96.6% in average). The aluminum specimen provided less attenuation than the PVC specimen; therefore, the energy carried by the waves is better preserved. The SA results presented in Table 5-4 are consistent with the PTP results from Table 5-1: the vacuum grease couplant is more effective than the glue. In general, it allowed the coupled surface of the specimen to deform freely, whereas the glue provided a rigid constraint to the surface.

For the attenuation analysis, it is important to determine the dispersive nature of the medium. The cylindrical shape of the samples allows Lamb waves to be generated when the surface waves interact with the boundaries. At high frequencies, the medium thickness is large in relation to the wavelength (Section 2.2.3); therefore, Rayleigh waves propagated freely at the surface and the specimen behaved as a half-space medium.

Dispersion curves (phase velocity vs. frequency) provide information about the phase velocity as a function of the frequency. At high frequencies, the phase velocity tends towards the R-wave velocity, because the generated wavelengths were small enough such that no interaction with the other boundary occurred. If this frequency is known, then the corresponding wavelength can be computed with the R-wave velocity. The effective thickness of the medium can be determined from this wavelength.

The dispersion curves for PVC and aluminum cylinders were calculated by evaluating the complex roots of Equation (5-2). Poisson's ratio of 0.23 and 0.41 were assumed for aluminum and PVC, respectively. The P-wave velocity was measured and presented in Table 5-2; the S-wave and Rayleigh wave velocities were calculated using Equations (2-14) and (2-16). The dispersion curves for both specimens are presented in Figure 5-1. For higher

frequencies, the phase velocity tends towards the R-wave velocity. The cut-off frequencies were determined to be 50 kHz for the PVC specimen and 150 kHz for the aluminum specimen.

Wavelengths are related to frequency by Equation (2-1). Thus, the curve of frequency vs. wavelength can be computed from the dispersion curve (Figure 5-10). For a thickness equal to one wavelength (51.3 mm for PVC specimen and 50.2 mm for aluminum specimen), the corresponding frequencies are 19 kHz and 65 kHz, respectively.

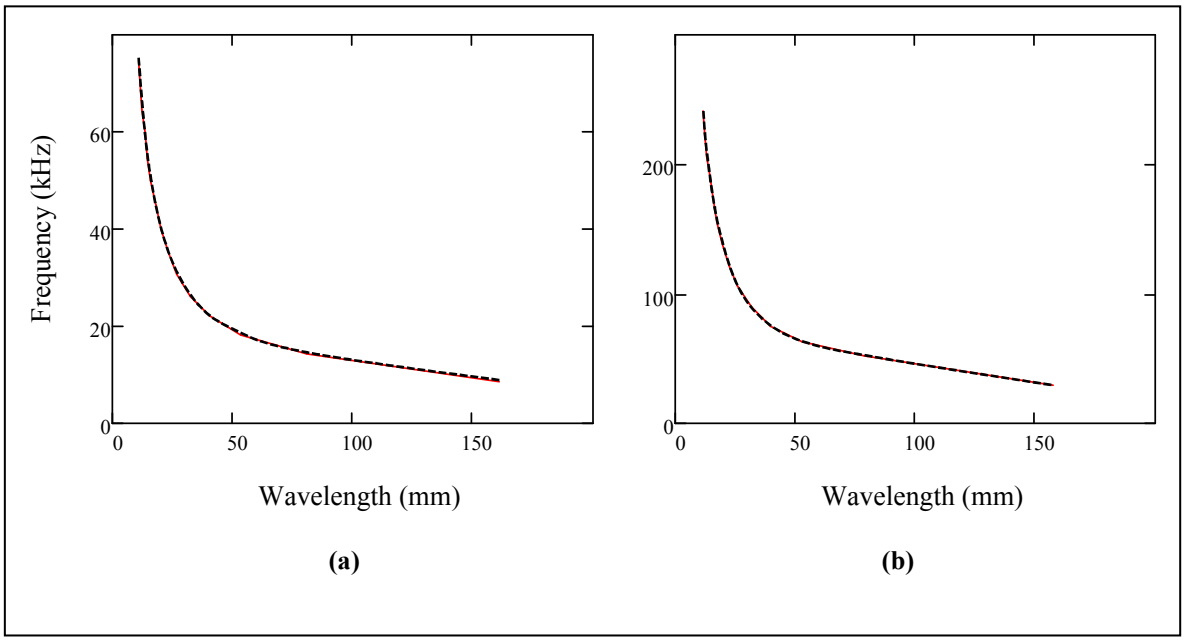

Figure 5-10. Frequency vs. wavelength for: **(a)** PVC and **(b)** aluminum specimens

The theoretical wavelengths corresponding to the cut-off frequencies of 50 kHz and 150 kHz are 16.1 mm and 18.3 mm, respectively for PVC and aluminum specimens (Figure 5-1). These wavelengths are smaller than the actual diameter of the specimens. However, most of the energy was concentrated between the surface and one-third of the wavelength, which corresponded to 17.1 mm for the PVC and 16.78 mm for the aluminum cylinder. For the PVC specimen, roughly 6% of difference is noted; in contrast, for the aluminum specimen, a 9% difference exists. These variations may be attributed to the assumed values for Poisson's ratio and R-wave velocities. Furthermore, the frequency equations were derived for computing the dispersion curves for infinite cylinders, and may not be entirely valid for the

cases studied herein. Short cylindrical solids may experience wave phenomena such as reflection and high modes that can affect the outcome of the test.

The arrival time of the surface waves may be obtained directly from the time signals. However, this task is difficult, because due to wave reflections, the R-wave arrival is usually not clear. The R-wave arrival can be enhanced by computing the particle displacement in the time domain using the original acceleration signal. The displacement is obtained by completing the double integration of the acceleration in time. Rayleigh waves have larger amplitudes and lower frequencies than P-waves. Displacements are most affected by lower frequencies; thus, the R-wave arrival can be obtained by measuring the arrival in the displacement plot.

A transfer function, Equation (5-1), can be computed to characterize the couplants: grease and glue (Figure 5-11). The transfer functions were determined for both specimens. The aluminum medium shows a lower material attenuation than the PVC; therefore, the amplitudes of the transfer function of the aluminum are expected to be larger than the PVC. Moreover, these transfer functions present various frequency peaks ranging from 25 kHz to 50 kHz, which corresponds to the main frequency of the transmitter.

The ratio between the transfer functions of PVC + grease and PVC + glue allows canceling of the transfer functions corresponding to the medium, the transmitter and the receiver. Similarly, a transfer function ratio can be computed for the aluminum specimen, as shown in Equation (5-3). The average transfer function ratio between grease and glue couplants is plotted in Figure 5-12.

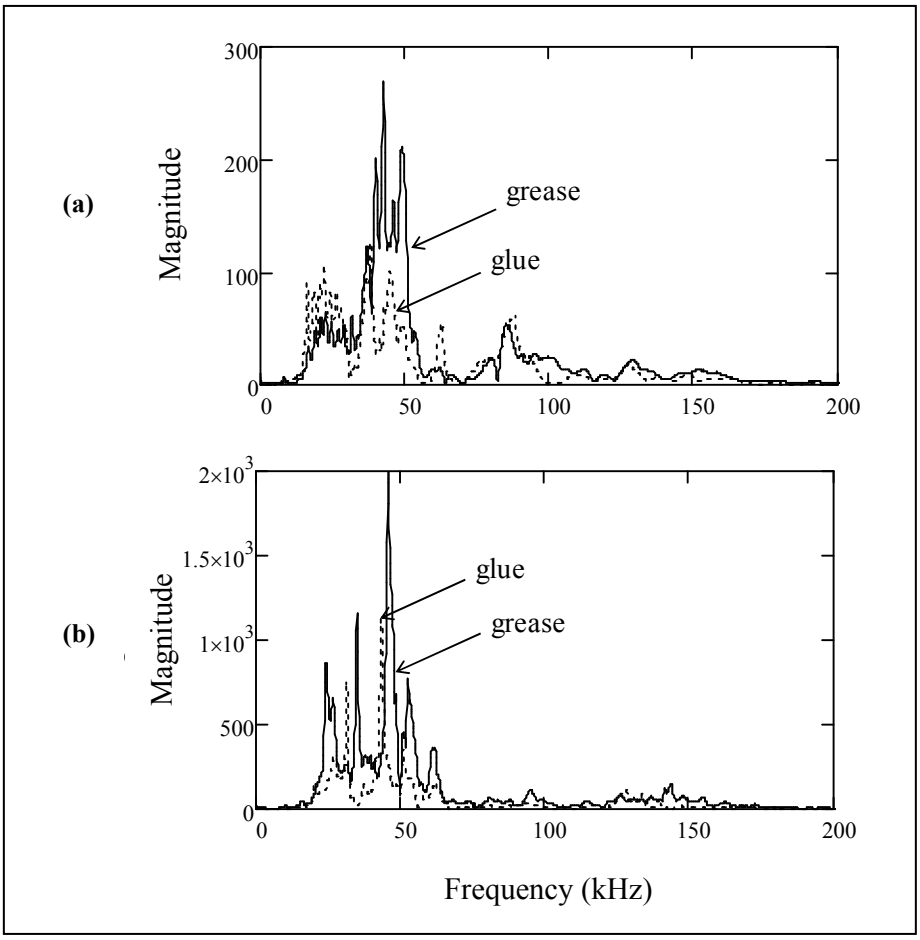

Figure 5-11. Mean transfer function for grease and glue couplants: **(a)** PVC and **(b)** aluminim specimens.

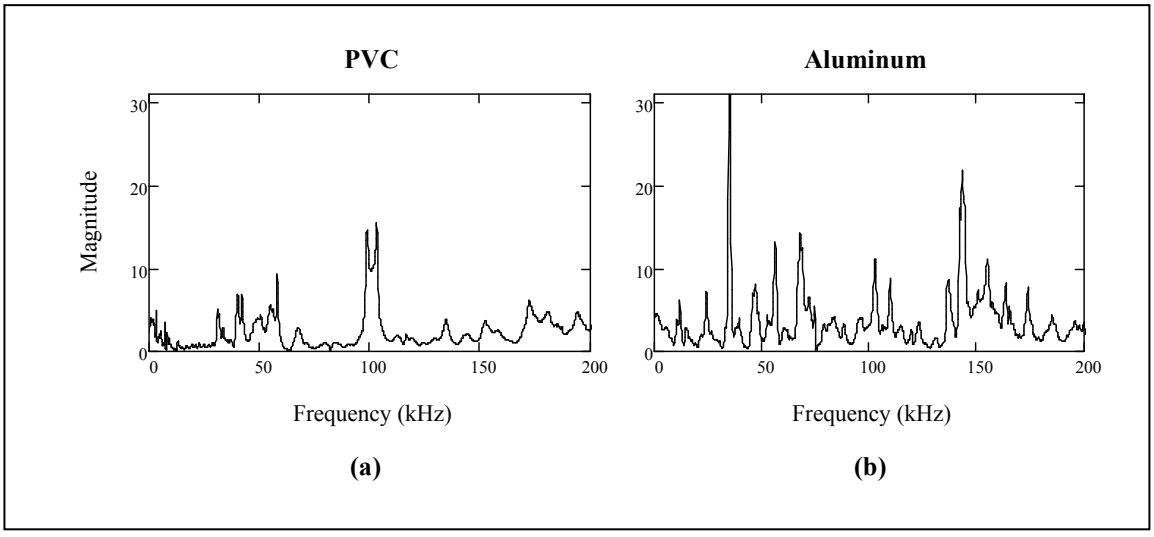

Figure 5-12. Mean grease/glue transfer function ratio: **(a)** PVC and **(b)** aluminum specimens.

The ratio between the transfer functions of the grease and the glue couplant for both specimens should in theory be identical. However, Figure 5-12 shows that the grease and glue transfer function ratio for PVC is not the same as the computed ratio for the aluminum specimen. In the case of PVC, main frequency peaks are at 40 kHz, 60 kHz and 100 kHz. Conversely, the transfer function ratio computed for the aluminum specimen presents an uneven behavior consisting of several frequency peaks.

The results of the calibration procedure showed that a proper selection of receivers (accelerometers) and coupling agents should be made for a given experimental measurement. This relative characterization of receivers is important in the signal processing stages to remove any undesirable effects induced by manufacturer and coupling differences between accelerometers.

5.5 Chapter Summary

This chapter presents the results of a ultrasonic pulse velocity (UPV) calibration performed on two specimens: PVC and aluminum cylinders. Two coupling agents were considered: silicone-high vacuum grease and cyanoacrylate glue. The UPV tests were executed in four sets combining calibration bars and the coupling system: (1) PVC bar with vacuum grease, (2) PVC bar with glue, (3) aluminum bar with vacuum grease, and (4) aluminum bar with glue. Twenty accelerometers were used in each set of tests, and the amount of coupling agent and pressure load was constant.

The results showed that the glue couplant is less effective than vacuum grease; the presence of air gaps present in the glue resulted in a decrease in energy. The PTP amplitudes obtained from the aluminum specimen, independent from the couplant agent, were higher (by 104% in average) than the amplitudes from the PVC specimen, indicating, as expected, that the aluminum specimen has less damping (attenuation) than the PVC. Results also indicate that the spectral area values for the aluminum specimen are higher than the values of the PVC (by 96.6% in average). The spectral area results were consistent with the PTP results.

Relative transfer functions were computed for each specimen relating the grease couplant with the glue. The conditions of the source, the receiver, and the medium remain constant;

thus, their transfer functions did not change. The selection of receivers and coupling agents for testing the asphalt slab and steel plate samples was based on the results of the calibration procedure presented in this chapter.

CHAPTER 6. ULTRASONIC TESTING OF ASPHALT SLAB FOR CONDITION ASSESSMENT OF JOINTS (STUDY 1)

6.1 Introduction

An innovative nondestructive test for condition assessment of longitudinal joints in asphalt pavements was developed at the University of Waterloo in collaboration with the Ministry of Transportation, Ontario (Jiang, 2007). Novel experimental and signal processing techniques (WTC) were used to minimize the variability associated with unknown limitations of different factors such as properties of transducers, wave propagation paths, and the effects of source/receiver coupling. One limitation of this technique is that it requires user input, because the peak values from the wavelet transform are selected manually, making the automatic processing difficult. Another limitation of the WTC technique is that the transducers are epoxied to the asphalt surface using aluminum plates. This procedure is not practical for in-service roads.

This study presents an improved coupling system and a new data processing technique to reduce user input and improve the reliability of the system. The effects of different coupling mechanisms on a fabricated pavement slab with a construction joint are studied. The experimental coupling configurations considered are: aluminum plate, using vacuum grease or glue as couplant, applying vertical pressure, and using cylindrical foam wrap as an isolator.

A new robust experimental and analytical methodology called instantaneous transmission coefficient (ITC) is proposed. It is based on the calculation of instantaneous frequencies and damping ratios using the Hilbert transform. A density controlled asphalt slab was used to evaluate the results from the new methodology and from the previous FTC and WTC methods. As opposed to the WTC technique, user input for the ITC is minimal; hence, the procedure can be performed automatically. The presence of a joint induces larger attenuation effects that increase the damping coefficient of the medium.

Exploratory ground penetrating radar (GPR) measurements were also used to evaluate its potential as a complementary method to wave-based tests.

6.2 Evaluation of Coupling Effects

The coupling between the transducers and the specimen is critical in ultrasonic testing. This section presents a study of the effects of different coupling mechanisms on a fabricated pavement slab with a construction joint. The experimental coupling mechanisms considered are: aluminum plates, silicone-high vacuum grease, cyanoacrylate glue, applied weights, and polyurethane foam isolators. A 80 mm-square configuration is used with the objective to improve the previously proposed wavelet transmission coefficient technique.

6.2.1 Testing Methodology and Experimental Setup

A 50 kHz ultrasonic transmitter was used to generate mechanical waves into the specimen. The response Fourier spectra of the ultrasonic transmitter suggested three main frequency components at 25.4 kHz, 36.6 kHz and 49.8 kHz (Tallavo et al., 2009). Two Dytran 3055B3 accelerometers (35 kHz nominal resonant frequency and 500±10 mV/g sensitivity) were used as receivers. The excitation pulse was generated by an electric pulser. The power supply of the accelerometers (Dytran 4123B) has selectable amplification factors of 1, 10 and 100. The time signals were recorded on a 24-channel data acquisition system with a 1 MHz sampling rate (LDS Nicolet Genesis).

Six coupling configurations were used for testing the slab:

1 - Accelerometers glued on aluminum plates fixed to the asphalt surface with epoxy.
2 - Accelerometers coupled directly to the pavement with vacuum grease.
3 - Accelerometers coupled with vacuum grease on aluminum plates with a weight placed directly on top of the accelerometers.
4 - Accelerometers coupled with vacuum grease on aluminum plates with a weight placed on top of the receivers, and a foam wrap used around the receivers.

5 - Accelerometers coupled directly to the pavement with vacuum grease with a weight placed directly on top of the receivers.

6 - Accelerometers coupled directly to the pavement with vacuum grease with a weight placed on top of the receivers, and a foam wrap used around the receivers.

In configurations 3 to 6, an extra weight wass placed on top of the receiver to achieve a consistent pressure. A cylindrical foam wrap can be used, when applicable, to isolate the receivers from the weight on top. Table 6-1 summarizes the six test configurations used.

Figure 6-1 shows a schematic plan view of the different air void contents that resulted from the compaction procedure used in the construction of the slab (Du Tertre, 2010). The tests were performed on an 80 mm-square experimental configuration (Section 4.2.3.6).

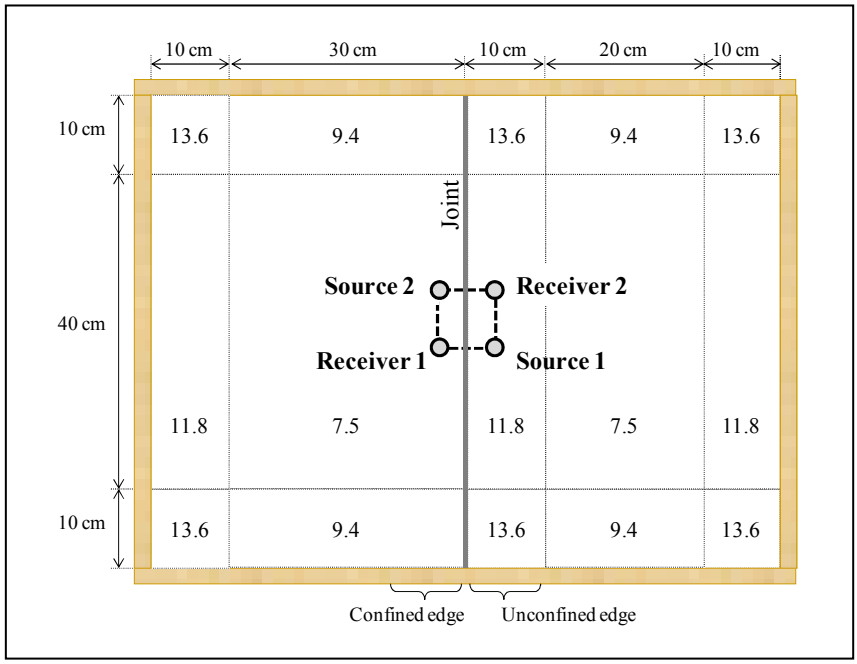

Figure 6-1. Air voids (%) in the fabricated slab with the joint, and the location of the equally-spaced test setup.

Table 6-1. Experimental setup for evaluation of coupling configurations.

Setup No.	Plate	Couplant	Foam	Weight	Figure
1	Yes	Glue	No	No	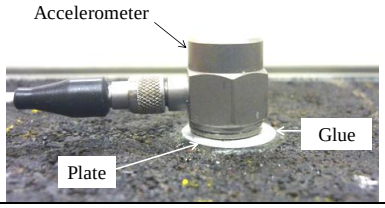
2	Yes	Grease	No	No	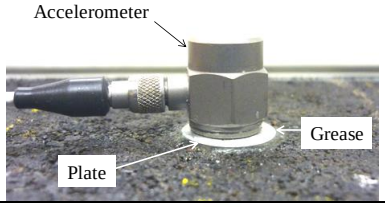
3	Yes	Grease	No	Yes	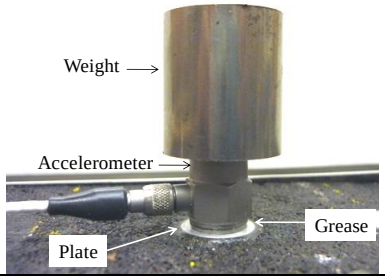
4	Yes	Grease	Yes	Yes	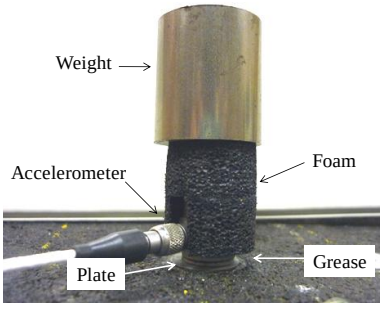
5	No	Grease	No	Yes	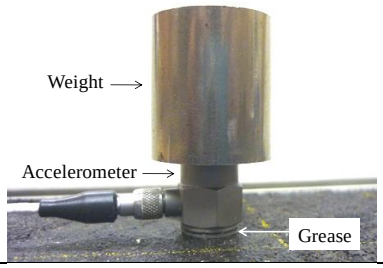
6	No	Grease	Yes	Yes	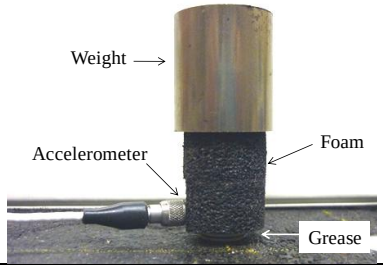

6.2.2 Results

Figure 6-2 shows a typical normalized time signal and its respective Fourier spectra, corresponding to the data collected from the configuration set 1. Removal of the DC component and zero padding were applied to the original signals to improve the frequency resolution. From the time signals, the P-wave velocity and S-wave velocity were determined to be V_P = 3200 m/s and V_R= 1633 m/s, respectively. A dominant frequency of approximately 36 kHz can be observed from the frequency spectra. Figure 6-3 to Figure 6-7 show the normalized time signals and Fourier spectra of all the configurations. An additional frequency peak at 76 kHz was observed for configurations 3 through 6. This is possibly an effect of the added weight which increases the reaction force between the transducer and the asphalt surface, and thus changes the response of the system and the fundamental modes and frequencies of vibration.

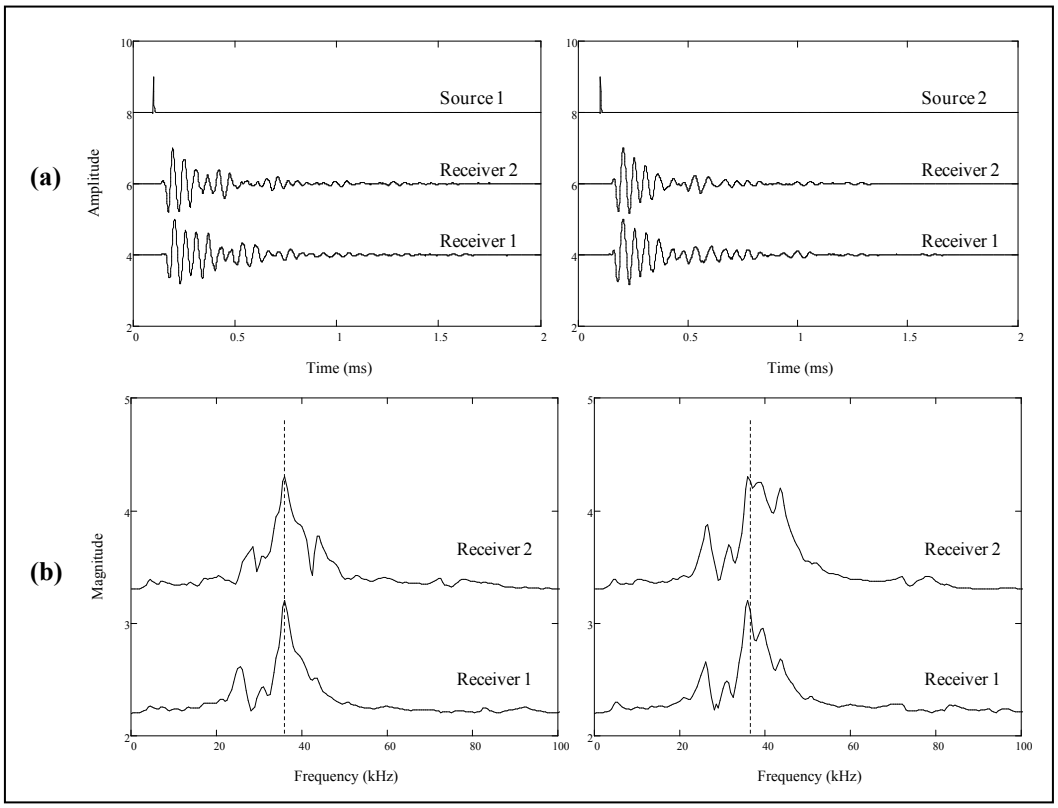

Figure 6-2. (a) Time signal and **(b)** normalized Fourier spectra for configuration 1.

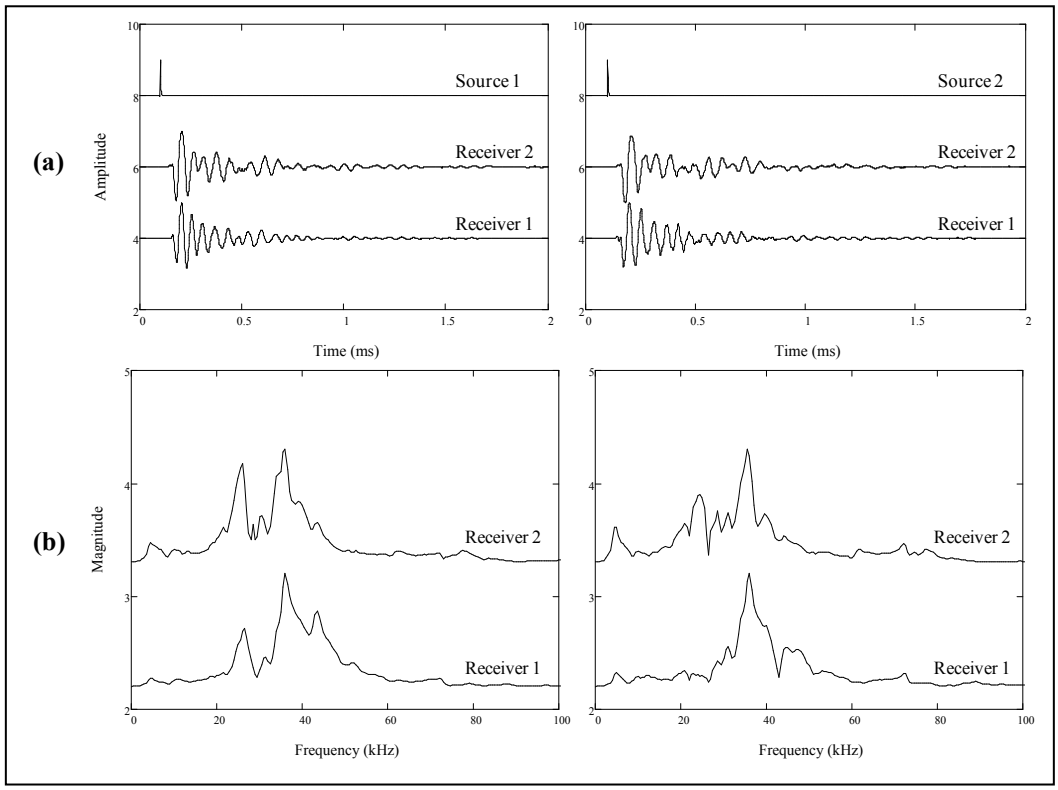

Figure 6-3. (a) Time signal and **(b)** normalized Fourier spectra for configuration 2.

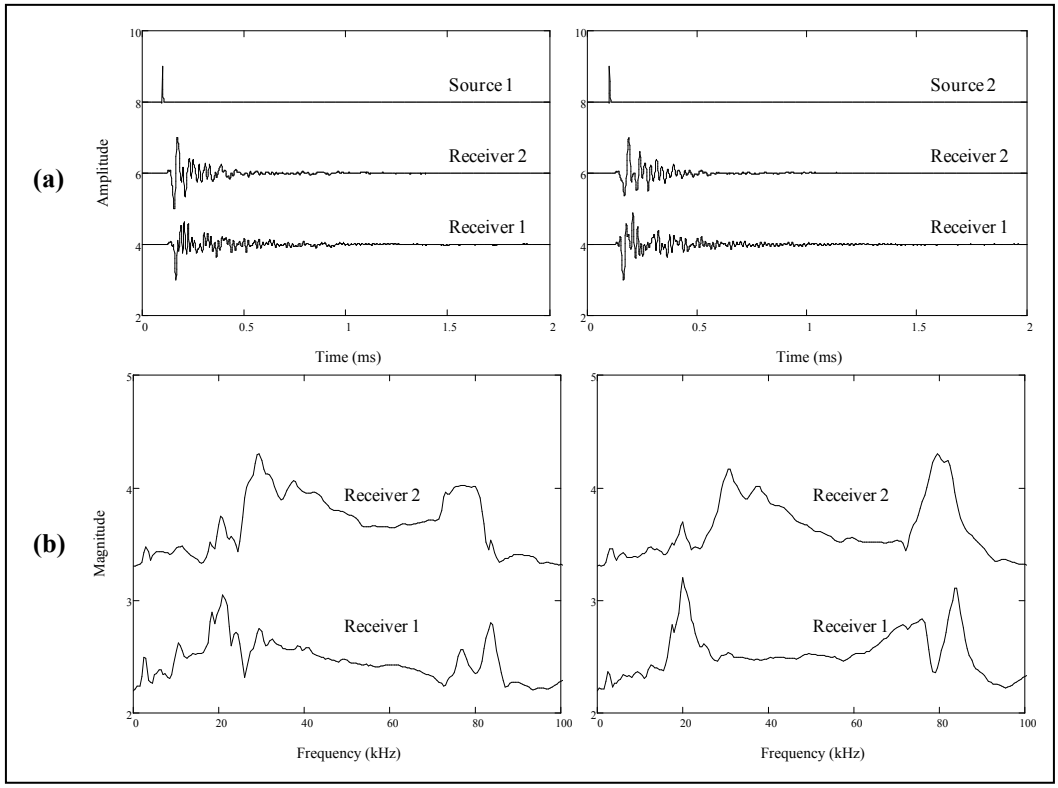

Figure 6-4. (a) Time signal and **(b)** normalized Fourier spectra for configuration 3.

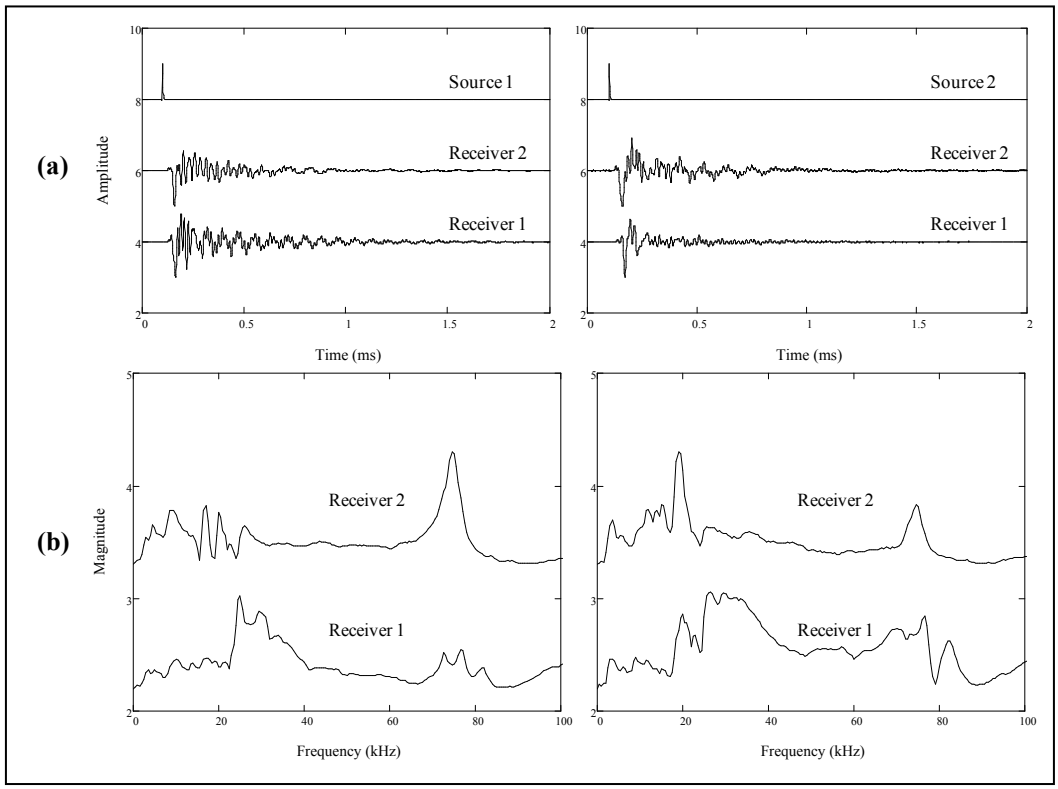

Figure 6-5. (a) Time signal and **(b)** normalized Fourier spectra for configuration 4.

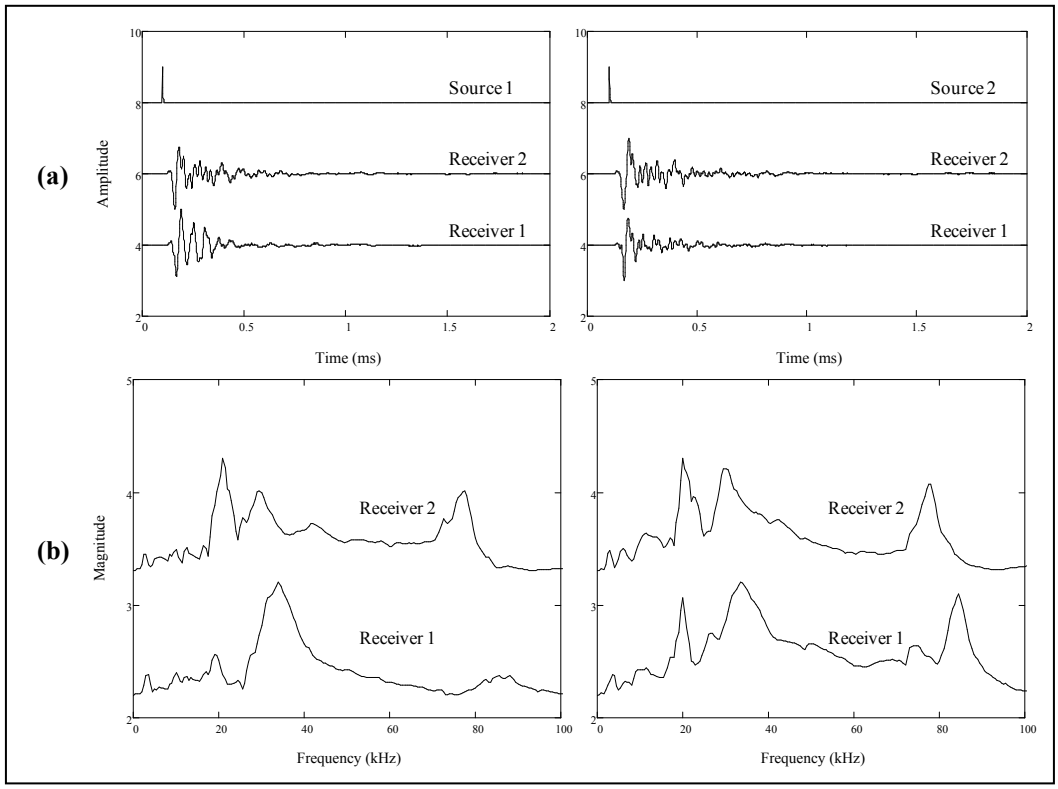

Figure 6-6. (a) Time signal and **(b)** normalized Fourier spectra for configuration 5.

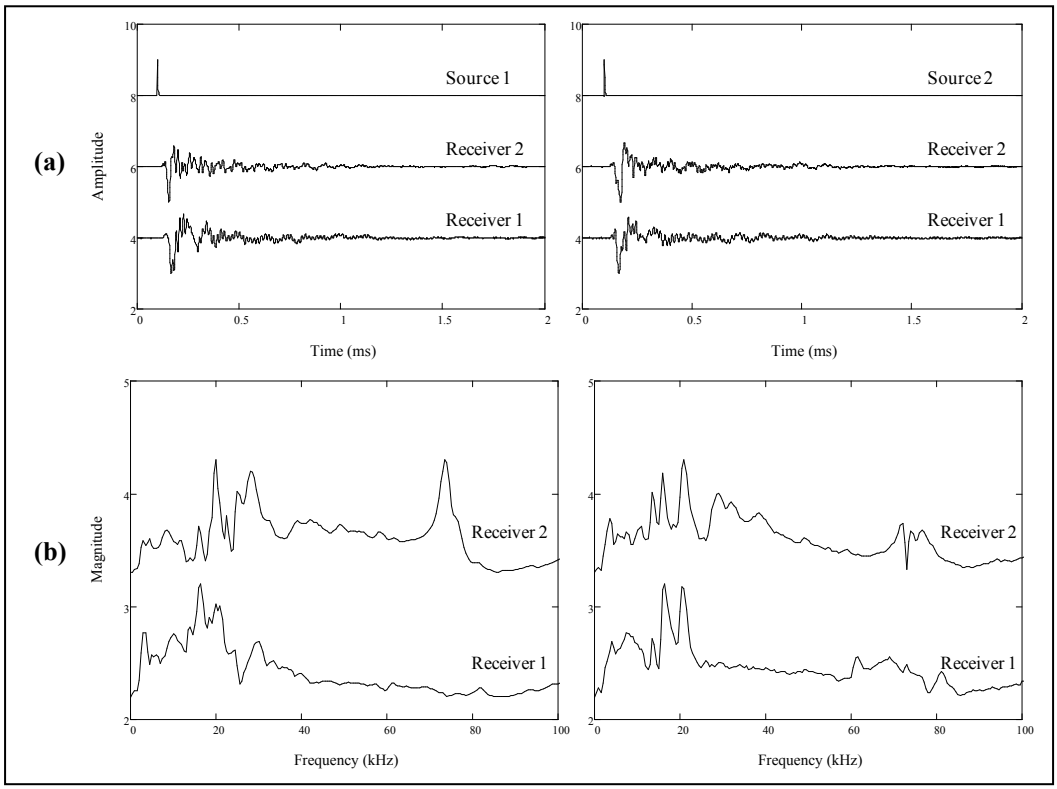

Figure 6-7. (a) Time signal and **(b)** normalized Fourier spectra for configuration 6.

Fourier transmission coefficients (FTC) were calculated for each configuration and averaged for a bandwidth of 50 kHz (ranging from 10 to 60 kHz). Figure 6-8 plots the FTC vs. frequency for the selected bandwidth of 50 kHz. The mean values of FTC are calculated and summarized in Table 6-2.

Table 6-2. FTC results for a 50 kHz bandwidth.

Test configuration	FTC
1	1.02
2	0.90
3	0.75
4	1.05
5	0.80
6	0.75

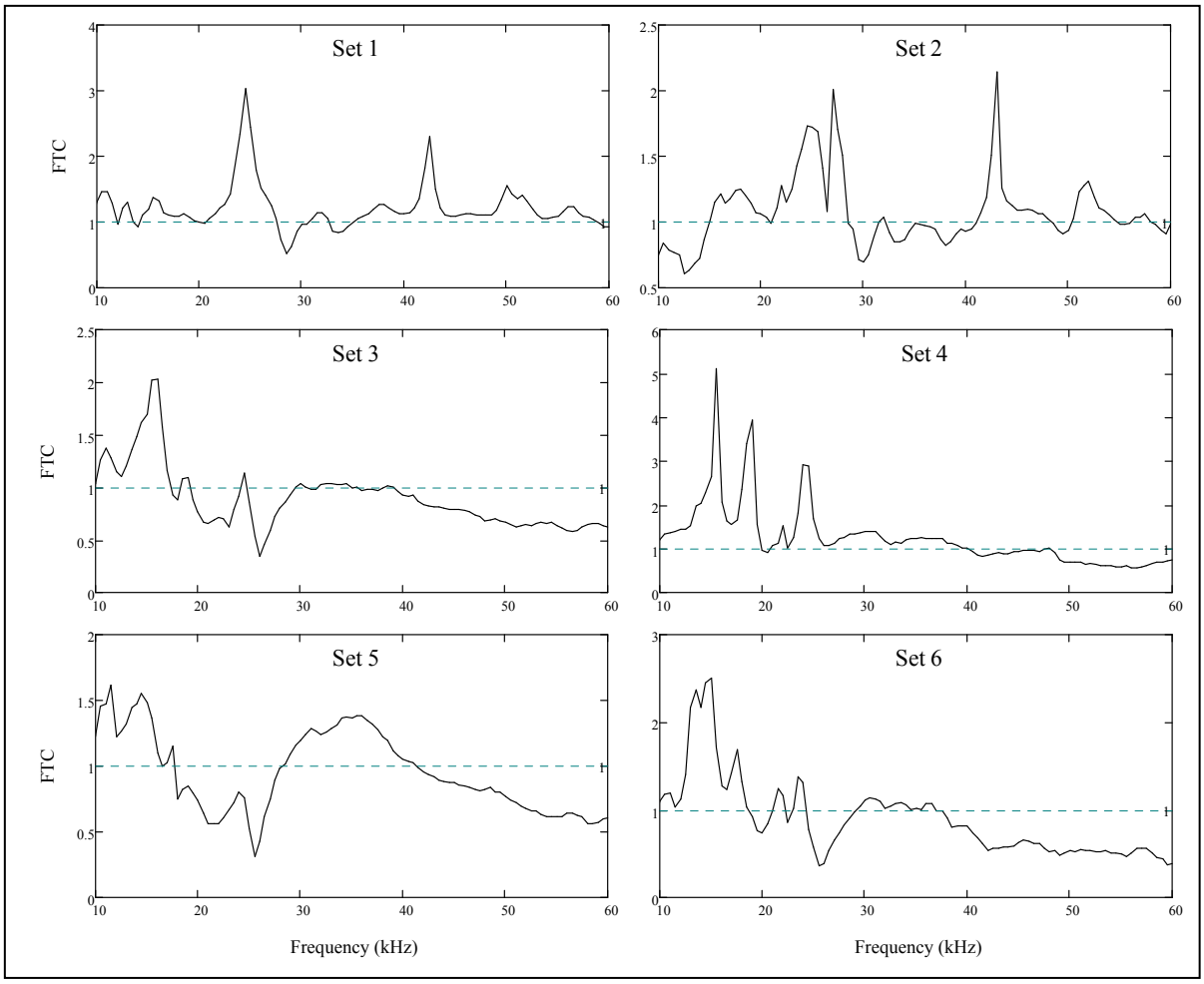

Figure 6-8. FTC vs. frequency for all configuration sets.

Wavelet transmission coefficients were also computed. The selection of the center frequency of the Morlet function has a large impact on the outcome of the WTC calculation. A logical choice corresponds to the frequency associated to the maximum spectral magnitude. However, different dominant frequencies were observed; the ultrasonic source showed a resonant frequency around 50 kHz whereas the signals recorded with the accelerometers presented a significant amount of energy at around 36 kHz. Therefore, the WTC was calculated for a range of center frequencies: from 10 kHz to 60 kHz by increments of 5 kHz.

Figure 6-9 shows the results of WTC with respect to frequency for all six configurations. The Morlet functions were defined for different center frequencies, and the wavelet transforms for each frequency and test configuration are presented in Appendix C. The condition of the joint using different coupling configurations was compared.

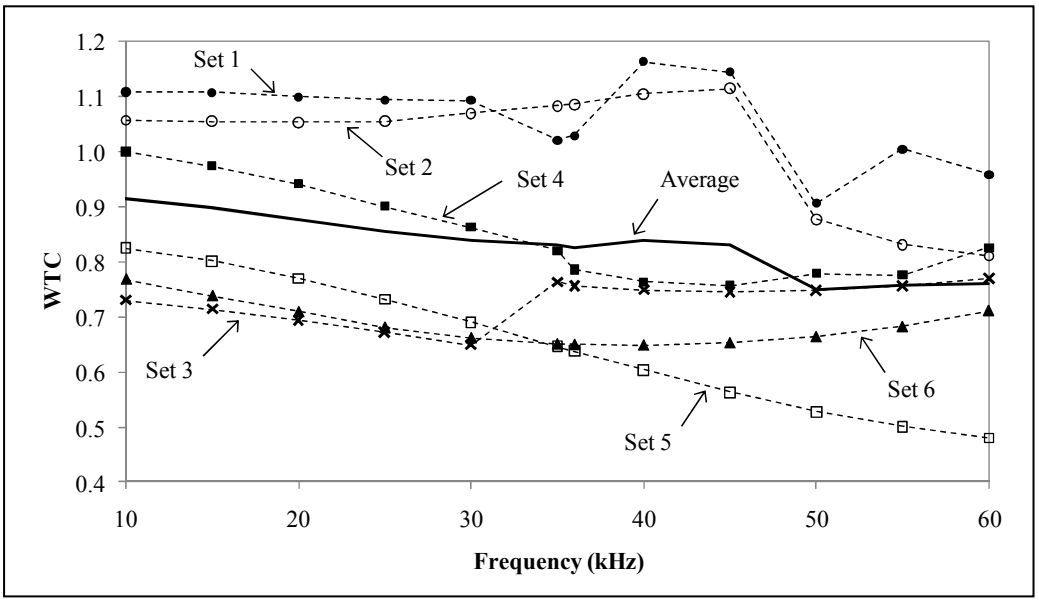

Figure 6-9. WTC measurements for a frequency range of 10 to 60 kHz, for all configuration sets. With standard deviation of 0.18.

Figure 6-9 indicates that the WTC for configuration sets 1 and 2 are very similar for frequencies up to 50 kHz. Both sets included the aluminum plate in their setup configuration, but did include the weight or the foam isolator; glue is used in configuration set 1 whereas vacuum grease is used in set 2. These two configurations did not include the application of a vertical pressure. In both situations, the WTC calculations yielded results above one for most of the frequencies, indicating little to no attenuation due to the joint. The average WTC were 1.06 and 1.02, for configuration set 1 and 2, respectively.

Sets 2 and 3 included similar configurations. Both were coupled with vacuum grease to an aluminum plate; however, a weight was used in configuration set 3. The results are significantly different; measurements from set 3 showed attenuation across the joint whereas set 2 did not. The average WTC for set 3 were computed to be 0.73.

Configuration sets 3 and 4 differed only in the use of the foam isolator. Both were coupled to an aluminum plate with vacuum grease and a consistent vertical pressure was applied on both cases; however, set 3 did not include the foam isolator. Set 4 provided higher WTC values for low frequencies, but decreased with increasing frequency, and converged to the results from set 3 at around 36 kHz (Figure 6-9). The foam behaved as an isolator between the accelerometer and the applied weight, allowing the accelerometer to vibrate freely. The effect

of the foam was more noticeable in the lower frequencies, up to a dominant frequency of 36 kHz. Configuration set 3 showed more attenuation at low frequencies than set 4, indicating the possible effect of the foam isolator. The average WTC for set 4 was computed as 0.85.

Measurements in configuration sets 5 and 6 were performed by coupling the accelerometers directly on the asphalt surface with vacuum grease (without the aluminum plate). The setup configuration included the applied weight; measurements in set 5 were performed without the foam isolator whereas set 6 included the isolator. Figure 6-9 shows that the WTC from set 5 decreased with increasing frequency; nevertheless, at 35 kHz, set 5 provided the same WTC result as set 6. This same effect was observed for both configuration sets 3 and 4, where the only coupling difference is the foam. The average WTC for configuration sets 5 and 6 were 0.65 and 0.68, respectively.

In general, while the use of an aluminum plate ensured a good quality coupling, using grease directly on the asphalt surface gave also consistent results.

Furthermore, a comparison between the calculated FTC and the average WTC was carried out. Figure 6-10 shows the FTC and WTC values obtained for each configuration set. The FTC was particularly high in set 4. Comparing with set 3, where the isolator was the only coupling difference, the FTC values showed the effects of the foam.

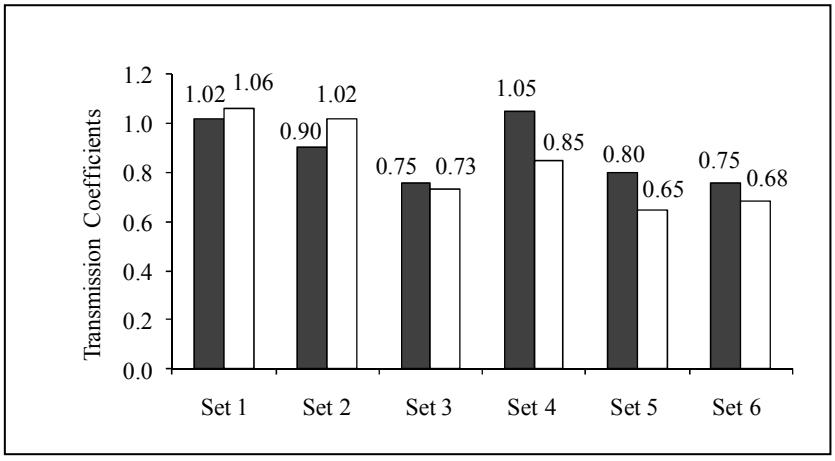

Figure 6-10. Mean FTC (solid fill) and WTC (no fill) results for all test sets. With std. dev. between 0.04 and 0.12.

WTC values at the dominant frequency were also computed for all configuration sets (Figure 6-11). In general, a slight difference between the WTC at the dominant frequency and the

mean WTC can be observed in all sets. The average value appears to be lower than at dominant frequency, with the exception of configuration set 2. This means that the WTC at the dominant frequency is not a consistent representation of the frequency range, since the resonant frequency of the accelerometers may have affected the results. Therefore, the WTC should be computed for a range of frequencies to achieve a good representation of the joint.

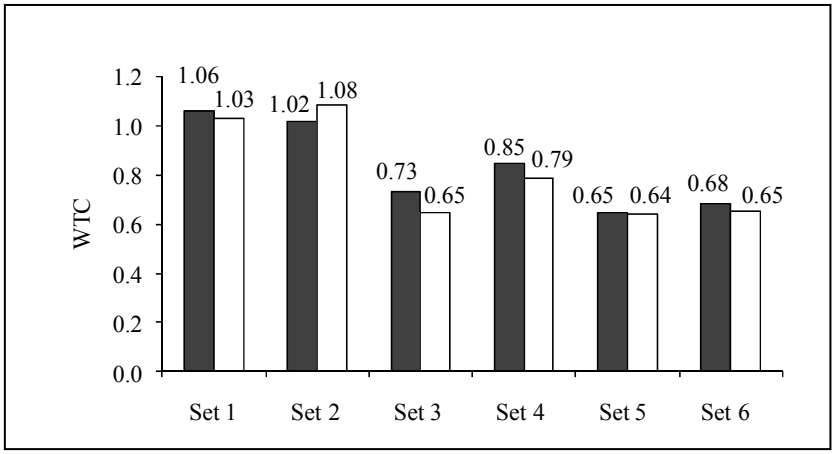

Figure 6-11. Mean WTC (solid fill) and WTC at dominant frequency (no fill) results for all test sets.
With std. dev. between 0.04 and 0.12.

6.2.3 Concluding Remarks

- Measurements performed with no applied vertical pressure were unable to detect any effects of attenuation at the joint. In contrast, the measurements including the weight indicated higher attenuation effects up to 30% across the joint.
- At the nominal resonant frequency of the accelerometer (35 kHz, λ = 46 mm) and when vacuum grease is applied directly on the pavement, the WTC results showed less attenuation (between 2% and 4%) when using the foam isolator. Hence, the foam did not affect the results significantly.
- When vacuum grease is used directly on the asphalt surface, the results agreed well with those using the aluminum plate configuration (within 10% difference). These results suggest that the plate is not necessary.

- The WTC at the dominant frequency was not an accurate representation of the frequency range, giving more than 12% of difference. Thus, WTC should be computed for a range of frequencies to achieve a good representation of the joint.

6.3 New Joint Evaluation Procedure using Instantaneous Transmission Coefficient (ITC)

The instantaneous frequency and instantaneous damping, extracted from analytic signals, has the potential for the characterization of material attenuation (Section 4.2.3.7). The presence of a joint allows larger attenuation effects that increase the damping characteristics of the medium. This section studies the application of instantaneous wave characteristics to assess the condition of joints.

6.3.1 Testing Methodology and Experimental Setup

The experimental setup for the test is schematically illustrated in Figure 6-12. The testing equipment and instrumentation were described in Section 6.2.1.

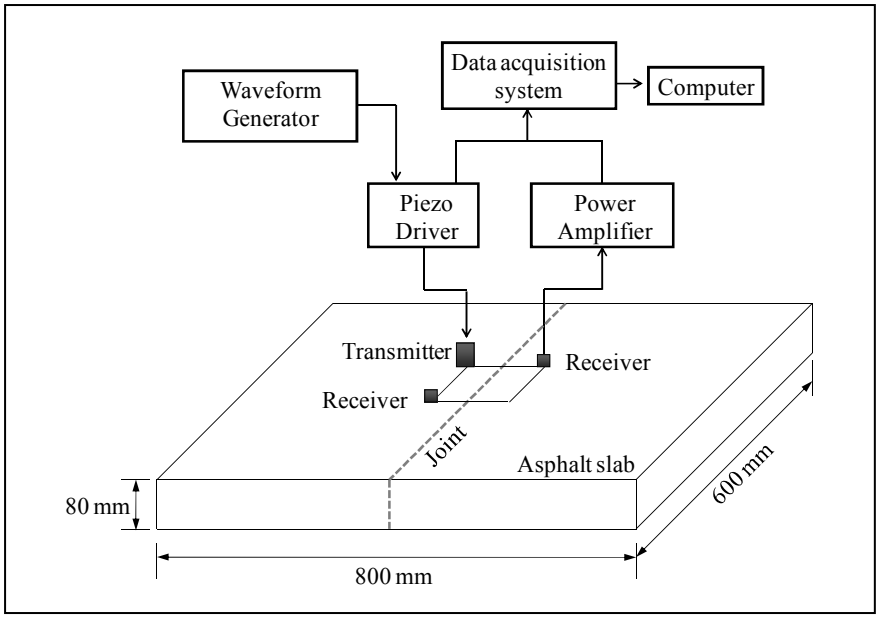

Figure 6-12. Experimental setup for joint evaluation test.

The tests were performed on a fabricated asphalt slab with a construction joint of controlled density; this slab was also used for testing the coupling configurations discussed in Section 4 (Figure 6-1). The tests were performed on equally-spaced experimental configurations at different sections of the slab, as shown in Figure 6-13.

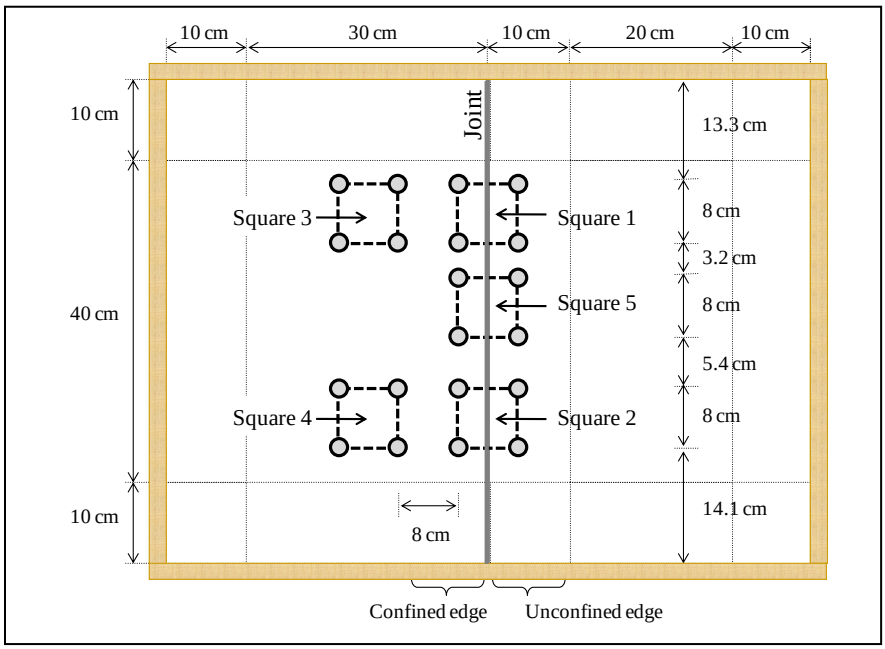

Figure 6-13. Location of test areas on the fabricated slab.

The transmitter and receivers were glued to aluminum plates attached to the asphalt surface with epoxy, as illustrated in Figure 6-14.

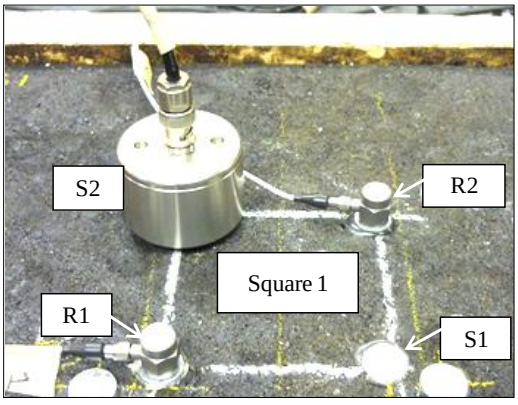

Figure 6-14. Square setup.

Measurements were performed at two locations along the joint: Square 1 and Square 2. Initially, only one location with joint free surface was considered (Square 4). Later, measurements were conducted on another joint free location (Square 3). Instantaneous transmission coefficients (ITC) were calculated for each square configuration and compared to FTC and WTC. Square 5 was used for conducting tests to evaluate the coupling effects, as discussed in the previous section.

6.3.2 Results

Figure 6-15 shows a typical normalized time signal and its respective Fourier spectra that correspond to the data collected form Square 1. Removal of the DC component and zero padding are applied to the original signals to improve the frequency resolution. P-wave and S-wave velocities were determined in time domain: V_P = 3175 m/s and V_R= 1618 m/s. These velocities agreed well with the values computed on the same slab in Section 4.3. A dominant frequency of approximately 32.5 kHz was observed from the frequency spectra. Figure 6-16 to Figure 6-18 show the normalized time signals and Fourier spectra for Square 2, Square 3 and Square 4. The measurements on squares 1, 2 and 4 were performed using the same configuration. Only tests on Square 3 differ as measurements were conducted after with a time delay of 0.1 ms in the trigger source.

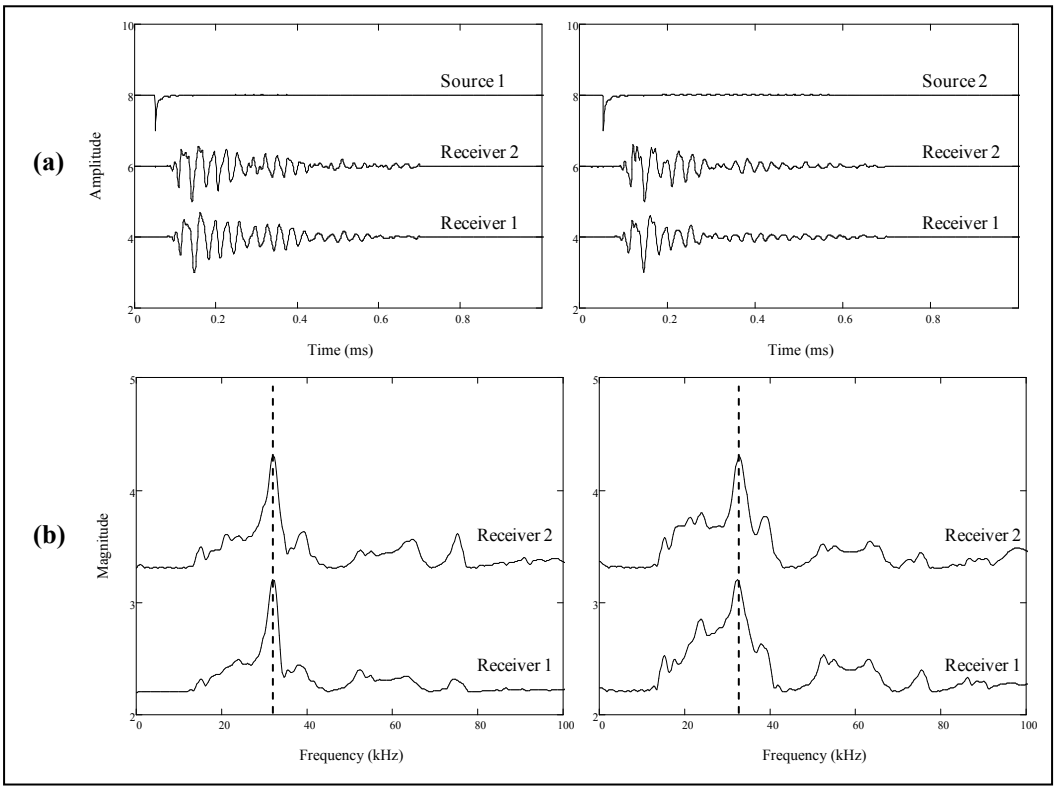

Figure 6-15. (a) Time signal and **(b)** normalized Fourier spectra for Square 1.

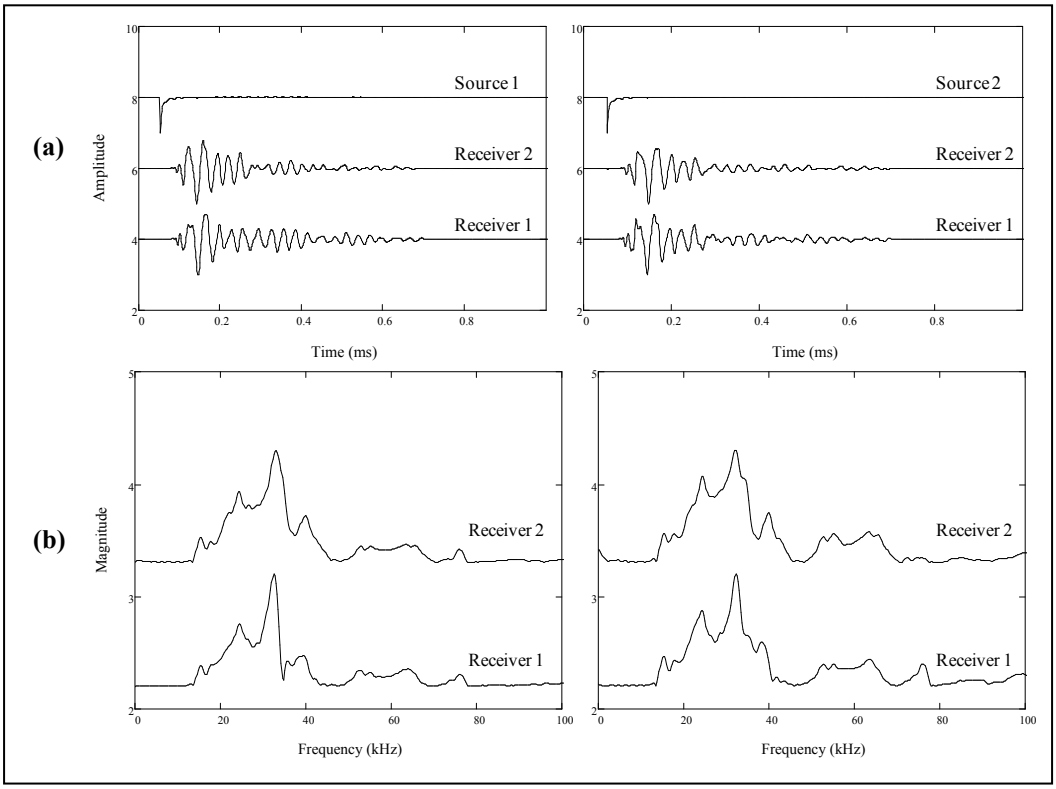

Figure 6-16. (a) Time signal and **(b)** normalized Fourier spectra for Square 2.

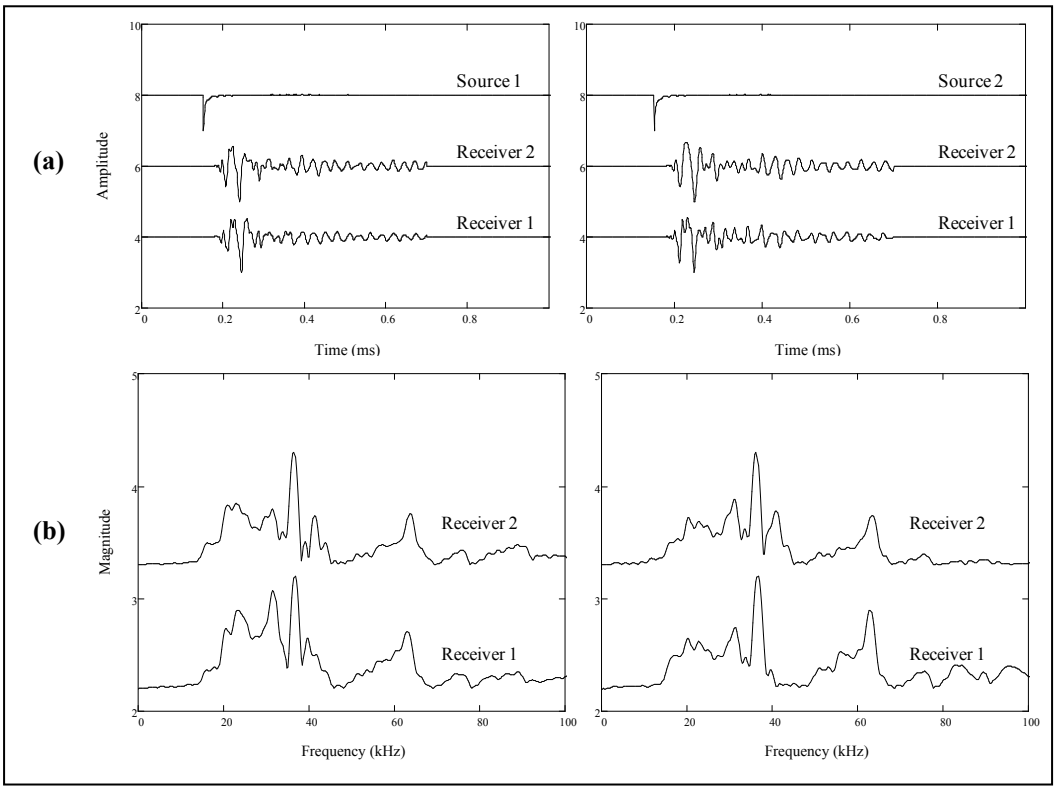

Figure 6-17. (a) Time signal and **(b)** normalized Fourier spectra for Square 3.

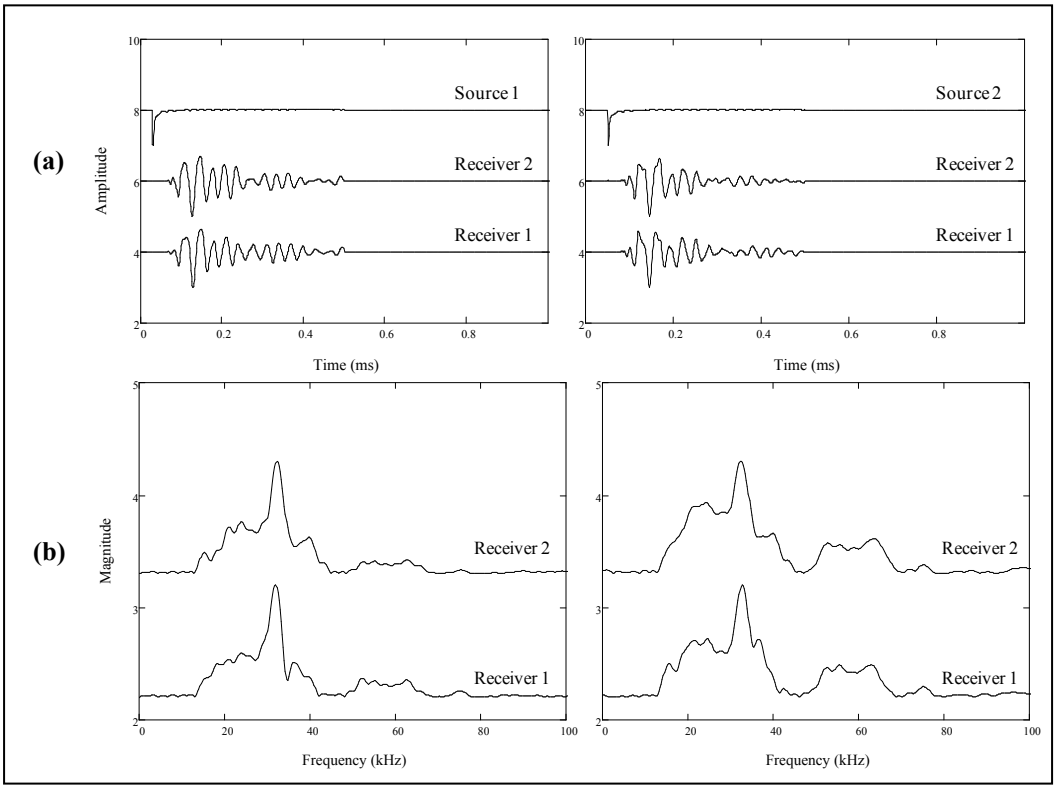

Figure 6-18. (a) Time signal and **(b)** normalized Fourier spectra for Square 4.

The Fourier spectra show that the wave energy was mainly concentrated within a frequency range of 10 kHz to 60 kHz.

Fourier transmission coefficients (FTC) were calculated for each square and averaged for a bandwidth of 50 kHz (ranging from 10 to 60 kHz). Figure 6-19 plots the calculated FTC vs. frequency for the selected bandwidth of 50 kHz. The mean values of FTC were calculated and summarized in Table 6-3.

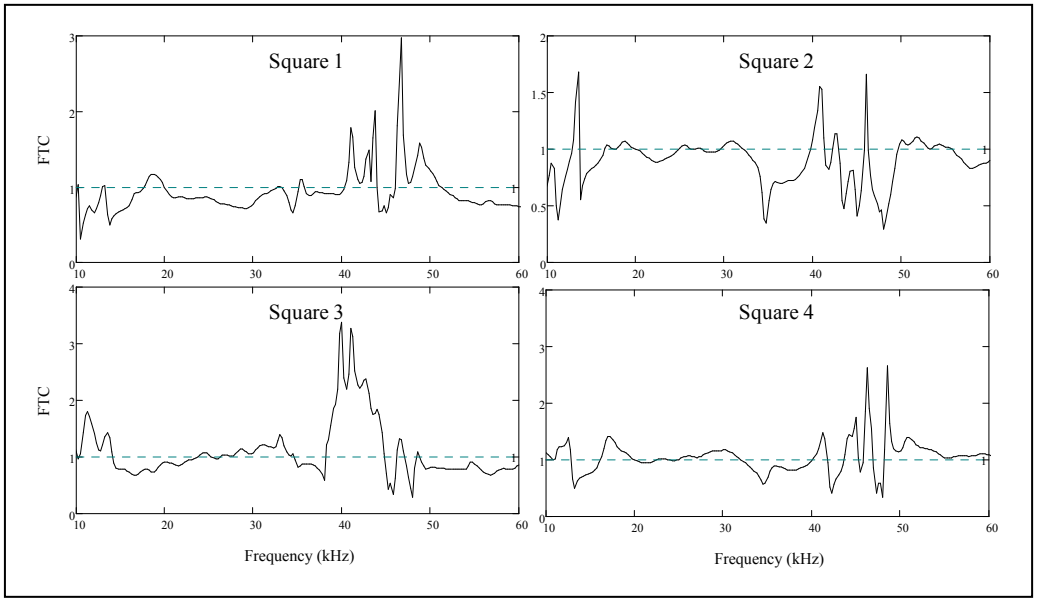

Figure 6-19. FTC vs. frequency for different test locations: squares 1 to 4.

Table 6-3. Average FTC for each test location.

Test location	FTC
Square 1	0.72
Square 2	0.76
Square 3	0.97
Square 4	0.96

As expected, the calculated FTC values of jointed locations (Square 1 and 2) were lower (by 31%) than those of the joint-free locations (Square 3 and Square 4).

Next, the WTC was computed for a range of center frequencies: from 10 kHz to 60 kHz by increments of 5 kHz. The Morlet functions were defined for different center frequencies, and the wavelet transforms for each frequency and test sets are presented in Appendix D.

Figure 6-20 shows the results of WTC with respect to frequency for all four squares and the average at each frequency. The WTC values for Squares 3 and 4 were clearly higher than for Squares 1 and 2. This result was anticipated, as the joint did not cross Squares 3 and 4; in contrast, Squares 1 and 2 included the joint.

The average WTC values were calculated as 0.84, 0.83, 0.97 and 0.97 for Square 1, Square 2, Square 3 and Square 4, respectively. It is also clear that both jointed locations gave WTC values below the average calculated for the asphalt slab.

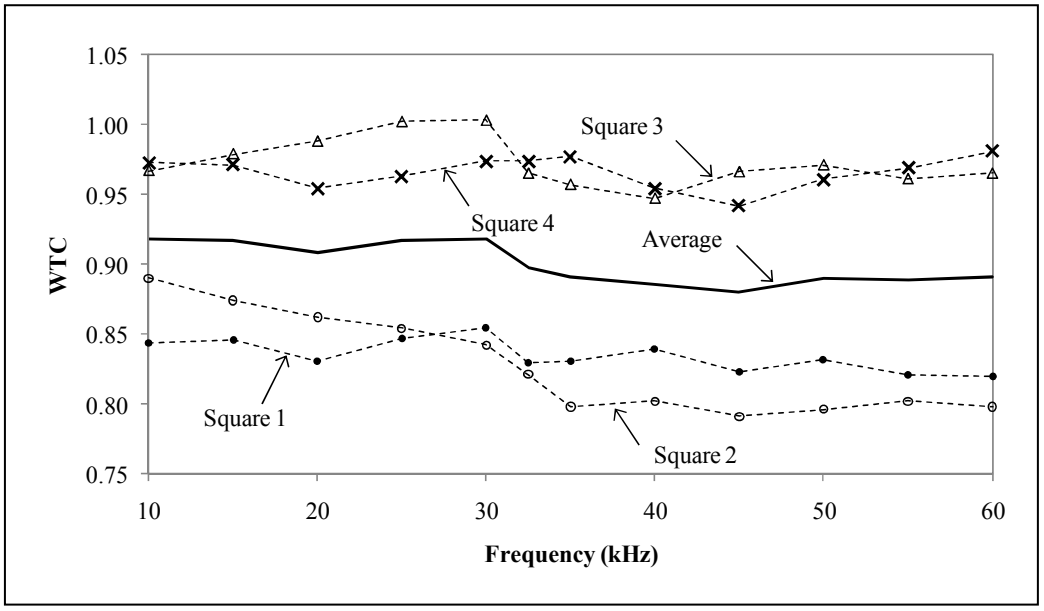

Figure 6-20. WTC vs. frequency for: Square 1, Square 2 and Square 4.
Average calculated with standard deviations between 0.01 and 0.03.

Because the selection of the Morlet center frequency is very important, the assessment of WTC at the dominant frequency and comparisons to the WTC for all frequencies are recommended. Figure 6-21 presents the comparison between the average WTC values and the WTC calculated for a frequency of 32.5 kHz (dominant frequency).

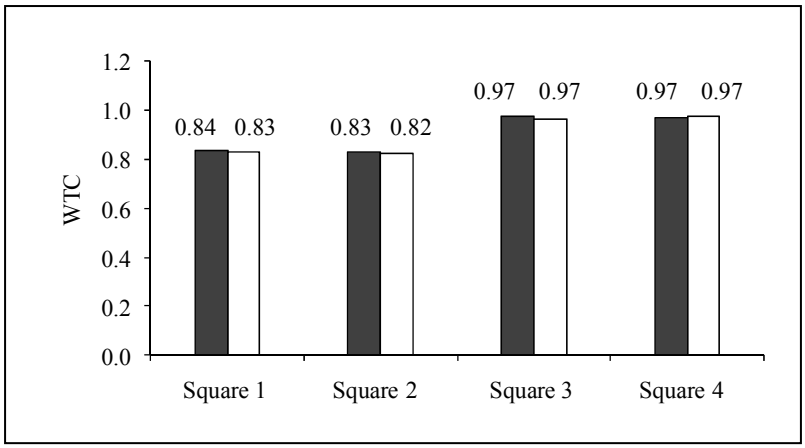

Figure 6-21. Comparison between average WTC (solid fill) and WTC at 32.5 kHz (no fill), for different square locations.
With standard deviations between 0.01 and 0.03.

The WTC at the dominant frequency was consistent with the average values for each square location (Figure 6-21). Thus, the WTC values at 32.5 kHz were a good approximation of the frequency range used in the test.

Next, the ITC was computed. Figure 6-22 shows typical original time signals with their corresponding Hilbert transform (imaginary component) and the magnitude of their analytic signal, for Square 1 and 2; Figure 6-23 for Square 3 and 4.

The magnitude of the analytic signal is the complex envelope of the original time signal (Figure 6-22 and Figure 6-23).

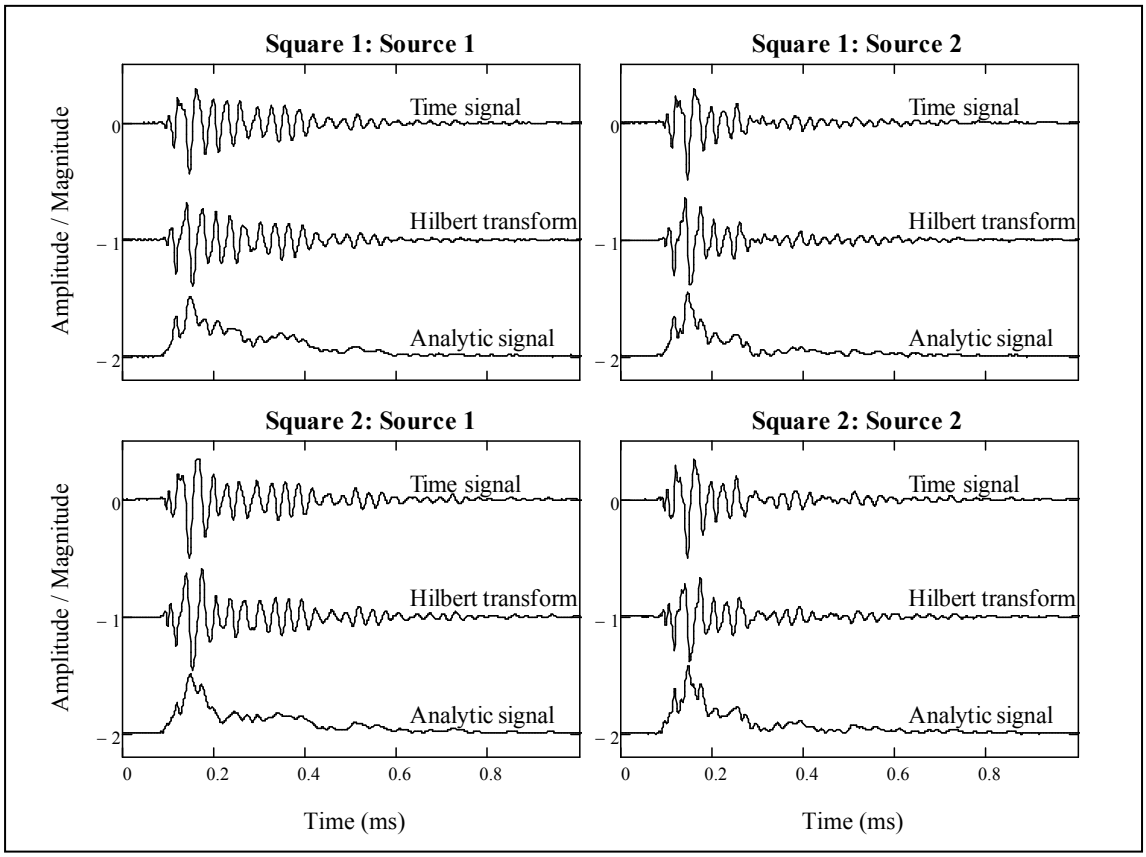

Figure 6-22. Typical original time signal, Hilbert transform and magnitude of analytic signal for receiver 1 in measurements from squares 1 and 2.

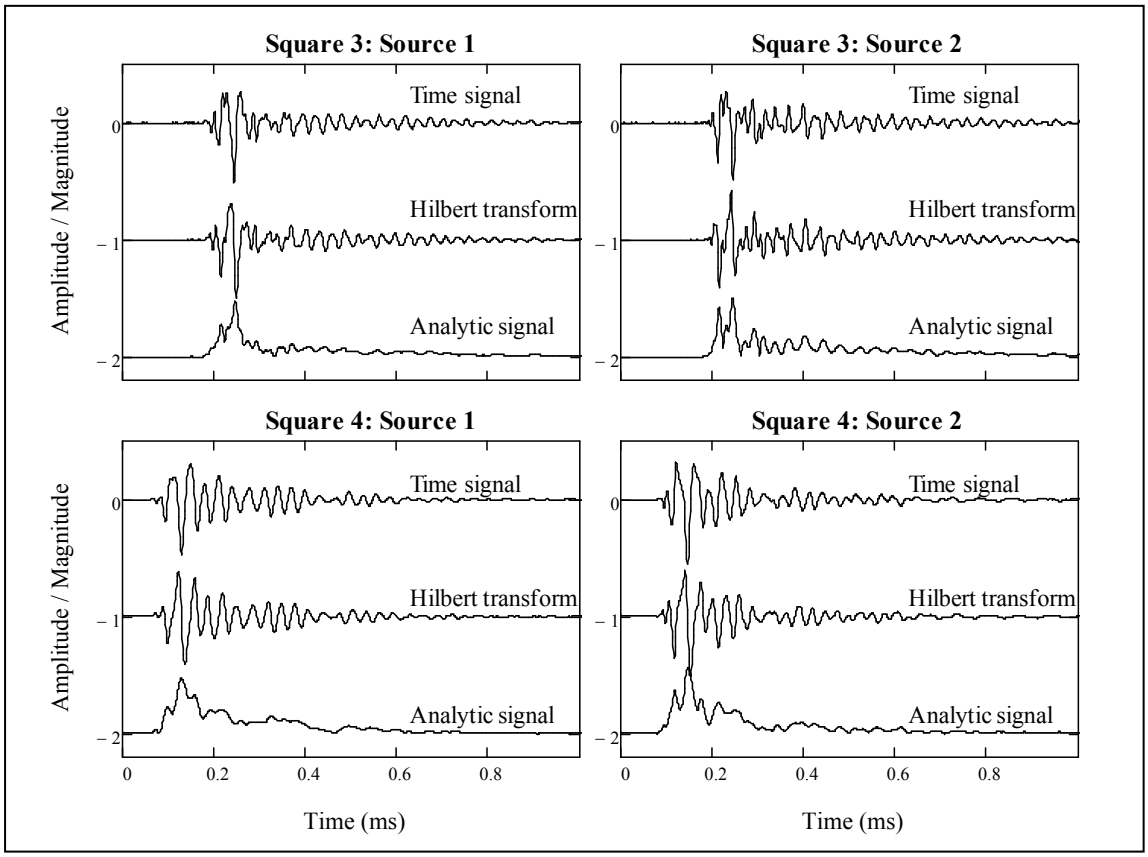

Figure 6-23. Typical original time signal, Hilbert transform and magnitude of analytic signal for receiver 1 in measurements from squares 3 and 4.

Time dependent information, such as the instantaneous frequency, was computed for each analytic signal. The unwrapped phase plots were curve-fitted with a Gaussian kernel function for a bandwidth of 0.30 ms (Figure 6-24); the instantaneous frequencies in function of time (Figure 6-26 and Figure 6-26) were computed from the slope of the unwrapped phase.

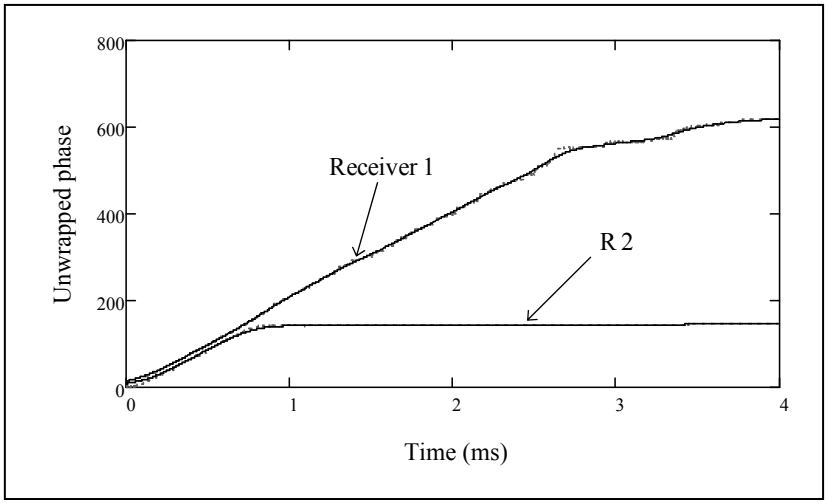

Figure 6-24. Typical unwrapped phase for Square 1 and source 1.
(Curve-fitted with Gaussian kernel function, 0.30 ms bandwidth).

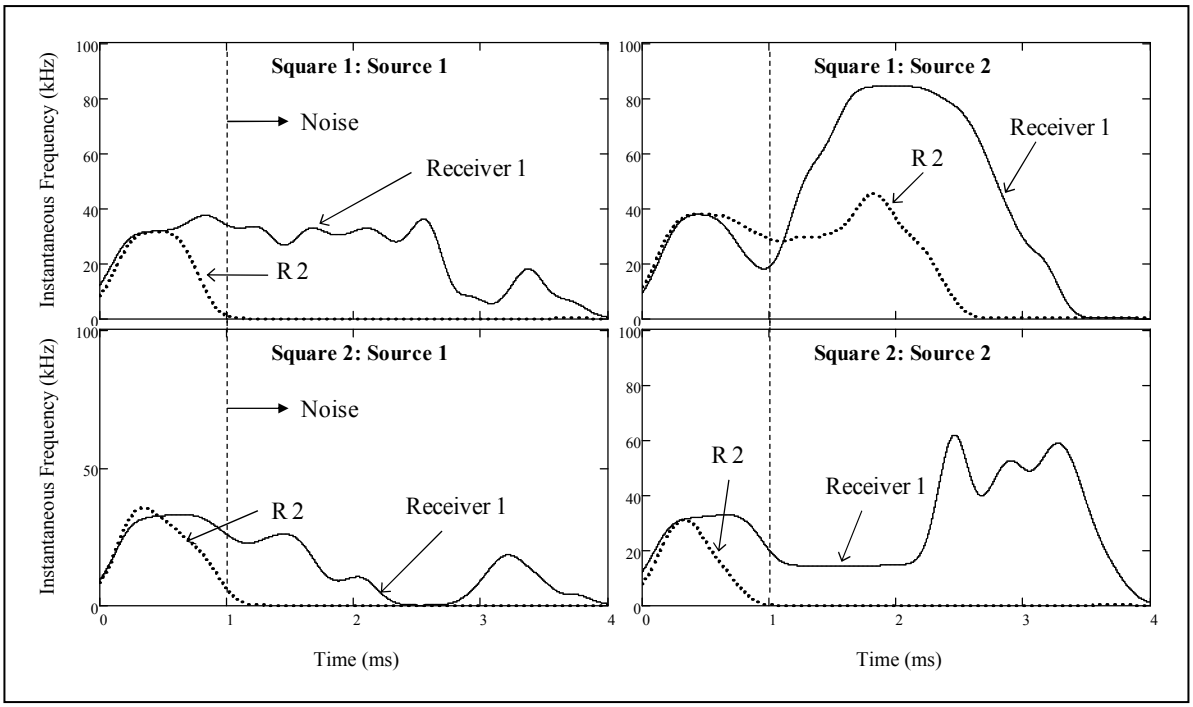

Figure 6-25. Instantaneous frequency vs. time for squares 1 and 2.

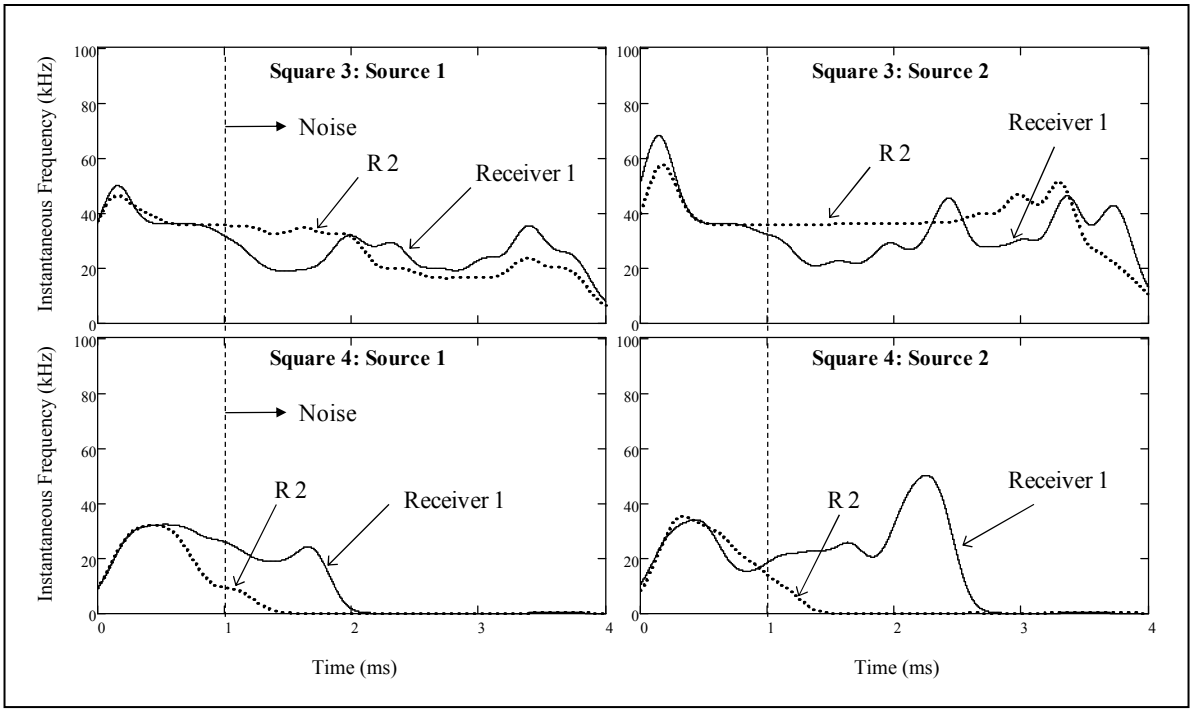

Figure 6-26. Instantaneous frequency vs. time for squares 3 and 4.

The Fourier spectra plots (Figure 6-15 to Figure 6-18) show that most of the energy is concentrated within a range of frequencies (10 to 60 kHz); however, these plots do not provide information about the location of each frequency content. Instantaneous frequency plots retain the frequency information in time (Figure 6-26 and Figure 6-26). The original time responses (Figure 6-26 and Figure 6-26) show the decay of the signal's energy, which was almost completely attenuated at 1 ms. This attenuation effect can be observed in the instantaneous frequency plots as well, particularly from Receiver 2. The instantaneous frequency plots from Receiver 1 show a significant amount of noise after the signals have decayed completely (at 1 ms). Measurements on Square 3 show noise content at the beginning of the signal. Nevertheless, the response from both receivers shows constant dominant frequencies of about 32 kHz before the signals are attenuated entirely, consistent with the Fourier spectra. As a result, the instantaneous frequency appears to allow locating the proper time window for further analysis.

The instantaneous damping ratios were computed using Equation (3-14); the plots of the magnitude of the analytic signal and instantaneous frequency were smoothed using a Gaussian kernel function for a bandwidth of 0.25 ms. Moving window algorithms with different window sizes were used to determine the location and value of the damping ratio with the maximum correlation coefficient. Table 6-4 summarizes the results obtained for each square location. These damping values comprise geometric and material damping.

Table 6-4. Damping ratios using moving window algorithm.

Square No.	Window size (ms)	Damping ratio (%)			
		Source 1		Source 2	
		S1-R1	S1-R2	S2-R1	S2-R2
1	0.025	3.27	2.14	1.54	1.95
	0.050	3.26	2.14	1.55	1.96
	0.075	3.23	2.14	1.57	1.96
	0.100	3.19	2.14	1.59	1.96
	0.125	3.14	2.14	1.61	1.96
2	0.025	2.35	2.19	1.81	2.77
	0.050	2.35	2.19	1.82	2.78
	0.075	2.35	2.19	1.83	2.78
	0.100	2.34	2.20	1.84	2.79
	0.125	2.34	2.20	1.86	2.80
3	0.025	1.74	1.55	1.42	1.27
	0.050	1.74	1.54	1.42	1.26
	0.075	1.73	1.54	1.41	1.25
	0.100	1.73	1.52	1.40	1.24
	0.125	1.72	1.51	1.39	1.22
4	0.025	2.71	2.12	2.35	1.95
	0.050	2.71	2.14	2.35	1.96
	0.075	2.71	2.15	2.35	1.97
	0.100	2.71	2.18	2.35	2.00
	0.125	2.71	2.20	2.35	2.02

The damping ratio values were determined to be ranging between 1.2% and 3.3%. In the cases of jointed surfaces (square 1 and 2), the signals recorded by the receivers across the joint gave higher values of damping than the receivers recording the joint-free propagation. This can be noticed in the results obtained for squares 1 and 2 (Table 6-4), as the signals S1-R1 (Source 1 to Receiver 1) and S2-R2 (Source 2 to Receiver 2) gave higher damping values than the joint-free signals: S1-R2 and S2-R1. Also, it is important to note that the air content

at the right-hand side of the joint was higher than the left-hand side (Figure 6-1); hence, the damping values computed with the S1-R2 signal were higher than the values from S2-R1. Tests conducted on the jointed locations (Square 1 and Square 2) showed a variation of the damping values measured in the joint-free signals (S1-R2 > S2-R1), resulting in damping ratios of 2.14% > 1.57% for Square 1, and 2.19% > 1.83% for Square 2.

Squares 3 and 4 did not include a joint; very consistent damping values were obtained for each square location. Damping ratios between approximately 1.2% and 1.7% were observed for measurements in Square 3, and between 2.0% and 2.7% for Square 4. These damping values are within the expected range for the tested asphalt slab (Du Tertre, 2010).

The computed damping values were high with respect to low strain damping in granular materials due to the viscoelastic behavior of asphalt. The dynamic properties of asphalt depend on the characteristics of the mix; typical damping ratios for a highway asphalt pavement mix were found to be between 5% and 8% (Zhong et al., 2002).

Finally, the ITC values were computed for each square location using Equation (3-15). The mean values were calculated and compared to the FTC and WTC results (Figure 6-27).

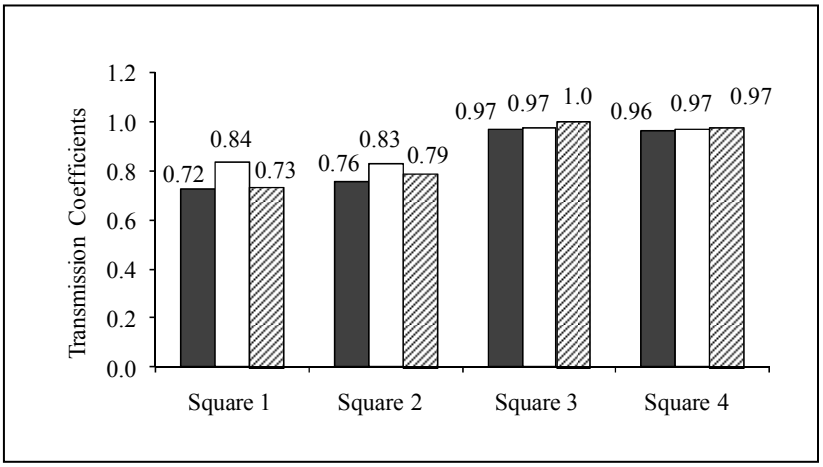

Figure 6-27. Mean FTC (solid fill), WTC (no fill) and ITC (pattern fill) for all square locations.
With standard deviations between 0.01 and 0.03.

The ITC values were consistent with the FTC and WTC ratios for each square location; the ITC values for squares 1 and 2 (with joint) were significantly higher than those for the joint-

free squares 3 and 4. The wavelet method gave slightly higher transmission coefficient values for jointed surfaces; in contrast the FTC and ITC results were very similar. This may be due to the generated wavelength, since the WTC method is only valid for surface waves. For lower frequencies (e.g. 20 kHz) larger wavelengths were generated (e.g. 82 cm); thus, for wavelengths larger than the slab thickness, wave reflections can significantly affect the results.

The advantage of ITC over the FTC method is that the Fourier transform does not contain any wave information in time. High frequency content due to noise is present after the signals have attenuated completely (Figure 6-26), which may cause a negative impact on the FTC calculations. Hence, signals should be either filtered for high frequency noise or windowed before processing. Both the filtering and windowing process may also affect the results if the wave reflections are mistakenly removed or if the window width is selected incorrectly.

The ITC overcomes the limitations associated with the WTC technique, which involves selecting peak values from the wavelet transform. This peak selection is usually subjective and is not always obvious, and thus requires more user input.

The fabricated joint was detected by the ITC method, giving an average of 0.76 for the jointed sections and 0.97 for the joint free sections. Nevertheless, these results do not provide information about the condition of the joint. Hence, it is important to conduct more experimental tests on slabs with controlled joint conditions (e.g. poor, medium and good).

According to a recent study that used wave attenuation measurements to compute WTC (Jiang, 2007), the quality of the joints were identified as: good (WTC > 0.49), medium (0.32 < WTC < 0.34), and weak (WTC < 0.13). Based on these results, the tested joint is in good condition, as the computed mean WTC was 0.83. More tests should be conducted on joints with different conditions.

6.3.3 Concluding Remarks

- The damping values (1.2% to 3.3%) were calculated from the information extracted from the analytic signals, and they are within the acceptable range of those found in literature.

- Good agreement was observed between the FTC, WTC and ITC results for both jointed and joint-free surfaces, with an average difference of 1.1% and 6.3%, respectively.
- The resonance of the transducers was detected (32.5 kHz), where most of the wave energy is found. This could have a negative impact on the FTC calculations.
- The WTC results in the lower frequencies (f < 20 kHz and λ > 80 cm) for the jointed surface ware higher (by 10%) than the FTC and ITC results.
- The ITC method overcomes the main limitations of the FTC and WTC, as it retains the frequency information in time and does not require the manual selection of peak values.

6.4 Improvement of Signal Quality and Evaluation of Poor Joint

Experimental tests with different coupling mechanisms provided promising results for the condition assessment of longitudinal joints in asphalt pavements (Section 6.2). Nonetheless, additional work is required to: (1) test the use of different weights to optimize the coupling, and to (2) test the use of a coupling stud on the receivers to improve the signal quality and avoid the use of a couplant.

The results from Section 6.3 suggested that the tested joint is in good condition. Therefore, the calibration of the ITC method is carried out, in the following section, by testing a joint in poor condition.

6.4.1 Testing Methodology and Experimental Setup

Four different testing procedures were followed. First, three stainless steel disks of different sizes were used as coupling devices to improve the transmitted signal. The smallest disk had a diameter of 9.5 mm and a thickness of 4.08 mm; the medium disk was 12.7 mm in diameter and 4.10 mm thick; the largest disk measured 15.8 mm and 3.86 mm in diameter and thickness. Figure 6-28 shows the experimental setup using the 12.7 mm steel disk. The disks were glued to the aluminum plates attached to the asphalt pavement with epoxy. Measurements were performed with one transmitter and one accelerometer.

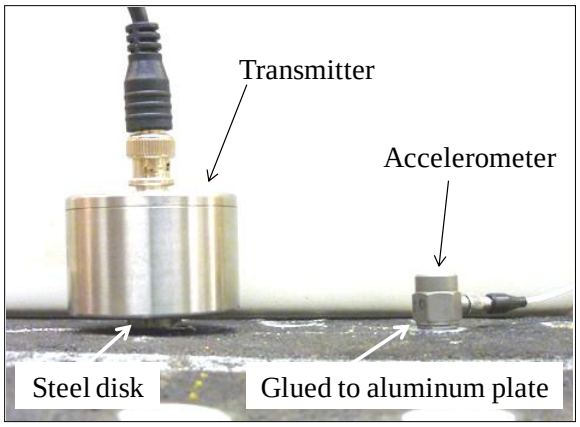

Figure 6-28. Typical setup using a steel disk as coupling device for the transmitter.

Next, different weights were considered for improving the coupling of the receivers, and thus eliminating the use of aluminum plates epoxied to the asphalt surface. Vacuum grease and foam isolators were proposed as an alternative. The use of a vertical pressure and vacuum grease as couplant was found to be effective for improving the coupling between the receiver and the asphalt (Section 6.2). Three calibrated weights were tested in this section: 50 g, 100 g, and 200 g. Polyurethane foams are used to provide a spring action on the transducers and isolation between the transducer and the added weight. A typical experimental setup is shown in Figure 6-29.

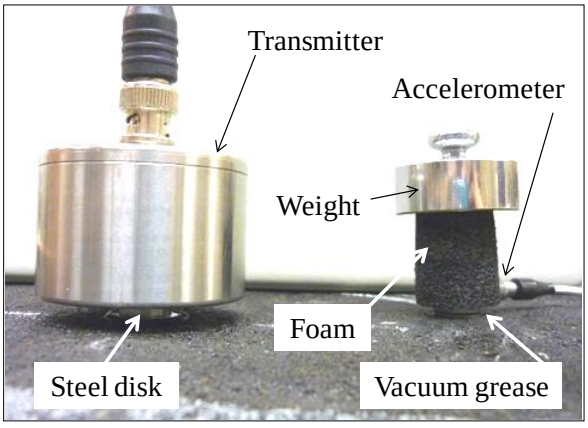

Figure 6-29. Typical setup using vacuum grease, foam isolator and 100 g weight.

Next, a new coupling device was tested, consisting of a steel stud screwed into the accelerometers, as shown in Figure 6-30. This device was used for improving the signal quality and avoiding the use of a couplant (vacuum grease); different weights were also applied to analyze the effects of the applied vertical pressure.

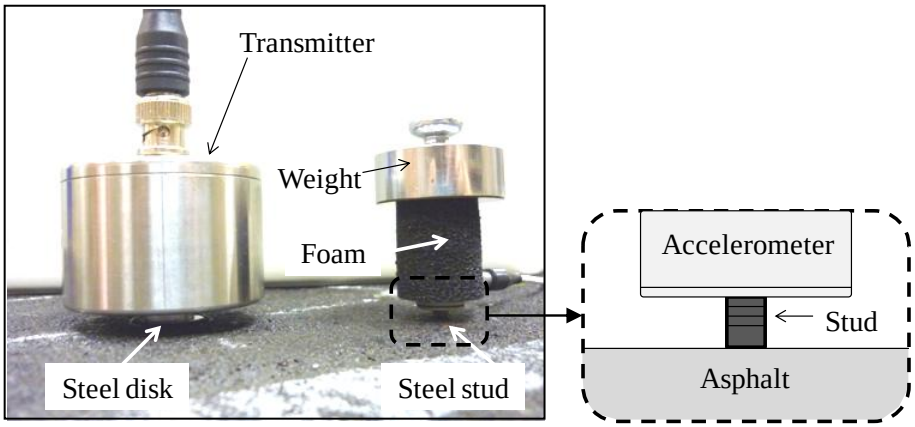

Figure 6-30. Typical setup using steel stud and weights.

Finally, a poor condition joint was created by cutting a narrow notch (3 mm wide and 30 mm deep) in the fabricated slab; tests were conducted for the evaluation of the joint condition. Figure 6-31 shows the location of the notch. The instrumentation was described in Section 6.2.

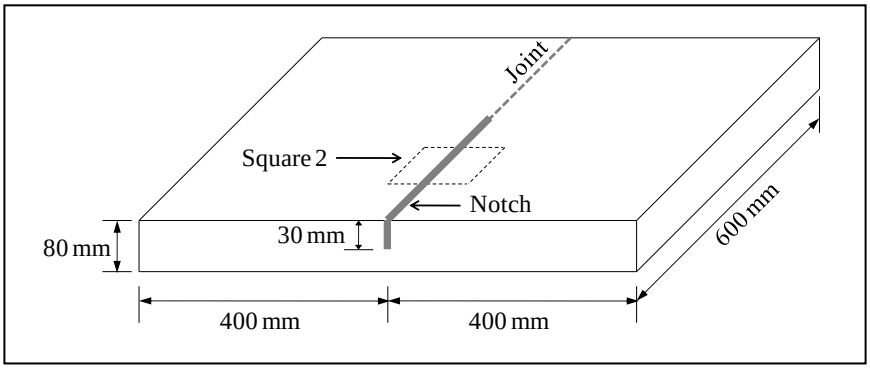

Figure 6-31. Location of the 3 mm wide notch in the fabricated slab.

6.4.2 Results

Figure 6-32 shows the response signals recorded using the steel disks.

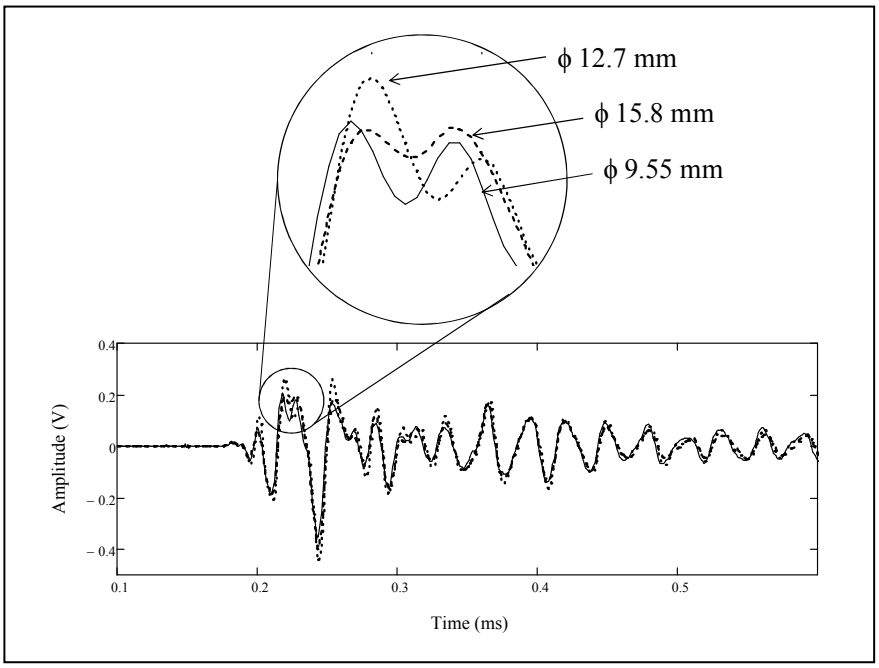

Figure 6-32. Effect of steel disks of different diameters (ϕ) as coupling between the ultrasonic source and the pavement surface – Time signals.

Figure 6-32 shows that the plate with a diameter of 12.7 mm provided the larger peak-to-peak (PTP) amplitude. The PTP values were calculated as: 0.56 V, 0.71 V, and 0.60 V, for the small, medium and large disks, respectively. Nevertheless, the shape of the response signal and frequency content were almost constant with all three disks (Figure 6-33). Two main frequency components were observed at 36 kHz and 61 kHz.

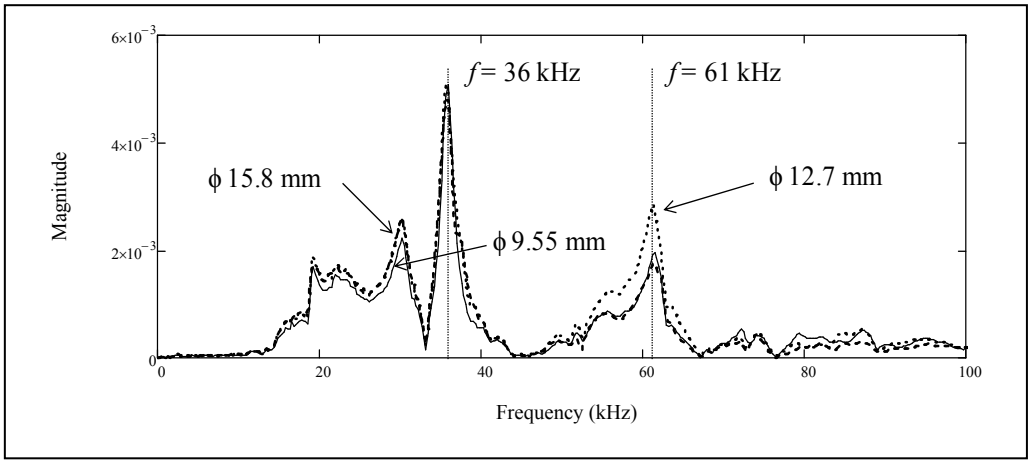

Figure 6-33. Effect of steel disks of different diameters (ϕ) as coupling device between the ultrasonic source and the pavement surface – Frequency spectra.

The steel disk with a diameter of 12.7 mm is the coupling option that provided the highest intensity (largest PTP amplitude) and widest frequency content. It was therefore used for the subsequent experimental tests. The response obtained with the accelerometer glued to an aluminum plate was used as a reference signal for selecting the best coupling system between the receiver and the asphalt surface.

Different weights (50 g, 100 g and 200 g) were placed on top of the receiver; vacuum grease and foam isolators were proposed as an alternative to aluminum plates and glue. Figure 6-34 shows that as the vertical pressure increased, the intensity of the response signal increased slightly while the frequency content remained constant. The PTP values were calculated as: 146 mV, 153 mV, and 158 mV, for weights of 50 g, 100 g and 200 g, respectively, giving an increase of 4.8% (between 50 g and 100 g) and 8.2% (between 50 g and 200 g). The main frequency components matched those observed in the reference signal.

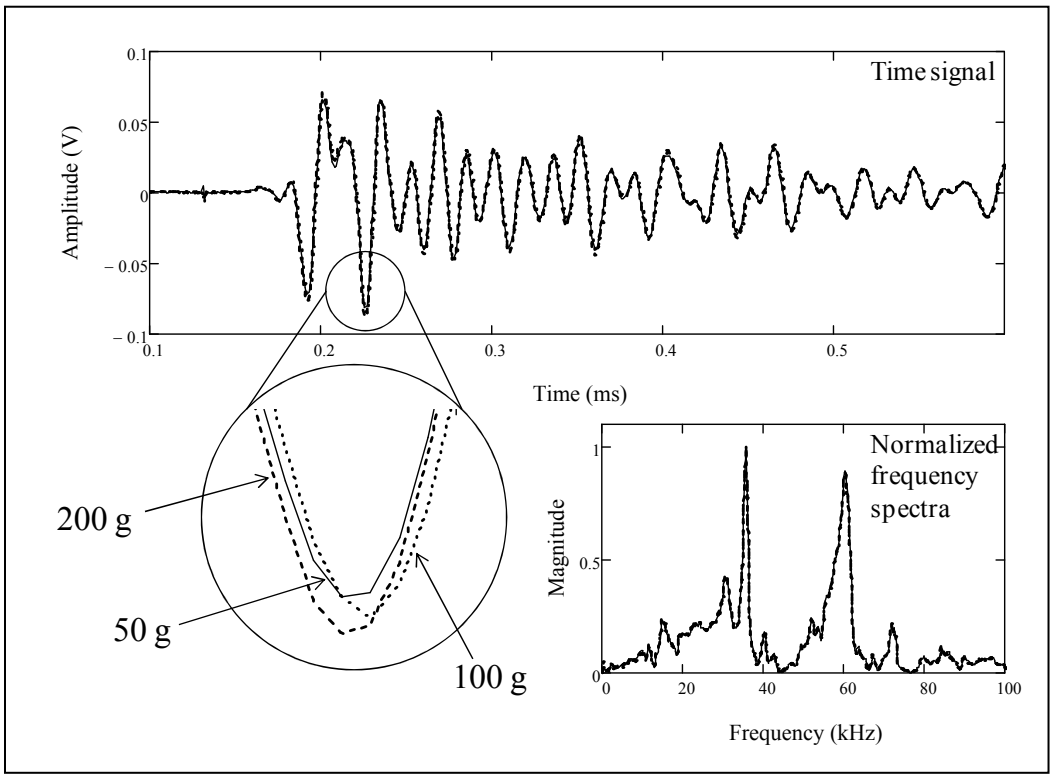

Figure 6-34. Effect of a vertical pressure applied on the accelerometers. Weights of 50 g, 100 g and 200 g are used.

Next, a new coupling system (steel stud) was used for improving the signal quality to avoid the use of a couplant (vacuum grease). Figure 6-35 shows that the 100 g weight provided the highest response intensity; the frequency content was not significantly affected. The PTP values were increased by 42.3% with the 100 g weight, but decreased by 13.5% with the 200 g weight. Main frequencies were found at 36 kHz and 51 kHz, matching the nominal resonant frequencies of the accelerometer and the transmitter, respectively.

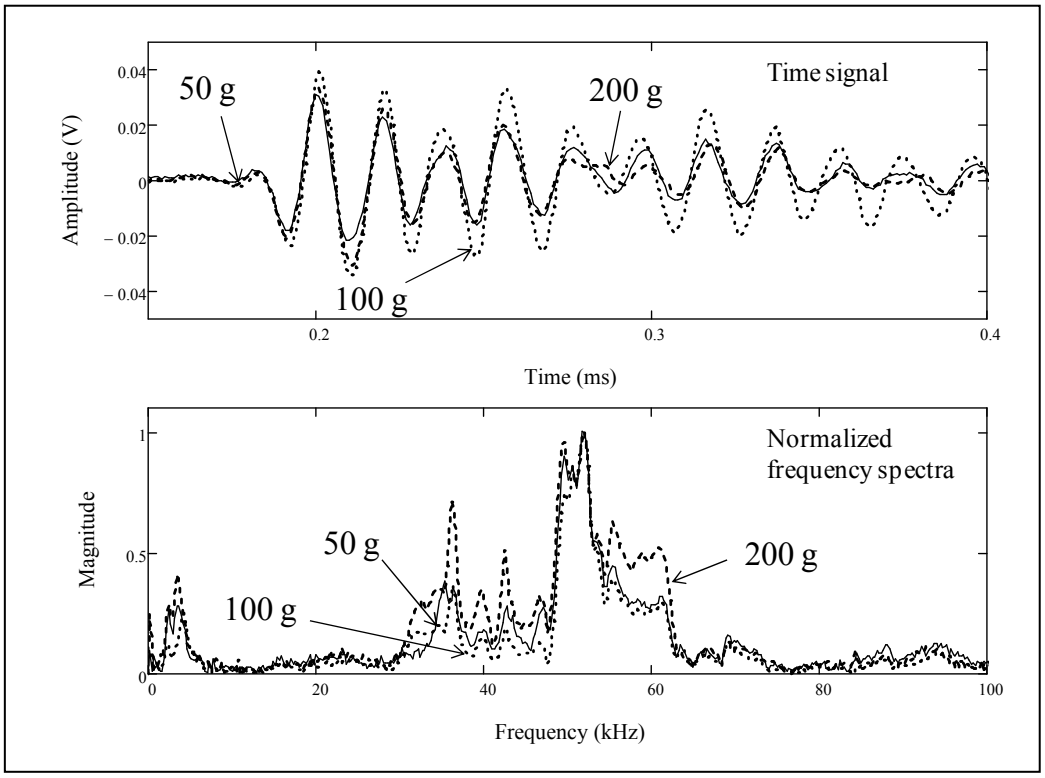

Figure 6-35. Effect of a vertical pressure applied on the accelerometers with a steel coupling stud. Weights of 50 g, 100 g and 200 g are used.

Figure 6-36 shows the effect of the steel stud. The two larger amplitude cases are plotted: using the 200 g weight without the stud, and the 100 g weight including the stud. The first configuration gave the largest PTP value and signal intensity. The configuration with the stud gave slightly lower frequency content when compared to the case without the stud.

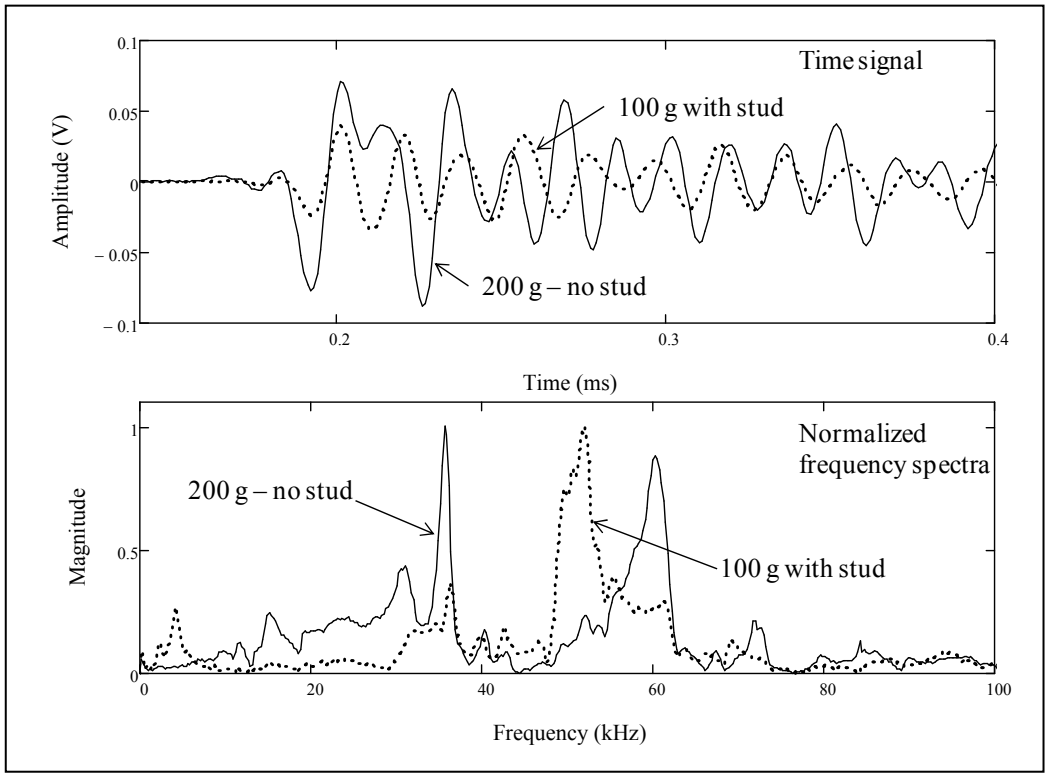

Figure 6-36. Effect of a steel coupling stud attached to the accelerometers.

The signals (with and without the stud) are compared to the response obtained previously with the accelerometer glued to an aluminum plate and without applied pressure (Figure 6-32). The time signals obtained by using the 200 g weight without the coupling stud correlated the best to the reference signal, but showed significantly less intensity (Figure 6-37). The frequency spectra matched very well, showing two main frequencies at 36 kHz and 61 kHz. The results show that a relatively good-quality signal was recorded by the accelerometer when coupled directly on the asphalt surface with vacuum grease, thus eliminating the need for the aluminum plate. This coupling configuration wass used for the subsequent tests on Square 2 before and after cutting the notch.

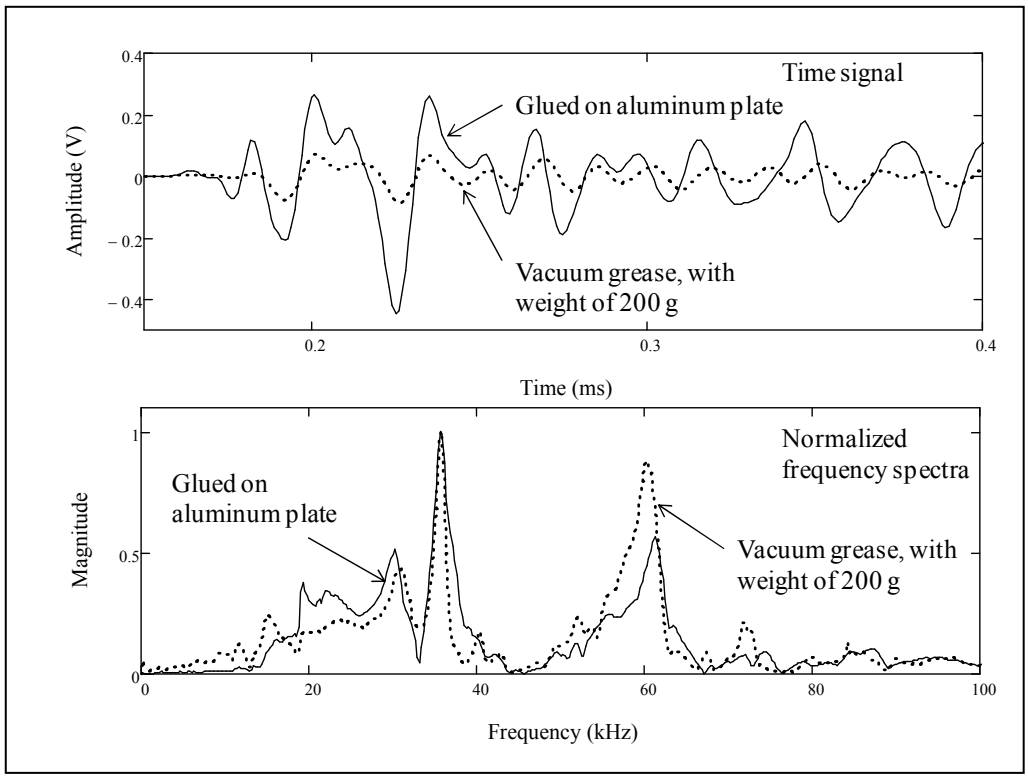

Figure 6-37. Effect of eliminating the aluminum plate coupling.

Finally, a poor condition joint was created by cutting a narrow notch in the fabricated slab, and tests were conducted for the evaluation of the joint condition. The shallow cut was meant to test the ability of the ITC methodology to detect a lack of coupling, where there is no wave transmission. Transmission coefficient values (FTC, WTC and ITC) were calculated for the same location (Square 2) before and after the saw cut. The new coupling configuration is illustrated in Figure 6-29, using the 200 g weight, the foam isolator, and the accelerometers coupled directly to the asphalt surface with vacuum grease (without the coupling stud). The transmitter was glued to the pavement using a steel disk measuring 12.7 mm in diameter.

Figure 6-38 summarizes the results obtained on Square 2 before cutting the notch using the new coupling configuration and compares these results to those obtained in Section 6.3.2 (Figure 6-27) using the traditional aluminum plate and epoxy configuration. The new coupling configuration gave consistent WTC and ITC values equal to 0.74. The FTC results of both configurations were lower than the respective WTC and ITC values. The new coupling configuration appeared to be consistent and reliable for assessing a relatively good joint.

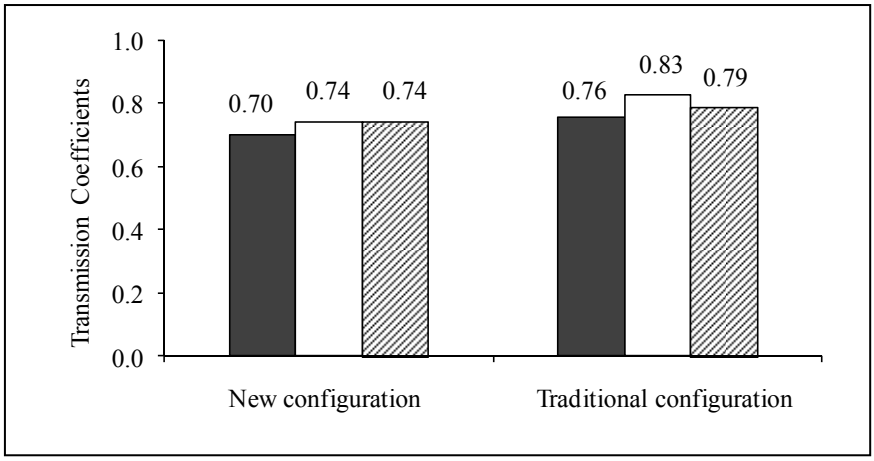

Figure 6-38. Mean FTC (solid fill), WTC (no fill) and ITC (pattern fill) for Square 2 using two different coupling configurations.
With standard deviations between 0.01 and 0.05.

Next, a narrow notch was cut into the asphalt slab, as illustrated in Figure 6-31. Measurements were repeated on Square 2, using the new coupling configuration. Results are presented in Figure 6-39 and compared to the values obtained in the same location before the saw cut.

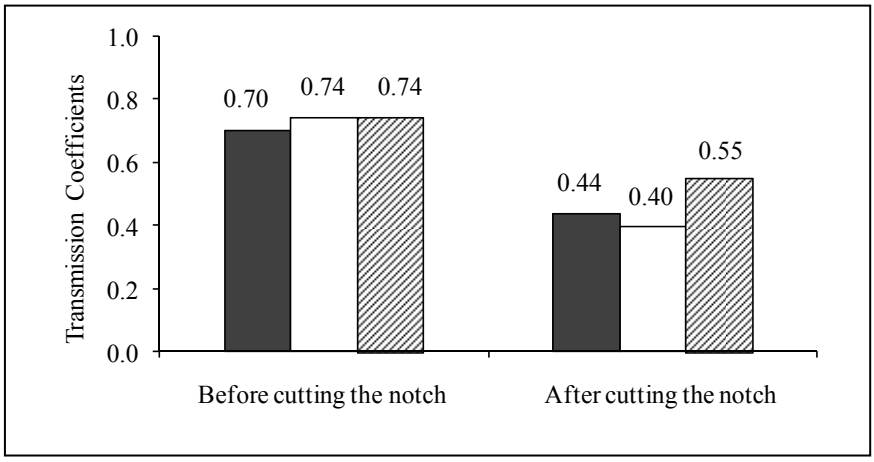

Figure 6-39. Mean FTC (solid fill), WTC (no fill) and ITC (pattern fill) for Square 2 before and after cutting the notch, using the new configuration.
With standard deviations between 0.003 and 0.05.

As expected, the transmission coefficients obtained on Square 2, after cutting the notch (poor condition), were significantly lower than before the cut (good condition). The FTC and WTC

values showed major differences between the different joint conditions, 37% and 46% respectively. In contrast, the ITC calculated for the poor condition joint decreased only 26% compared to the joint in good condition. The ITC results suggest that the instantaneous damping measurements are not sensitive to abrupt changes in density (e.g. notch). Longitudinal joints in on-service asphalt pavements are generally characterized by the gradual decrease in density at the interface between lanes. This is due to poor compaction and poor binding between the aggregate and the matrix. The shallow crack is meant to test the ability of the new methodology to detect a lack of coupling up to a certain depth. The cut could actually represent a very fine crack (same effect as there is no wave transmission). The ITC method appears to be effective for testing asphalt joints; nevertheless, more tests should be conducted on joints with controlled conditions (Section 6.3.2).

6.4.3 Concluding Remarks

- Coupling between the source and asphalt slab was assessed. Good-quality signals were transmitted when coupled to the asphalt surface with a stainless steel disk of 12.7 mm in diameter.
- The new coupling configuration (accelerometers coupled directly on the asphalt surface with vacuum grease) provided relatively good-quality signals. The added 200 g weight provided the largest intensity increase of 8.2%.
- The steel coupling stud has the effect of reducing the main frequency component of the signal by 17%.
- A new coupling configuration was proposed: the accelerometers coupled directly on the asphalt with vacuum grease, with an applied 200 g weight on top, and using a foam cylinder to isolate the vibration effects induced by the weight. This configuration was found to be more practical than the traditional aluminum plate and epoxy arrangement, reducing the testing time by 50%.
- Good agreement was observed for the FTC (7.9% variation), WTC (10.8%) and ITC (6.3%) results between the new coupling configuration and the traditional configuration. The ITC method appeared slightly less affected by the coupling system than the FTC and WTC methods.

- A notch was cut into the asphalt pavement to simulate a poor condition joint. Measurements were conducted at one location on the slab before and after the cut. The transmission coefficients computed for the poor condition joint were significantly lower (37% in average) than the measurements without the notch.
- The FTC and WTC values showed larger differences between the poor joint and the good joint: 37% and 46% respectively; the ITC results decreased by 26%, suggesting that the instantaneous damping measurements are not sensitive to abrupt changes in density, like those found at a notch.
- The ITC method appears to be effective for evaluating the condition of a medium with gradual changes in density, such as in-service asphalt pavement joints.

6.5 MASW Measurements

The multi-channel analysis of surface waves method is used to assess the poor condition (with notch) and good condition (without notch) joints.

6.5.1 Experimental Setup

Two arrays of 12 receivers were placed on the fabricated asphalt slab: one across the fabricated joint with no notch and the other across the notch, as shown in Figure 6-40. As the previous sections suggested, the accelerometers were coupled directly on the asphalt surface with vacuum grease, a foam wrap was used as an isolator, and a 200 g weight was placed on top of each accelerometer. Plastic cylinders were also used in these tests to maintain the stability of each accelerometer, but were not in contact with the asphalt or the weights. The instrumentation was described in Section 6.2.

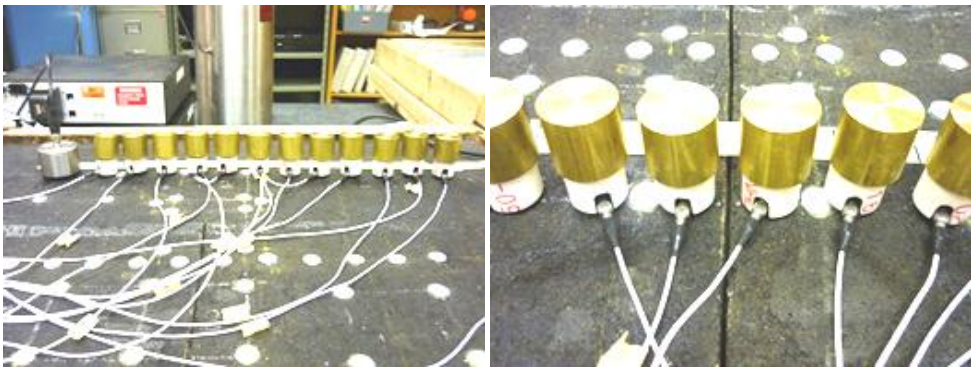

(a) (b)

Figure 6-40. MASW setup on the asphalt slab: (a) across the joint, and (b) across the notch.

6.5.2 Results

The measured time signals of both cases (joint and notch) were used to compute the FK plots (Section 4.2.3.4), as shown in Figure 6-41. The theoretical anti-symmetrical Lamb modes were superimposed to show the agreement of the high energy regions. The FK model shows the theoretical wave modes for the asphalt slab, which was assumed to be homogeneous and isotropic (Yang, 2009). Three parameters were given to compute the symmetric and anti-symmetric modes: P-wave velocity V_P = 3247 m/s, R-wave velocity V_R = 1638 m/s, and half the plate thickness h = 40 mm.

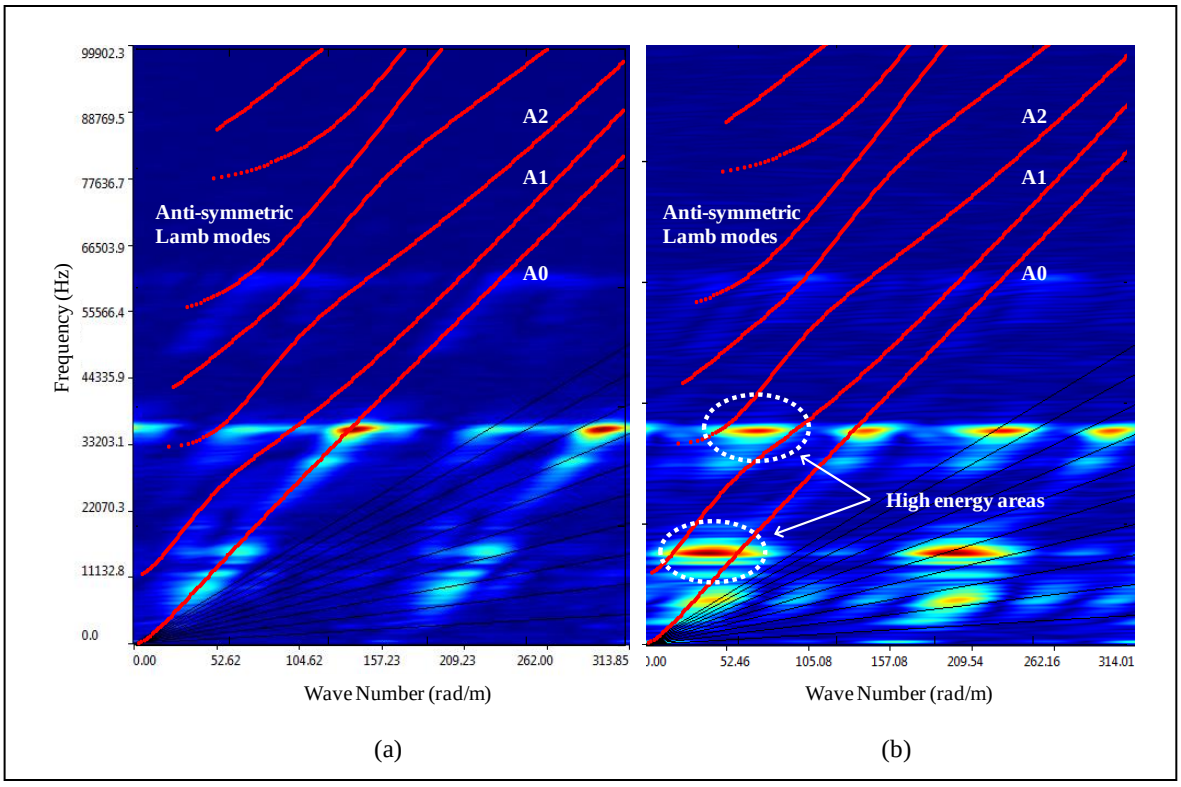

Figure 6-41. Experimental FK plots and theoretical anti-symmetric Lamb modes for the MASW measurements on the asphalt slab: (a) across the joint and (b) across the notch.

The measurements with the notch showed additional high energy concentration regions at approximately 13 kHz and 35 kHz, which were not observed in the measurements across the joint (with no notch) (Figure 6-41). These regions do not correspond to anti-symmetric modes, and suggest the presence of other wave modes (e.g. symmetric Lamb modes). The high energy areas were found to be corresponding to the theoretical symmetric modes S0 and S1 (Figure 6-42).

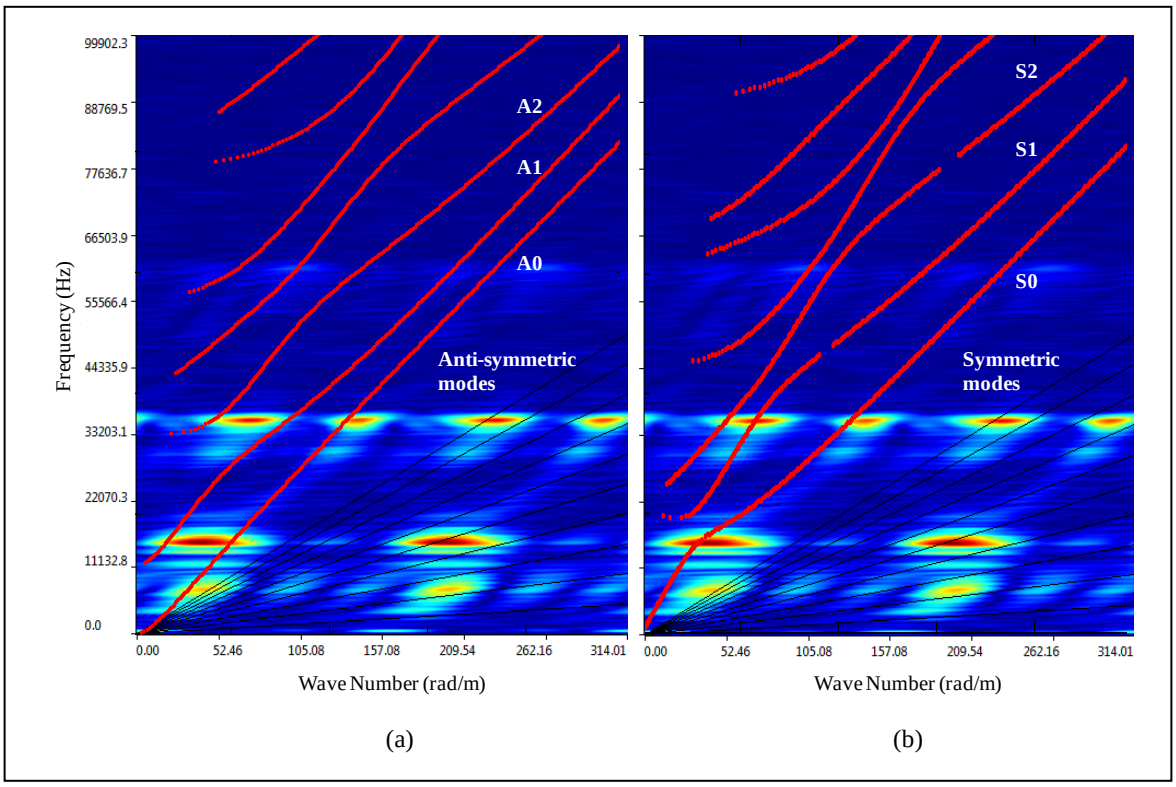

Figure 6-42. Experimental FK plots for the MASW measurements across the notch with superimposed (a) anti-symmetric modes and (b) symmetric modes.

Next, the experimental dispersion curves were plotted with the theoretical Lamb modes. Figure 6-43 shows good agreement between the experimental data and the fundamental anti-symmetric mode (A0). No significant difference was observed when the notch was present.

Figure 6-43 shows that the high energy areas are associated to the symmetric modes (S0 and S1), as suggested by the FK plots. In most cases, the perpendicular direction of the input excitation would generate purely flexural modes (i.e. anti-symmetric) in the medium, as illustrated by Figure 6-41(a). However, the notch creates a vertical disturbance in the wave propagation path. The disturbance is significant enough that other wave modes, such as extensional modes, can be generated. To achieve a better understanding of this phenomenon, numerical simulations and finite elements analysis should be conducted, which are not within the scope of this research.

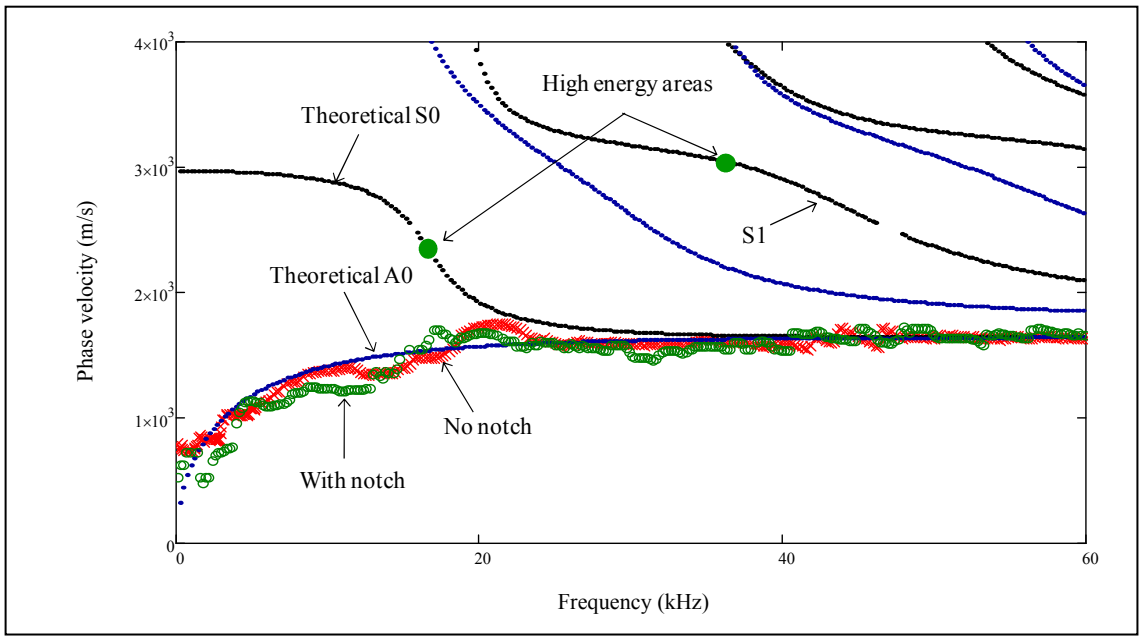

Figure 6-43. Dispersion curves measured across the joint (no notch) and across the notch.

Both measurements, with and without notch, displayed high energy areas (FK plot) associated to the fundamental anti-symmetric Lamb mode. No significant difference was detected between the two experimental dispersion curves. The change in wave velocity is widely used for flaw detection; however, using only the velocity properties is not conclusive. Conversely, attenuation measurements appear to be more reliable for the characterization of discontinuities and flaws.

6.5.3 Concluding Remarks

- The notch created a significant vertical disturbance in the wave propagation path, such that the reflections of the flexural wave modes generated extensional modes.
- The change in velocity should not be the only deterministic factor when applied to flaw evaluation. Other factors, such as attenuation values, should also be considered.

6.6 Pavement Condition Evaluation with Ground Penetrating Radar

Exploratory ground penetrating radar (GPR) measurements were used to evaluate its potential as a complementary method to wave-based tests.

6.6.1 Background

The purpose of this evaluation was to test the effectiveness of GPR at detecting and characterizing longitudinal construction joints in asphalt pavements. The tests were conducted with the support and assistance of Sensors & Software Inc.

Grid data were collected on three separate test slabs of 80-90 mm thick, two of which were transplanted from actual test sites, while the third was manufactured in the lab and included a longitudinal joint (Figure 6-1). This analysis concentrates primarily on the third slab, which was used for the ultrasonic testing. The GPR tests were conducted prior to the cut of the notch.

6.6.2 Instrumentation

Data was collected with a pulse EKKO PRO 1000 MHz GPR unit based on a standard 600 x 600 mm grid at both normal and high resolution. Only the high resolution data is discussed here. Data processing was performed using EKKO_Mapper 4 to obtain depth slice images, and with EKKO_View 2 to perform visual inspection of the individual cross-section data. Figure 6-44 shows the grid lines for data collection on slab 3.

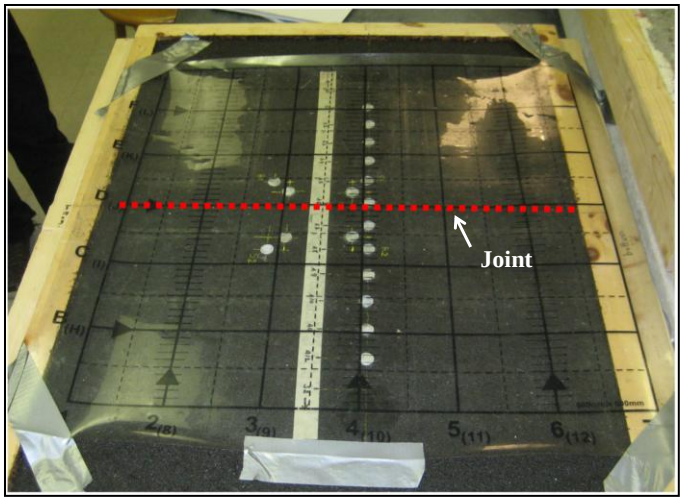

Figure 6-44. Photo of slab 3 showing the orientation of grid lines as well as the position and orientation of the pavement joint.

6.6.3 Results

Figure 6-45 shows a 30-40 mm depth slice image of slab 3 with the location of the joint indicated. The depth shown corresponds to approximately half way down into the pavement, and should, therefore be sensitive to the joint. The depth slice did not, however, show any indication of a horizontal feature in the vicinity of the joint. Similarly, when visually inspecting the cross-section, no visible changes were observed when crossing the location of the joint. This can be seen in Figure 6-46, where a representative cross section running perpendicular to the joint is shown.

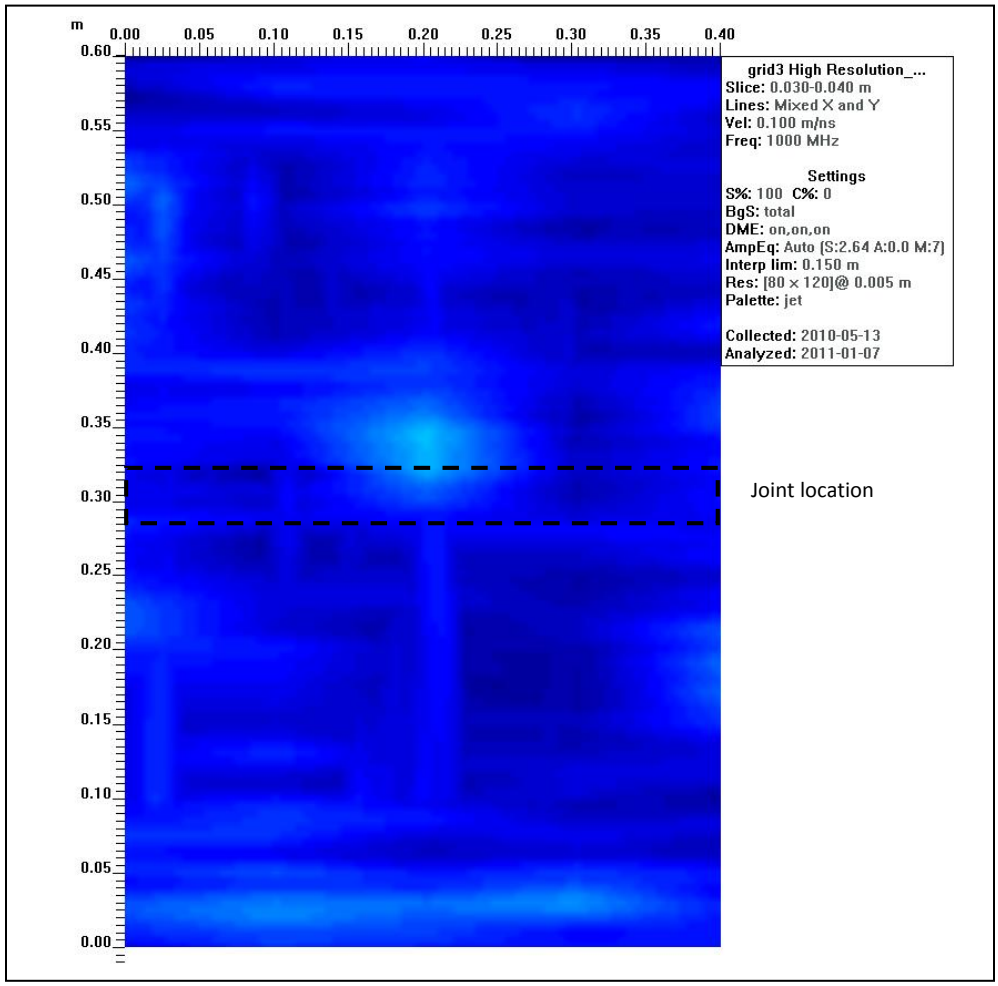

Figure 6-45. Depth slice image of Slab 3 with known joint running left to right at 0.30 m.

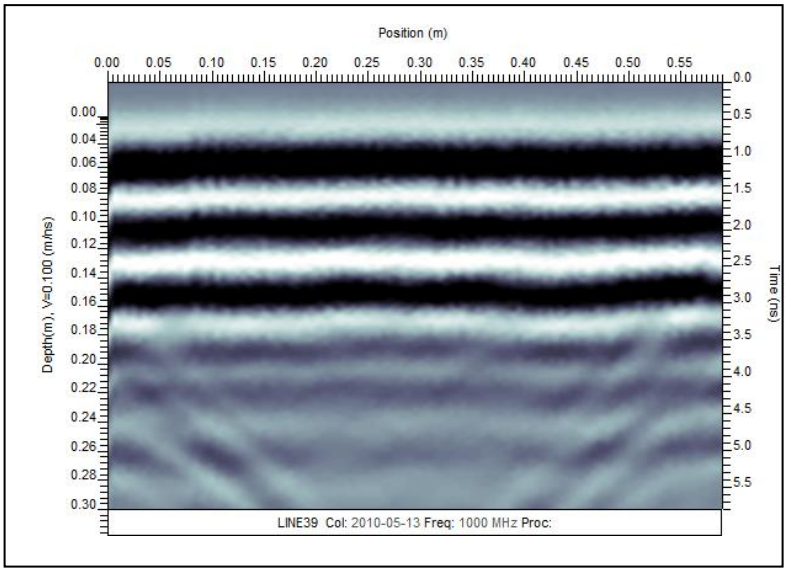

Figure 6-46. Cross-section image of a line perpendicular to the pavement joint (occurring at a position of 0.30 m).

A few profiles were also collected across the asphalt joint with the dipoles oriented perpendicular to the joint. These cross-sections did not show any significant response from the pavement joint.

A similar analysis was performed on both slab 1 and slab 2, however no significant features were detected in either the cross-section or depth slice images from these slabs which could be attributed to a pavement joint. There was a distinct feature visible in the slab 2 data, as shown in Figure 6-47, however this occurs at a depth (150 mm) nearly twice the thickness of the slab. This was most likely caused by the object highlighted in Figure 6-48 – a support bar between the slab and table.

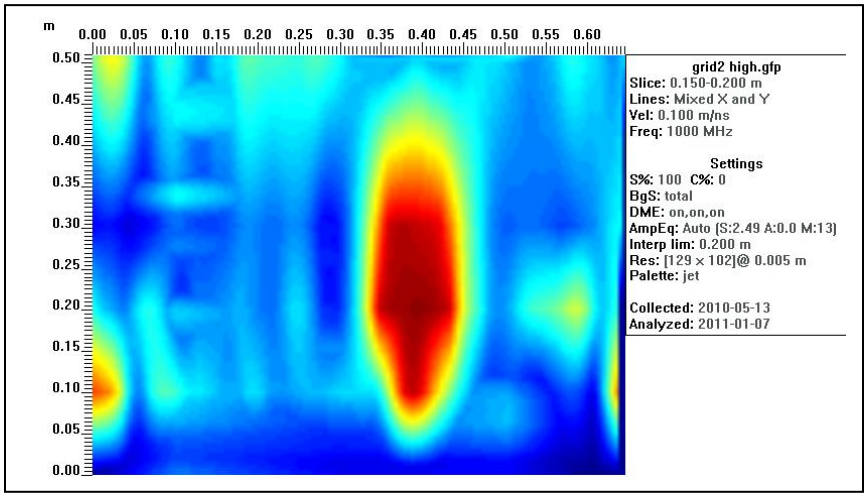

Figure 6-47. Depth slice image of slab 2 feature detected at a depth of 150 mm.

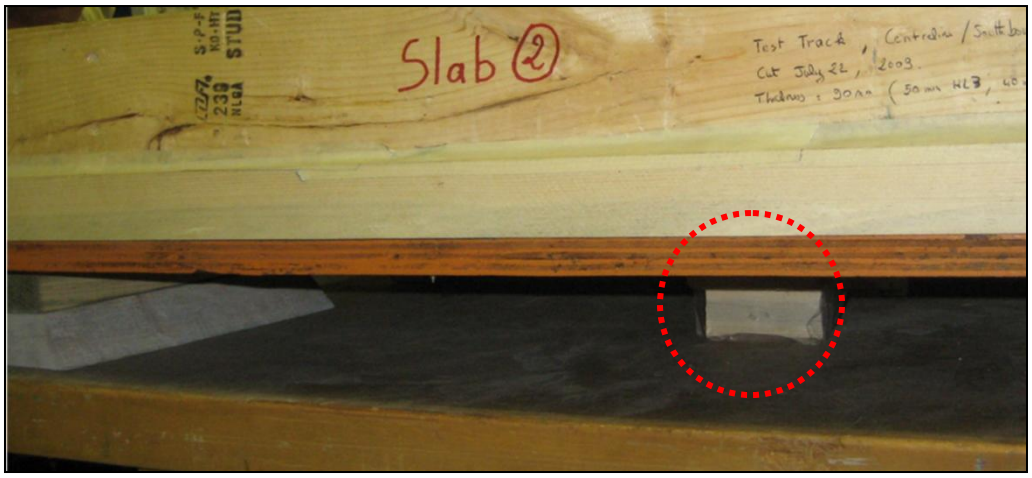

Figure 6-48. Photo of slab 2 showing a wood support bar between the table and the slab.

6.6.4 Concluding Remarks

The results did not show any clear evidence of the longitudinal joints measured in the laboratory. However, the presence of moisture and other debris in an existing pavement joint will have a greater effect on the GPR response. Therefore, more measurements should be carried out on new and old pavement in the field.

Higher frequency antennae (e.g. 1.5 GHz-2 GHz) used in recent studies (Ahmad et al., 2011; Surette et al., 2010) for thickness and crack detection in asphalt pavements showed good results. However, due to equipment limitation, only the 1000 MHz antenna was used. Further measurements are recommended.

CHAPTER 7. ULTRASONIC TESTING OF STEEL PIPES FOR THICKNESS EVALUATION (STUDY 2)

7.1 Introduction

NDT technologies are used to measure material thickness in a wide variety of industries, such as manufacturing quality control and in-service monitoring (Basravi, 2004). Nondestructive methods have the ability to precisely measure wall thickness in situations where access is available to only one side of a test piece. They are applicable for pipe assemblies in heat exchangers and heat generators at power plants and petrochemical facilities. The loss of wall thickness in pipelines can affect the reliability and safety of the plant (Hwang et al., 2002).

Electromagnetic NDT methods (Section 4.3.1), such as the eddy current and the remote field testing methods, are common tools for thickness measurement of conductive materials (Angani et al., 2010; Park et al., 2010; Robers and Scottini, 2002). The ultrasonic thickness gauge is currently one of the most popular methods for determining steel plate thicknesses (Damgaard, 2009). A major drawback of this method is that the equipment must be calibrated prior to the test for the sound velocity and zero offset appropriate for the application at hand. Furthermore, these methods give only localized results where measurements are made, making the process time consuming and inaccurate for assessing the full cross-sectional area of the pipe (Section 4.3.3).

Lamb waves can be used for the thickness evaluation of metal tubing (Silk and Bainton, 1979). In particular, the time of flight (TOF) measurement techniques have been used to obtain the Lamb wave phase velocity, which can be related to the thickness of a steel wall (Pei et al., 1996). The TOF measurement of a zero-order anti-symmetric Lamb wave was fitted to the theoretical dispersion curve to compensate for the electronic time delays; the calibrated phase velocity was then used to compute an average thickness value.

In a similar study, an ultrasonic inspection technique using Lamb waves was evaluated to detect and determine the location of flaws in long steel pipes (Park et al., 1996). Using the

TOF measurements and the wedge excitation method to generate a specific Lamb wave mode, the inspection of a long axial length of piping using Lamb waves generated from a single location was possible. It was found that the A0 mode had the minimum energy loss over long carbon steel pipes (365 cm), and yielded the best inspection results. However, this technique requires a liquid couplant between the transducer and the plate.

Lamb waves are used for the evaluation of steel pipes; however, the existing techniques require prior calibration to a known wave mode and, due to wave attenuation effects, lose accuracy for evaluating great lengths (Park et al., 1996; Pei et al., 1996).

The multichannel analysis of surface waves (MASW) method is able to identify and separate the different modes of surface waves. The dispersion curve obtained with this technique comprises the fundamental modes and the higher modes, providing an improved wave velocity profile.

The study presented in this chapter utilizes the MASW technique for the evaluation of average thickness of steel plates and pipes. The experimental dispersion curves are generated and compared to the theory. The wall thickness of the steel can be determined from this process.

7.2 Thickness Evaluation of Steel Plates

Steel plates with different thicknesses were used for the testing procedure; next, the experimental dispersion curves were constructed with the computer program SWAN (Russo, 2006). Finally, the thickness values were determined by comparing the experimental curves to theory (Section 2.2.3), where the symmetric and anti-symmetric fundamental modes converge to the R-wave velocity at wavelengths of half the plate thickness.

7.2.1 Testing Methodology and Experimental Setup

Lamb waves (also known as plate waves) were generated from the interaction of the surface waves with the boundaries, in a medium with two free surfaces and with a thickness of

approximately one wavelength. The frequency range required for the testing procedure depends on the thickness of the plate samples.

Three cold rolled steel plate samples with different thicknesses were used for the test: 1/2 in (12.7 mm), 1/4 in (6.3 mm) and 1/8 in (3.2 mm). The average P-wave and R-wave velocities of steel were determined to be approximately 5200 m/s and 2750 m/s, respectively. It is necessary to select suitable receiver devices, capable of capturing specific frequency ranges. Given the surface wave velocity, wavelengths larger than the plate thickness (1/2 in, 1/4 in and 1/8 in) can be generated by frequencies lower than 200 kHz, 400 kHz and 800 kHz, respectively.

Two transmitters were selected to generate mechanical waves in the specimen: 50 kHz and 1 MHz (Panametrics V102, 1 in diameter). A piezoelectric transducer (PCB 352A60) with a resonant frequency of 95 kHz was used to capture the response signals. The excitation pulse was generated by a waveform generator (HP 33120A) and a piezo driver (E1340). The power supply of the accelerometers (Dytran 4123B) has selectable amplification factors of 1, 10 and 100. The time signals were recorded on a 24-channel data acquisition system with a 1 MHz sampling rate (LDS Nicolet Genesis). The experimental setup for the test is schematically illustrated in Figure 7-1. An array of 59 positions (with 5 mm spacing) was located on the surface of each plate; the receiver captured the response at each location while the source was located at 25 mm from the first position.

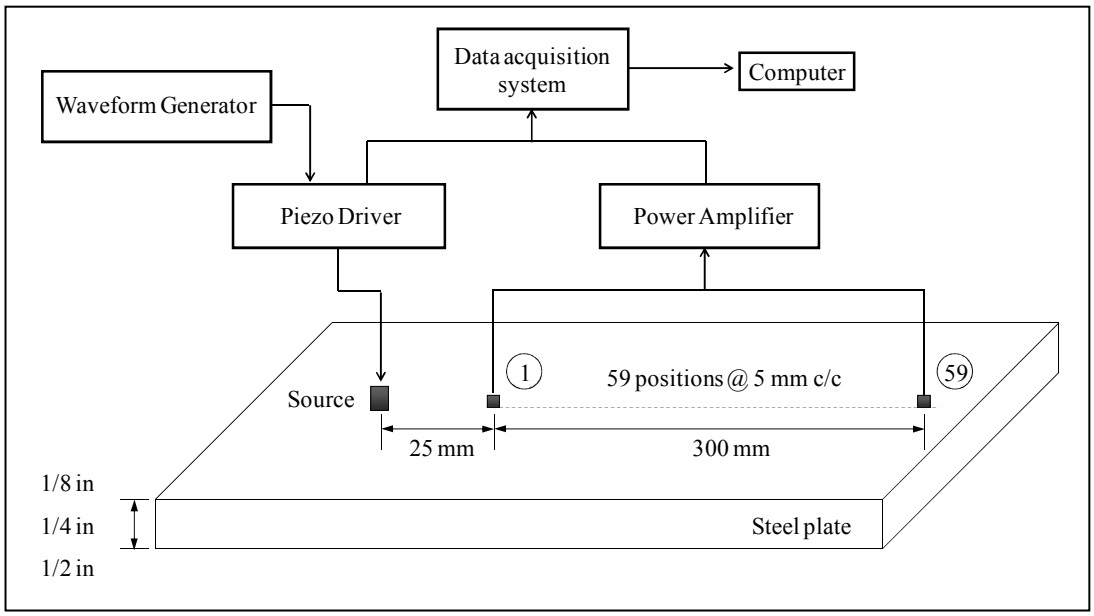

Figure 7-1. Experimental setup for the thickness evaluation test.

7.2.2 Results

Steel plate with thickness of 1/2 in (12.7 mm)

The 50 kHz transducer was used as the transmitter while the PCB receiver was used to capture the response signals at the 59 inline locations. Time signals were recorded with a sampling rate of 1 MHz over a period of 4 ms. Normalized signals are presented in Figure 7-2. The P-wave arrival was determined from the graphs (dotted line), and the P-wave velocity was approximated as 5150 m/s. However, the surface wave arrival was not obvious due to the high reflection content. Thus, the R-wave velocities were calculated using the experimental dispersion curves. Figure 7-3 shows typical normalized Fourier spectra.

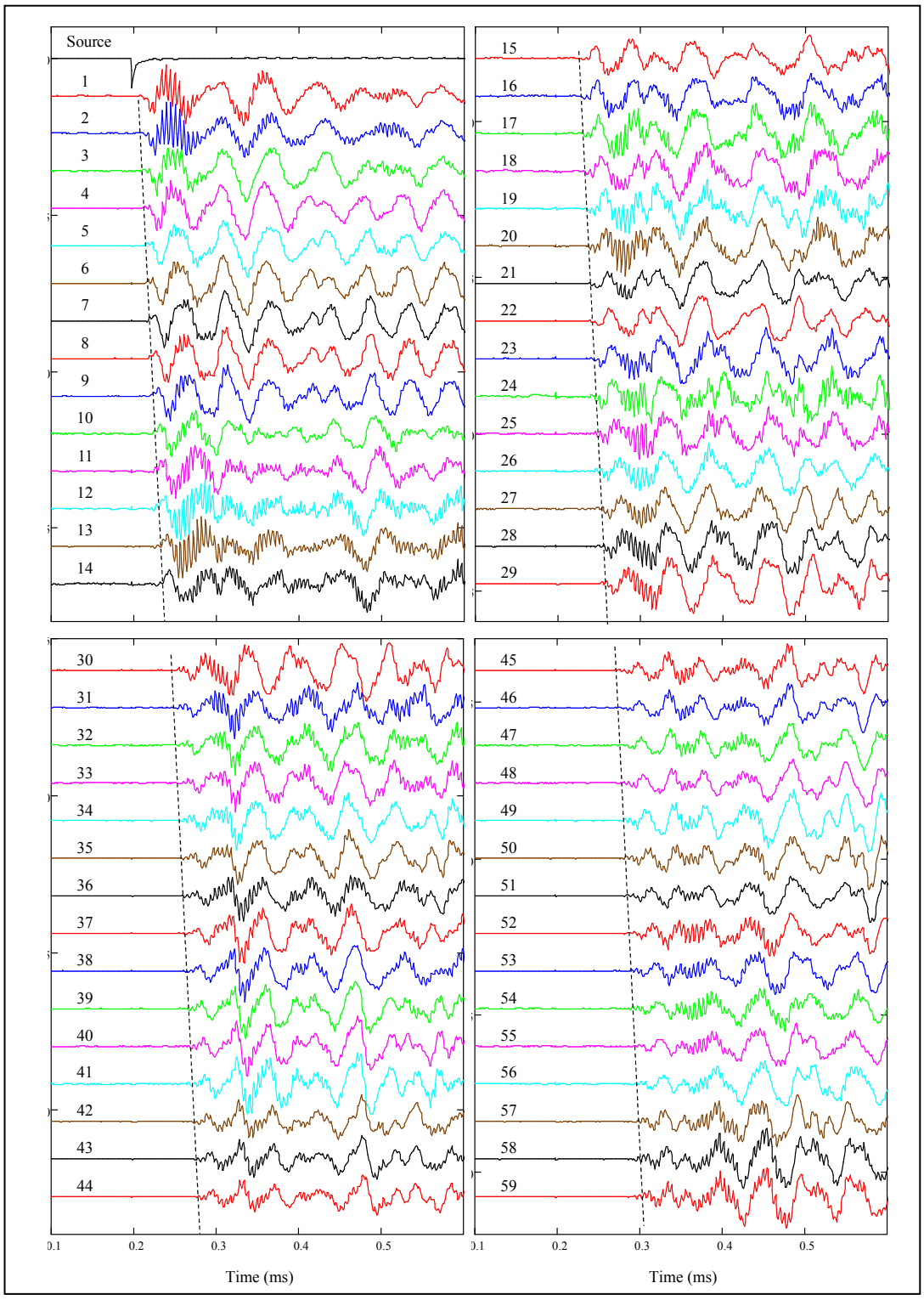

Figure 7-2. Normalized time signals for all 59 positions; steel plate thickness: 12.7 mm.

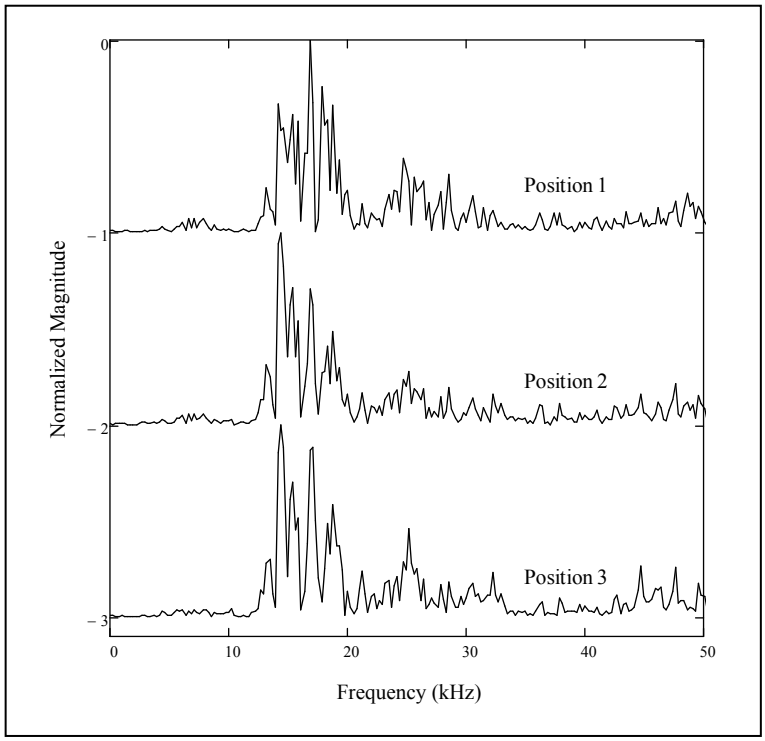

Figure 7-3. Normalized Fourier spectra for positions 1, 2 and 3.

The experimental dispersion curves were constructed using the program SWAN from raw data collected by the receiver at 59 locations from the source. First, the DC component and the noise were removed from the time signals. Then, the frequency vs. wave number (FK) spectrum was computed, providing the energy distribution of the different propagation modes (Figure 7-4). Most of the wave energy was detected at frequencies between 15 kHz and 40 kHz (Figure 7-3), corresponding to Lamb modes. In theory, surface waves propagate at frequencies above 200 kHz. Consequently, mainly Lamb waves were generated in the plate. Next, the maxima of the FK spectrum were selected to extract the experimental dispersion curve.

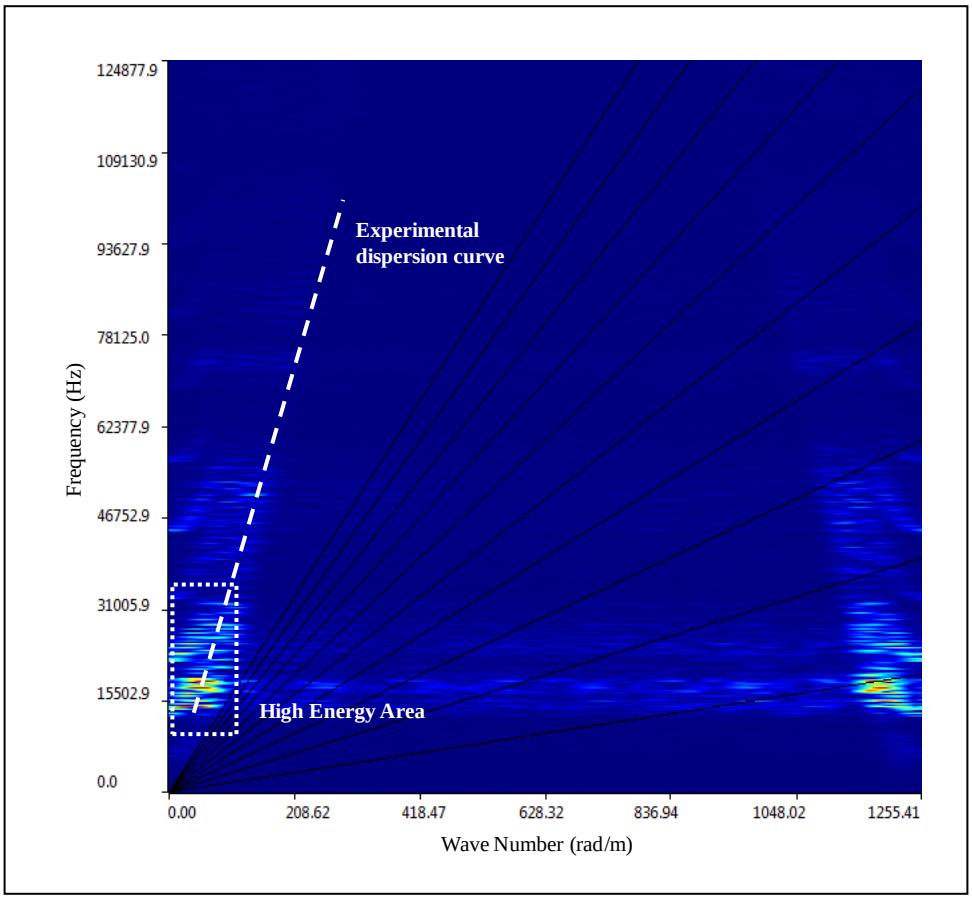

Figure 7-4. FK spectrum for the steel plate with a thickness of 12.7 mm.

The experimental dispersion curves were computed using the FK spectrum. At high frequencies where the plate thickness is large relative to the wavelength, the plate behaves like a half-space for R-wave propagation, and surface waves can propagate independently on the top surface of the plate without any interference from the bottom surface. Hence, Lamb wave modes tend toward a constant Rayleigh velocity at high frequencies. The R-wave velocity was then determined from the dispersion curve to be approximately 2750 m/s. The dispersion curves (phase velocity vs. frequency) were computed from the experimental data and were compared to the theoretical dispersion curves (Figure 7-5). The theoretical dispersion curves of the fundamental anti-symmetric (A0) and symmetric (S0) Lamb modes were computed using V_P = 5400 m/s, V_R = 3000 m/s and a half plate thickness of h = 6.35 mm (Yang, 2009). The experimental data matches very well with the theoretical curves. Furthermore, higher-order modes were captured (at nascent frequencies of around 200 kHz)

and appear to follow the theoretical A1 mode. The appearance of the waveforms depends critically on the frequency range provided in the test.

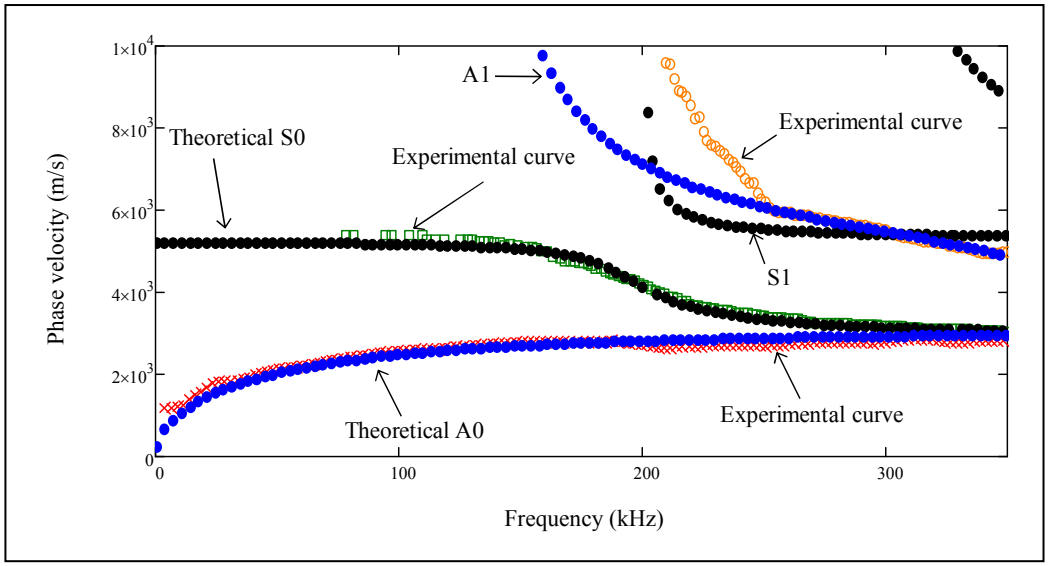

Figure 7-5. Dispersion curves for the steel plate with a thickness of 12.7 mm.

Steel plate with thickness of 1/4 in (6.3 mm)

The 1 MHz transducer was used as the transmitter while the PCB accelerometer was used to receive the response signals at all 59 positions. Time signals were recorded with a sampling rate of 1 MHz over a period of 4 ms; normalized signals are presented in Figure 7-6. The P-wave arrivals can be determined from the graphs (dotted line), and the P-wave velocity was computed to be approximately 5090 m/s. The S-wave velocity can be determined from the dispersion curve, as previously discussed.

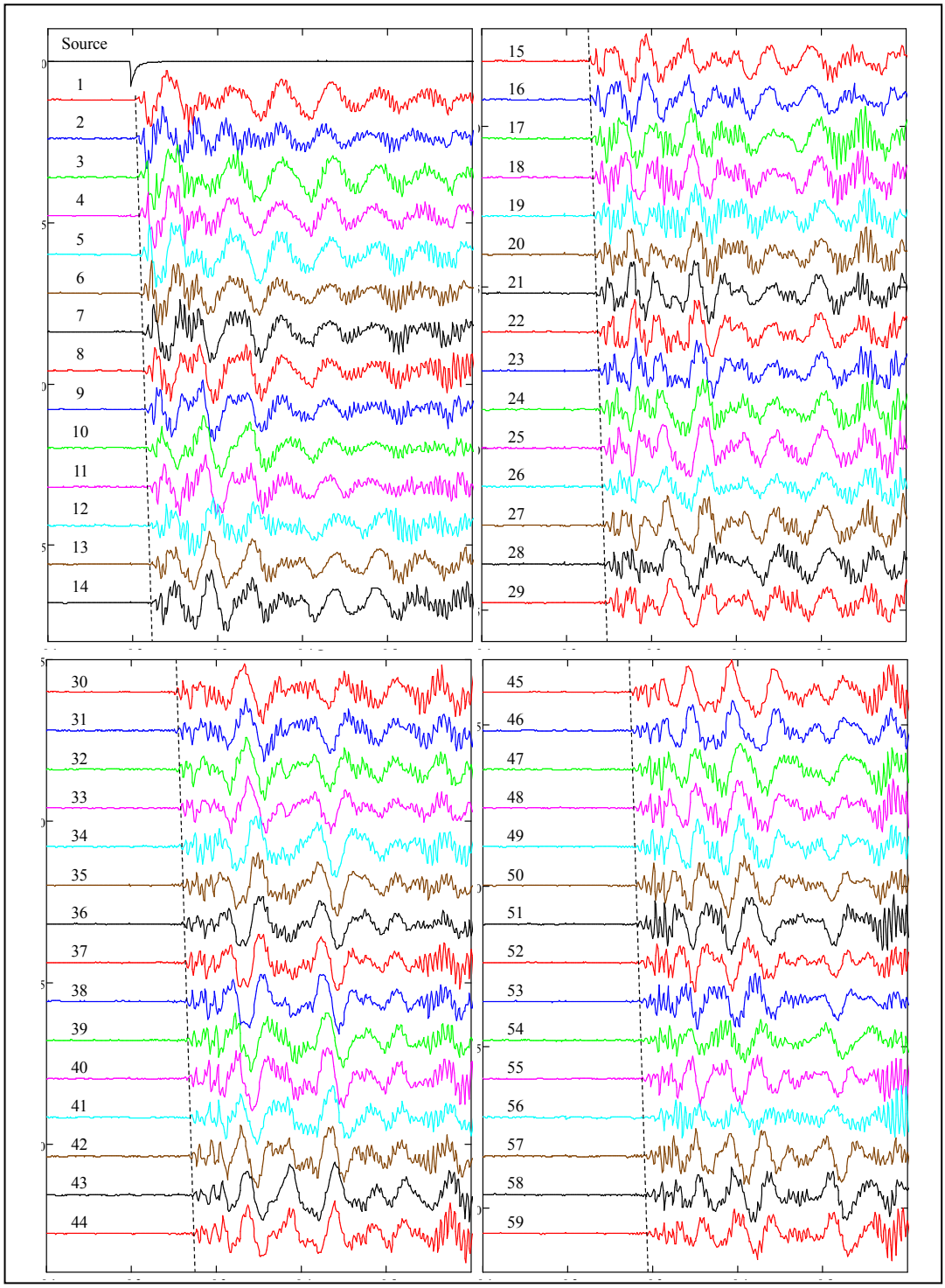

Figure 7-6. Normalized time signals for all 59 positions; steel plate thickness: 6.3 mm.

Similar to the 12.7 mm plate, the experimental dispersion curves were constructed using the program SWAN from raw data collected by the receiver at 59 locations from the source. The

DC offset and the noise was removed from the time signals, and the FK spectrum was computed, as shown in Figure 7-7. Most of the wave energy was observed at frequencies between 15 kHz and 60 kHz, which correspond to Lamb modes. In 6.3 mm steel plates, surface waves propagate at frequencies above 400 kHz.

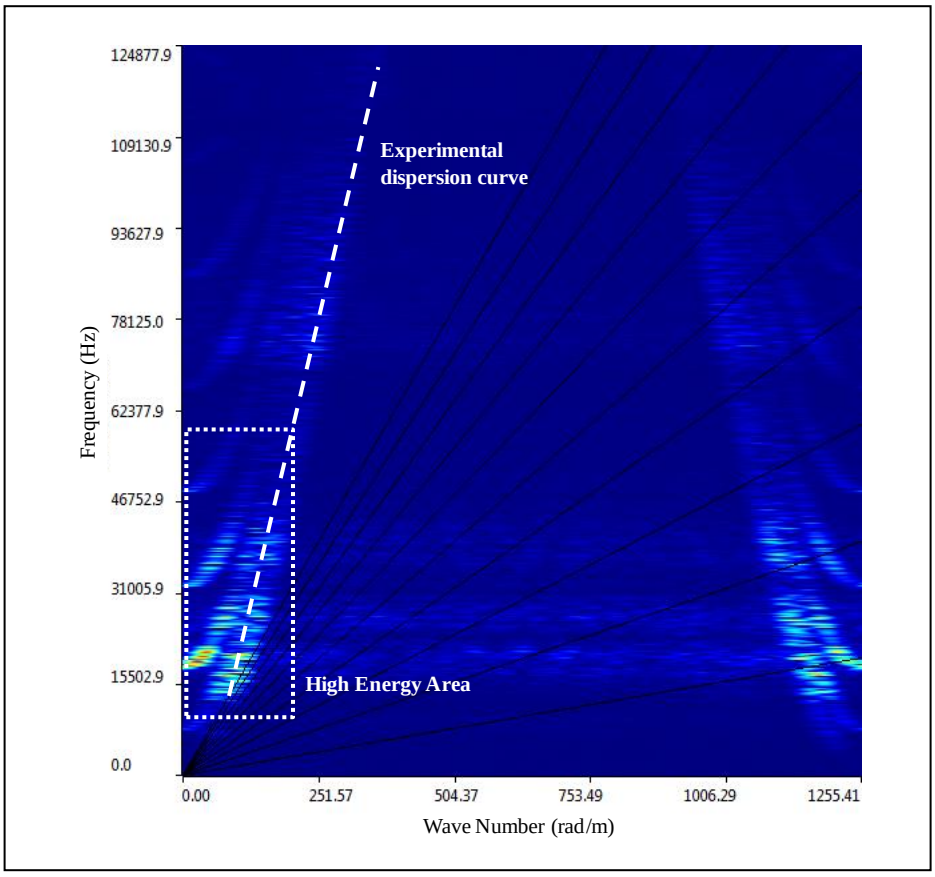

Figure 7-7. FK spectrum for the steel plate with a thickness of 6.3 mm.

Next, the experimental dispersion curves were computed using the FK spectrum. The R-wave velocity was determined from the dispersion curve as approximately 2690 m/s. The theoretical and experimental dispersion curves are presented in Figure 7-8; frequencies up to 500 kHz were captured. The theoretical dispersion curves were computed using V_P = 5000 m/s, V_R = 2650 m/s and a half plate thickness of h = 3.15 mm (Yang, 2009). The dispersion curve appears constant at 870 kHz, which corresponds to wavelengths half of the plate thickness and surface waves propagate at a constant velocity.

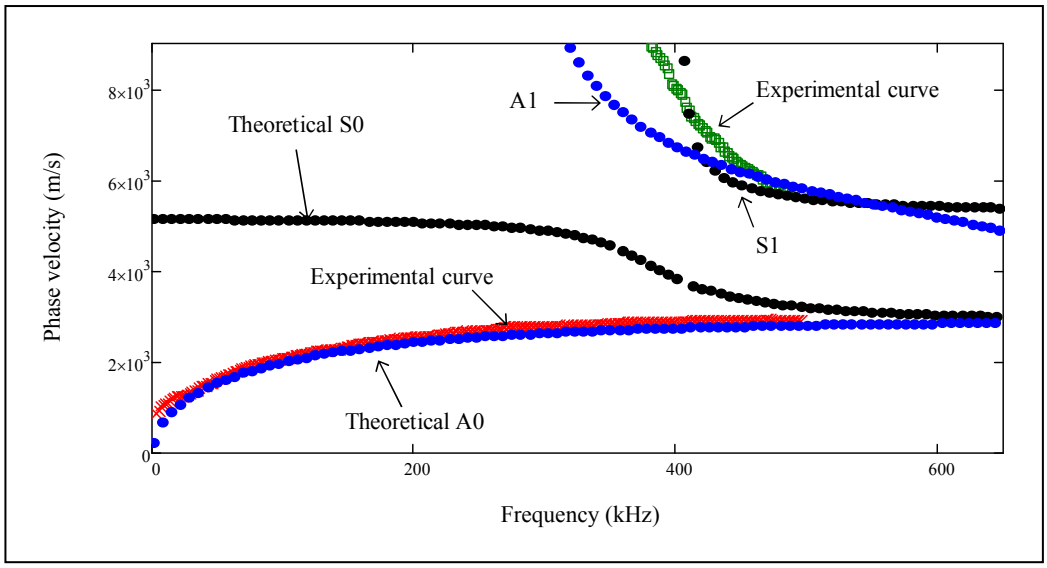

Figure 7-8. Dispersion curves for the steel plate with a thickness of 6.3 mm.

The experimental dispersion curve appears to follow the theoretical A0 mode; the fundamental symmetric mode was not generated. The source excitation was positioned perpendicular to the surface of the plate, generating flexural Lamb wave modes (anti-symmetric) as opposed to extensional modes (symmetric). Higher-order modes were detected to be corresponding to the A1 mode. Frequencies above 500 kHz were not captured by the receiver's limited frequency range.

Steel plate with thickness of 1/8 in (3.2 mm)

Analogous to the 6.3 mm thick plate, the 1 MHz transducer was used as the source and the PCB receiver was used to capture the response signals at all 59 positions. Time signals were recorded with a sampling rate of 1 MHz over a period of 4 ms; normalized signals are presented in Figure 7-9. The P-wave velocity was determined as 5068 m/s; the S-wave velocity can be determined using the dispersion curve.

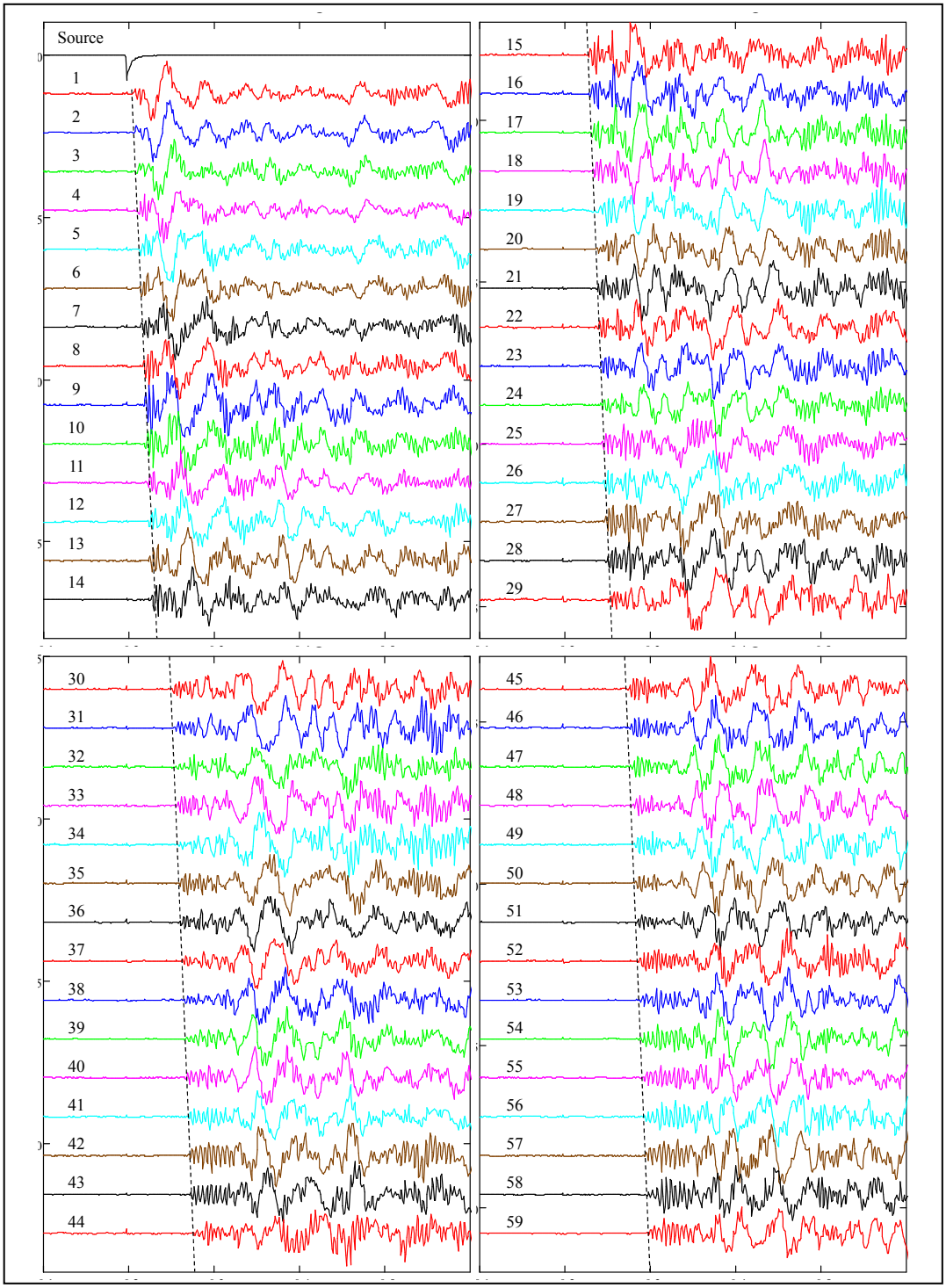

Figure 7-9. Normalized time signals for all 59 positions; steel plate thickness: 3.2 mm.

Next, the experimental dispersion curves were constructed using the program SWAN from the data at 59 locations from the source. The DC offset and the noise were removed from the

time signals. The FK spectrum is shown in Figure 7-10. Most of the wave energy was observed at frequencies between 15 kHz and 80 kHz, which correspond to Lamb modes.

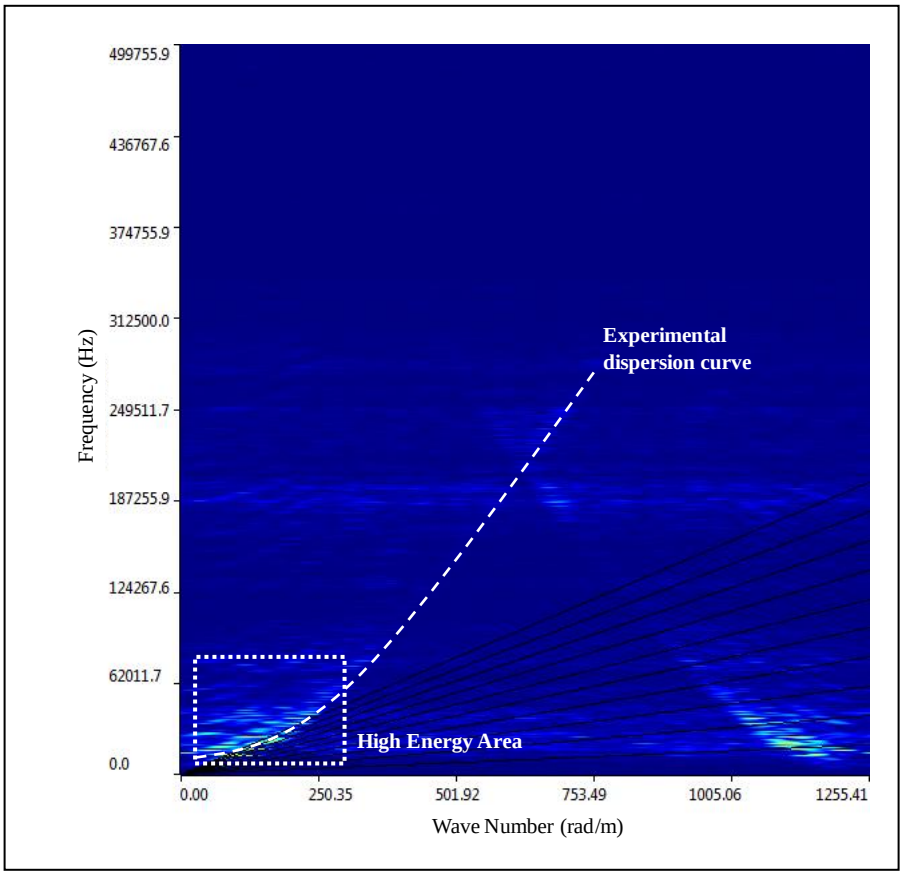

Figure 7-10. FK spectrum for the steel plate with a thickness of 3.2 mm.

The experimental dispersion curves were computed from the FK spectrum. In the 3.2 mm steel plate, surface waves propagate at frequencies above 800 kHz. Due to the frequency limitations of the receiver and the program SWAN, surface waves were not captured. The R-wave velocity could not be determined from the experimental dispersion curve. However, assuming the same velocity determined for the 6.3 mm plate (2690 m/s), the theoretical dispersion curves were computed (Figure 7-11) using V_P = 5000 m/s, V_R = 2650 m/s and a half plate thickness of h = 1.65 mm (Yang, 2009). The theoretical curves tend towards a constant value at frequencies higher than 1 MHz that corresponds to wavelengths shorter than the plate thickness. At this frequency, the medium is no longer dispersive and surface waves can propagate at a constant velocity.

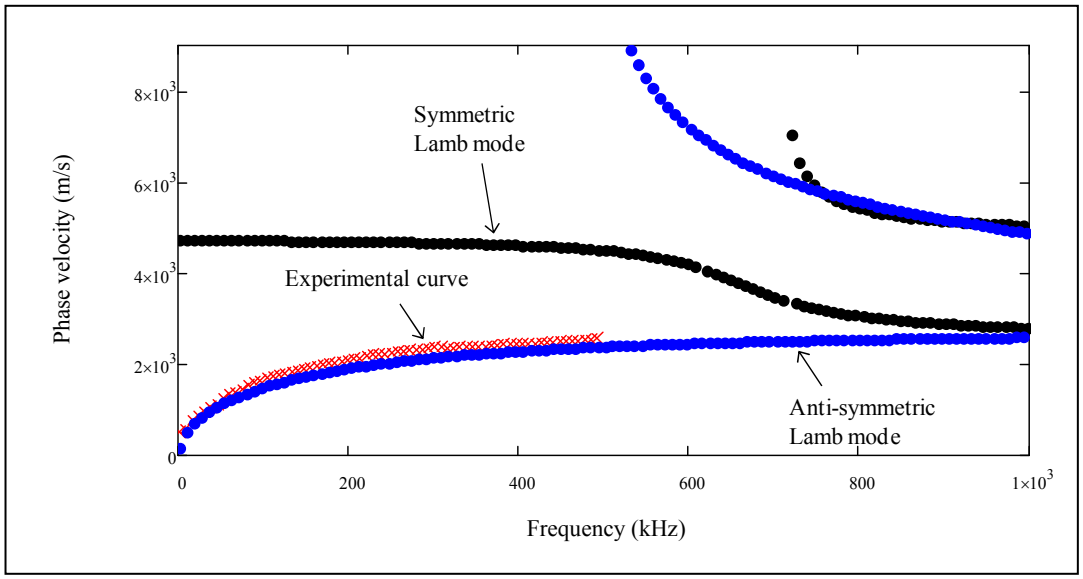

Figure 7-11. Dispersion curves for the steel plate with a thickness of 3.2 mm.

The experimental dispersion curve followed the theoretical anti-symmetric mode at frequencies lower than 500 kHz.

7.3 Thickness Evaluation of Steel Pipe

The same experimental setup and testing configuration was used to test on a steel pipe with an internal diameter of 204 mm and a wall thickness of 6 mm (Figure 7-12). The 1 MHz transducer was used as the source and the PCB receiver was used to capture the response signals at all 59 positions. Time signals were recorded with a sampling rate of 1 MHz over a period of 4 ms.

As discussed in the previous section, the frequencies above 500 kHz were not captured by the limited range of the accelerometer.

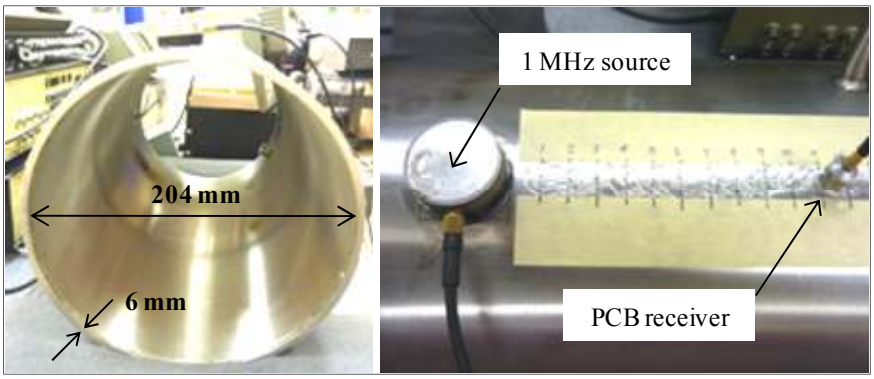

Figure 7-12. Test setup of the steel pipe with a wall thickness of 6 mm, and input excitation perpendicular to the surface.

Similar to the 6.3 mm steel plate results, the experimental dispersion curve matched well to the theoretical A0 mode, as shown in Figure 7-13. Higher-order modes were not detected. The results using MASW methodology showed good agreement with the theoretical A0 mode. The curvature effect of the pipe on the fundamental anti-symmetric mode was not detected in the Lamb wave mode structure.

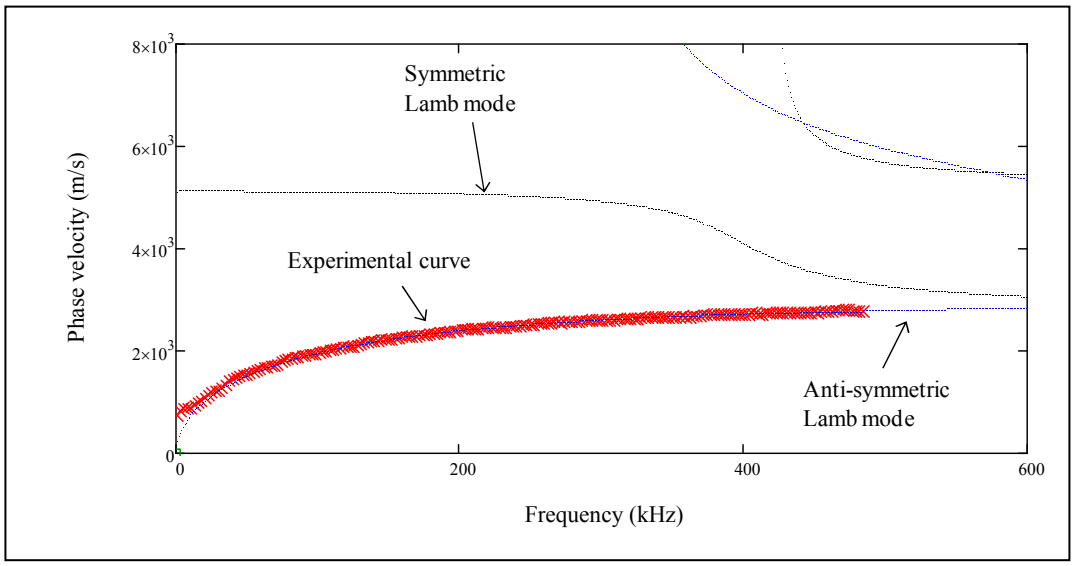

Figure 7-13. Dispersion curve for the steel pipe with input excitation perpendicular to the surface.

Next, the source excitation was positioned parallel to the surface of the plate, as shown in Figure 7-14, generating extensional Lamb wave modes (symmetric) as opposed to flexural modes (anti-symmetric).

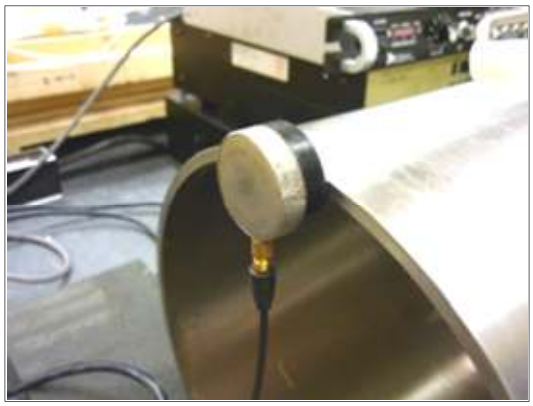

Figure 7-14. Test setup of the steel pipe with the input excitation parallel to the surface.

Figure 7-15 shows that a higher energy concentration is associated with the fundamental symmetric mode (S0). Another energy region was detected to follow the fundamental anti-symmetric mode (A0). Consequently, the input excitation parallel to the pipe surface successfully generated extensional vibration modes.

The dispersion curves were computed (Figure 7-16). Both experimental curves appeared to be in good agreement with the fundamental modes (S0 and A0). Hence, Lamb waves were generated.

These preliminary results show the capability of the MASW methodology for providing reliable thickness information about the steel pipe wall. The average thickness can be determined from the inversion process once the experimental dispersion curves were obtained. This process consisted of constructing a theoretical dispersion curve by assuming a shear wave velocity profile. The experimental and theoretical curves were compared, and the assumed shear wave velocity was modified through an iterative process until the two curves match within a reasonable tolerance.

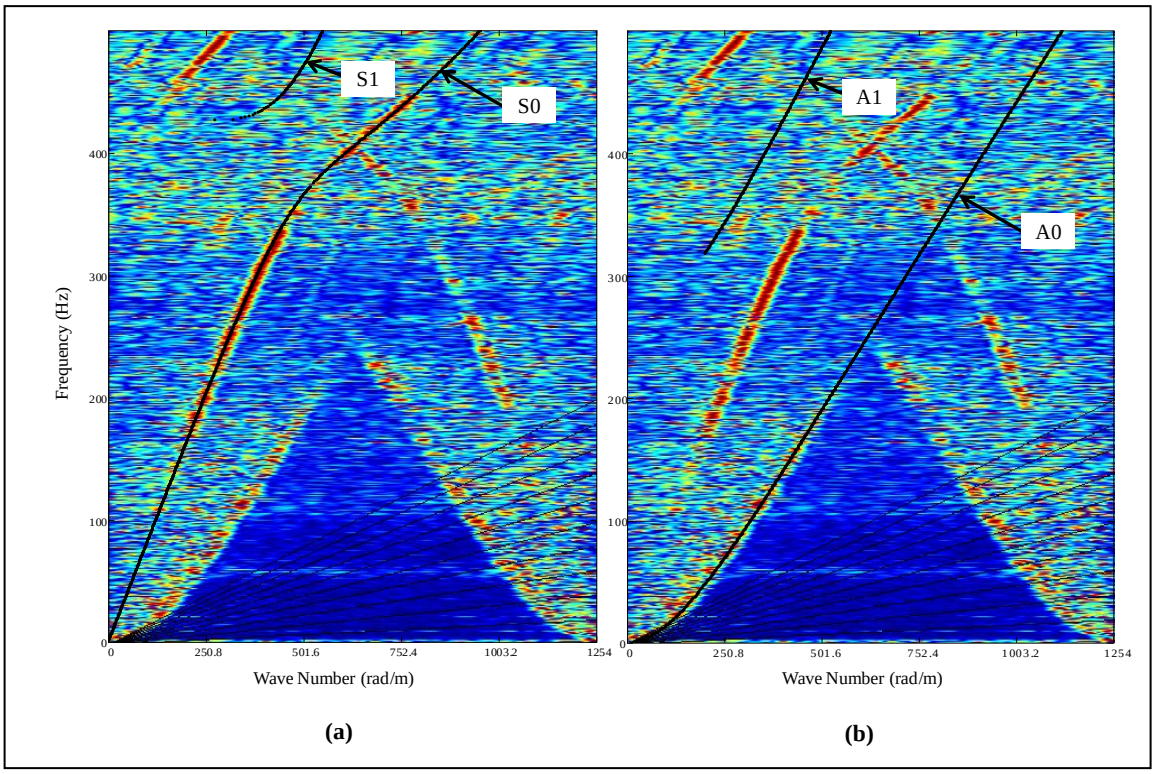

Figure 7-15. Experimental FK plots for the steel pipe with an input excitation parallel to the surface, showing superimposed (a) symmetric modes and (b) anti-symmetric modes.

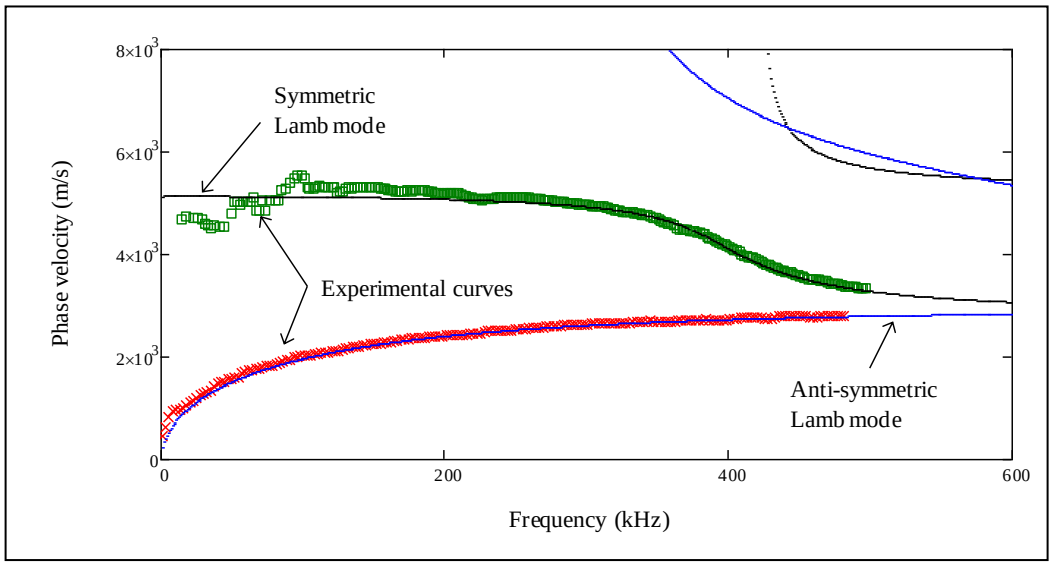

Figure 7-16. Dispersion curve for steel pipe with an input excitation parallel to the surface.

7.4 Concluding Remarks

- Lamb waves were generated in the steel plates. The FK spectra revealed energy concentration at frequencies between 15 kHz and 80 kHz, corresponding to Lamb modes.
- The experimental data matched very well with the theoretical dispersion curves of the fundamental modes in all three cases of steel thickness.
- The zero-order (or fundamental) modes were observed in the experimental dispersion curves for all three steel samples. As the frequency increases and the wavelength approaches the plate thickness, the fundamental modes begin to converge towards the Rayleigh wave velocity.
- The fundamental anti-symmetric mode (A0) was observed to be highly dispersive in the low frequencies.
- In the test for the 12.7 mm plate, both symmetric and anti-symmetric fundamental modes were excited and detected; only the anti-symmetric mode was detected for the 6.3 mm and 3.2 mm plates. Due to the input pulse configuration (perpendicular to the surface), the anti-symmetric mode was the more easily excited of the two fundamental modes.
- In the case of the 12.7 mm and 6.3 mm plates, higher-order modes were observed in the experimental dispersion curves (at nascent frequencies of around 200 kHz and 400 kHz, respectively). On the contrary, no higher-order modes were detected in the thinnest plate of 3.2 mm. The appearance of the waveforms depends critically on the frequency range (or wavelength generation) provided for the testing.
- The MASW methodology shows promising results for thickness estimation of steel plates. The provided frequency range is critical and must be suitable for the piece under investigation. The proposed testing configuration allows the captured signal to be viewed in real time; thus, making it possible to change the testing frequency to best fit the thickness under investigation.
- Transducers with higher centre frequencies (> 500 kHz) are needed for generating suitable wavelengths used in the investigation of plate thickness, particularly for thinner plates (< 6 mm).

- This technique can be used to assess any plate thickness by adjusting the testing frequency such that the generated wavelengths are approximately equal to the plate thickness.
- The MASW methodology allows for the estimation of thickness in larger structures such as concrete slabs and asphalt pavements. Lamb waves are generated in the medium as the surface waves interact with the two free surface boundaries and with a thickness of approximately one wavelength.
- The curvature effect of the pipe specimen on the low order Lamb wave modes did not affect the Lamb wave mode structure.

CHAPTER 8. ULTRASONIC TESTING OF GROUTED STEEL TANK FOR DEBONDING EVALUATION AND VOID DETECTION (STUDY 3)

8.1 Introduction

Detection of voids or debonding conditions is a common application for nondestructive evaluation in a variety of engineering and construction situations. This study involves the use of ultrasonic techniques for the detection of voids and debonding conditions in a grouted steel tank.

Despite recent advances in the performance of geophysical methods, the detection of voids is still a challenging problem. At shallow depths, ground-penetrating radar (GPR) has been used successfully; however, when high conductivity materials such as metals are involved, penetration problems arise. When there are changes in the water content, microwave radiometric and electromagnetic radio imaging methods also lose their applicability. New nondestructive testing (NDT) methods are needed for the detection of voids.

The multichannel analysis of surface waves (MASW) is a geophysical technique that is gaining acceptance for the detection of underground cavities. The MASW method was developed for the soil profile estimation and has been successfully used to estimate the soil stiffness profile of a site. It allows an effective noise removal process, identification of high order Rayleigh wave modes, and a faster data collection procedure (Park et al., 1999). The MASW method is performed on the surface of the medium without disturbing the existing conditions. Since Rayleigh waves carry a large portion of the excitation energy close to the surface (Richart et al., 1970), a relatively low energy seismic source is required for the test. The dispersion curve obtained with this technique comprises the fundamental mode and the higher modes, providing an improved wave velocity profile.

In this study, four ultrasonic experimental setup configurations are used with different frequency ranges to test a laboratory scale grouted steel tank. The MASW method is used to generate the experimental dispersion curves; a comparison with the theoretical dispersion curves is used to detect debonding conditions between the tank walls and the grout. Low-frequency acoustic waves are generated to penetrate into the grout material where the effect of the voids is assessed.

8.2 Background

The application involved the decommissioning of a large steel tank in an industrial environment; where the dismantling or demolishing the tank was not feasible, so it was proposed to solidify the tank for permanent decommissioning using a lightweight cementitious grout. The proposed procedure would involve pumping grout into the tank through tremie pipes to displace water stored in the tank while filling the tank volume. The grout would solidify the tank to maintain its structural integrity, and the high pH of the cement-based grout would protect the inner surfaces of the steel tank against corrosion over the long-term. A highly flowable, lightweight cement-bentonite grout was developed for this application.

The geometry of the tank was not regular, and included several internal stiffening beams on the bottom of the tank. This required the grout to flow over and through a series of obstacles to fill the tank while minimizing void space caused by trapped water. Due to the challenging placement conditions, it was decided to conduct a grout placement trial to assess the viability of the proposed solidification method and to verify the performance of the grout under realistic conditions. A steel mock-up of a portion of the tank was constructed, as shown in Figure 8-1.

The mock-up included two full-scale stiffening beams that subdivided the tank into three sections. Copes, or openings, were present in the bottom and top corners of the web of the stiffening beams to facilitate water flow between the tank sections. The thickness of all steel plate in the mock-up was 6.35 mm (0.25 in). The test tank was filled with water to simulate the working conditions, and then solidified with the cement-bentonite grout by injection of

the grout through a tremie tube inserted below the water level. The tremie tube was kept in one position during grouting, requiring the grout to flow through the openings in the stiffening beams, and over the top of the stiffening beams, in order to completely fill the tank.

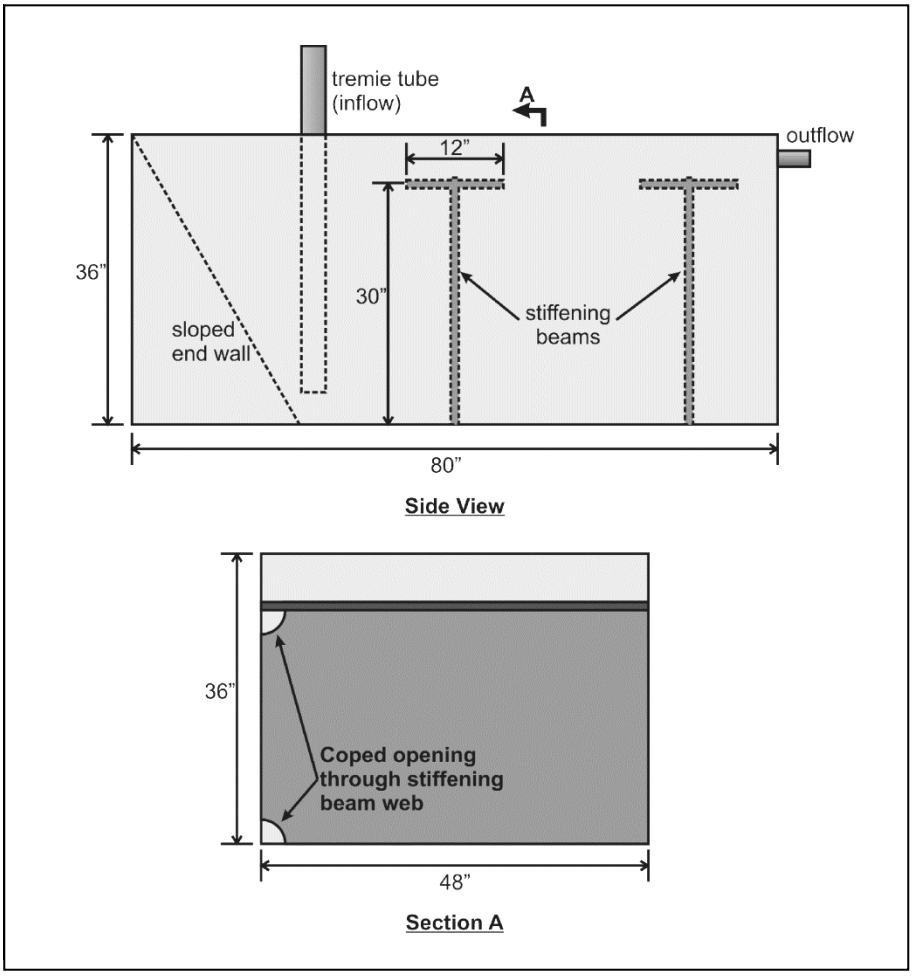

Figure 8-1. Details of steel tank mock-up used for grouting trial.

The adequacy of the grouting operation was observed during placement through two viewing windows provided in the mock-up walls. As well, a destructive examination was conducted after the grout had hardened to assess the completeness of the grouting and the presence of any voids or trapped water. Furthermore, since the conditions of the actual application do not allow for the grouting operation to be observed directly, nondestructive methods were used to detect voids in the grout, as well as debonding conditions between the grout and the interior surface of the tank due to grout shrinkage after hardening.

8.3 Testing Methodology and Experimental Setup

The details of the steel tank mock-up are shown in Figure 8-1. The flow of grout during filling was expected to entrap water under the flanges of the stiffening beams, as illustrated in Figure 8-2. MASW tests were used to detect void locations under the beam flanges, and two plastic bottles (one air-filled and one water-filled) that were placed in the tank immediately after grouting to simulate air- and water-filled voids. The bottles were placed against the tank walls at the locations shown in Figure 8-2.

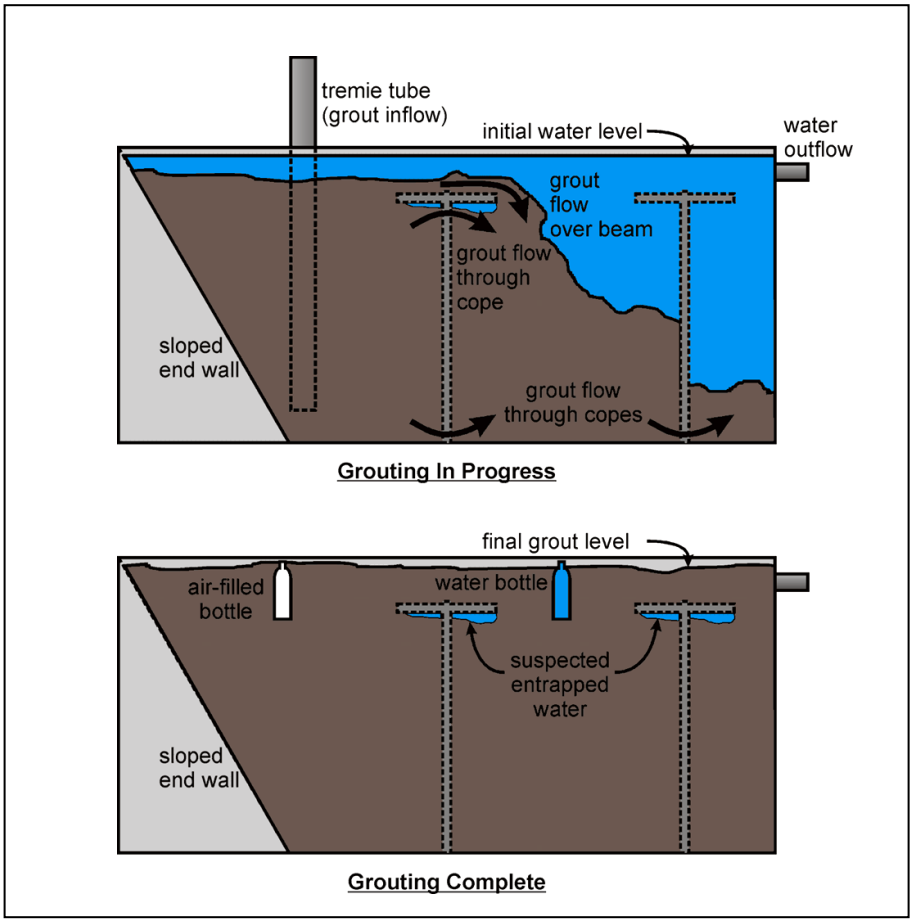

Figure 8-2. Grouting operation and location of suspected and intentional voids.

The testing methodology consisted of four sets of ultrasonic testing:

- **Test 1:** Ultrasonic measurements along the side of the tank near the grout surface, adjacent to and away from the voids simulated by the bottles.
- **Test 2:** MASW measurements along the side of the tank near the bottom and with no stiffening beam.
- **Test 3:** Twelve receivers placed around the flange of the stiffening beam with two source locations.
- **Test 4:** Twelve source locations around the flange of the stiffening beam.

A 50 kHz ultrasonic transmitter was used in Test 1. Whereas for Tests 2 through 4, three different sources were used: (A) hammer with plastic tip, (B) hammer with aluminum tip, and (C) 50 kHz ultrasonic source. The hammer tests with plastic and aluminum tips generate low and intermediate frequencies, respectively; the 50 kHz source was used to obtain higher frequencies. Low and intermediate frequencies can generate larger wavelengths, thus allowing a deeper penetration into the tank; in contrast, higher frequencies produce smaller wavelength with very limited penetration.

In Test 1, two receivers were used, and the source was located at two different distances from the first receiver: 10 cm and 20 cm. Three main cases were considered, as shown in Figure 8-3:

- **Case 1:** Void between one source and the receivers
- **Case 2:** No void
- **Case 3:** Void between the sources

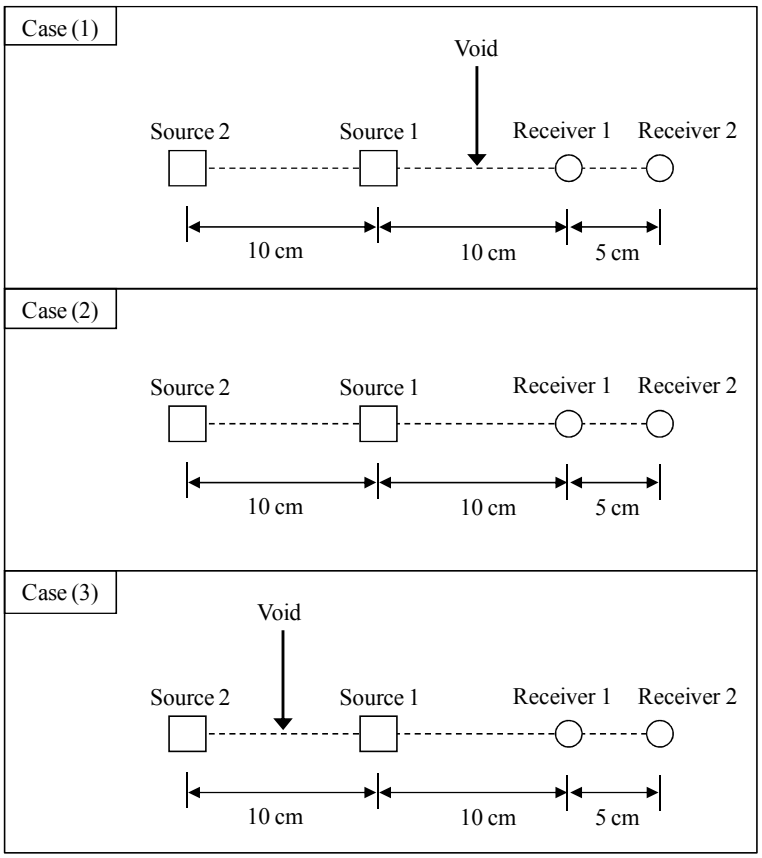

Figure 8-3. Cases studied for Test 1.

Test 2 consisted of a MASW configuration with an array of twelve receivers glued on the steel plate. The source was placed at two distances: 10 cm and 20 cm from the first receiver (Figure 8-4).

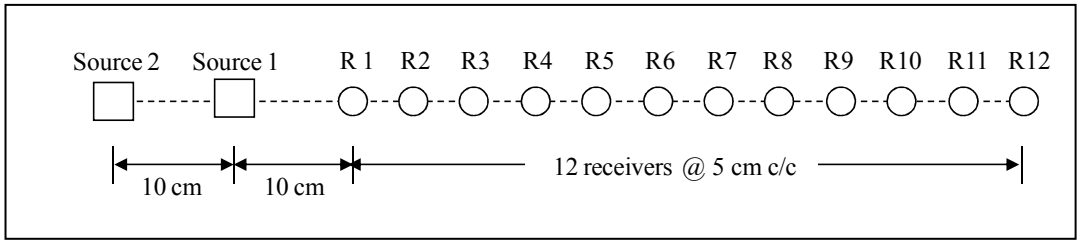

Figure 8-4. Experimental setup for Test 2.

As described previously, voids were formed below the flange of the stiffening beam during the process of filling the tank with grout (Figure 8-2). Two voids were observed from the backside of the tank, as shown in Figure 8-5. The larger void (void 1) is approximately 4 cm

thick, and the smaller void (void 2) is about 0.5 cm thick. The voids extended across the full width of the tank.

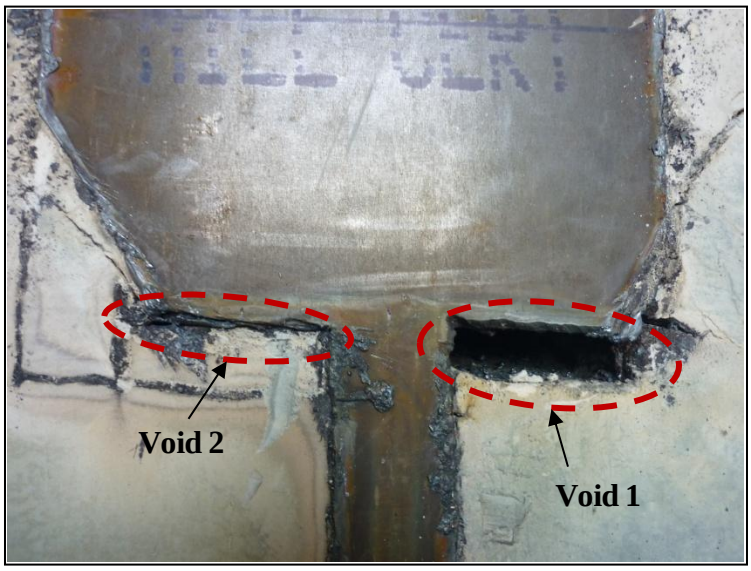

Figure 8-5. Voids beneath the top flange of stiffening beam; backside of tank.

The setup for Test 3 consisted of twelve receivers placed in two lines around the flange; six above and six below the flange. Two source locations were considered: 10 cm and 20 cm from the first receiver. Figure 8-6 illustrates the experimental setup.

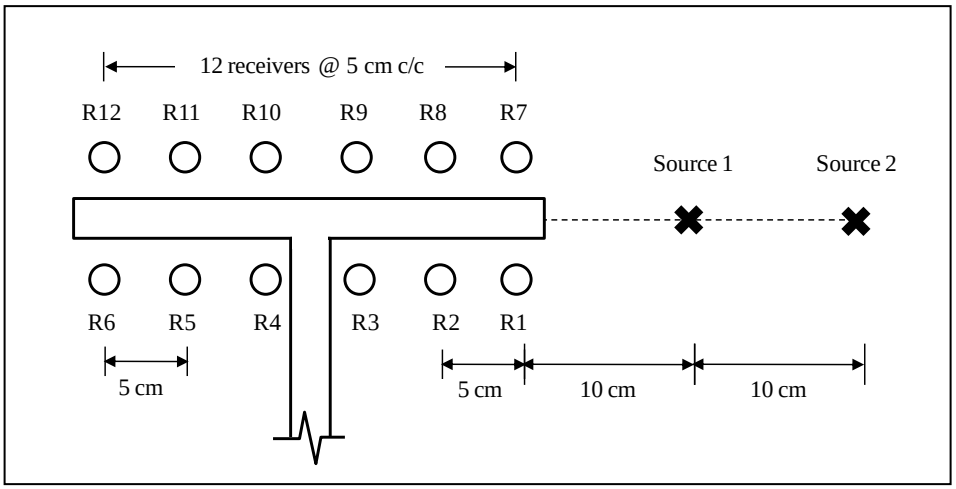

Figure 8-6. Experimental setup for Test 3.

Test 4 consisted of moving the source along twelve different locations around the flange while measuring with an array of six receivers. The first receiver was placed at a distance of 15 cm from the first source location, as shown in Figure 8-7.

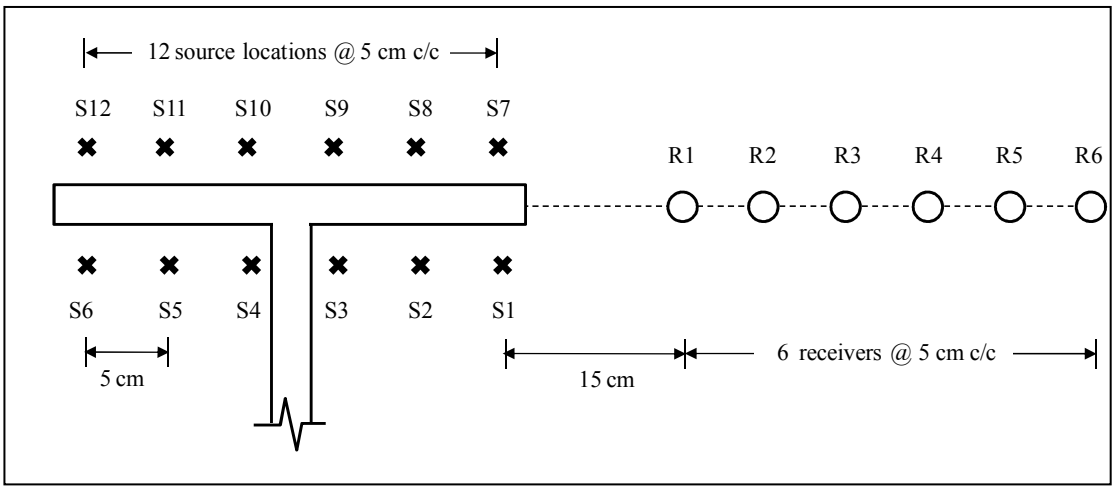

Figure 8-7. Experimental setup for Test 4.

In the case of the ultrasonic transmitter (source A), the electrical excitation was generated by a pulse generator (Model Pundit); in the case of sources B and C, the excitation impact was generated by an instrumented hammer (Dytran 5850B) with a plastic and an aluminum tips, respectively. Dytran 3055B3 accelerometers with a 35 kHz resonant frequency (500±10 mV/g sensitivity) were used as receivers. The power supply of the accelerometers (Dytran 4123B) has selectable amplification factors of 1, 10 and 100. The time signals were recorded on a 24-channel data acquisition system with a 1 MHz sampling rate (LDS Nicolet Genesis).

8.4 Results

As described in the previous section, the testing methodology consisted of four sets of ultrasonic testing:

- **Test 1**: Ultrasonic measurements along the side of the tank near the grout surface, adjacent to and away from the voids simulated by the bottles.
- **Test 2**: MASW measurements along the side of the tank near the bottom and with no stiffening beam.
- **Test 3**: Twelve receivers placed around the flange of the stiffening beam with two source locations.
- **Test 4**: Twelve source locations around the flange of the stiffening beam.

The results of all four tests are presented and analyzed in the next sections.

8.4.1 Test 1: Ultrasonic measurements near the free grout surface

Ultrasonic measurements were performed along the side of the grout tank near the top surface of the grout. A 50 kHz transmitter was used; six accelerometers were used at different distances from the source to record surface responses. The first two accelerometers provided the most consistent information in terms of wave attenuation; therefore, they were used for the analysis of wave attenuation in the time and frequency domain.

The relative change in amplitude can suggest the presence of a void (Tallavo et al., 2009; Nasseri-Moghaddam et al., 2007). If a void is located underneath the ultrasonic transmitter, the amplitude of the generated pulse is reduced because of the high reflection and scattering of energy introduced by the void.

For each source location, a window was applied. For Case 1 the windowed time signals and the normalized Fourier spectra are shown in Figure 8-8 (for source at 10 cm and at 20 cm).

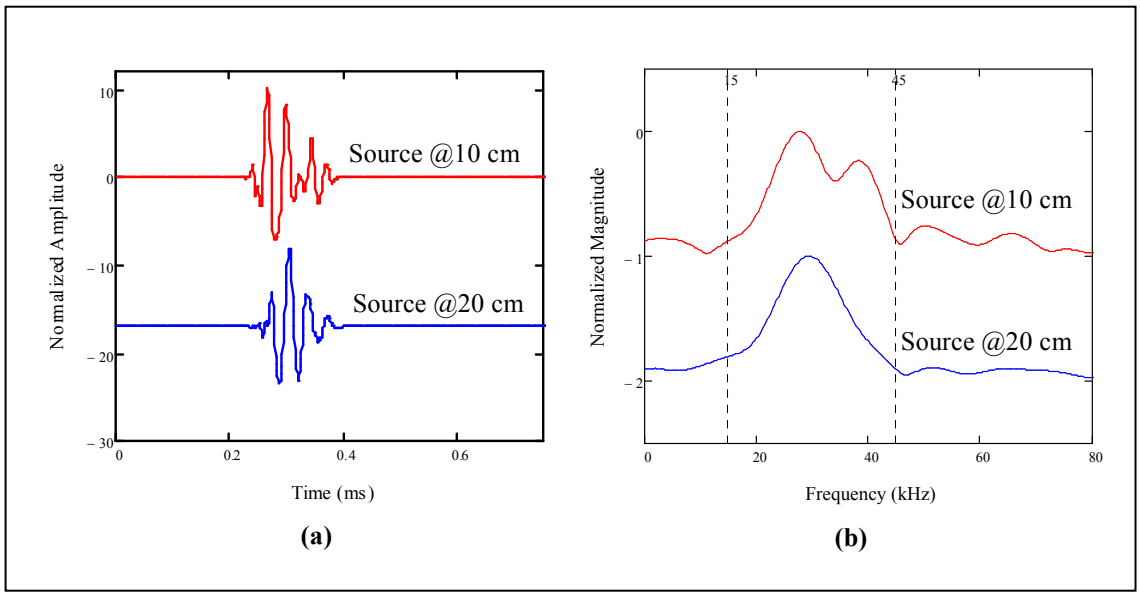

Figure 8-8. For case 1: (a) windowed time signals, and (b) normalized Fourier spectra.

From the Fourier spectra plots, the spectral areas were calculated for a frequency bandwidth of 30 kHz (starting at 15 kHz); typical results are presented in Figure 8-9. The recorded signal from the source at 10 cm was stronger than the recorded signal from the source at 20 cm because of geometrical spreading. Both of these measurements were affected by the presence of the void in Case 1. In Case 2 (no void) the signal amplitudes are stronger than in Case 1, where the propagating pulse was attenuated by the presence of the void. The results from Case 3 suggest that the presence of the void significantly affected the measurements when the source was at 20 cm. However, when the source is at 10 cm, the results are consistent with Case 2. The spectral area plot shows that the presence of the void had an impact on the waves propagating through the medium. The void reflects body waves and surface waves; thus, the observed decrease in energy could be an indication of the void.

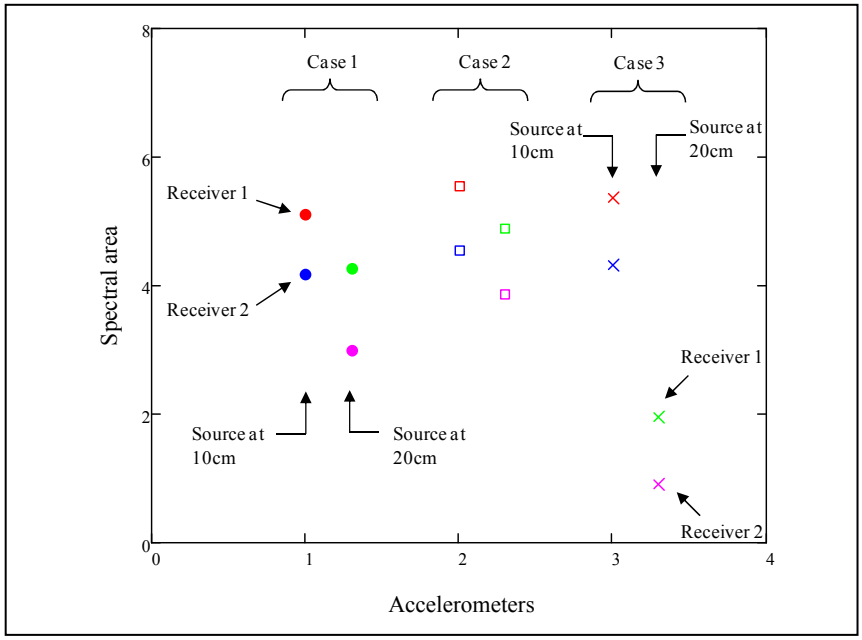

Figure 8-9. Spectral amplitude for the three cases studied.

The FK spectra were computed for all three cases and showed significant wave scattering when the source was located at 20 cm away from the receivers; therefore, the measurements with the source at 10 cm from the receivers were used to compute the dispersion curves.

The P-wave and S-wave velocities of the steel plate were evaluated from the time signals (V_P = 5418 m/s and V_S = 3159 m/s). These velocity values were used to compute the theoretical dispersion curve for Lamb waves in a 6 mm thick steel plate for further comparison with the measured dispersion curves (Figure 8-10; the average of cases 1, 2 and 3 are shown after 20 kHz).

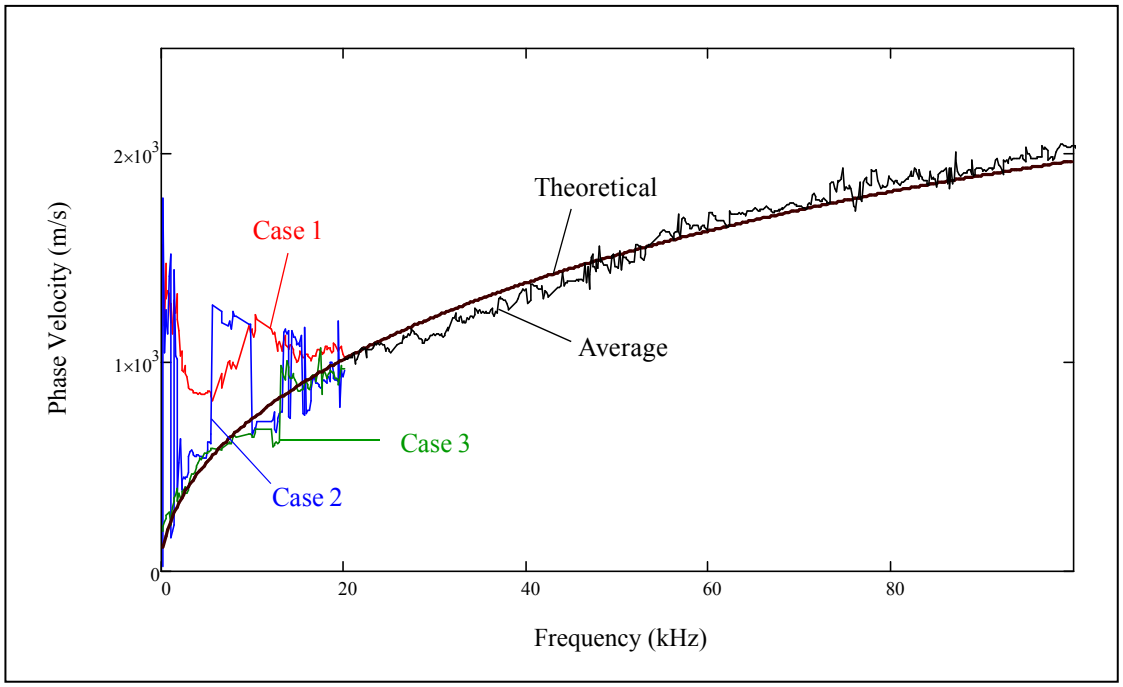

Figure 8-10. Dispersion curves for cases 1, 2 and 3; source 10 cm from the receivers.

From Figure 8-10, no significant difference was observed between the three dispersion curves measured at different distance from the void (cases 1, 2 and 3). The measured dispersion curves matched well with the theoretical dispersion curve of Lamb modes. Consequently, the measured surface responses correspond mainly to Lamb waves. This suggests that a poor bonding condition between the grout and the steel was detected. This debonding likely occurred due to shrinkage of the grout during drying, since the top surface of the grouted tank was exposed to the atmosphere (Test 1 measurements were taken near the top of the free surface of the grout). The generation of surface waves was limited because of the debonding condition.

8.4.2 Test 2: MASW measurements, no stiffening beam

The main objective of Test 2 was to identify the wave modes generated in the tank using the three different sources: Source A, hammer with plastic tip (low frequencies, f < 5 kHz); Source B, hammer with aluminum tip (intermediate frequencies, f < 12 kHz); Source C, 50 kHz ultrasonic transmitter (high frequencies, f < 45 kHz).

MASW tests were conducted on the side of the tank where there is no stiffening beam. The tests were performed near the bottom of the tank where debonding of the grout due to drying shrinkage was not expected to occur, thus good coupling between the grout and the wall was expected. Signals were recorded with an array of twelve receivers glued on the steel plate. The source was placed both at 10 cm or 20 cm from the first receiver (Figure 8-4). Wave arrivals were identified to calculate the wave velocities summarized in Table 8-1.

Table 8-1. Wave velocities – MASW tests

Source	A	B	C
V_P (m/s)	1799	1529	5291
V_R (m/s)	415	454	NA

In agreement with the results from Test 1, surface waves could not be identified when the ultrasonic source was used (source C); the measured P-wave velocity was also consistent with the results of Test 1 (2.3% difference). However, surface wave velocities between 400 and 450 m/s were determined when the low frequency sources were used (A and B). The measured surface wave velocity was close to the surface velocity of the grout alone; which was determined in the laboratory (V_R = 570 m/s). The compression wave velocities (V_P) determined using sources A and B were higher than the velocity of the grout alone (V_P = 1100 m/s) and lower than the velocity of the steel plate (V_P = 5500 m/s); thus the measured surface responses included the plate-grout interaction.

The energy distribution of the signals generated by source A is shown in the FK plot in Figure 8-11, where the measured dispersion curve is also shown. An area of high energy concentration is observed at frequencies below 4 kHz. The MASW analysis is capable of detecting energy at higher frequencies (f > 35 kHz) where the energy level is up to six orders of magnitude smaller.

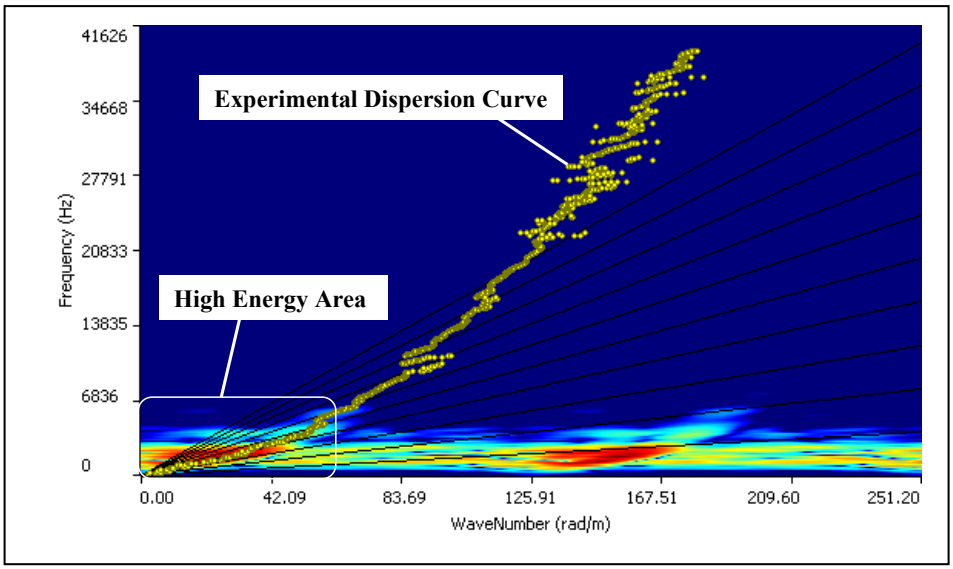

Figure 8-11. FK spectrum for source A.

The measured dispersion curves were smoothed with a Gaussian kernel function with a bandwidth of 500 Hz. Using the wave velocities of the steel measured in Test 1 (V_P = 5418 m/s and V_S = 3159 m/s), the theoretical dispersion curve of the anti-symmetric Lamb mode (A0) propagating in a 6 mm steel plate was computed and compared with the experimental curves (Figure 8-12). At low frequencies ($f < 3.5$ kHz), the phase velocity approaches the surface wave velocity of the grout. In contrast, for frequencies higher than 3.5 kHz ($\lambda < 13$ cm), the experimental dispersion curves matched the theoretical dispersion curve of the Lamb mode on a steel plate alone.

Similar dispersion curves were obtained with sources B and C. However, the energy distribution in the FK plot was significantly different. The source B generated frequencies below 7.5 kHz ($\lambda > 8$ cm); whereas source C produced frequencies between 11 kHz and 41 kHz ($5 < \lambda < 10$ cm). The dominant frequencies observed with source A and B were 1.65 kHz and 2.38 kHz, corresponding to wavelengths of 25 cm and 19 cm, respectively (for wave velocities of 415 m/s and 454 m/s, respectively). Assuming that the maximum penetration of surface waves is one wavelength, sources A and B successfully generated low frequency energy for investigating the grout properties up to a maximum depth of 25 cm.

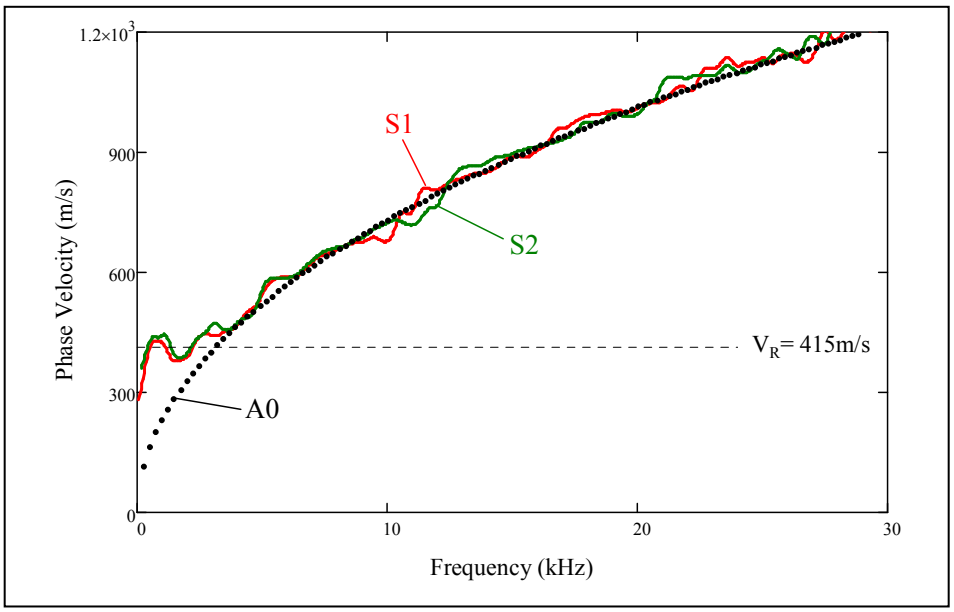

Figure 8-12. Dispersion curve for source A.
(S1: source at 10 cm; S2: source at 20 cm; A0: fundamental anti-symmetric mode)

8.4.3 Test 3: MASW measurements close to stiffening beam

Voids were formed below the flange of the stiffening beam during the process of pouring grout into the tank. Two voids were confirmed under the flanges by opening the side of the tank opposite to the location of Test 3 (Figure 8-5).

The relative change in amplitude of the recorded signals can be used to identify the presence of a void. If a void is located underneath the ultrasonic transmitter, the amplitude of the generated pulse is reduced by the energy reflection and scattering introduced by the void.

The three sources (A, B and C) were located at two different distances from the first receiver: 10 cm and at 20 cm. Three excitation pulses were used for each source, and the responses were recorded by the 12 receivers. Typical time signals and their normalized Fourier spectra are shown in Figure 8-13. The time signals were windowed and zero-padded to improve the resolution of the Fourier spectra. The spectral areas were calculated for different frequency ranges depending on the frequency content of the source (0.1 kHz to 6 kHz for sources A and B, and 15 kHz to 45 kHz for source C; for $\lambda > 10$ cm, and $5 < \lambda < 9$ cm, respectively). The

spectral areas were normalized to the input energy of the source and averaged for the three excitation pulses.

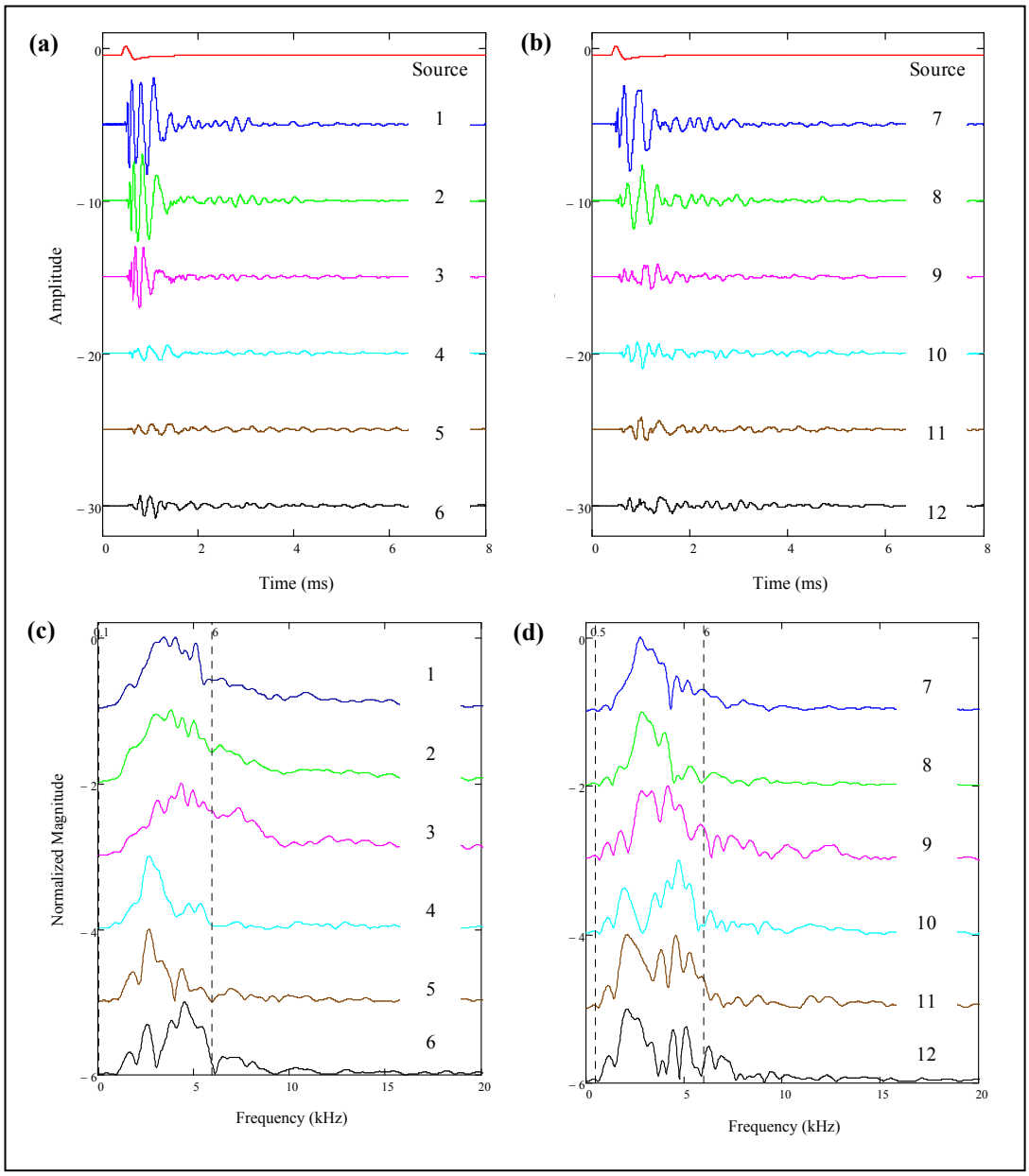

Figure 8-13. Time signals recorded from **(a)** receivers 1-6 below the flange; **(b)** receivers 7-12 above the flange; **(c)** and **(d)** normalized Fourier spectra for signals (a) and (b), respectively.

Figure 8-14 shows the spectral areas for each source. The receivers 1-6 were placed below the flange whereas receivers 7-12 were placed above the flange. For the hammer tests (sources A and B), two different trends are observed: before and after the web of the

stiffening beam (between receivers 3 and 4, and 9 and 10, respectively; Figure 8-6). The negative slope observed in the three first accelerometers before the web indicates a higher attenuation. This effect is observed both above and below the flange.

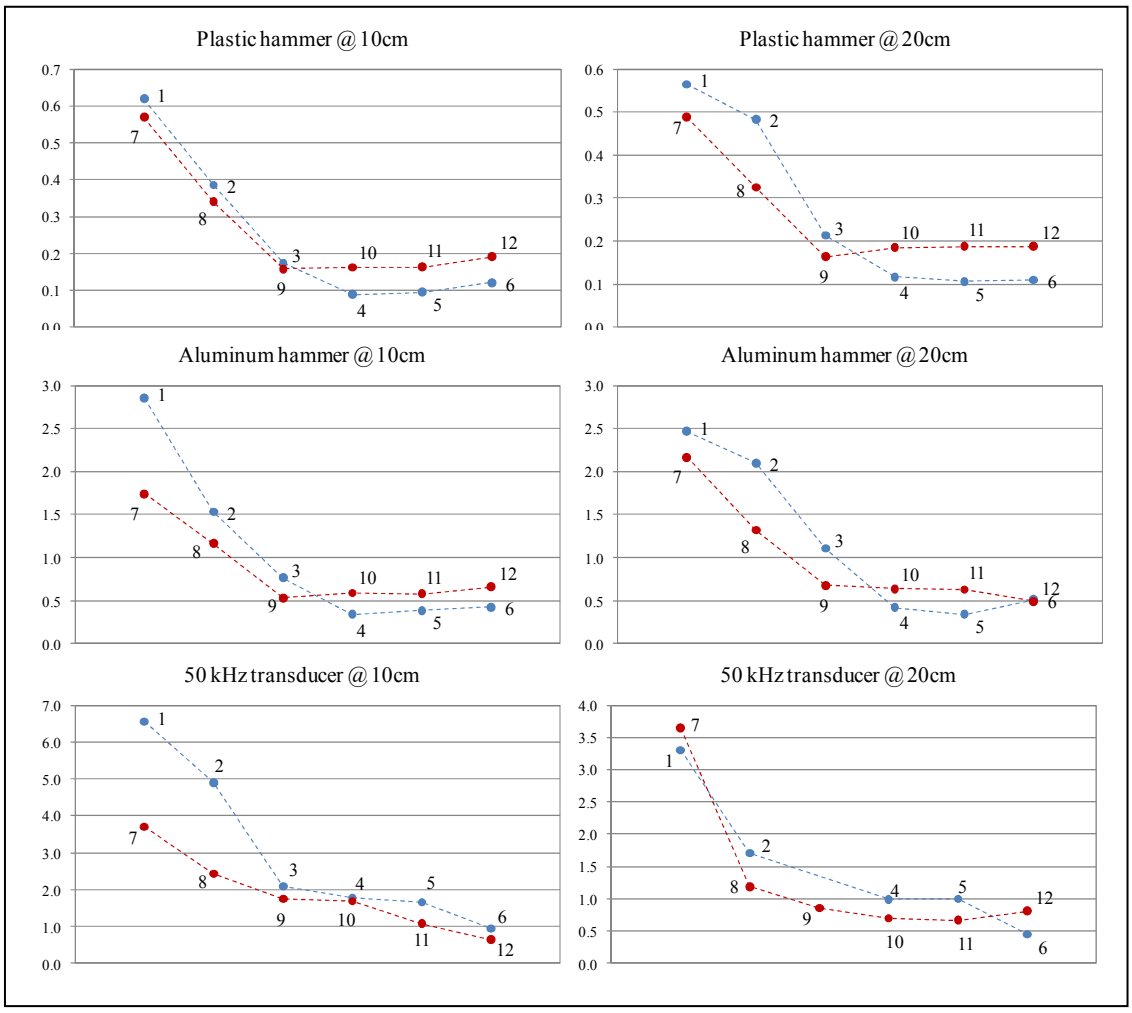

Figure 8-14. Spectral areas for the cases studied.

The measured wave attenuation is due to a combined effect of both the stiffening beam and the void. In theory, the low frequencies (f < 3.5 kHz) are affected by the void; however, the stronger effect of the stiffening beam might have overshadowed the effect of the void. In the case of source C (high frequencies), the first two receivers showed energy amplification on top of the void for the source at 10 cm. This result is mostly due to the higher frequencies (Lamb waves, f > 3.5 kHz) generated through the steel plate, as these waves are attenuated

by the grout. In general, the higher frequencies attenuated faster as predicted by the theory (higher attenuation for C than for A and B).

The experimental dispersion curves were computed; however, the variability of the results increased because of the low number of receivers. Figure 8-15 shows the average dispersion curves for source A (below and above the flange, before the web); the dispersion curves were smoothed with the Gaussian kernel function (500 Hz bandwidth).

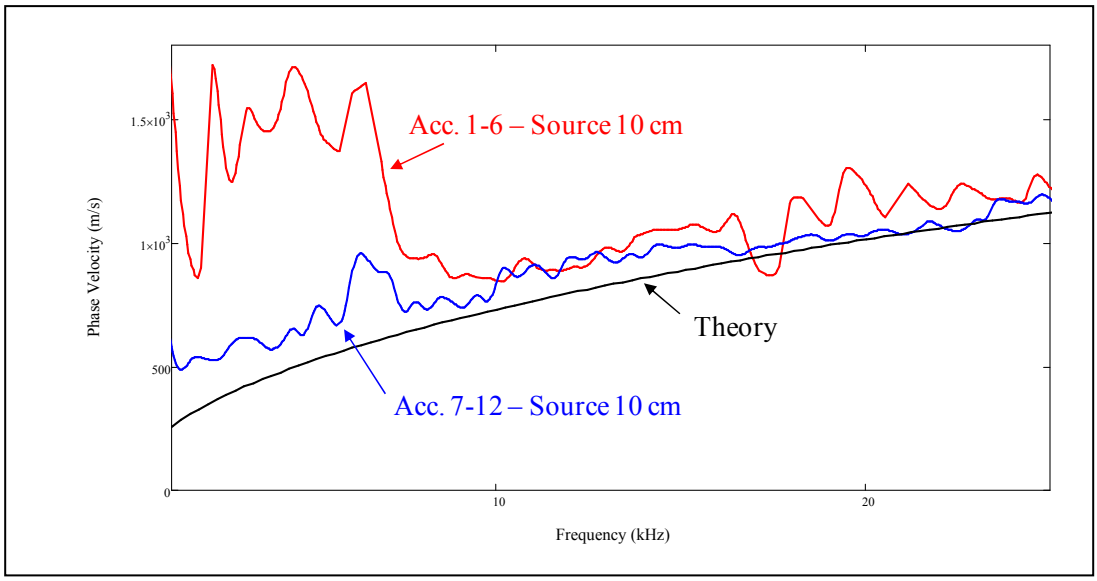

Figure 8-15. Average dispersion curves, source A.

The theoretical anti-symmetric lamb mode (A0) is also shown in Figure 8-15. The experimental dispersion curves computed for accelerometers 7 to 12 (above the flange), for both source locations (10 and 20 cm), were close to the theoretical curve for the anti-symmetric Lamb mode. On the contrary, the dispersion curves measured below the flange (accelerometers 1 to 6) showed higher velocities than the theoretical curve. This variation may be produced by the web of the stiffening beam, which seemed to enhance the participation of other Lamb modes (e.g., symmetric modes).

8.4.4 Test 4: Different source locations

An array of six receivers was placed at 15 cm away from the flange, and the source was moved along the 12 locations, as shown in Figure 8-7. Typical time signals and frequency

spectra recorded below and above the flange (locations 3 and 9) are presented in Figure 8-16 and Figure 8-17 for source A and B, respectively.

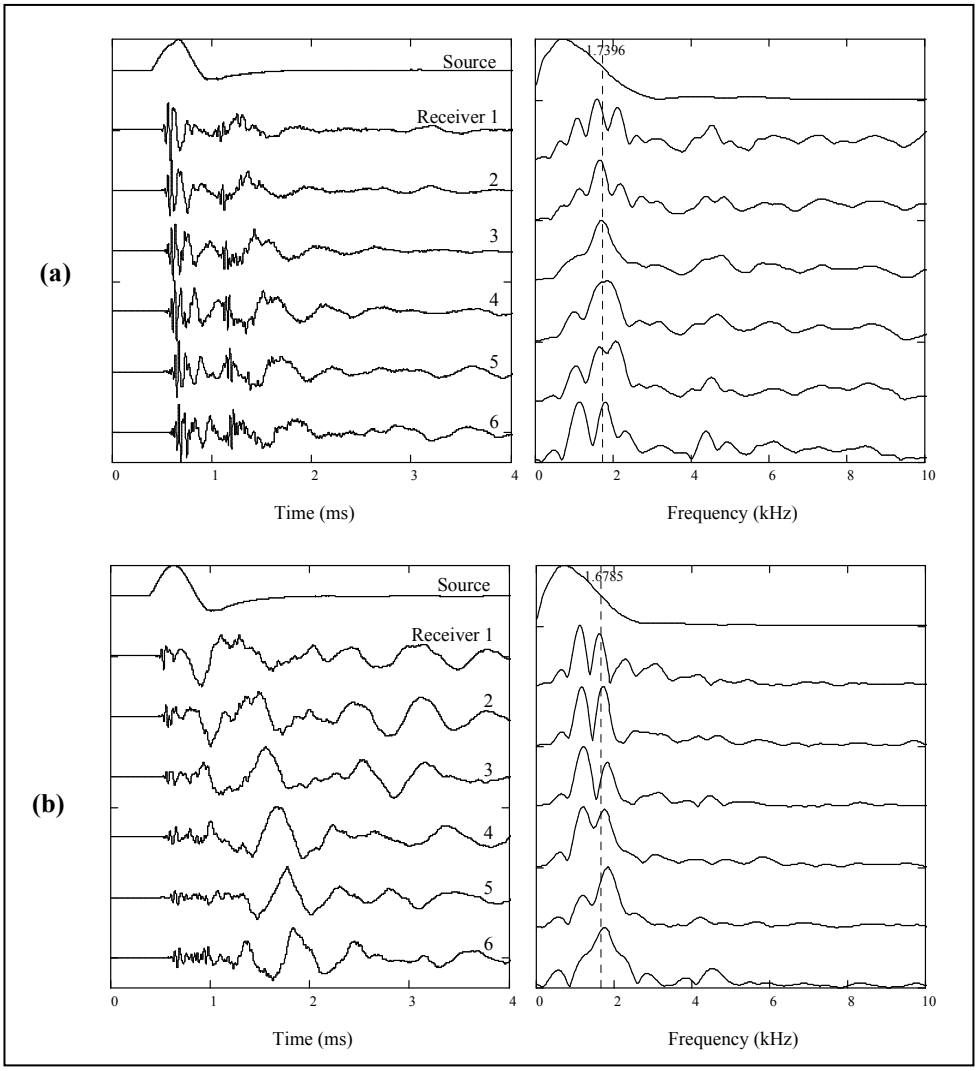

Figure 8-16. Normalized time signals and frequency spectra for source A at **(a)** location 3 and **(b)** location 9

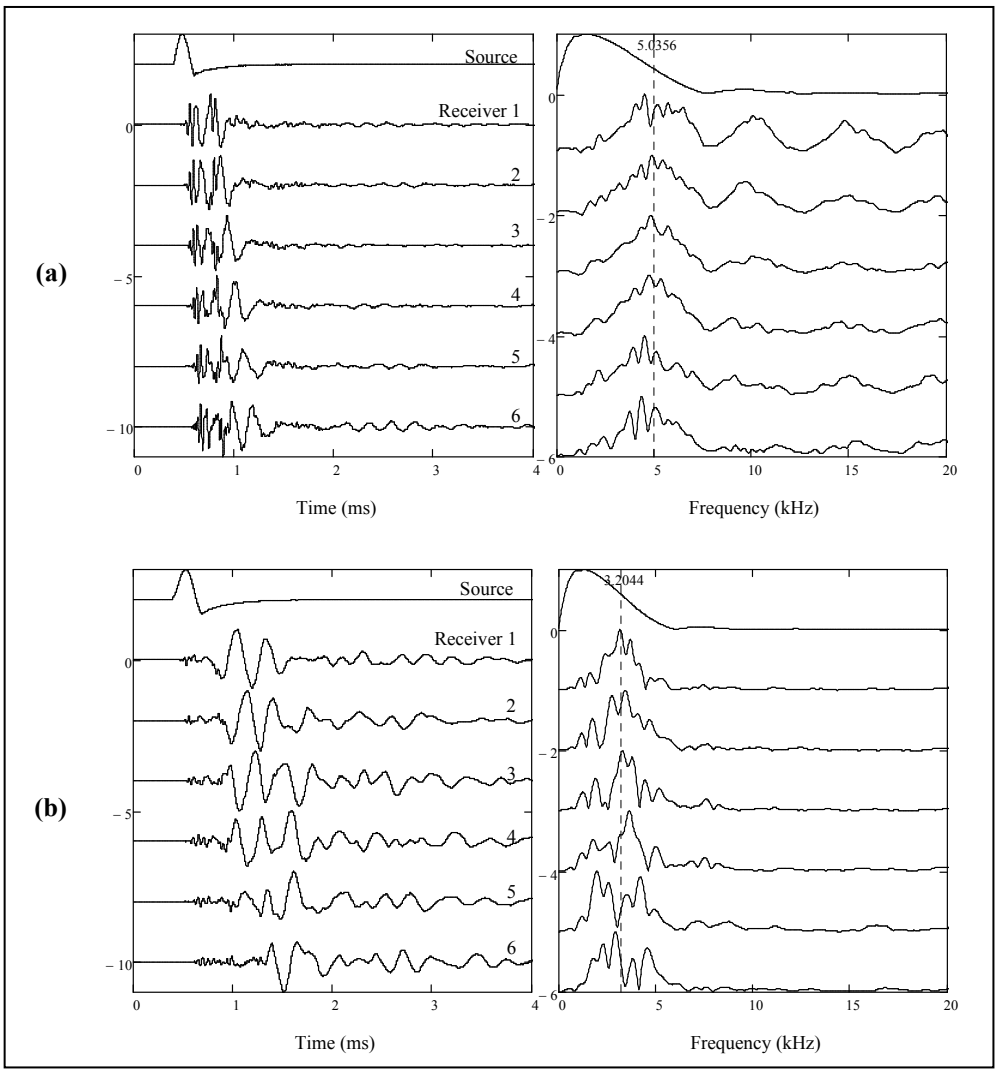

Figure 8-17. Normalized time signals and frequency spectra for source B at **(a)** location 3 and **(b)** location 9

The Fourier spectra obtained with the source below the flange showed a slightly higher frequency content than the spectra with the source above the flange. This result may be related to the presence of the void below the flange, since high frequency Lamb waves may be generated when there is no contact between the steel plate and the grout. Part of this difference might also be attributed to the variability of the excitation pulse.

The spectral areas were normalized to the spectral area of the pulse sent by the source, thus reducing the variability induced by the source. Then, they were normalized to the maximum spectral area recorded for the 12 source locations. Because of the significant difference

between the spectral areas measured before and after the web of the stiffening beam, the spectral areas were averaged according to the source locations: 1-3, 4-6, 7-9 and 10-12. Figure 8-18 shows that for sources A and B, the spectral areas recorded below the flange were three to five times higher before the web (locations 1-2-3) than after the web (4-5-6).

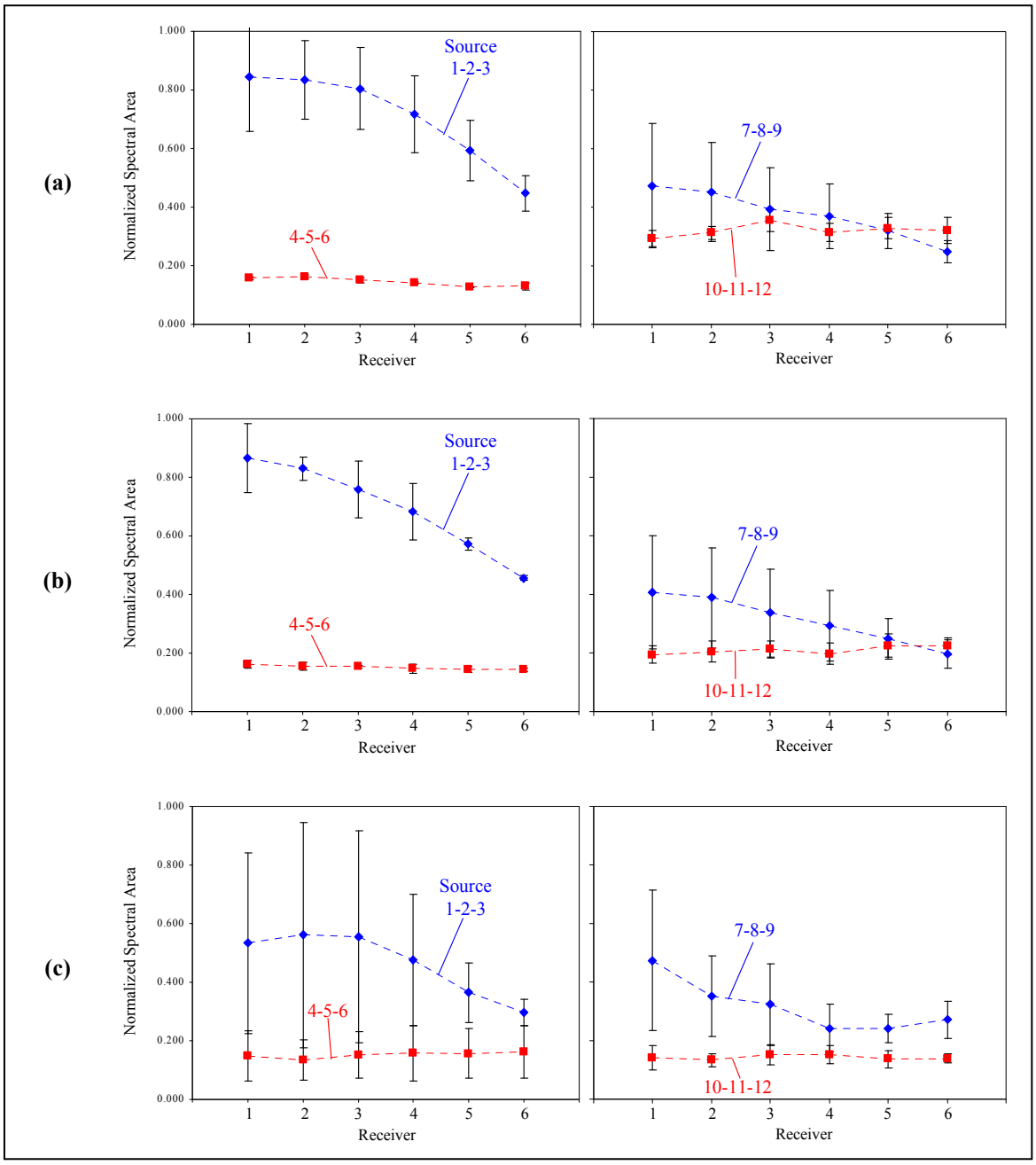

Figure 8-18. Normalized spectral areas for **(a)** source A, **(b)** source B, and **(c)** source C.

On the contrary, for measurements above the flange, spectral areas before the web (7-8-9) and after the web (10-11-12) were more consistent (2% to 50% difference). The web of the stiffening beam considerably attenuated the low frequencies propagating in the grout, up to 275% in average for source A and B. The impact of the web was less significant above the flange. The spectral areas recorded before and after the web for source C were more consistent than for source A and B. Thus, the high frequency waves generated by source C propagated mostly through the steel plate and were not significantly affected by the web of the stiffening beam.

Finally, dispersion curves were computed; however, measurements with the source at locations after the web (4, 5, 6, 10, 11 and 12) did not provide good quality FK spectra because of the high wave attenuation produced by the web; hence the dispersion curves were not computed for these locations. Figure 8-19 shows the average dispersion curves measured below the flange (source at 1-2-3) and above the flange (source at 7-8-9). The experimental curve measured above the flange was close to the theoretical anti-symmetric lamb mode (A0); in contrast, the curve measured below the flange appeared to be shifted from the theoretical curve. This difference in phase velocity may be related to the presence of the void and/or the web below the flange.

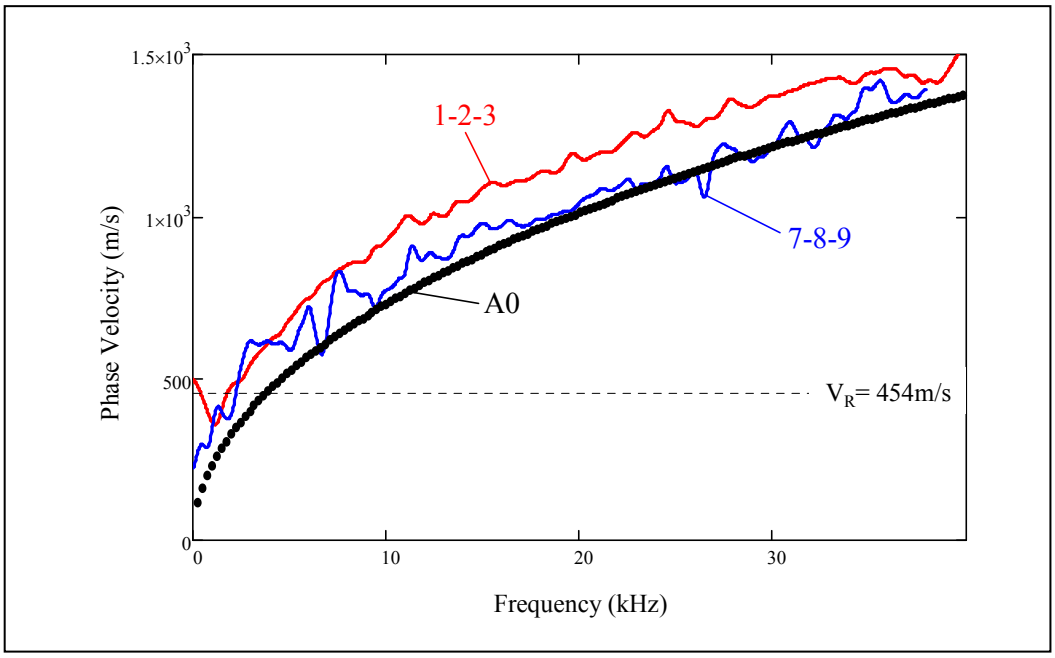

Figure 8-19. Dispersion curves for source B below (locations 1-2-3) and above (7-8-9) the flange.

8.5 Concluding Remarks

- The spectral area plot in Test 1shows that the presence of the void has an impact on the waves propagating through the medium; the observed decrease in energy might be an indication of the void.
- The ultrasonic testing with high frequency Lamb waves appears to be effective for the detection of poor bonding between the steel and the grout.
- Even though only Lamb waves were generated in the steel, the void was close enough to the plate that it affected the excitation pulse.
- Results from Test 2 indicate that low frequency surface waves were successfully generated by sources A and B whereas mostly high frequency Lamb waves were produced with source C.
- Appropriate wavelengths were generated with sources A and B. Thus, they can be used to investigate the properties of the grout up to a depth of 25 cm and 19 cm, respectively.
- Results suggest that the voids not immediately beneath the steel plate could be detected using surface waves, assuming no stiffening beams were welded behind the wall.
- The low frequencies were affected by the stiffening beam, which overshadowed the effect of the void.
- The web of the stiffening beam significantly attenuated the low frequencies generated by sources A and B in the grout. The high frequency waves generated by source C mainly propagated through the steel plate were less affected by the web.
- Phase velocities measured below the flange were higher than above the flange, which might be related to the presence of the void or the web below the flange.
- The plate vibrations (Lamb modes) of the steel wall can successfully be used to detect the presence of a void just beneath the wall because of the lower attenuation (amplification) measured on top of the void.
- Test 4 measurements were effective in the detection of the void, showing amplitudes up to 50% higher, likely because the deformation of the wall is attenuated by the grout.

CHAPTER 9. SUMMARY AND CONCLUSIONS

9.1 Ultrasonic Testing of Asphalt Slabs for Condition Assessment of Joints

Tests were conducted in three parts on a fabricated asphalt slab with a construction joint. The first part of this study consisted of the improvement of the coupling mechanisms between the testing equipment and the asphalt surface. The wavelet transmission coefficients (WTC) were computed using six different coupling configurations for investigating the coupling effects on the assessment of joint condition. The main conclusions are as follows:

- Measurements performed with no applied vertical pressure (weight) did not show any effects of attenuation due to the joint. In contrast, the test results with the added weight indicated higher attenuation effects (up to 30%) across the joint.
- Experimental results using the polyurethane foam as an isolator showed less attenuation at low frequencies, below the nominal resonant frequency of the accelerometer (35 kHz).
- At the nominal resonant frequency of the accelerometer (35 kHz, $\lambda = 46$ mm), when vacuum grease was directly applied on the pavement, the WTC results showed less attenuation (between 2% and 4%) when the foam isolator was used. Hence, the foam had no significant effects on the results.
- A new coupling configuration was proposed consisting of vacuum grease coupled directly on the asphalt surface, foam to provide a spring action on the transducers, and calibrated weights to generate a compression force. The results from this configuration agreed well with the mechanism using the aluminum plate and glue (within 10% difference), suggesting that the plate is not necessary; thus significantly reducing the testing time.
- The WTC at the dominant frequency was found not to give an accurate representation of the frequency range (more than 12% of variation). Thus, WTC should be computed for a range of frequencies to achieve a good representation of the joint.

The second part of the tests consisted of developing a new data processing technique that can be performed automatically to reduce user input. A new methodology, called instantaneous transmission coefficient (ITC), was developed based on the instantaneous frequency and damping ratio calculations. The main findings are discussed as follows:

- Material damping was determined from the instantaneous properties extracted from the analytic signals; the damping ratios were obtained between 2.0% and 3.3% for the jointed surface, and between 1.5% and 2.2% for the joint-free surface. As expected, the signals measured across the joint resulted in higher damping values than the joint-free signals.
- Wave attenuation measurements using the instantaneous transmission coefficient (ITC) were able to identify jointed (ITC < 0.79) and joint-free (ITC > 0.97) regions on the fabricated asphalt slab.
- Good agreement was observed between the FTC, WTC and ITC results for both jointed and joint-free surfaces. The results obtained from all three transmission coefficient methodologies had a variation of 1.1% in the jointed area, and 6.3% in the joint-free area.
- The computation of both the FTC and WTC required a significant amount of user input. In particular, the WTC required selecting peak values from the wavelet transform for each Morlet center frequency, making the procedure time consuming.
- Most of the transmitted wave energy (85%) propagated close to the resonant frequency of the accelerometers (20 kHz to 40 kHz); affecting the FTC calculations.
- The ITC method overcomes the main limitations of the FTC and WTC, as it retains the frequency information in time and does not require the manual selection of peak values.

The third part of the experimental tests consisted of conducting measurements adding different weights on top of the accelerometers to optimize the coupling. The addition of a coupling stud to the receivers to improve the signal quality and eliminate the use of a couplant was also evaluated. The main results are presented as follows:

- The coupling between the source and asphalt slab was assessed. Good-quality signals were transmitted by the source when coupled to the asphalt surface by means of a stainless steel disk 12.7 mm in diameter.
- Relatively good-quality signals were recorded by the accelerometers when coupled directly to the asphalt surface with vacuum grease. The application of a vertical pressure on top of the receivers improved significantly the signal intensity.
- The steel coupling stud was found to have an effect on the frequency content of the signal, undesirably reducing the main frequency component by 17%.
- The measurements with the accelerometers coupled directly on the asphalt surface with vacuum grease provided relatively good-quality signals. The addition of the 200 g weight provided the largest intensity increase (8.2%).
- The new coupling configuration was improved by using the accelerometers coupled directly to the asphalt surface with vacuum grease, a 200 g weight applied on top, and a polyurethane foam cylinder to isolate the vibration effects induced by the added weight. This configuration was found to be more practical than the traditional aluminum plate and epoxy arrangement, thus reducing the testing time by 50%.

Furthermore, a poor condition joint was simulated by cutting a 3 mm wide and 30 mm deep notch in the fabricated asphalt slab; measurements were conducted before and after the saw cut. Transmission coefficients were computed for the evaluation of the joint condition. The new coupling configuration was used. The main conclusions are as follows:

- Wave attenuation measurements using the instantaneous transmission coefficient (ITC) were capable of identifying a good condition joint (ITC = 0.74) and a poor condition joint (ITC = 0.55) on the fabricated asphalt slab.

- The transmission coefficients (FTC, WTC and ITC) computed for the poor condition were significantly lower (decreased in average 37%) than those for the good condition. Results showed good agreement between the two different joint conditions.
- Good agreement was obtained from the FTC, WTC and ITC results between the new coupling configuration and the traditional configuration, averaging less than 9% of variation. The ITC appeared less affected by the coupling system than the FTC and WTC methods.
- The FTC and WTC values showed larger variation between the poor joint and the good joint: 37% and 46% respectively. The ITC results decreased by 26%, suggesting that the instantaneous damping measurements are not as sensitive to abrupt changes in density as the other methods.
- The ITC method appears to be effective for evaluating the condition of a medium with gradual changes in density, such as in-service asphalt pavement joints. Nevertheless, more experimental tests are required.

Next, two MASW measurements were conducted on the asphalt slab: across the joint and across the notch. The main findings are as follows:

- The saw cut created a significant vertical disturbance in the wave propagation path, such that the reflections of the flexural wave modes generated extensional modes. The FK plots showed evidence of energy concentration associated to symmetric modes.
- The change in velocity should not be the only deterministic factor when applied to flaw evaluation. Other factors, such as attenuation effects, should also be considered.

Finally, exploratory ground penetrating radar (GPR) measurements were conducted to evaluate its potential as a complementary method to wave-based tests while testing its effectiveness at detecting and characterizing longitudinal joints in asphalt pavements. The results using a 1000 MHz antenna did not show any clear evidence of the longitudinal joints measured in the laboratory. The lack of moisture in the laboratory environment might have affected the GPR response, as the dielectric change provided by water plays a significant role

in GPR testing. Therefore, more measurements should be carried out on new and old pavement in the field. Further measurements using higher frequency antennae (e.g. 1.5 GHz-2 GHz) are also recommended.

9.2 Ultrasonic Testing of Steel Pipes for Thickness Evaluation

Cold rolled steel plates with different thicknesses (12.7 mm, 6.3 mm and 3.2 mm) were used for the MASW tests; experimental dispersion curves were constructed with the computer program SWAN, and the average thickness values were assessed. The main conclusions are as follows:

- Lamb waves were generated in the steel plates. Experimental FK spectra revealed energy concentration at frequencies between 15 kHz and 80 kHz, corresponding to Lamb modes. The experimental data agreed well with the theoretical dispersion curves of the fundamental modes in all three cases of steel thickness.
- The zero-order (or fundamental) modes were observed in the experimental dispersion curves for all three steel samples; as the frequency increased and the wavelength became comparable to the plate thickness, both the phase velocity and the group velocity began to converge towards the Rayleigh wave velocity.
- In the tests of the 12.7 mm plate, both fundamental symmetric and anti-symmetric modes were excited and detected; for the 6.3 mm and 3.2 mm plates, only the A0 mode was detected. The anti-symmetric mode was the most easily excited of the two fundamental modes, due to the input pulse configuration.
- In the case of the 12.7 mm and 6.3 mm plates, higher-order modes were observed in the experimental dispersion curves (at nascent frequencies of around 200 kHz and 400 kHz, respectively). On the contrary, no higher-order modes were detected in the thinnest 3.2 mm plate. The appearance of the waveforms depended critically on the frequency range (or wavelength generation) provided for the test.
- The MASW methodology appears effective for the thickness estimation of steel plates. The provided frequency range is critical and must be suitable for the piece under investigation. The proposed testing configuration allows the captured signal to

be viewed in real time; thus, making it possible to change the setup to best fit the thickness under investigation.

- In the investigation of plate thickness, transducers with higher centre frequencies (> 500 kHz) are needed for generating suitable wavelengths. This is particularly true for thinner plates (< 6 mm). The MASW technique can be used to assess any plate thickness by adjusting the testing frequency such that the generated wavelength is approximately equal to the plate thickness.
- The curvature effect of the pipe specimen on the low order Lamb wave modes was found not to affect the Lamb wave mode structure. Symmetric and anti-symmetric Lamb modes were generated with the input excitation parallel and perpendicular to the pipe surface.

9.3 Ultrasonic Testing of Grouted Steel Tank for Thickness Evaluation and Void Detection

The attenuation and dispersion effects of ultrasonic waves were used to detect voids and debonding conditions in a laboratory scale steel tank filled with grout. Four tests were performed combining different setup configurations and frequency ranges. The main conclusions are as follows:

- The change in the Fourier spectral area of the recorded signals suggested that the presence of the void has an impact on the waves propagating through the medium. The void can be observed as an obstruction to the propagation of the waves. However, more measurements are required to study the effect of the void on the surface waves for this application.
- Dispersion curves showed that the presence of Lamb waves was strong even when low-frequency sources were used. The waves propagating in the steel wall-grout system were similar to the ones in a steel plate alone. This effect is due to the poor coupling observed between the steel plate and the grout, which can be the result of the shrinkage experienced by the grout during curing.
- The ultrasonic testing with high frequency Lamb waves appeared effective for the detection of debonding between the steel wall and the grout. Voids not immediately

beneath the steel plate could potentially be detected using surface waves in areas where stiffening beams are not welded behind the wall.

- The instrumented hammer sources successfully generated low frequency surface waves with a penetration up to 25 cm of depth. Low frequencies are necessary for detecting the voids in the grout. However, the presence of the void was not obvious from the surface wave measurements. Interference with the stiffening beam constrained the surface displacements and the participation of Lamb waves in the response.
- The plate vibrations or Lamb modes, of the steel wall can successfully be used to detect the presence of a void beneath the wall due to the effect of lower attenuation (amplification) measured on top of the void.
- Measurements with the source placed at different locations were effective in the detection of the void, producing higher amplitudes (up to 50% higher) which may be attributed to the deformation of the wall attenuated by the presence of the grout.
- The use of different source locations generated the best results for locating voids and debonding conditions under the flanges. The void had an effect on the generated signal, and this change to the input was detected by all receivers. The tests performed on the grouted tank were limited by the frequency content of the transmitter. Hence, other sources with different frequency ranges (e.g. 10-20 kHz, 20-50 kHz, etc.) are recommended.
- If calibration tests can be conducted on a location of the tank that is considered to be in good condition, additional measurements can be compared to assess changes in the steel-wall-grout coupling. However, this procedure is applicable only if the boundary conditions around the location of the measurements are similar.
- The wall thickness of the lab scale tank used in the tests was 6 mm. In real applications the plate thickness can be 38 mm (1.5 in). Surface wave measurements are linear function of the frequency content of the excitation source, whereas dispersion curves depend on the thickness of the plate. Therefore, if the thickness of the plates and flanges are modified, then the frequency content of the transmitter and the frequency bandwidth of the receivers must be modified accordingly.

9.4 Recommendations and Future Work

The calibration of accelerometers allows for the proper selection of receivers and coupling configurations for the experimental testing stages. Each receiver should be characterized relative to a reference receiver, thus allowing for the removal of any undesirable effects induced by manufacturer differences between accelerometers.

The new transmission coefficient technique (ITC) showed good correlation to previous methodologies (FTC and WTC) based on the measurements performed on the fabricated slab. More experimental tests should be conducted on additional slabs with joints of different qualities. Field testing on in-service roads is recommended once the ITC technique is calibrated to different joint conditions.

All the methods used so far (FTC, WTC, and ITC) are based on non-calibrated ultrasonic signals recorded during testing. Thus, the response of ultrasonic transducers is not proportional to the actual displacement, velocity, or acceleration of the medium, due to the lack of an instrument capable of measuring displacements at frequencies higher than 100 kHz. Hence, the real excitation and the associated response of the medium cannot be measured; only the average wave propagation velocity can be measured. A novel nano-laser equipment should be used to measure the actual excitation and response generated by ultrasonic transducers on an asphalt pavement. From the measurement of the actual input and output responses, the ultrasonic transducers can be calibrated allowing for the reliability of the proposed ITC technique to be improved significantly. Finally, the actual effect of a longitudinal joint on each ultrasonic frequency used during testing can be determined; then, the actual condition of the joint can be evaluated with high certainty.

REFERENCES

Abo-Qudais, S., and A. Suleiman. 2005. Monitoring fatigue damage and crack healing by ultrasound wave velocity. *Nondestructive Testing Evaluation* 20: 125-45.

Achenbach, J. D. 1973. *Wave propagation in elastic solids*. Amsterdam: North-Holland Pub. Co.

Aggelis, D. G., E. Z. Kordatos, D. V. Soulioti, and T. E. Matikas. 2010. Combined use of thermography and ultrasound for the characterization of subsurface cracks in concrete. *Construction and Building Materials* 24 (10): 1888-97.

Ahmad, N., H. Lorenzl, and M. P. Wistuba. 2011. Crack detection in asphalt pavements - How useful is the GPR? Paper presented at Advanced Ground Penetrating Radar (IWAGPR) 6th International Workshop, Aachen, Germany.

Al-Qadi, I. 1992. Using microwave measurements to detect moisture in hot-mix asphalt. *Journal of Testing and Evaluation* 20: 45-50.

Angani , C. S., D. G. Park, G. D. Kim, C. G. Kim, and Y. M. Cheong. 2010. Differential pulsed eddy current sensor for the detection of wall thinning in an insulated stainless steel pipe. *Journal of Applied Physics* 107 (9).

Angani, C. S., C. G. Kim, P. Leela, P. Kollu, D. G. Park, and Y. M. Cheong. 2010. The pulsed eddy current differential probe to detect a thickness variation in an insulated stainless steel. *Journal of Nondestructive Evaluation* 29 (4): 248-52.

Basravi, M. F. 2004. Nondestructive technologies for local industries. *Proc. of 2nd Middle East Nondestructive Testing Conference* 9 (4).

Beutel, R., H. W. Reinhardt, C. U. Grosse, A. Glaubitt, M. Krause, C. Maierhofer, D. Algernon, H. Wiggenhauser, and M. Schickert. 2008. Comparative performance tests and validation of NDT methods for concrete testing. *Journal of Nondestructive Evaluation* 27 (1): 59-65.

Blitz, J., and G. Simpson. 1996. Ultrasonic methods of nondestructive testing. *Mechanical Engineering* 118 (7).

Bolt, B. A. 1978. *Earthquakes : A primer*. San Francisco; San Francisco: W.H. Freeman.

Celaya, M., and S. Nazarian. 2007. Stripping detection in asphalt pavements with seismic methods. *Transportation Research Record* TRB 86th Annual Meeting Compendium of Papers.

Damgaard, N. R. 2009. Prediction and prolongation of the service life of weathering steel highway structures. Master of Applied Science. University of Waterloo.

Dilek, U. 2007. Ultrasonic pulse velocity in nondestructive evaluation of low quality and damaged concrete and masonry construction. *Journal of Performance of Constructed Facilities* 21 (5): 337-44.

Du Tertre, A. 2010. Nondestructive evaluation of asphalt pavement joints using LWD and MASW tests. University of Waterloo.

Fowler, K. A., G. M. Elfbaum, K. A. Smith, and T. J. Nelligan. 1997. Theory and application of precision ultrasonic thickness gaging. *NDTnet* 2 (10).

Gammell, P. M. 1981. Analogue implementation of analytic signal processing for pulse-echo systems. *Ultrasonics* 19 (6): 279-83.

Gordon, M. O., K. Broughton, and M. Hardy. 1998. The assessment of the value of GPR imaging of flexible pavements. *NDT & E International* 31: 428-38.

Graff, K. F. 1975. *Wave motion in elastic solids*. Columbus; (Columbus): Ohio State University Press, 1975: Ohio State University Press.

Grimberg, R., L. Udpa, A. Savin, R. Steigmann, V. Palihovici, and S. S. Udpa. 2006. 2D eddy current sensor array. *NDT & E International* 39 (4): 264-71.

Heisey, J. S., K. H. Stokoe, W. R. Hudson, and A. H. Meyer. 1982. *Determination of in situ wave velocities from spectral analysis of surface waves.* Center for Transportation Research, University of Texas at Austin, Research Report 256-2.

Hellier, C. J., J. Drury, and M. Shakinovsky. 2001. Ultrasonic testing. *Handbook of Nondestructive Evaluation* 7: 1-115.

Honarvar, F., and A. N. Sinclair. 1996. Acoustic wave scattering from transversely isotropic cylinders. *Journal of the Acoustical Society of America* 100 (1) (07): 57-63.

Honarvar, F., E. Enjilela, A. N. Sinclair, and S. A. Mirnezami. 2007. Wave propagation in transversely isotropic cylinders. *International Journal of Solids and Structures* 44 (16) (08): 5236-46.

Hudson, G. 1943. Dispersion of elastic waves in solid circular cylinders. *Physical Review* 63 (1-2): 46-51.

Hwang, K. M., T. E. Jin, S. H. Lee, and S. C. Jeon. 2002. Wall thinning analyses for secondary side piping of korean NPPS using checworks code. Paper presented at Proceedings of the IJPGC 2002 International Joint Power Generation Conference.

In, C. -W, J. -Y Kim, K. E. Kurtis, and L. J. Jacobs. 2009. Characterization of ultrasonic Rayleigh surface waves in asphaltic concrete. *NDT and E International* 42 (7): 610-7.

Jiang, Z. 2007. Innovative nondestructive testing (NDT) for condition assessement of longitudinal joints in asphalt pavement. University of Waterloo.

Jiang, Z. Y., J. Ponniah, and G. Cascante. 2006. Improved ultrasonic pulse velocity technique for bituminous material characterization. Paper presented at Annual Conference of the Transportation Association of Canada, Charlottetown.

Kearey, P. 2002. *An introduction to geophysical exploration*, ed. rd ed. Oxford; Malden, MA: Blackwell Science.

Khan, Z., G. Cascante, and M. H. El Naggar. 2011. Measurement of dynamic properties of stiff specimens using ultrasonic waves. Canadian Geotechnical Journal 48 (1): 1-15.

Khazanovich, L., R. Velaquez, and E. Nesvijski. 2005. Evaluation of top–down cracks in asphalt pavements by using a self-calibrating ultrasonic technique. *Transportation Research Record: Journal of the Transportation Research Board* 1940.

Li, Song Song, Xianjiu Guo, and Xiaoming Chen. 2010. Optimum excitation of the Lamb wave modes in NDE. Paper presented at International Conference on Computer, Mechatronics, Control and Electronic Engineering.

Lockie, K. A., L. C. Suttora, k. D. Quigley, and N. Stanisich. 2007. Tank closure progress at the department of energy's idaho national engineering laboratory tank farm facility. Paper presented at Waste Management Conference, Tucson, AZ.

Mahoney, J. P., S. Muench, L. Pierce, S. A. Read, J. S. Uhlmeyer, H. Jakob, and R. Moore. 2000. Identification and assessment of construction-related asphalt concrete pavement temperature differentials. *Transportation Research Record: Journal of the Transportation Research Board* 1712: 93-100.

Maldague, X. 1999. Pipe inspection by infrared thermography. *Materials Evaluation* 57 (9): 899-902.

———. 1993. *Nondestructive evaluation of materials by infrared thermography*. Springer House 8 Alexandra Rd, London, SW19 7JZ, UK: Springer-Verlag (London).

Maser, K. R. 1999. Pavement characterization using ground penetrating radar: State of the art and current practice. *ASTM* West Conshohocken: 313-26.

Maser, K. R., T. J. Holland, R. Roberts, and J. Popovics. 2006. NDE methods for quality assurance of new pavement thickness. *International Journal of Pavement Engineering* 7: 1-10.

Nasseri-Moghaddam, A. 2006. Study of the effect of lateral inhomogeneities on the propagation of Rayleigh waves in an elastic medium. University of Waterloo.

Nasseri-Moghaddam, A., G. Cascante, C. Phillips, and D. J. Hutchinson. 2007. Effects of underground cavities on Rayleigh waves-field and numerical experiments. *Soil Dynamics and Earthquake Engineering* 27 (4): 300-13.

Nazarian, S., K. Stokoe II, and W. R. Hudson. 1983. Use of spectral analysis of surface waves method for determination of moduli and thicknesses of pavement systems. *Transportation Research Record* (19830101): 38-45.

Park, C. B., R. D. Miller, and J. Xia. 1999. Multichannel analysis of surface waves. *Geophysics* 64 (3): 800.

Park, C. B., R. D. Miller, J. Xia, and J. Ivanov. 2007. Multichannel analysis of surface waves (MASW)—active and passive methods. *The Leading Edge* 26: 60.

Park, D. G., C. S. Angani, G. D. Kim, and Y. M. Cheong. 2010. Pulsed eddy current system for monitoring the wall thinning of the pipeline covered with insulator. *Transactions of the American Nuclear Society* 102.

Park, D. G., C. S. Angani, G. D. Kim, C. G. Kim, and Y. M. Cheong. 2009. Evaluation of pulsed eddy current response and detection of the thickness variation in the stainless steel. *IEEE Transactions on Magnetics* 45 (10): 3893-6.

Park, M. H., I. S. Kim, and Y. K. Yoon. 1996. Ultrasonic inspection of long steel pipes using Lamb waves. *NDT & E International* 29 (1): 13-20.

Pei, J., M. I. Yousuf, F. L. Degertekin, B. V. Honein, and B. T. Khuri-Yakub. 1996. Lamb wave tomography and its application in pipe erosion/corrosion monitoring. *Research in Nondestructive Evaluation* 8 (4): 189-97.

Popovics, J. S., W-J Song, and M. Ghandehari. 2000. Application of surface wave transmission measurements for crack depth determination in concrete. *ACI Materials Journal* 97 (2) (March/April): 127-35.

Richart, F. E., J. R. Hall, and R. D. Woods. 1970. *Vibrations of soils and foundations*. Englewood Cliffs, N.J., Prentice-Hall.

Robers, M. A., and R. Scottini. 2002. Pulsed eddy current in corrosion detection. *Journal of Nondestructive Testing* 7 (10).

M. Russo, "SWAN (Surface Waves Analysis)" 2006, http://www.geoastier.com.

Saarenketo, R., and T. Scullion. 2000. Road evaluation with ground penetrating radar. *Journal of Applied Geophysics* 43: 119-38.

Sansalone, M. 1997. Impact-echo: The complete story. *American Concrete Institute Structural Journal* 94: 777-86.

Santamarina, J. C. 1998. *Introduction to discrete signals and inverse problems in civil engineering*, ed. Dante Fratta. Reston, Va.: ASCE Press.

Sebaaly, P. E., N. Tabatanee, and T. Scullion. 1991. Comparison of backcalculated moduli from falling weight deflectometer and truck loading. *Transportation Research Record: Journal of the Transportation Research Board* 1377: 17-25.

Shah, A. A., and Y. Ribakov. 2008. Non-destructive measurements of crack assessment and defect detection in concrete structures. *Materials and Design* 29 (1): 61-9.

Silk, M. G., and K. F. Bainton. 1979. The propagation in metal tubing of ultrasonic wave modes equivalent to lamb waves. *Ultrasonics* 17 (1): 11-9.

Song, W. J., J. S. Popovics, J. C. Aldrin, and S. P. Shah. 2003. Measurement of surface wave transmission coefficient across surface-breaking cracks and notches in concrete. *The Journal of the Acoustical Society of America* 113 (2): 717.

Stokoe II, K. H., and S. Nazarian. 1983. Effectiveness of ground improvement from spectral analysis of surface waves. Paper presented at Proceedings of the 8th European Conference on Soil Mechanics and Foundation Engineering: Improvement of Ground. Volume 2.

Surette E., C. Barnes, and N. Ali. 2010. Use of GPR and MASW to complement backcalculated moduli and design life calculations. Paper presented at 2010 Annual Conference of the Transportation Association of Canada, Halifax.

Tallavo, F., G. Cascante, and M. D. Pandey. 2009. New methodology for source characterization in pulse velocity testing. *Geotechnical Testing Journal* 32 (6): 537-52.

Tinkey, Y., L. D. Olson, and M. Hergert. 2011. Advances in stress wave scanning of decks and pavements. Paper presented at Engineering Mechanics Institute Conference, Boston, MA.

Tong, Jian Hua, and Shu Tao Liao. 2009. A new elastic-wave-based NDT system for imaging defects inside concrete structures. *Proceedings of the World Congress on Engineering* II.

Underwood, S., and Y. R. Kim. 2002. Determination of depth of surface cracks in asphalt pavements. *Transportation Research Record: Journal of the Transportation Research Board* 1853: 143-9.

Viktorov, I. A. 1967. *Rayleigh and Lamb waves: Physical theory and applications*. New York: Plenum Press.

Vilasmongkolchai, T., P. Kaewtrakulpong, M. Noipitak, and A. Prateepasen. 2010. Ultrasonic inspection system for detecting small flaws at far surface of steel plate. Paper presented at 7th Annual International Conference on Electrical Engineering/Electronics, Computer, Telecommunications and Information Technology.

Yang, Y. 2009. Nondestructive evaluation of the depth of cracks in concrete plates using surface waves. University of Waterloo.

———. 2005. Depth evaluation of surface-breaking cracks in concrete using mechanical waves. University of Waterloo.

Yin, W., and A. J. Peyton. 2007. Thickness measurement of non-magnetic plates using multi-frequency eddy current sensors. *NDT&E International* 40 (1): 43-8.

Zemanek, J. J. 1971. An experimental and theoretical investigation of elastic wave propagation in a cylinder. *The Journal of the Acoustical Society of America* 51: 265.

Zhong, X.G.; X. Zeng , and J. G. Rose. 2002. Shear modulus and damping ratio of rubber-modified asphalt mixes and unsaturated subgrade soils. *Journal of Materials in Civil Engineering* 14 (6): 496.

APPENDIX A: Example of calculation of instantaneous frequency and instantaneous damping from an analytic signal

This appendix shows the steps for computing the instantaneous properties from an analytic signal. A free-decay waveform with a linearly varying frequency (1 to 2 Hz) and a damping ratio of 1% is used.

1. INDEX

$ORIGIN \equiv 1$

$N := 40000$ $\quad j := 1..N$ $\quad k := 1..N$

2. DEFINING TIME AND FREQUENCY VALUES

$\Delta t := 0.001$

$t_j := \Delta t \cdot (j - 1)$ $\quad \Delta f := \frac{1}{t_N} = 0.025$ $\quad fr_k := (k - 1) \cdot \Delta f$

3. INITIAL CONDITIONS

$x_0 := 0$ $\quad v_0 := 0$ $\quad \xi := 0.01$

$\omega_0 := 2 \cdot \pi$ $\quad \omega_f := 4 \cdot \pi$ $\quad \omega_j := \frac{(\omega_f - \omega_0)}{N} \cdot j + \omega_0$

$f_0 := \frac{\omega_0}{2 \cdot \pi} = 1$ $\quad f_f := \frac{\omega_f}{2 \cdot \pi} = 2$ $\quad \omega_{d_j} := \omega_j \sqrt{1 - \xi^2}$

4. TIME AND PHASE SHIFT, AND MAXIMUN SIGNAL AMPLITUDE

$t_0 := 0$ $\quad \phi := 0$ $\quad A := 0.5$

5. RESPONSE

5.1 At time t = 0

$$v_j := A\, e^{-\xi \cdot \omega_j \cdot t_j} \cdot \sin\left(\omega_{d_j} \cdot t_j + \phi\right)$$

5.2 With time shift

$$w_j := A\, e^{-\xi \cdot \omega_j \cdot \left(t_j - t_0\right)} \cdot \sin\left[\omega_{d_j} \cdot \left(t_j - t_0\right) + \phi\right]$$

5.3 Response

$$zz_j := \begin{cases} 0 & \text{if } t_j \le t_0 \\ w_j & \text{otherwise} \end{cases}$$

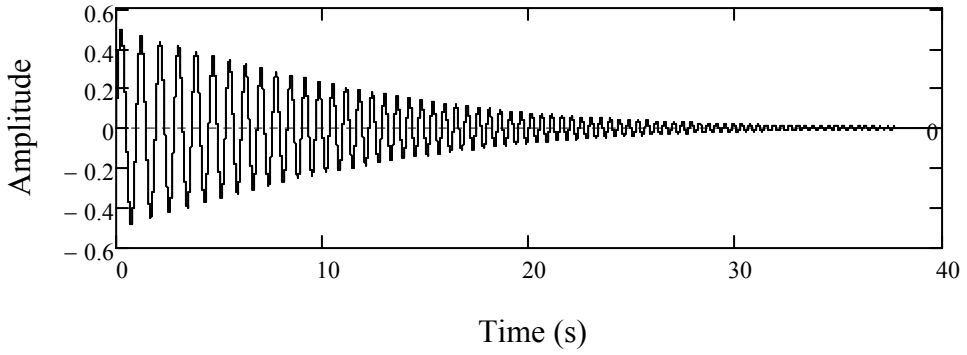

6. FOURIER TRANSFORM

$$ZZ := \mathrm{CFFT}(zz) \qquad ZZR_k := \mathrm{Re}\left(ZZ_k\right) \qquad ZZI_k := \mathrm{Im}\left(ZZ_k\right)$$

7. ANALYTIC SIGNAL (INDIRECT METHOD)

7.1 REMOVAL OF THE FREQUENCIES ABOVE THE NYQUIST FREQUENCY

$$ZZmod_k := \begin{cases} 0 & \text{if } fr_k \geq \frac{1}{2 \cdot \Delta t} \\ ZZ_k & \text{otherwise} \end{cases}$$

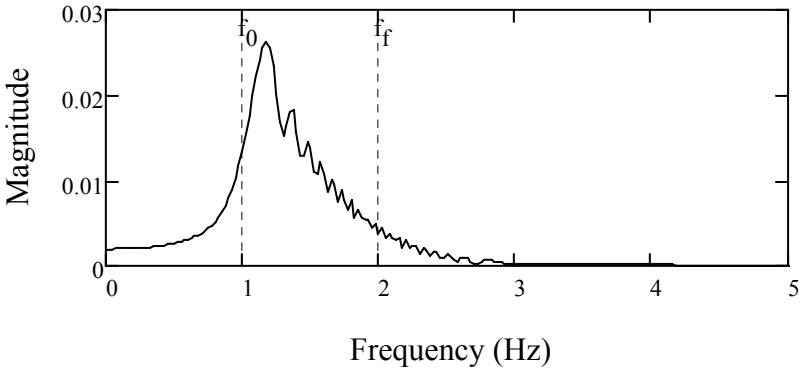

7.2 INSTANTANEOUS MAGNITUDE

$$zza := ICFFT(ZZmod) \cdot 2$$

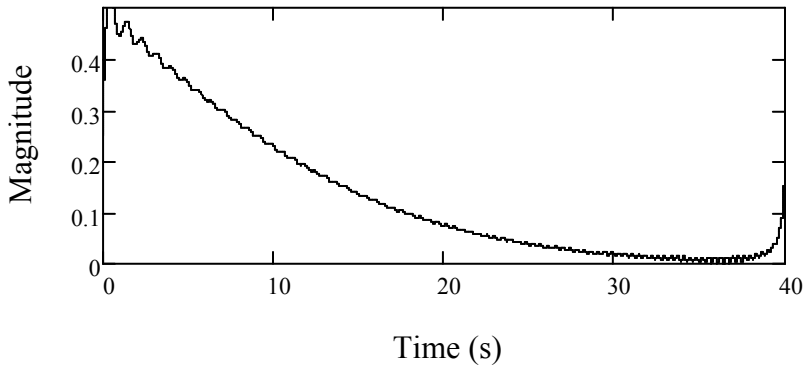

7.3 INSTANTANEOUS PHASE

$$ipzza := phase(zza)$$

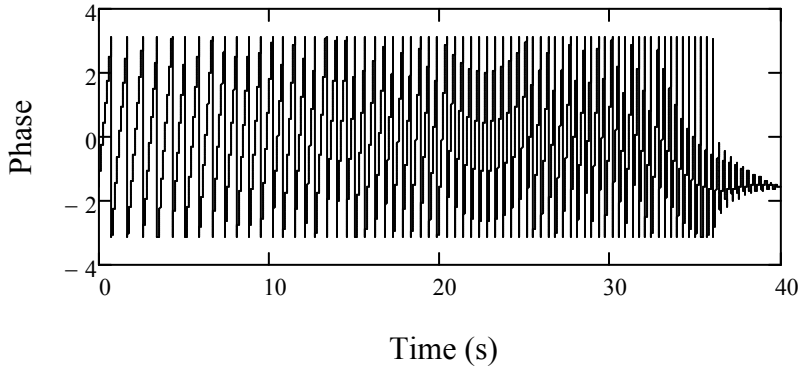

7.4 INSTANTANEOUS FREQUENCY

Unwrapped phase $\quad upzza := phasecor(ipzza)$

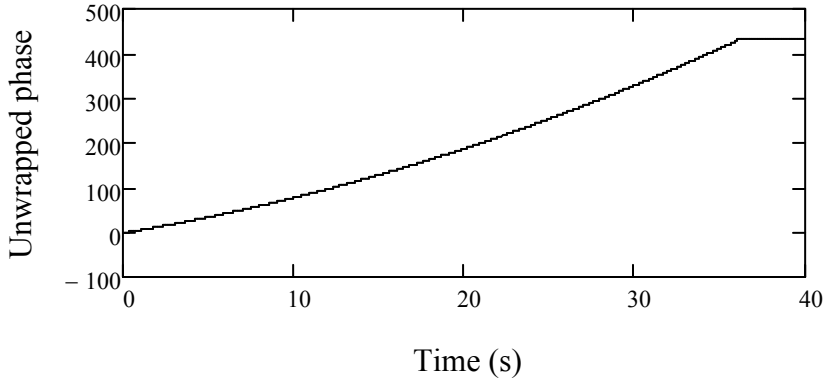

Instantaneous frequency

$$kk := 1..N - 1$$

$$fzza_{kk} := \frac{\left|upzza_{kk} - upzza_{kk+1}\right|}{\Delta t} \cdot \frac{1}{2\pi}$$

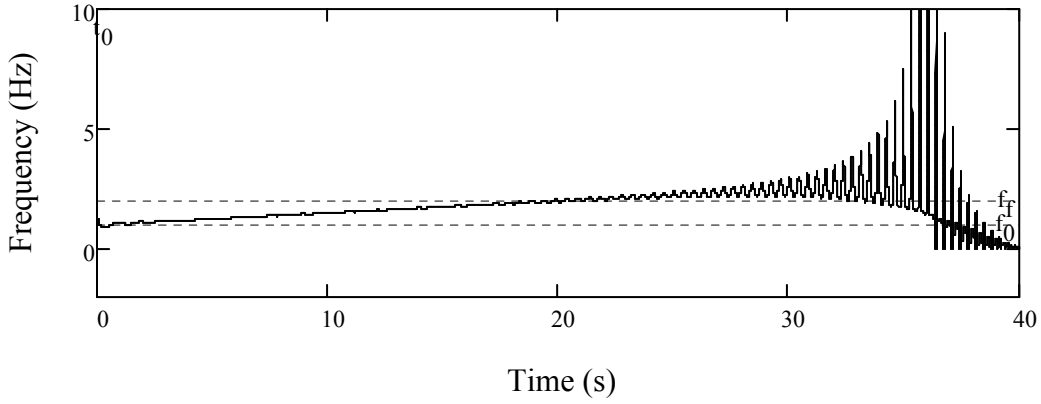

7.5 INSTANTANEOUS FREQUENCY (SMOOTHING)

$$Nxx := \frac{40}{\Delta t} = 4 \times 10^4 \qquad jx := 1..Nxx \qquad t\_S_{jx} := t_{jx} \qquad upzz\_S_{jx} := upzza_{jx}$$

7.5 INSTANTANEOUS FREQUENCY (SMOOTHING)

$Nxx := \frac{40}{\Delta t} = 4 \times 10^4$ $\quad jx := 1 .. Nxx$ $\quad t\_S_{jx} := t_{jx}$ $\quad upzz\_S_{jx} := upzza_{jx}$

SUPSMOOTH (ADAPTIVE METHOD)

Unwrapped phase $\quad upzz\_s := supsmooth(t\_S, upzz\_S)$

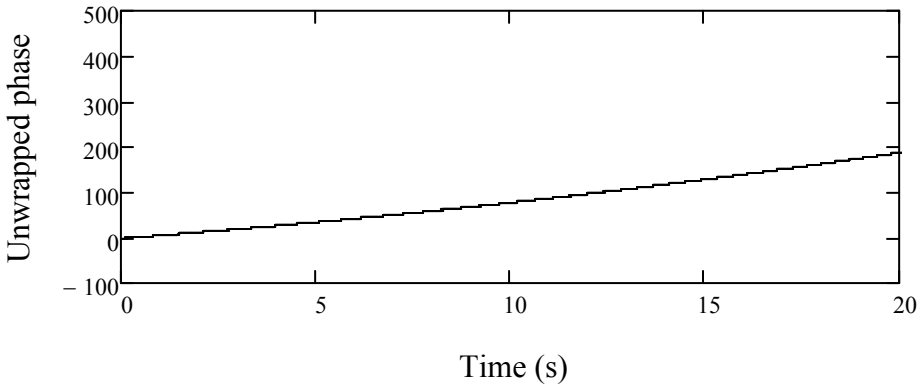

Instantaneous frequency $\quad j\_S := 1 .. Nxx - 1$

$$fzza\_s_{j\_S} := \frac{\left| upzz\_s_{j\_S} - upzz\_s_{j\_S+1} \right|}{\Delta t} \cdot \frac{1}{2\pi}$$

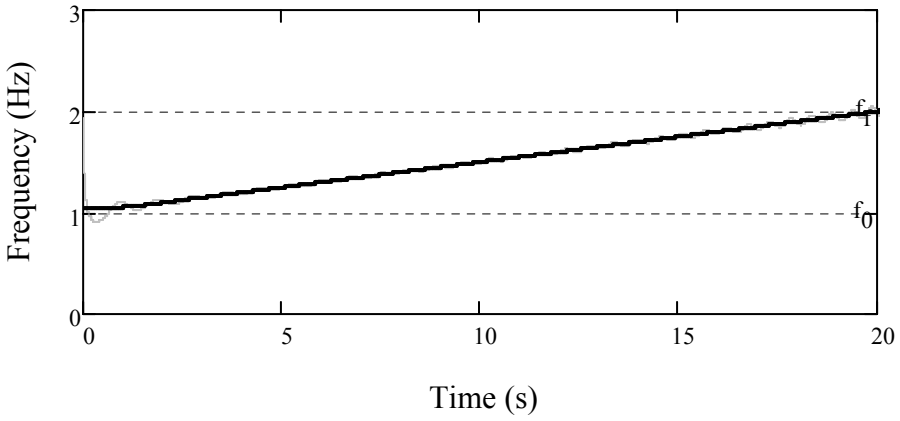

8. ANALYTIC SIGNAL (DIRECT METHOD USING HT)

yy := hilbert(zz) xx:= zz + i·yy XX := CFFT(xx)

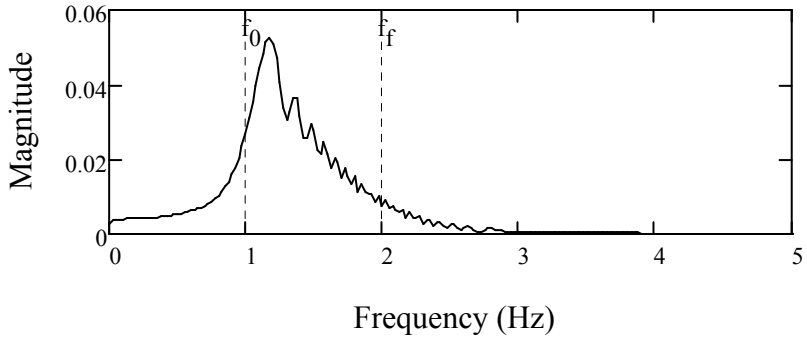

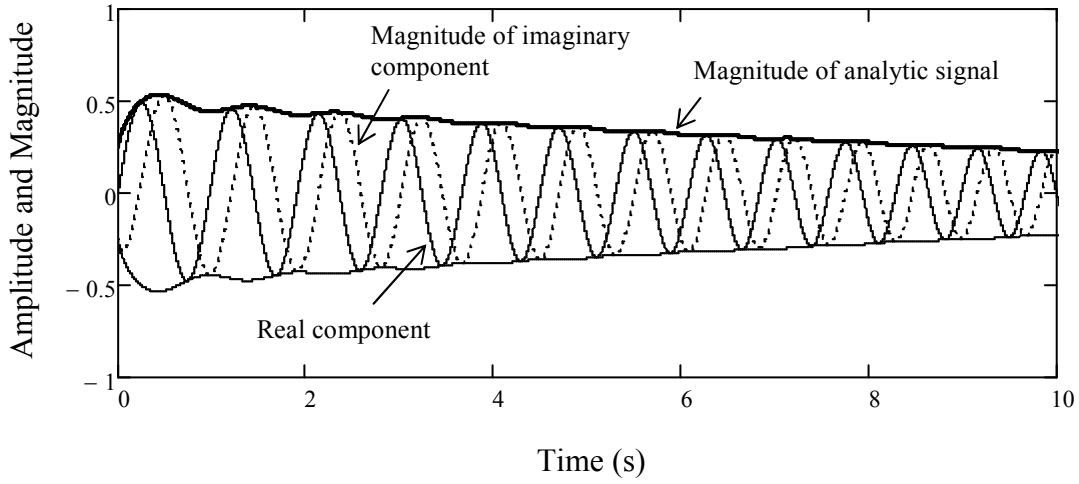

The magnitude of the analytic signal xx is the complex envelope of the original signal zz

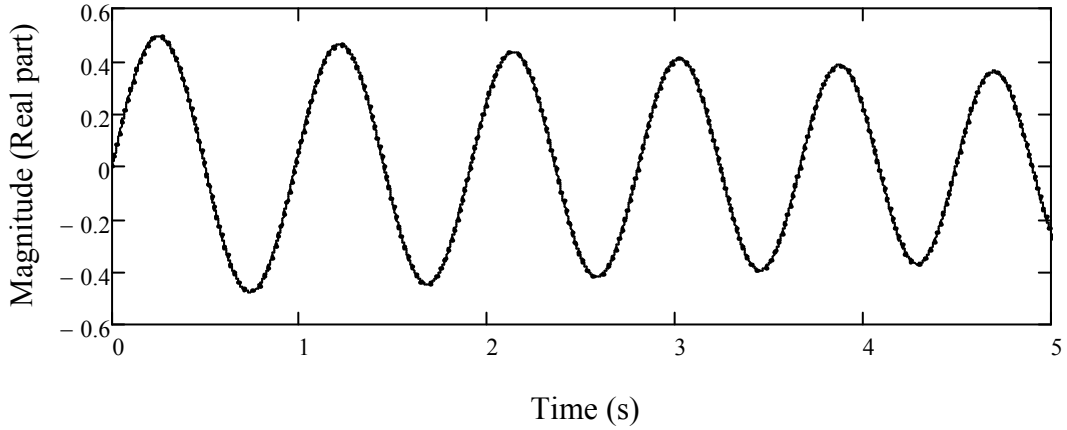

The real component of zza is the same as the original signal.

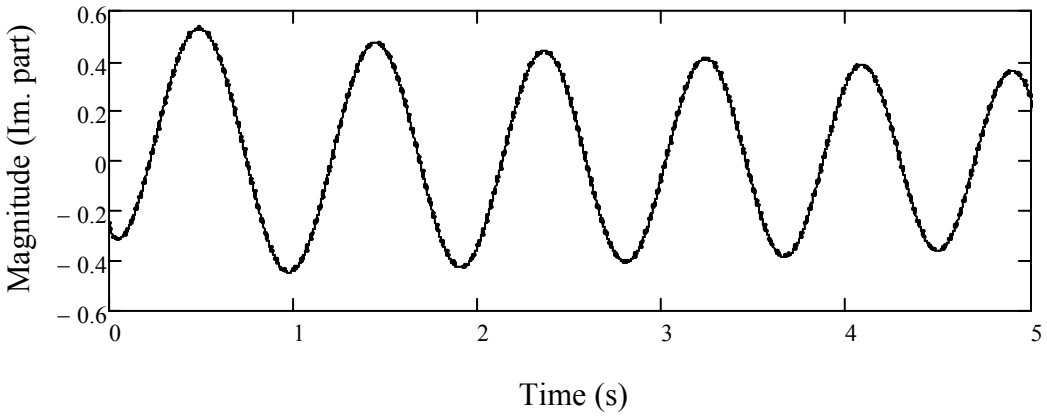

The imaginary component of zza is the same as the hilbert transform of the original signal zz.

8.1 INSTANTANEOUS FREQUENCY

Unwrapped phase $upxx := phasecor(phase(xx))$

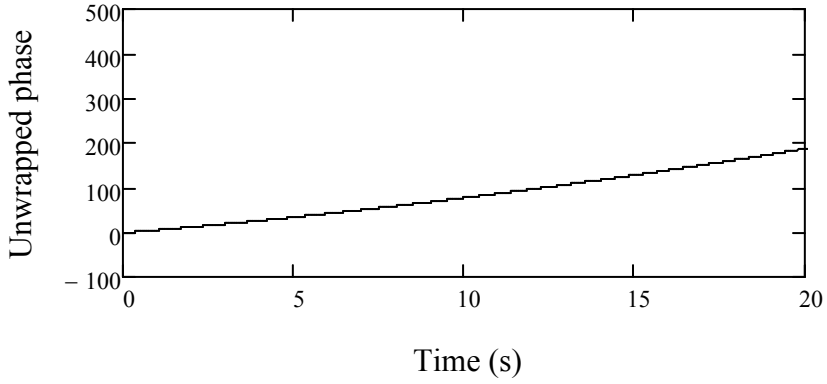

Instantaneous frequency $\omega_j(t) = \frac{\Delta\theta}{\Delta t}$

$kk := 1 .. N - 1$ $\qquad fxx_{kk} := \frac{\left|upxx_{kk} - upxx_{kk+1}\right|}{\Delta t} \cdot \frac{1}{2\pi}$

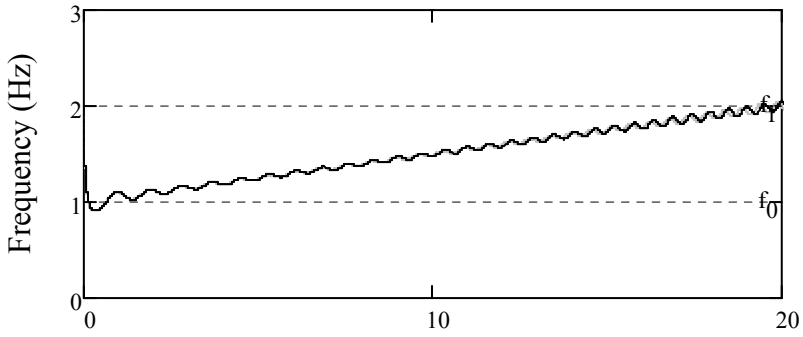

8.2 INSTANTANEOUS FREQUENCY (SMOOTHING)

$Nxx := \frac{40}{\Delta t} = 4 \times 10^4$ $\quad jx := 1 .. Nxx$ $\quad t\_S_{jx} := t_{jx}$ $\quad upxx\_S_{jx} := upxx_{jx}$

Defining time and phase vectors with new index

SUPSMOOTH (ADAPTIVE METHOD)

Unwrapped phase $\quad upxx\_s := supsmooth\ (t\_S, upxx\_S)$

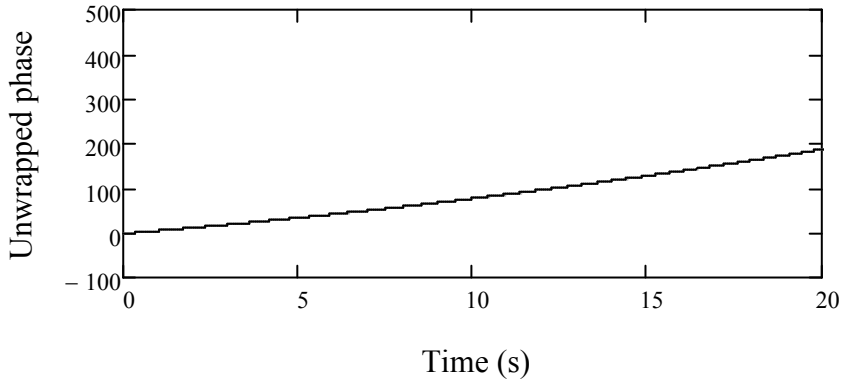

Instantaneous frequency

$j\_S := 1 .. Nxx - 1$ $\quad fxx\_s_{j\_S} := \frac{\left| upxx\_s_{j\_S} - upxx\_s_{j\_S+1} \right|}{\Delta t} \cdot \frac{1}{2\pi}$

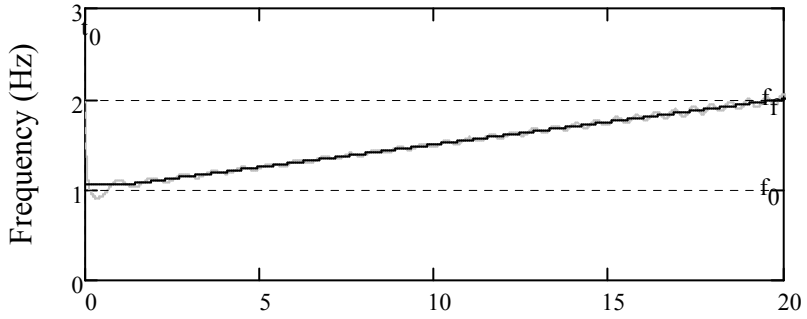

9. EVALUATION OF DAMPING

9.1 IN(MAGNITUDE) vs TIME

lnxx:= ln(mag(xx))

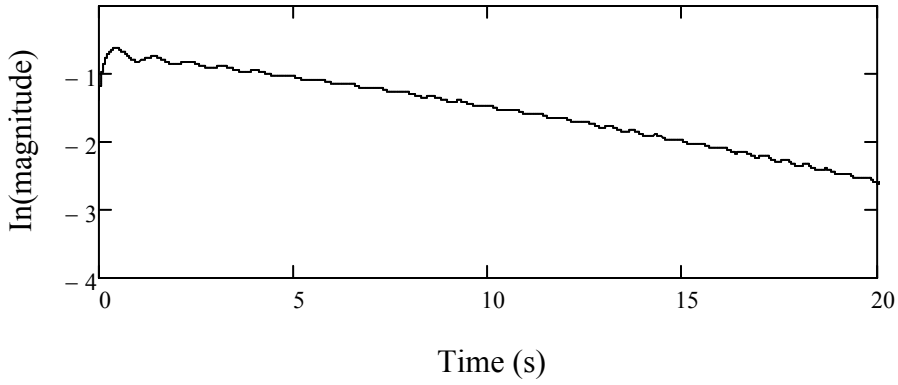

SUPSMOOTH (ADAPTIVE METHOD)

$t\_S_{jx} := t_{jx}$ $\quad lnxx\_S_{jx} := lnxx_{jx}$

lnxx_s:= supsmooth (t_S, lnxx_S)

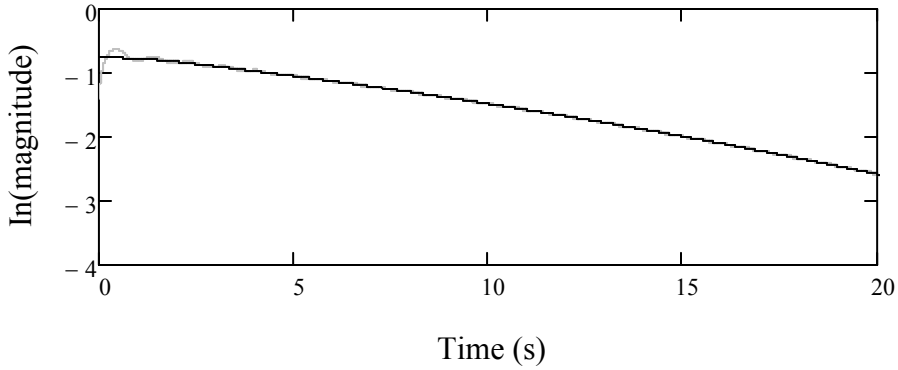

10. CALCULATING DAMPING WITHOUT MOVING WINDOW $\xi_j(t) = \frac{1}{\Delta\theta}\ln\frac{A_j}{A_{j+1}} = \frac{\ln A_j - \ln A_{j+1}}{\theta_j - \theta_{j+1}}$

10.1. CALCULATING DAMPING USING UNSMOOTHED DATA

$sxx_{j\_S} := (lnxx)_{j\_S} - (lnxx)_{j\_S+1}$ $fxx_{j\_S} := (upxx)_{j\_S} - (upxx)_{j\_S+1}$ $damps_{j\_S} := \frac{sxx_{j\_S}}{fxx_{j\_S}}$

$ll := \frac{0.001}{\Delta t} = 1$ $ul := \frac{35}{\Delta t} = 3.5 \times 10^4$

$sm := submatrix(damps, ll, ul, 1, 1)$ $|mean(sm)| \cdot 100 = 0.78$

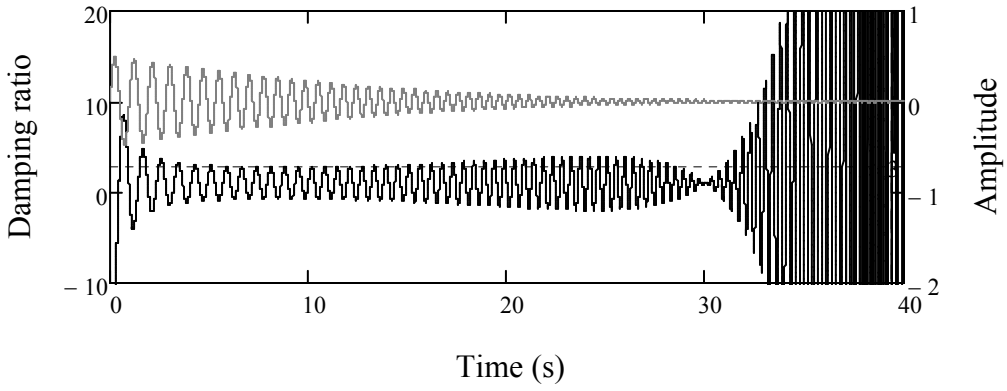

10.2. CALCULATING DAMPING USING SUPSMOOTH (ADAPTIVE METHOD)

$sxx\_s_{j\_S} := (lnxx\_s)_{j\_S} - (lnxx\_s)_{j\_S+1}$ $fxx\_s_{j\_S} := (upxx\_s)_{j\_S} - (upxx\_s)_{j\_S+1}$

$damps\_s_{j\_S} := \frac{sxx\_s_{j\_S}}{fxx\_s_{j\_S}}$

$sm\_s := submatrix(damps\_s, ll, ul, 1, 1)$ $|mean(sm\_s)| \cdot 100 = 0.976$

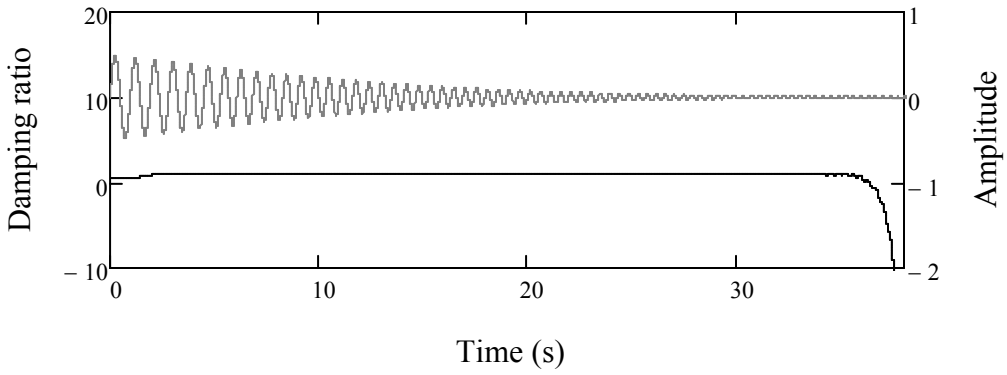

The last graph shows that the calculated instantaneous damping agrees well with the theoretical value (1%).

APPENDIX B: Calibration measurements

Appendix B shows the accelerometer identification, the arrival time determination, the phase information of the signals, and the P-wave velocity calculation for all 20 receivers. The test methodology and results are discussed in Chapter 5.

The arrival times for only a few accelerometers are presented herein; the complete set of time signals is available in the Appendix CD.

Table B-0-1. Accelerometer identification number

ID No.	Acc. S/N	ID No.	Acc. S/N	ID No.	Acc. S/N	ID No.	Acc. S/N
1	5631	6	5636	11	5634	16	5619
2	5640	7	5627	12	5618	17	5639
3	5625	8	5635	13	5661	18	5630
4	5622	9	5624	14	5637	19	5620
5	5629	10	5628	15	5632	20	5638

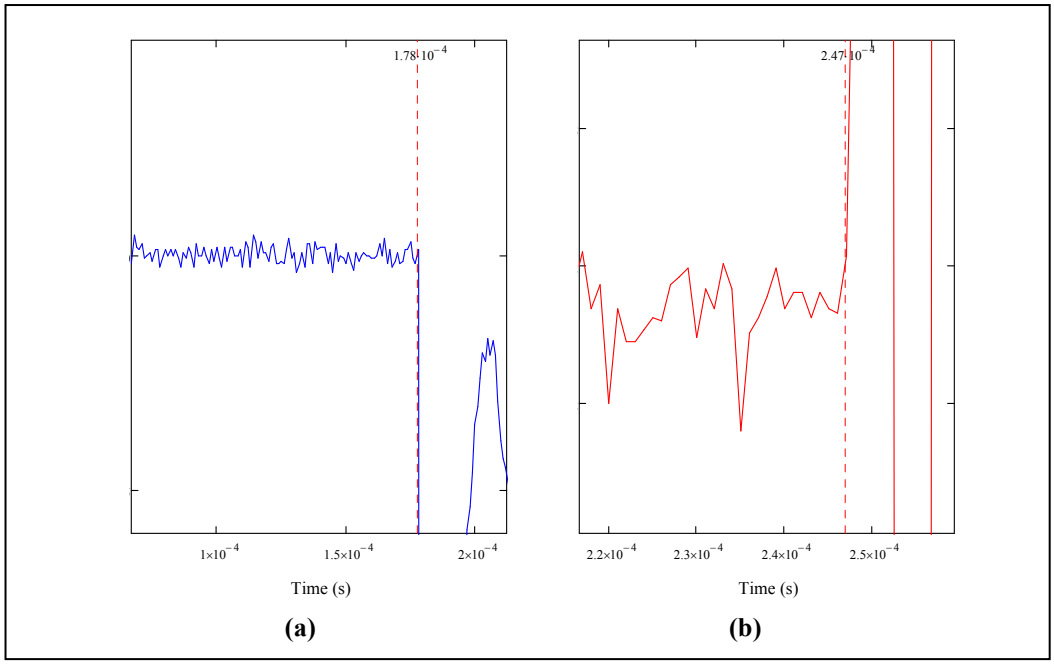

Figure B-1. Arrival time for Accelerometer No. 2, test with PVC+grease: **(a)** source input signal and **(b)** response signal

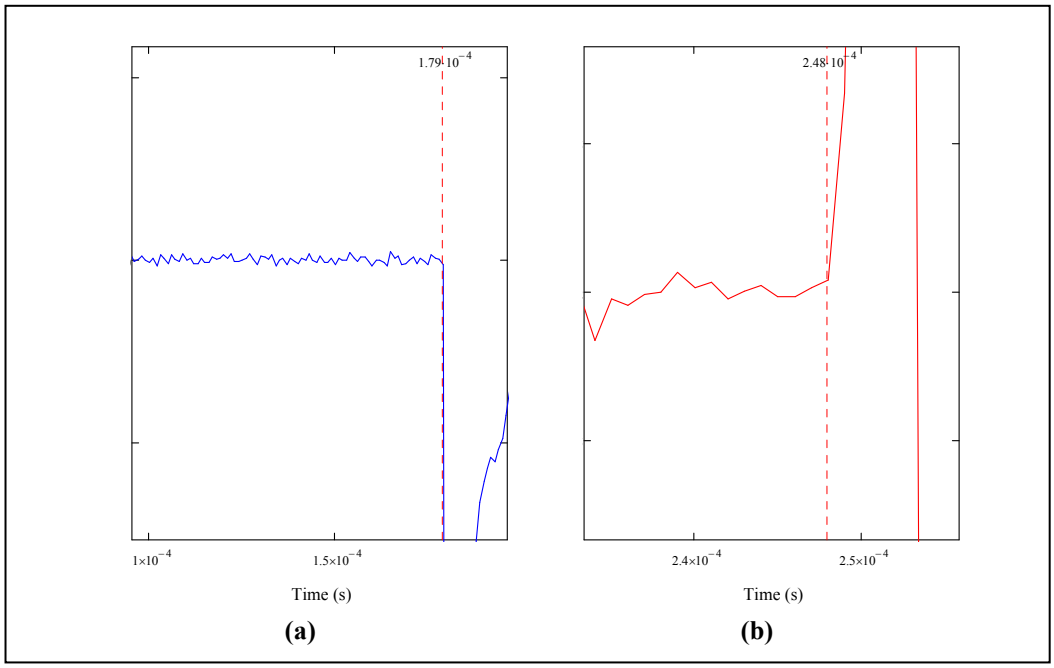

Figure B-2. Arrival time for Accelerometer No. 6, test with PVC+grease: **(a)** source input signal and **(b)** response signal

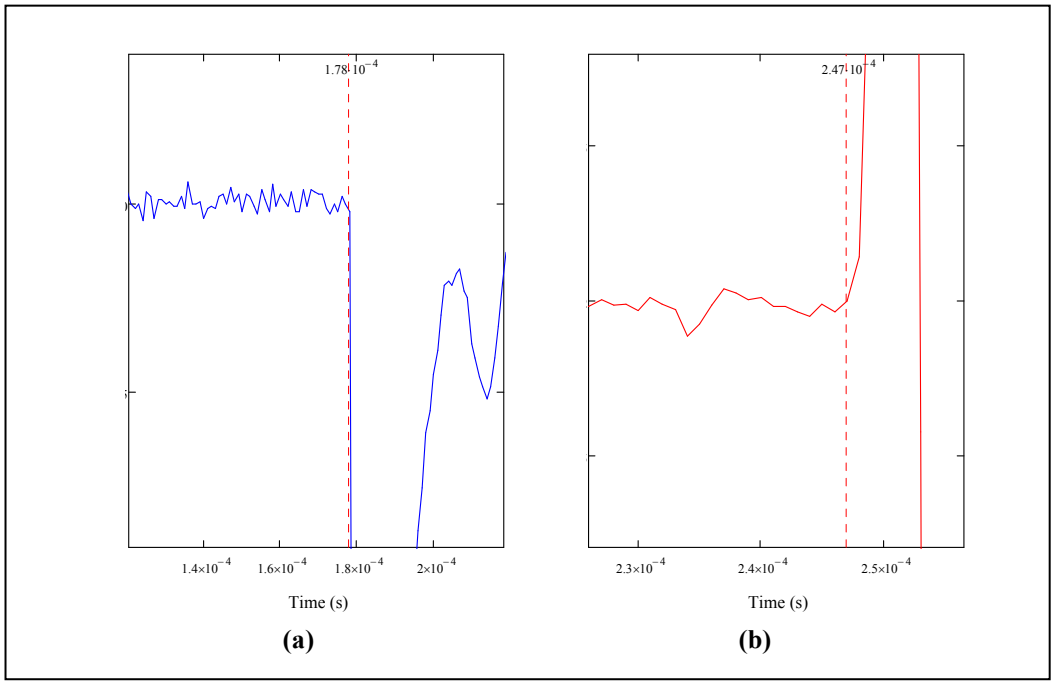

Figure B-3. Arrival time for Accelerometer No. 12, test with PVC+grease: **(a)** source input signal and **(b)** response signal

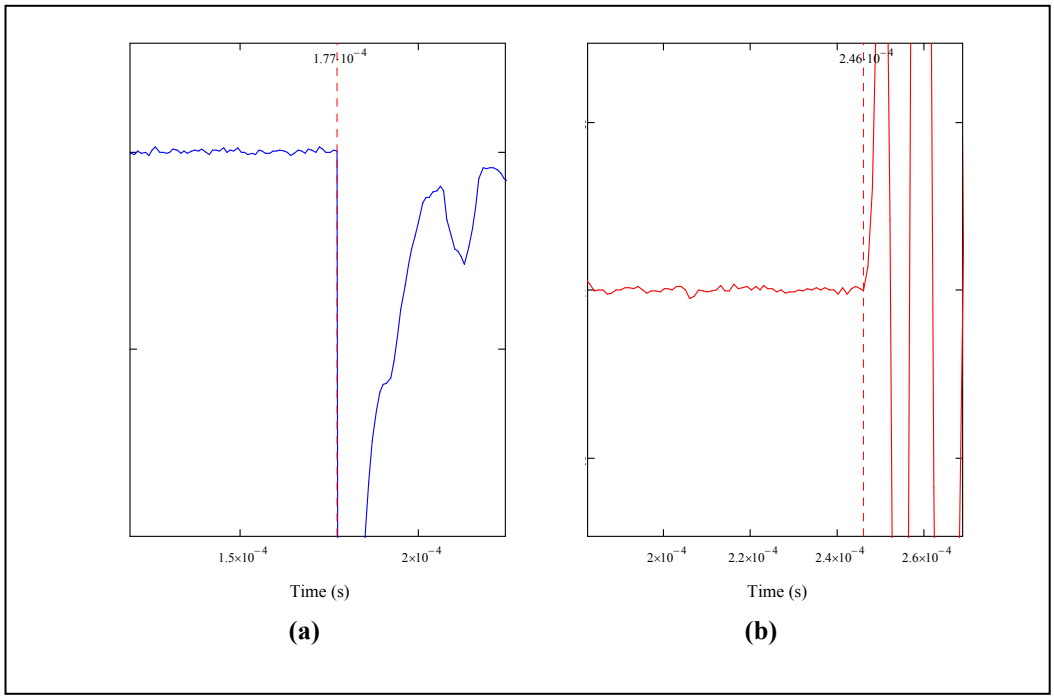

Figure B-4. Arrival time for Accelerometer No. 3, test with PVC+glue: **(a)** source input signal and **(b)** response signal

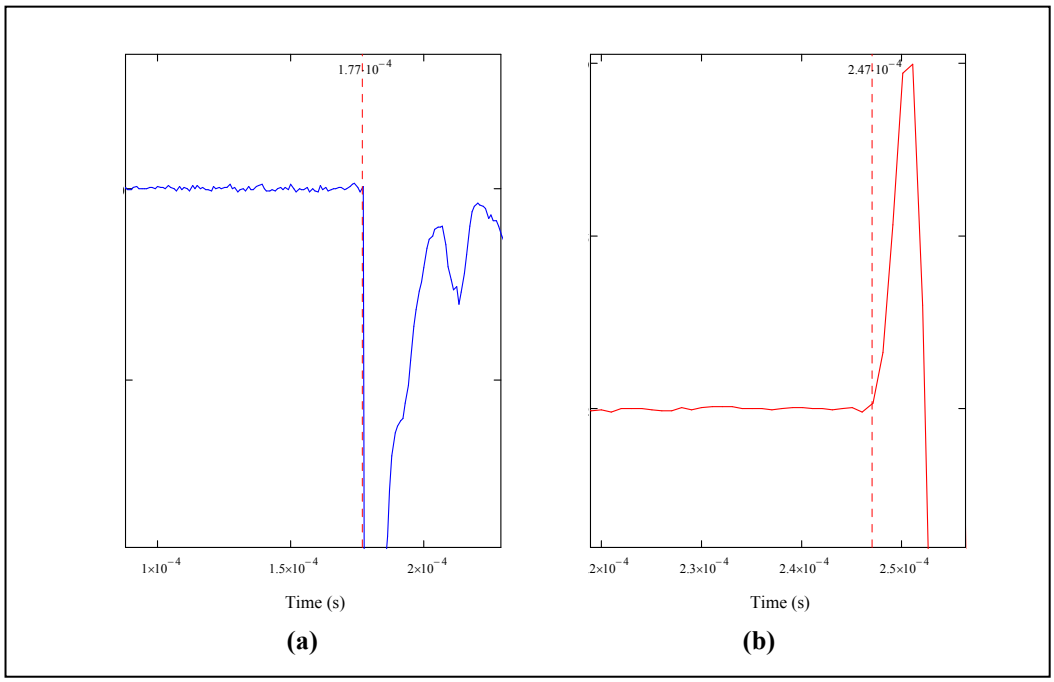

Figure B-5. Arrival time for Accelerometer No. 4, test with PVC+glue: **(a)** source input signal and **(b)** response signal

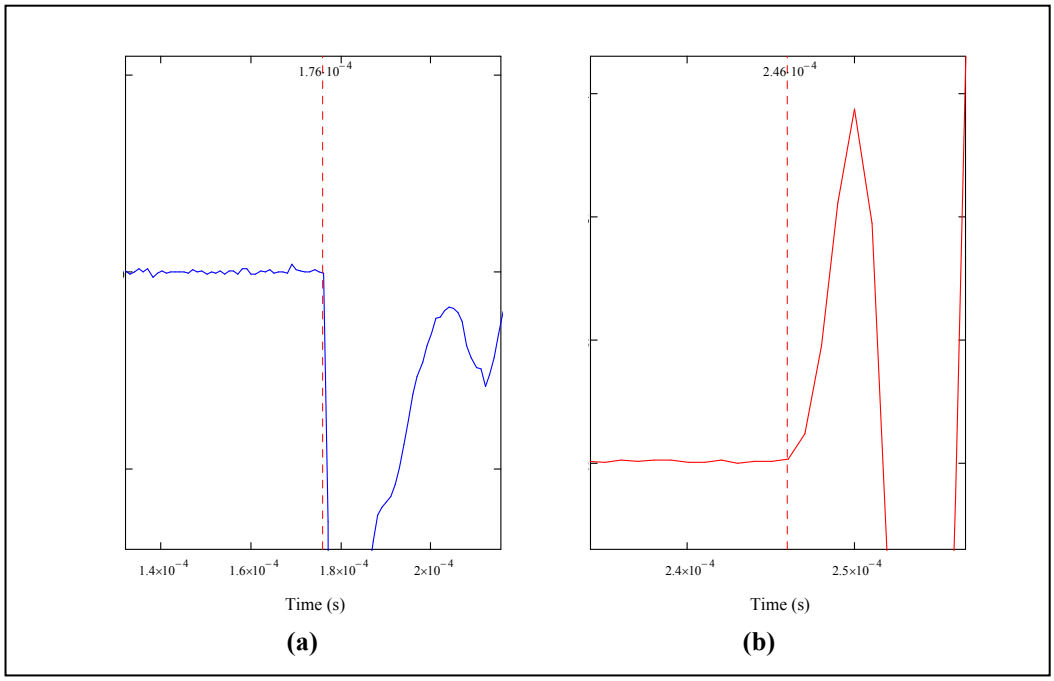

Figure B-6. Arrival time for Accelerometer No. 15, test with PVC+glue: **(a)** source input signal and **(b)** response signal

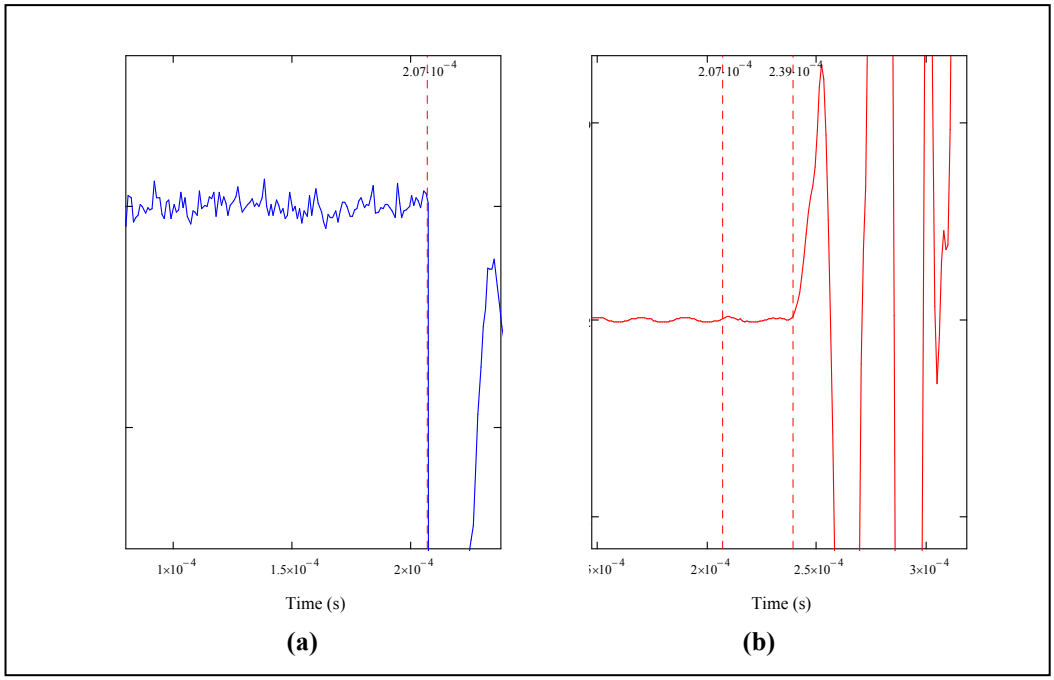

Figure B-7. Arrival time for Accelerometer No. 2, test with aluminum+grease: **(a)** source input signal and **(b)** response signal

APPENDIX C: Wavelet transforms using Morlet function for measurements on jointed surface

Appendix C shows the wavelet transform using Morlet wavelet functions of varying center frequencies: from 10 kHz to 60 kHz, with increments of 5 kHz. The measurements were conducted on the jointed surface of the density-controlled asphalt slab. Six sets of tests with different coupling configurations were conducted. The peak values were determined to compute the WTC. The test methodology and results are discussed in Chapter 6. Only the wavelet functions for Set 1 are presented herein; the complete results (for all six sets) are available in the Appendix CD.

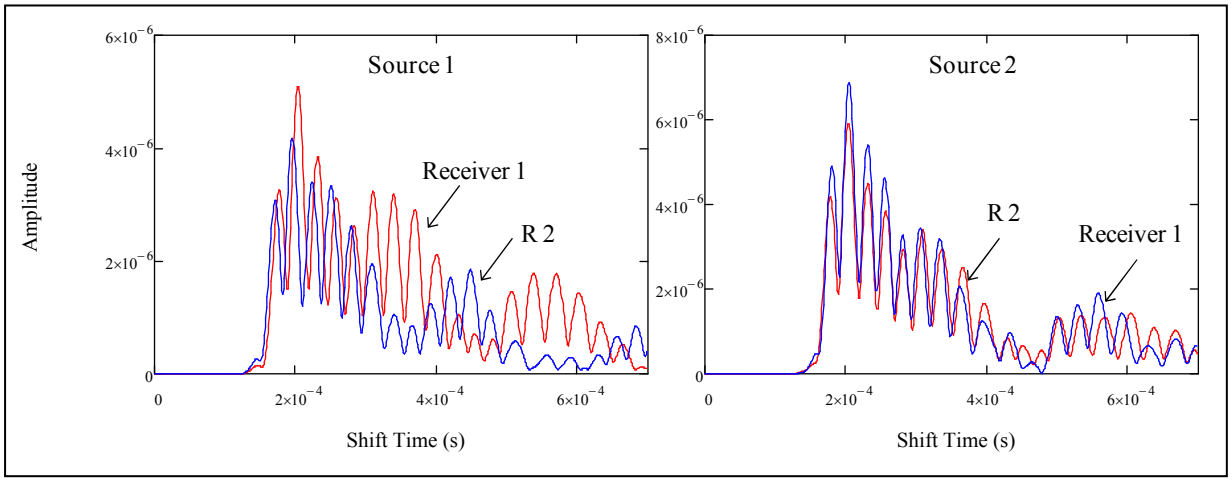

Figure C-1. Wavelet transform for Set 1, Morlet center frequency of 10 kHz.

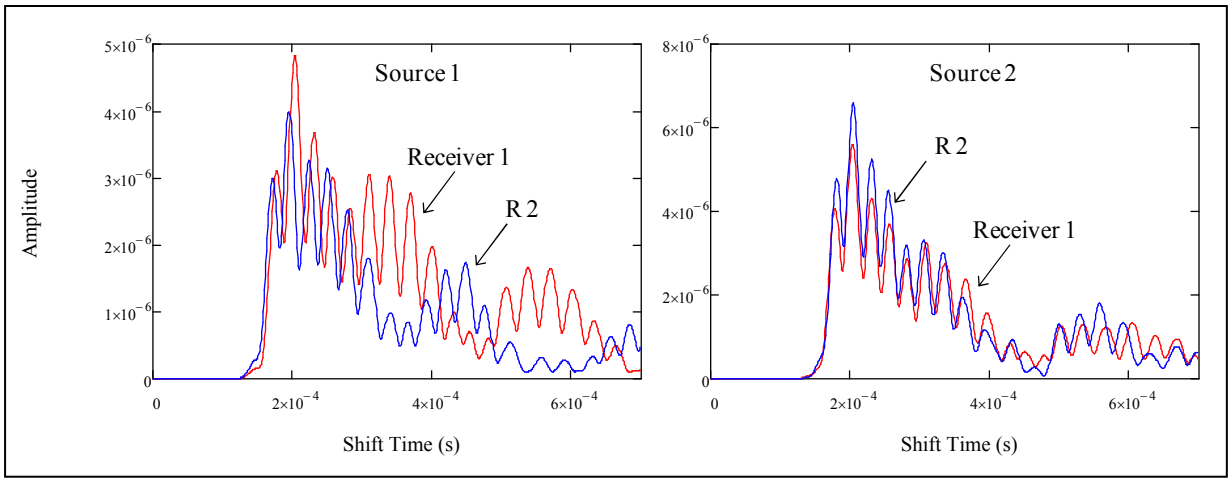

Figure C-2. Wavelet transform for Set 1, Morlet center frequency of 15 kHz.

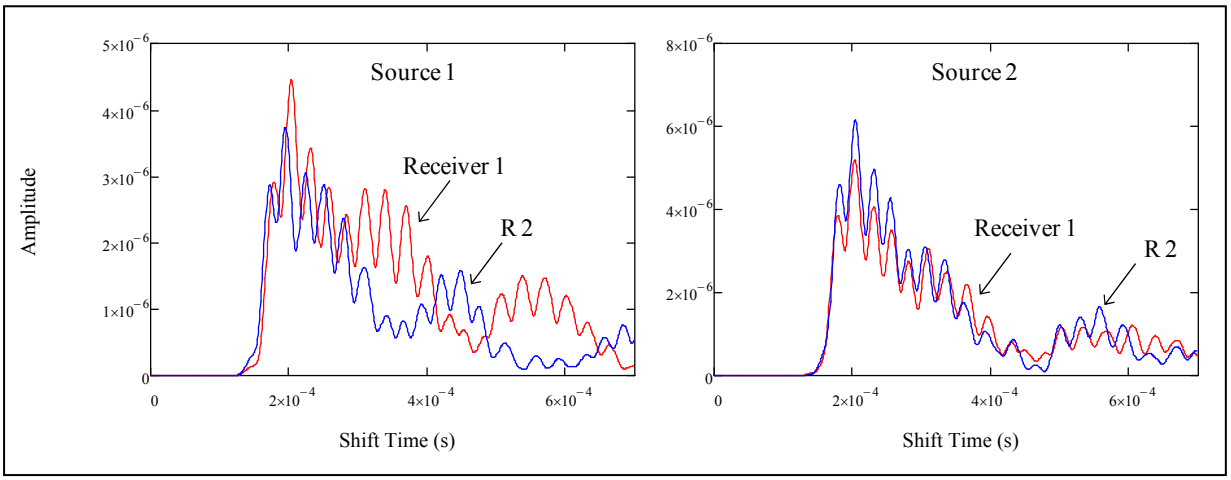

Figure C-3. Wavelet transform for Set 1, Morlet center frequency of 20 kHz.

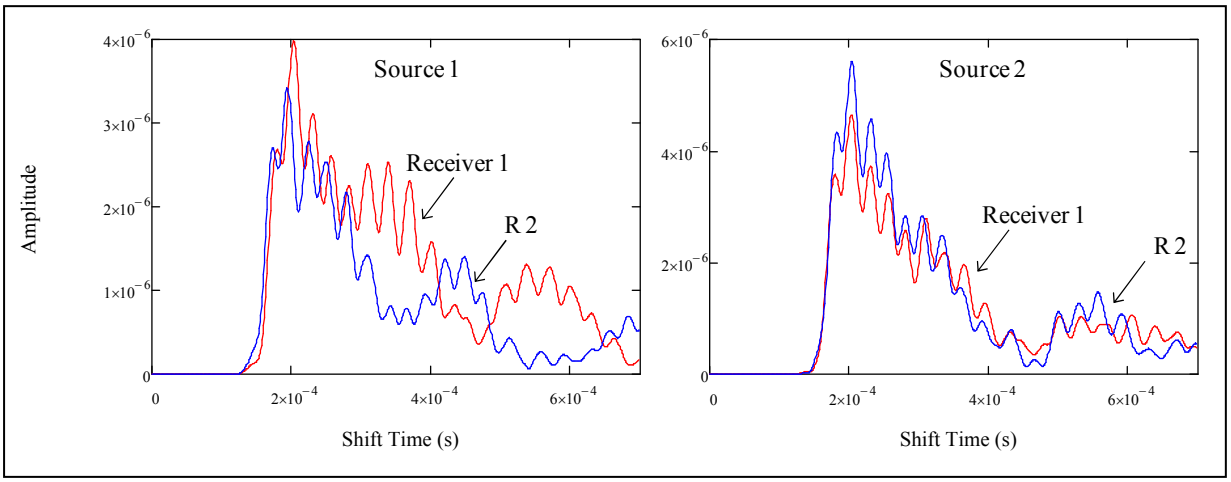

Figure C-4. Wavelet transform for Set 1, Morlet center frequency of 25 kHz.

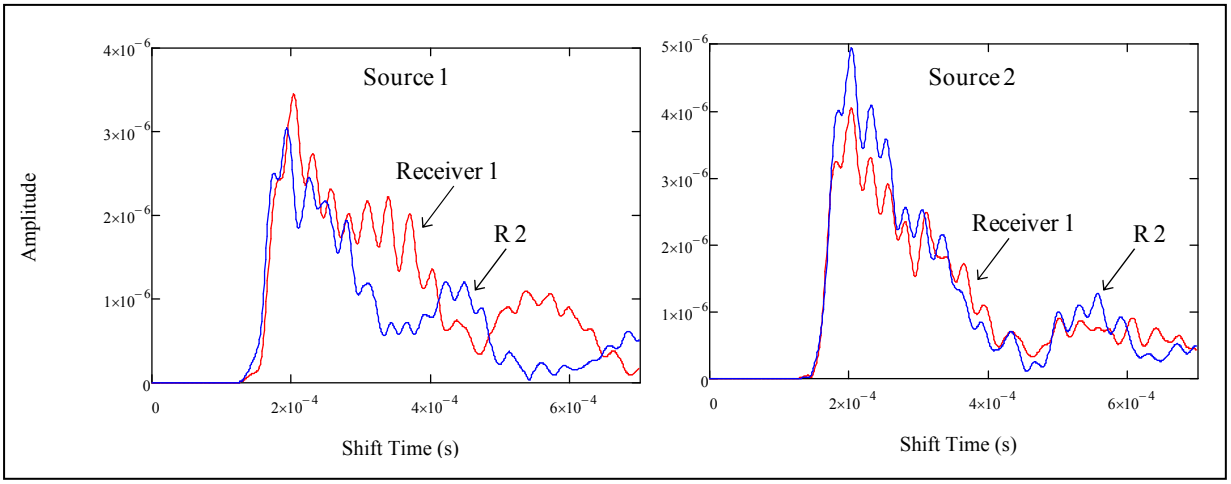

Figure C-5. Wavelet transform for Set 1, Morlet center frequency of 30 kHz.

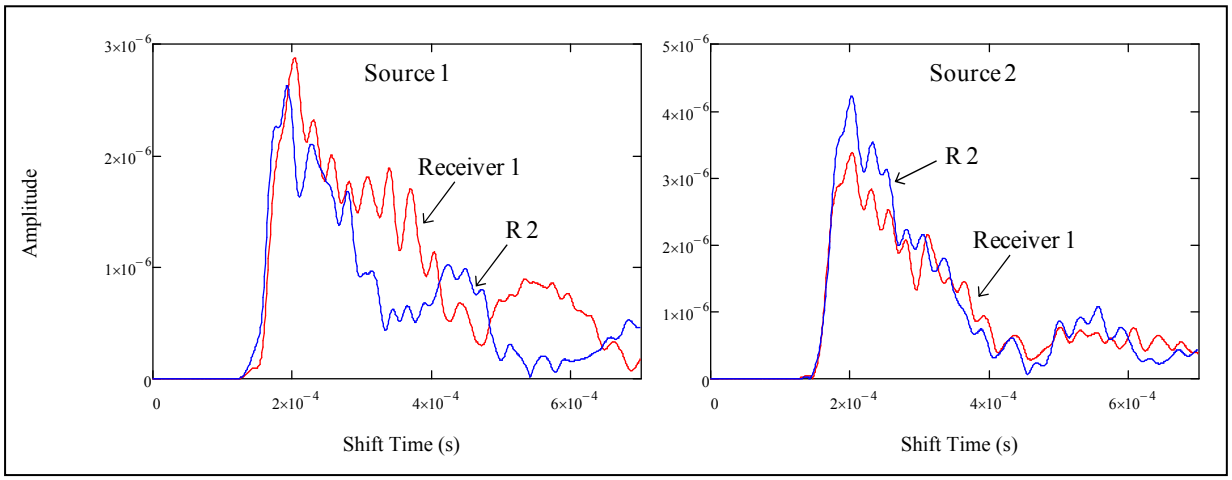

Figure C-6. Wavelet transform for Set 1, Morlet center frequency of 35 kHz.

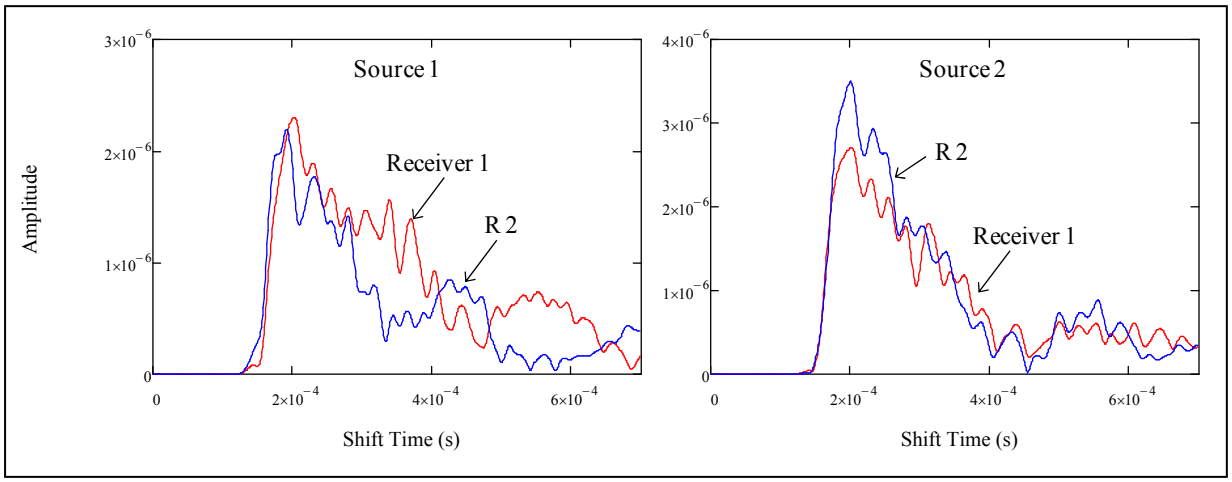

Figure C-7. Wavelet transform for Set 1, Morlet center frequency of 40 kHz.

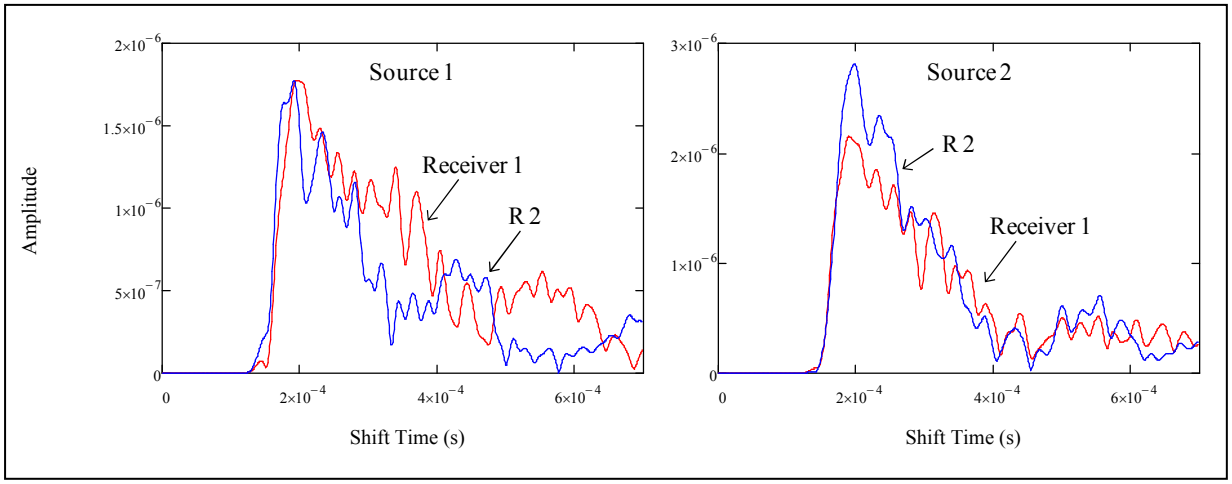

Figure C-8. Wavelet transform for Set 1, Morlet center frequency of 45 kHz.

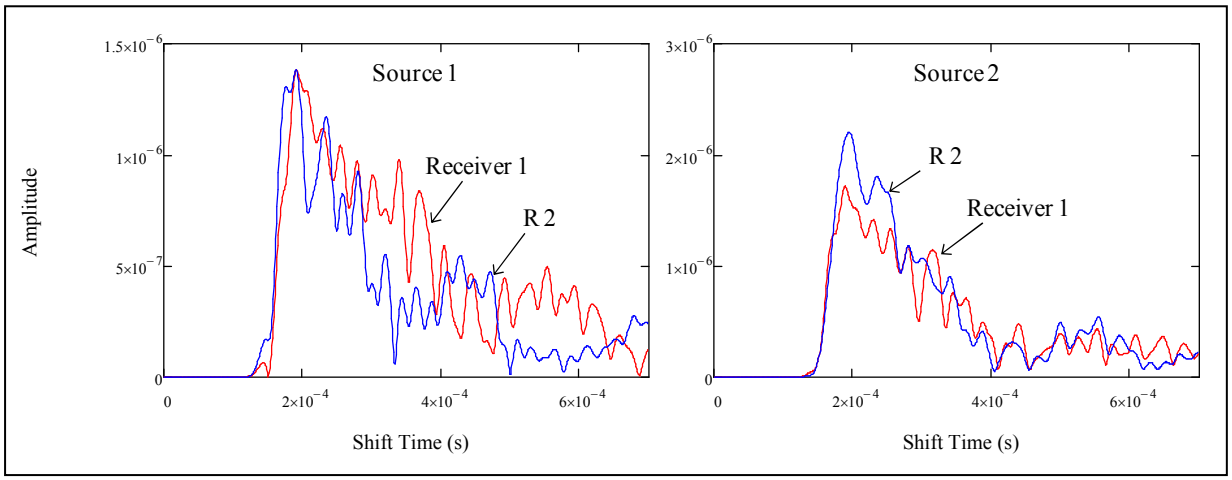

Figure C-9. Wavelet transform for Set 1, Morlet center frequency of 50 kHz.

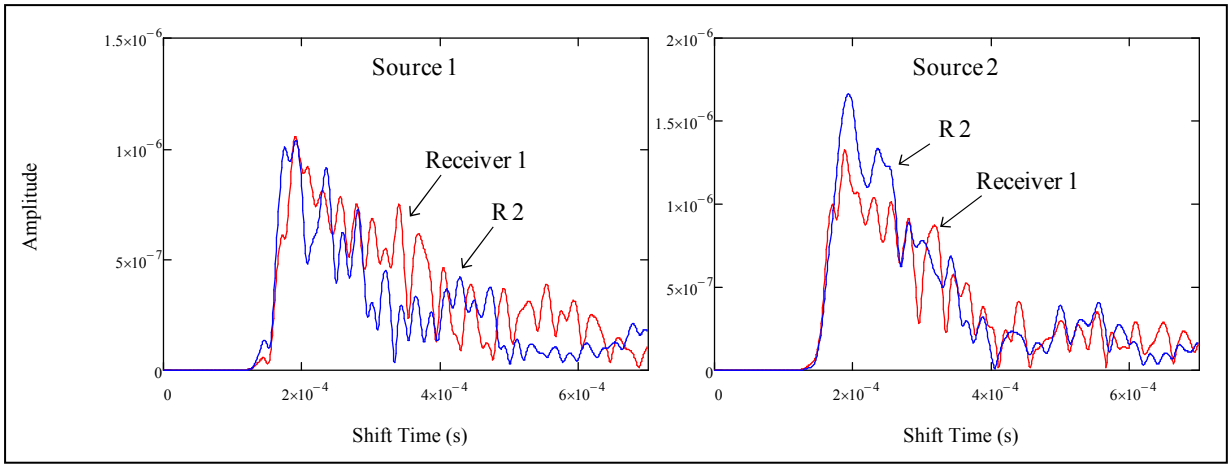

Figure C-10. Wavelet transform for Set 1, Morlet center frequency of 55 kHz.

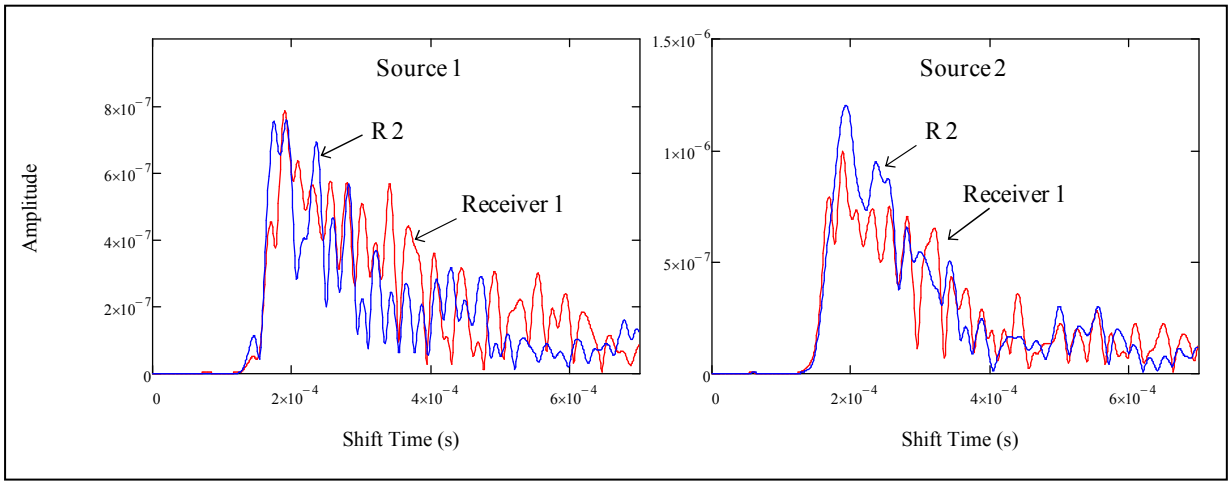

Figure C-11. Wavelet transform for Set 1, Morlet center frequency of 60 kHz.

APPENDIX D: Wavelet transforms using Morlet function for measurements on different square locations on the slab

Appendix D shows the wavelet transform using Morlet wavelet functions of varying center frequencies: from 10 kHz to 60 kHz, by increments of 5 kHz. The measurements were conducted on four different square locations of the density-controlled asphalt slab: Squares 1 and 2 were placed on jointed areas whereas Squares 3 and 4 were on joint-free areas. The peak values were determined to compute the WTC. The test methodology and results are discussed in Chapter 6. Only the wavelet functions for Square 1 are presented herein; the complete results (for all four square locations) are available in the Appendix CD.

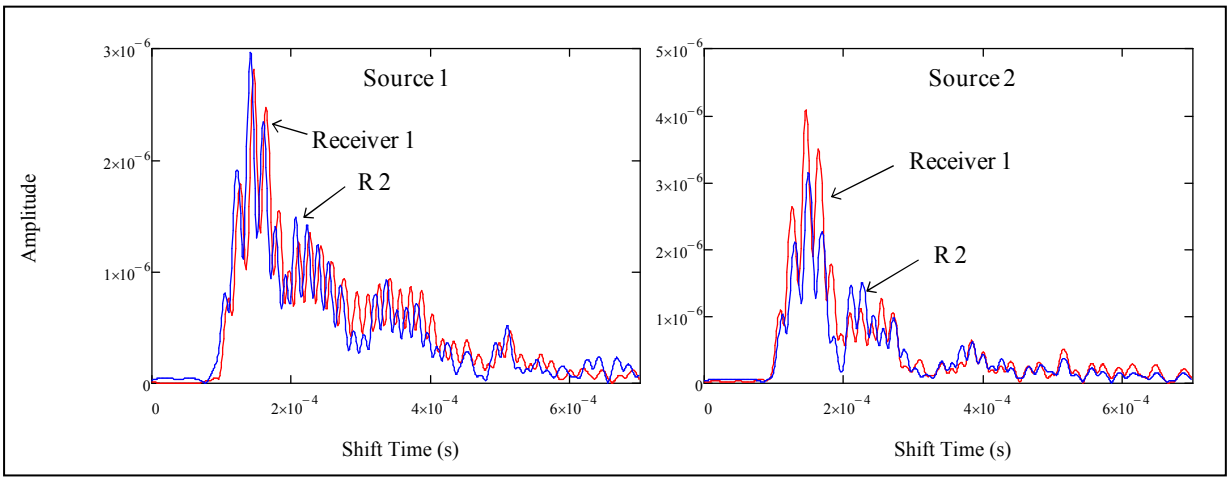

Figure D-1. Wavelet transform for Square 1, Morlet center frequency of 10 kHz.

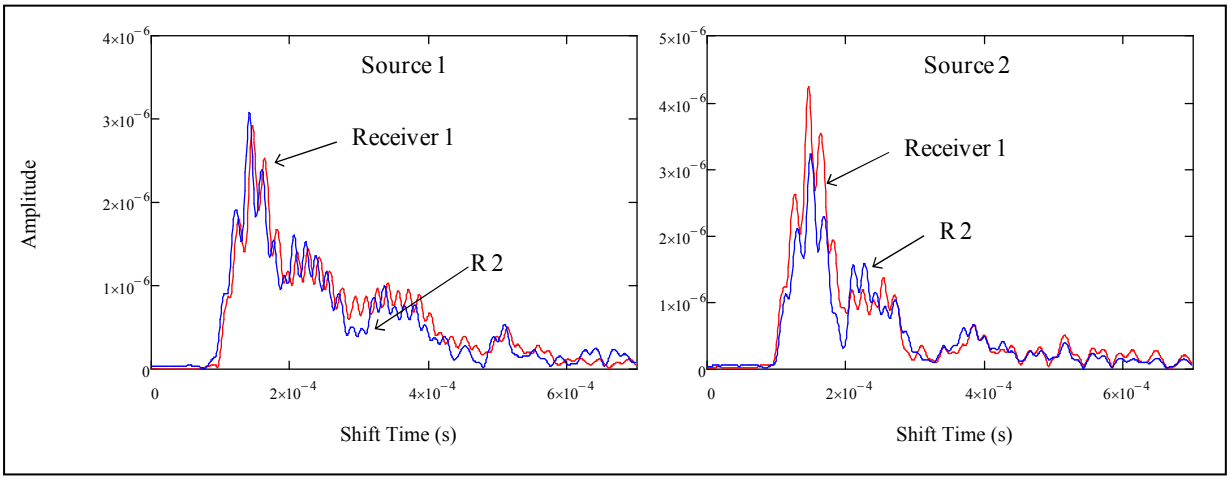

Figure D-2. Wavelet transform for Square 1, Morlet center frequency of 15 kHz.

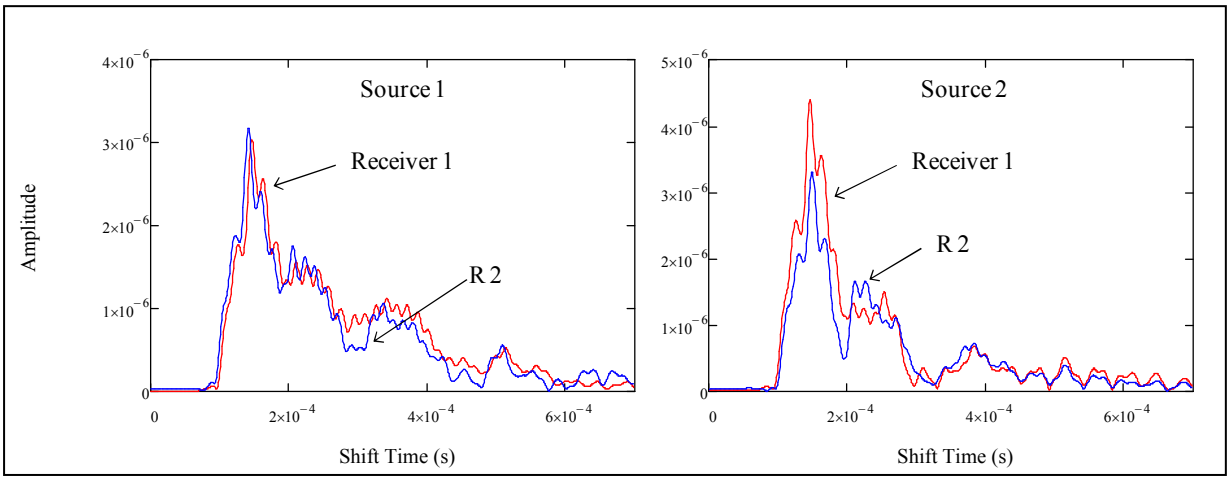

Figure D-3. Wavelet transform for Square 1, Morlet center frequency of 20 kHz.

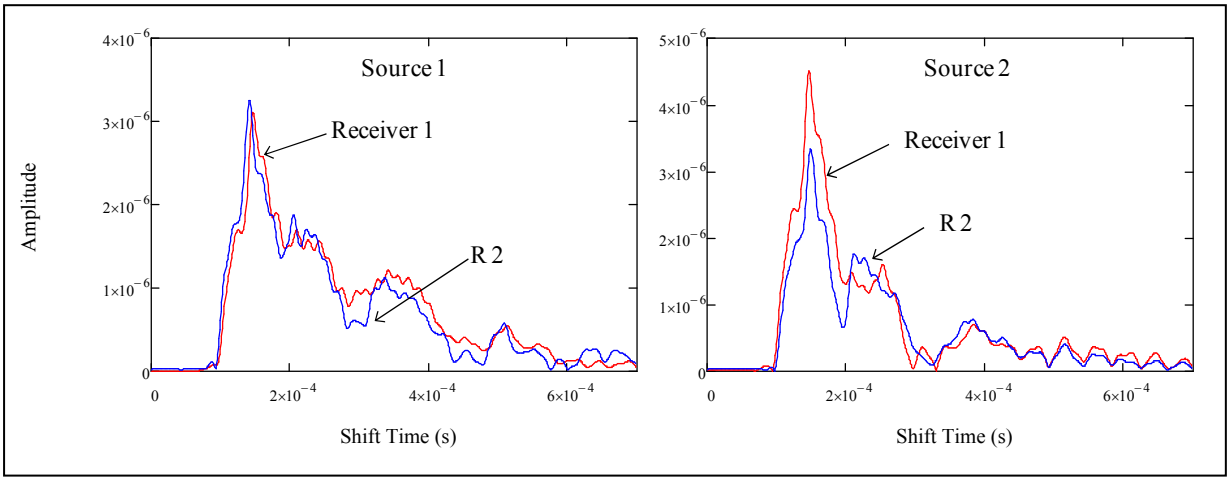

Figure D-4. Wavelet transform for Square 1, Morlet center frequency of 25 kHz.

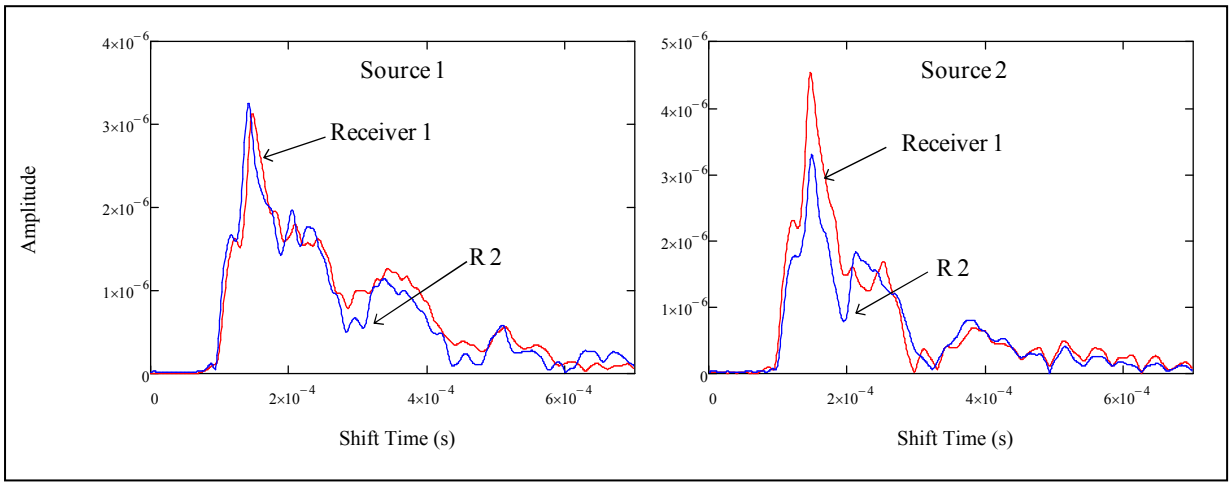

Figure D-5. Wavelet transform for Square 1, Morlet center frequency of 30 kHz.

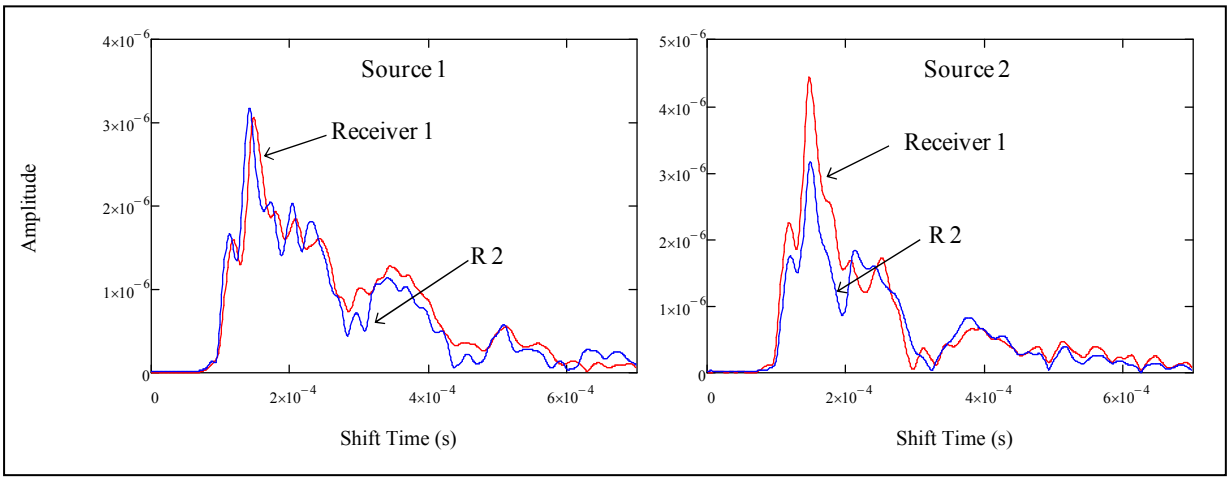

Figure D-6. Wavelet transform for Square 1, Morlet center frequency of 35 kHz.

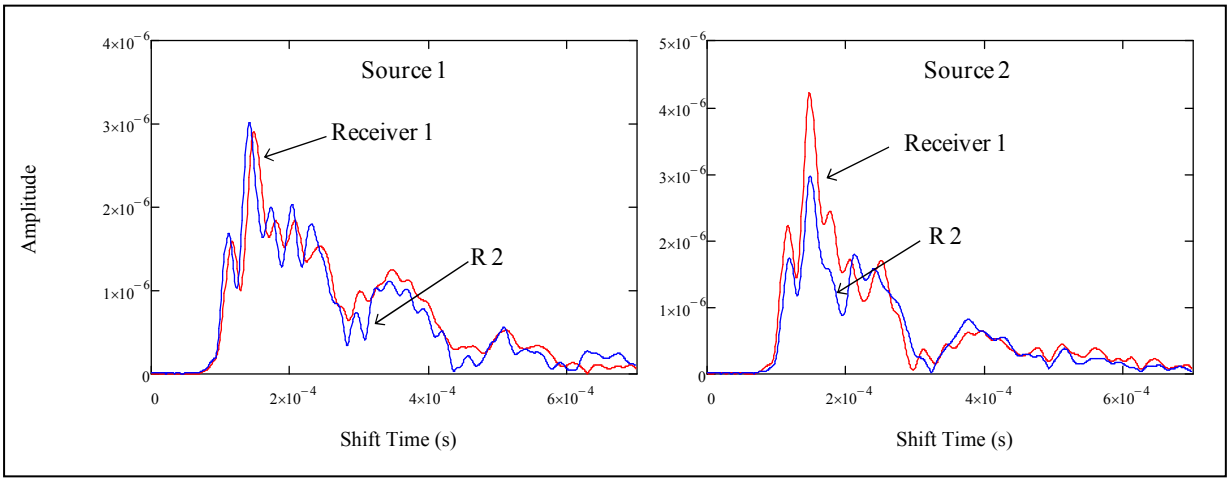

Figure D-7. Wavelet transform for Square 1, Morlet center frequency of 40 kHz.

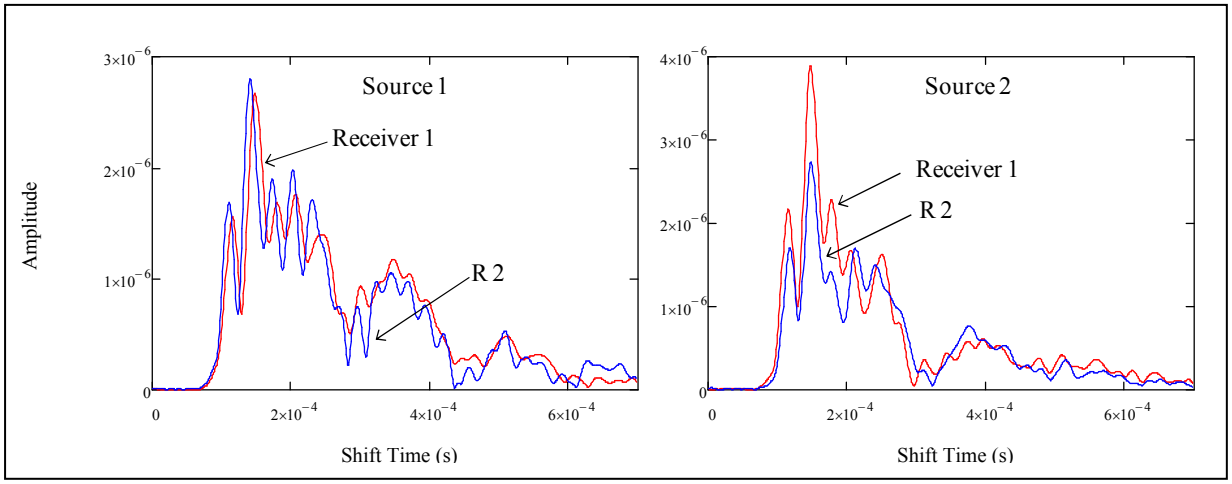

Figure D-8. Wavelet transform for Square 1, Morlet center frequency of 45 kHz.

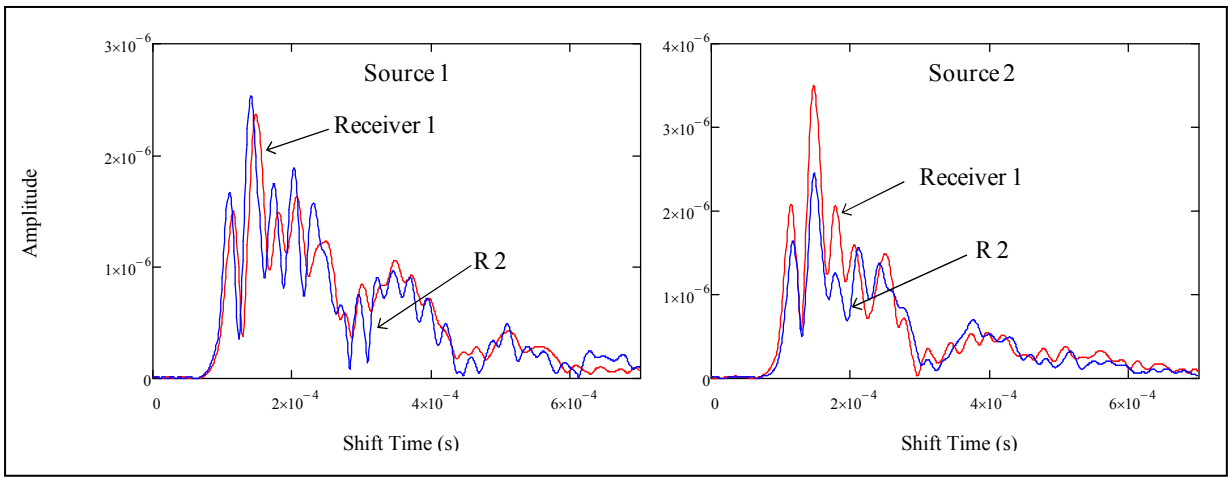

Figure D-9. Wavelet transform for Square 1, Morlet center frequency of 50 kHz.

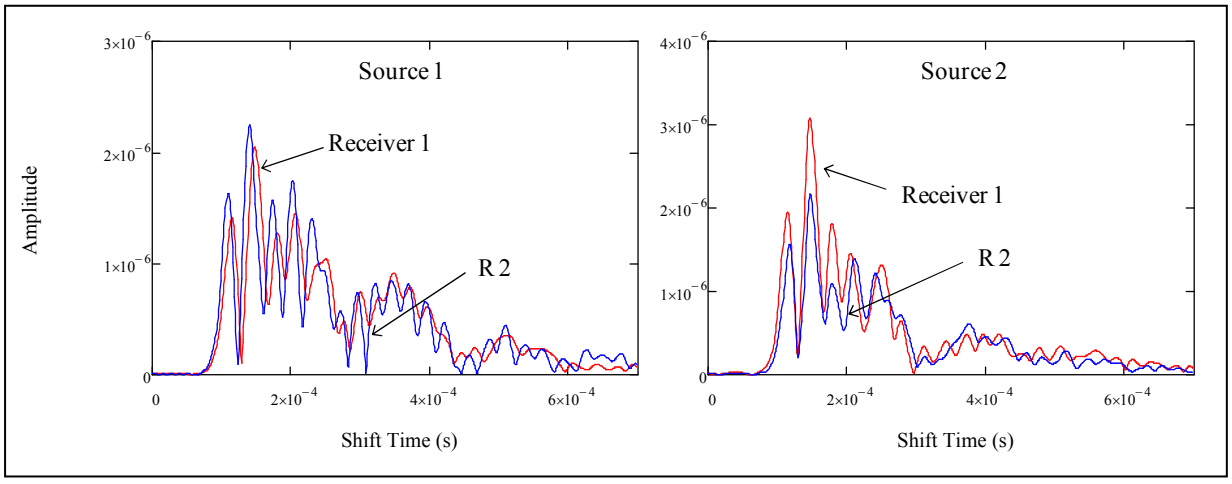

Figure D-10. Wavelet transform for Square 1, Morlet center frequency of 55 kHz.

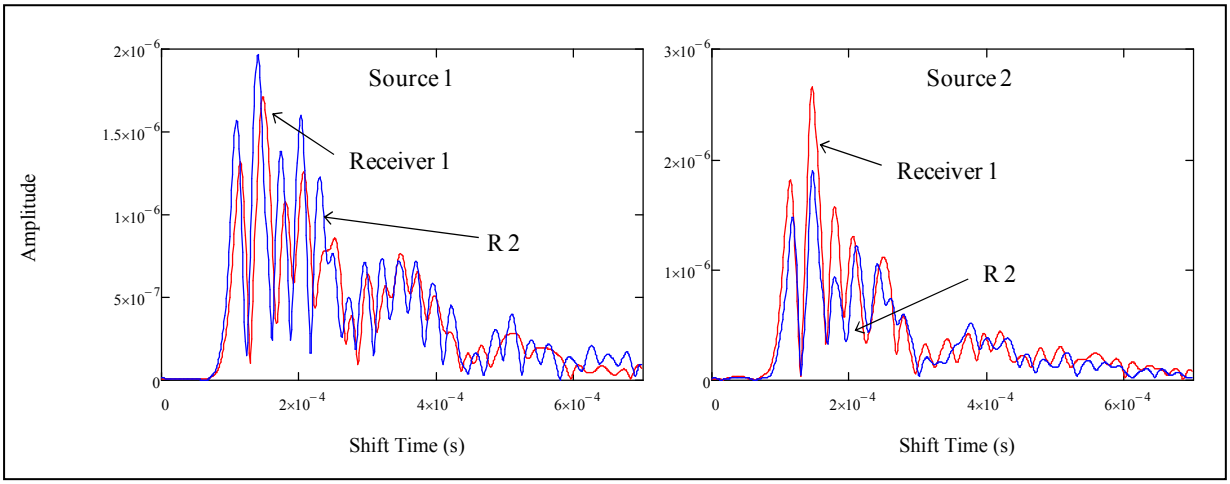

Figure D-11. Wavelet transform for Square 1, Morlet center frequency of 60 kHz.